Superconducting Circuit Architectures Based on Waveguide Quantum Electrodynamics

Thesis by
Xueyue Zhang

In Partial Fulfillment of the Requirements for the
Degree of
Doctor of Philosophy

CALIFORNIA INSTITUTE OF TECHNOLOGY
Pasadena, California

2023
Defended February 21st, 2023

Xueyue Zhang
ORCID: 0000-0001-8994-0629

To my parents 李春玲 and 张启明.
And to my partner Tianyi Peng.

ACKNOWLEDGEMENTS

It has been five and a half years since I started my journey as a PhD student on the beautiful campus of Caltech. This is a fantastic journey full of cherished experiences. Whether rosy or frustrating, these experiences have transformed me from a student who has always marveled at the progress of science and technology to a researcher who can contribute to the frontier of quantum information and physics. In studying light-matter interaction and qubit-qubit interaction, I have realized that the driving force of scientific progress is rooted in human-human interaction. Deeply and dearly, I adore the interaction with *everyone* throughout my PhD journey, especially my mentors, colleagues, collaborators, friends, and family, who made me a better researcher and, above all, a better person.

First, I want to express my deepest gratitude to my advisor, Oskar Painter, for his unwavering support and guidance throughout these years. His encouragement and belief in my abilities were instrumental for me to venture into the quantum research despite my initial lack of experience. I enjoyed every single discussion with Oskar, who epitomizes the mantra of dreaming the wildest dreams while digging into the most down-to-earth details. On the one hand, his passion and faith in research have always inspired me to get through difficult moments. On the other hand, his high standard and striving for excellence have constantly pushed me to reach beyond where I would have stopped on my own. In addition, his open-mindedness and trust in me allow me to take the ownership and responsibility of steering and shaping the projects, in which process I truly grow as a researcher. Most importantly, the resources he has secured for the group and the team he has assembled are the foundation for everything I have accomplished during my PhD. I cannot thank Oskar more or convey how indebted I am to have him as my advisor.

Now I want to highlight my gratefulness to a special team member, my closest colleague Eunjong Kim. We have been in the same subgroup for the entire span of my PhD, and this human-human interaction has been the direct cornerstone of my thesis work. Eunjong's keen insights, technical expertise, and unyielding work ethic have played a critical role in the success of our research projects. I have learned so much from him in both the most detailed technical aspects and his rigorous and systematic approach toward research. Especially, I want to thank Eunjong for taking on many, sometimes literally, heavy-lifting tasks, which allows me to focus on other aspects in order to push the projects forward with minimal distraction. I am really

fortunate to have spent the majority of my PhD discussing, collaborating, and having scientific fun with such a talented and dedicated individual.

The rest of the group are just as fabulous. Vinicius Ferreira and Jash Banker were the other two members of our then "junior" club, along with Eunjong and me. Together, we studied pedagogical materials, attended a winter school, and designed waveguide QED systems. Their optimistic attitude, constant camaraderie, and unconditional support have made them the best companion I could ever wish to have for five years. The former postdocs in the group, Mohammad Mirhosseini, Alp Sipahigil, and Andrew Keller, are among the most brilliant researchers and inspiring mentors I have ever met. I am forever grateful for the time and effort they have invested in me, which helped me to take the first few baby steps in my PhD, to build my knowledge and skill networks from the ground up, and to tackle different problems with a better mindset. When I feel lost, I always benefit from thinking about how they would approach this issue if they were me. My former office mates Jie (Roger) Luo and Hengjiang (Jared) Ren offered me the warmest welcome and invaluable help when I started to navigate the new environment. Their entrepreneurial mindset and exceptional execution ability have always been an inspiration for me. I cannot express enough gratitude for their steadfast friendship and support throughout my journey. As a junior student, I also received constant guidance and assistance from Michael Fang, Mahmoud Kalaee, Greg MacCabe, and Kejie Fang, who answered my numerous questions and trained me to use cleanroom tools.

New faces always bring fresh perspectives into the group. On the superconducting circuit side, Clai Owens, Mo Chen, Andreas Butler, and Gihwan Kim are never afraid of investigating novel directions. Mo's optimistic attitude always makes our conversations inspiring and uplifting. Gihwan and Andreas have grown to be extremely capable researchers, and I am sure the future of our experiments is in good hands. On the transduction and optomechanics side, Srujan Meesala, David Lake, Steven Wood, Piero Chiappina, Sameer Sonar, and Utku Hatipoglu have never failed to amaze me with the complexity of their fabrication and measurement during our lunch chats. Their broad knowledge in multiple different fields and their great perseverance against difficulties are what I admire deeply. My mentees (SURF students) Aziza Almanakly, Zhaoyi (Joy) Zheng, and Emily Parnell elevated my position to a mentor. Teaching them and answering their excellent questions allowed me to consolidate my knowledge, think extra layers deeper, and even learn something new. It is also extremely fulfilling to see them grow as researchers and

take on more responsibilities.

In the group, students and postdocs come and go, but “the fabulous ones” are always there. I want to express my heartfelt appreciation to the technical staff Barry Baker, Matthew McCoy, Brendon Larrowe, and (former members) Kamal Yadav, Xinyu (Harry) Liu, and Alireza Ghaffari, as well as Guy DeRose and Mathew Hunt at KNI, who have maintained the labs and the cleanrooms in good shape to enable all the great science. I am especially indebted to Barry for helping me in the cleanroom on a few Friday evenings. I also want to thank the administrative staff Angie Riley, and (former members) Christy Jenstad, Jonathan Gross, and Elizabeth Rodriguez. Specifically, Angie and Christy are so on top of things that purchasing and ordering have been extremely streamlined to make our lives much easier.

Beyond the group, I have greatly benefited from engaging in discussions with our collaborators and other brilliant minds. I want to express my sincere gratitude to our theory collaborators Soonwon Choi, Daniel Mark, Alejandro González-Tudela, Miguel Bello, Joe Iverson, Darrick Chang, and Ana Asenjo-Garcia. In the most recent project, I have acquired a good amount of many-body physics knowledge from Soonwon and Daniel, who are able to explain to experimentalists the most abstract concepts in the most crystal clear way. Their insights and perspectives were instrumental in taking this project to another level. Alejandro has been my theory guide in waveguide QED, who always replies to my questions in great detail and with patience. During the brainstorming stage of the projects and when I sought career advice, I am privileged to have talked to many exceptional scholars, including Alexey Gorshkov, Olexei Motrunich, Ruichao (Alex) Ma, Fernando Brandão, Gil Refael, Manuel Endres, Andrei Faraon, Xie Chen, Hans Peter Büchler, Joonhee Choi, Norman Yao, David Schuster, Amir Safavi-Naeini, and Jonathan Simon. These conversations have always been enlightening and have had a long-lasting impact on both my research and my path forward.

Outside of research, I want to extend my gratitude to the people who have made my journey smooth and enjoyable. Jennifer Blankenship, Christy Jenstad, Marcia Brown, and Tiffany Kimoto have been organizing wonderful events and seminars that hold the tightly-knit community together, even during the difficult time of the pandemic. Laura Flower Kim and other members of the ISP have provided great assistance regarding my international scholar status. Erin Burkett at the writing center has spent numerous sessions offering excellent writing advice and helping me polish my materials, including part of this thesis. I also want to thank all the staff members, especially the gym staff, the dining service members, and the residential community team, who have made my Caltech experience truly wonderful.

I am fortunate and grateful to have a group of friends who have been with me through this journey. My cohort, especially the quantum gang Mi Lei and Andrei Ruskuc, have shared so many common experiences with me in taking classes, attending seminars and conferences, and thinking about the next stop after graduate school. I spent most of my spare time with my sports friends, who have always kept me in great companionship during and after the training sessions, celebrating many holidays together. Especially, the badminton club has been an extended family for me and many other scholars far away from our home. In particular, I want to highlight my thankfulness to my badminton club members, including Shao-Min (Sean) Hung (coach), Yue Yang, Po-Chih Chen, and Anqi Liu (also my mentor in the Women Mentoring Women program), as well as my martial art instructors Ricardo Hassan and William Glenn, and my running group leader Charley Lu. All of them have trained me from a complete novice to the level where I can enjoy these sports. The quantum random chat group organized by Tian-Xing Zheng and Pai Peng is another gem. The passion and curiosity of this group of friends have been a constant source of inspiration for me. In more relaxed settings, I cherish all the ordinary yet memorable moments when I hang out, have good food, or just chat with my friends, including Linghui Wang, Xiang Li, Cheng Zhang, Yujia Huang, Yuelin Shi, Lixue Cheng, Shumao Zhang, Guanya Shi, and Prachi Thureja.

Finally, I could have never come this far without my dearest family. Despite my parents' moderate academic background, they have always placed my education above their needs. The most important part of this education has instilled in me virtues such as perseverance and compassion, which I value more than any knowledge I have learned. Their unconditional and unending love and support have allowed me to pursue my dreams regardless of all the ups and downs. I am also extremely fortunate to have my partner Tianyi, who has been holding my hands through five years of a coast-to-coast relationship. His optimism, patience, understanding, and unwavering encouragement have been the sunshine that lights me up even in the darkest moments. Tianyi has joined my parents as my most robust safety net and a constant source of strength. I could never show enough appreciation but dedicate this thesis to them, with all my love.

ABSTRACT

Quantum science and technology provides new possibilities in processing information, simulating novel materials, and answering fundamental questions beyond the reach of classical methods. Realizing these goals relies on the advancement of physical platforms, among which superconducting circuits have been one of the leading candidates offering complete control and read-out over individual qubits and the potential to scale up. However, most circuit-based multi-qubit architectures only include nearest-neighbor (NN) coupling between qubits, which limits the efficient implementation of low-overhead quantum error correction and access to a wide range of physical models using analog quantum simulation.

This challenge can be overcome by introducing non-local degrees of freedom. For example, photons in a shared channel between qubits can mediate long-range qubit-qubit coupling arising from light-matter interaction. In addition, constructing a scalable architecture requires this channel to be intrinsically extensible, in which case a one-dimensional waveguide is an ideal structure providing the extensible direction as well as strong light-matter interaction.

In this thesis, we explore superconducting circuit architectures based on light-matter interactions in waveguide quantum electrodynamics (QED) systems. These architectures in return allow us to study light-matter interaction, demonstrating strong coupling in the open environment of a waveguide by employing sub-radiant states resulting from collective effects. We further engineer the waveguide dispersion to enter the topological photonics regime, exploring interactions between qubits that are mediated by photons with topological properties. Finally, towards the goals of quantum information processing and simulation, we settle into a multi-qubit architecture where the photon-mediated interaction between qubits exhibits tunable range and strength. We use this multi-qubit architecture to construct a lattice with tunable connectivity for strongly interacting microwave photons, synthesizing a quantum many-body model to explore chaotic dynamics. The architectures in this thesis introduce scalable beyond-NN coupling between superconducting qubits, opening the door to the exploration of many-body physics with long-range coupling and efficient implementation of quantum information processing protocols.

PUBLISHED CONTENT AND CONTRIBUTIONS

[1] Xueyue Zhang, Eunjong Kim, Daniel K. Mark, Soonwon Choi, and Oskar Painter. "A superconducting quantum simulator based on a photonic-bandgap metamaterial". In: *Science* 379.6629 (2023), pp. 278–283. DOI: 10.1126/science.ade7651.
X.Z. came up with the concept and planned the experiment, performed the design, simulation, and fabrication of the device, performed the measurement, analyzed the data, and participated in the writing of the manuscript. X.Z. and E.K. contributed equally to this work.

[2] Eunjong Kim, Xueyue Zhang, Vinicius S. Ferreira, Jash Banker, Joseph K. Iverson, Alp Sipahigil, Miguel Bello, Alejandro González-Tudela, Mohammad Mirhosseini, and Oskar Painter. "Quantum electrodynamics in a topological waveguide". In: *Phys. Rev. X* 11.1 (2021), p. 011015. DOI: 10.1103/PhysRevX.11.011015.
X.Z. came up with the concept and planned the experiment, performed the design, simulation, and fabrication of the device, performed the measurement, analyzed the data, and participated in the writing of the manuscript. X.Z. and E.K. contributed equally to this work.

[3] Mohammad Mirhosseini, Eunjong Kim, Xueyue Zhang, Alp Sipahigil, Paul B. Dieterle, Andrew J. Keller, Ana Asenjo-Garcia, Darrick E. Chang, and Oskar Painter. "Cavity quantum electrodynamics with atom-like mirrors". In: *Nature* 569.7758 (2019), pp. 692–697. DOI: 10.1038/s41586-019-1196-1.
X.Z. participated in the design, simulation, and fabrication of the device, performed the measurement, analyzed the data, and participated in the writing of the manuscript.

TABLE OF CONTENTS

LIST OF FIGURES

LIST OF TABLES

Chapter 1

INTRODUCTION

A little over a century ago, the efforts to address what Kelvin noted as a "cloud" in the otherwise "beautiful and clear sky" of physical theory [1] introduced quantum mechanics, a new pillar of physics. From the early study of black-body radiation [2] and the photoelectric effect [3], to the progress over decades in testing Bell's inequality and its generalizations [4–8], quantum mechanics has been shown to govern the microscopic world. Although peculiar on its own, quantum mechanics underpins major branches of modern physics, including atomic, molecular, and optical (AMO) physics, condensed matter physics, and high energy physics. Beyond these areas, quantum mechanics has also deeply influenced and spawned new directions in material science, electrical engineering, and chemistry.

Another paradigm shift happened in the 1970s and 1980s when people started to view the quantum systems, traditionally as the object to understand, from a new angle: as the object for us to *design* and *control*. In particular, the connection to computer science and information theory has predicted the usage of quantum systems in a broad range of tasks to achieve advantages beyond the capability of classical systems [9]. This paradigm shift has stimulated the rapid development of experimental techniques across various physical platforms, including superconducting circuits [10, 11], solid-state spin systems [12], trapped ions [13], ultracold atoms or molecules [14–16], and quantum optical systems [17]. The experimental advance has in turn presented intriguing questions for theorists to ponder. This lively interaction has been pushing the frontier of quantum science and engineering, especially in answering the questions at the heart of this field: (i) how to build versatile and accurately controlled quantum systems on a large scale, and (ii) how to use them to further our understanding of important subjects.

This introductory chapter provides an overview of the background and context for a broad audience, setting the stage for our efforts in answering the above two questions. More specifically, with the goal of quantum computation and quantum simulation in mind, we focus on one of the most promising platforms—superconducting circuits. We discuss the advantages of this platform and point out a gap between the conventional superconducting circuit architectures and a large-scale versatile quantum system with good control. After the introduction of the tool—quantum light-matter interactions—to fill this gap, we end this chapter by outlining our work of building controlled quantum systems and using them to study questions that were out of experimental reach before.

1.1 Quantum information science

Based on the principles of quantum mechanics, a quantum computer works differently compared to its classical counterpart. The building block of a typical classical computer is a *bit* with the value of either "0" or "1". In analogy, the most common type of a discrete-variable quantum information processor is based on *quantum bits* (*qubits* in short), which not only takes the value of $|0\rangle$ or $|1\rangle$ but also the *superposition* of the two states $|\psi\rangle = \alpha|0\rangle + \beta|1\rangle$ where α, β are complex numbers satisfying $|\alpha|^2 + |\beta|^2 = 1$. Intuitively, a *qubit* carries a greater amount of information than a *bit* (Fig. 1.1a). This advantage scales favorably for a quantum information processor where the *entanglement* among the qubits exponentially extends the dimension of the computational space. Lastly, we extract the result from quantum operations via measurements that, for example, collapse a qubit into either $|0\rangle$ or $|1\rangle$. In the end, we are back to the classical world. Nonetheless, the clever design of quantum algorithms can utilize the quantumness, e.g., by quantum interference and mapping the results to a state whose measurement outcome can be interpreted easily. Among the best-known quantum algorithms are Shor's algorithm for finding prime factors of an integer that offers beyond-polynomial speedup [18] and the Grover's search algorithm with a more modest speedup [19]. Contemporary quantum algorithms (a growing *Quantum Algorithm Zoo* can be found in [20]) have extended to areas including approximation, optimization, and machine learning.

The grand vision of quantum information processing also comes with grand challenges. In addition to reliably controlling and reading out the quantum states, we need to cope with errors in the process. On the one hand, the richer content of a qubit $|\psi\rangle$ gives rise to a broader range of errors than the classical bit-flip errors. On the other hand, the quantum states, usually microscopic or residing at the bottom of the energy landscape, are more susceptible to occasional random perturbations, even in the form of slight changes in the nearby atomic arrangements or the presence of a single photon. Therefore, error correction is necessary in order to process quantum information faithfully. For example, the classical repetition code [24] encodes "x" in, e.g., "xxx" with x = 0 or 1. The quantum version of this repetition code also

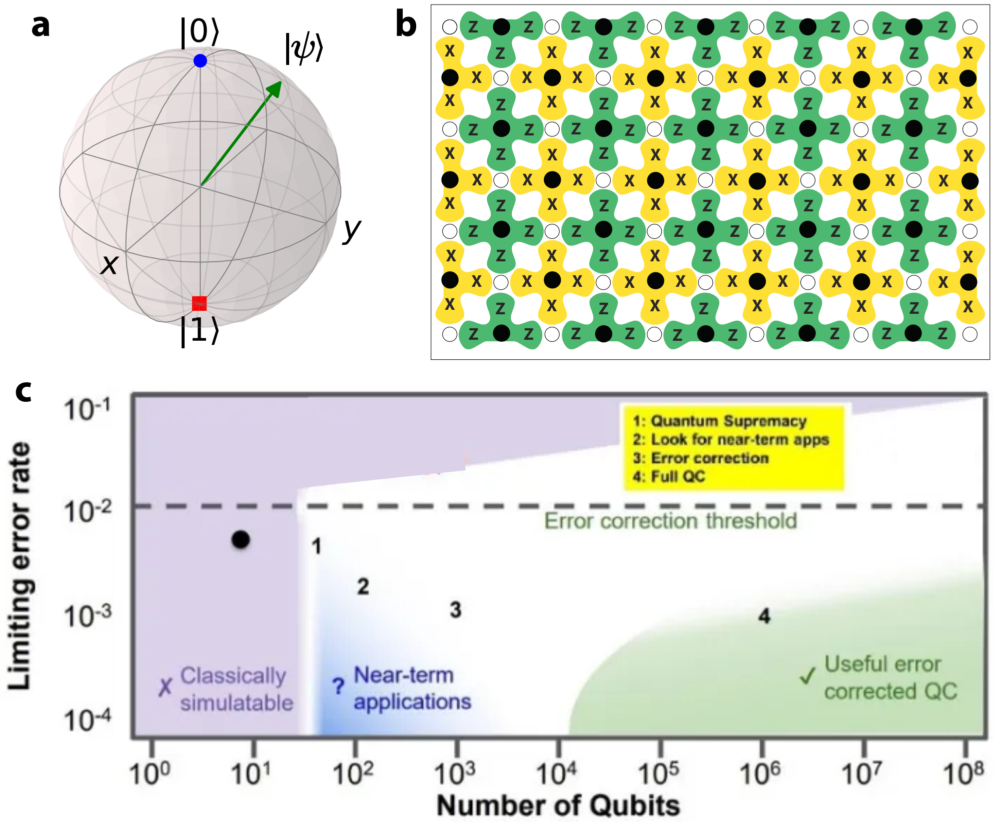

Figure 1.1: **Quantum information processing.** **a**, Comparison between a classical bit and a quantum bit. A classical bit takes the value of "0" (blue dot) or "1" (red square), whereas a quantum bit $|\psi\rangle$ (green arrow) can represent any point on a Bloch sphere. This panel was generated using QuTiP [21]. **b**, Schematic of the surface code [22]. Each white (black) circle represents a data (ancilla) qubit. The green and yellow marks represent operations to check whether an error has happened. The panel is adapted from [23], reprinted with permission from the copyright holder, APS. **c**, Different developing stages of quantum information processing as a function of error rate and the number of qubits. The panel is adapted from a presentation by Dr. John Martinis in his tenure at Google, reprinted with permission from Dr. Martinis.

uses redundancy to overcome bit-flip or/and sign-flip errors for a qubit [25, 26]. For a quantum error correction code, important metrics include n, the number of physical qubits to implement the code, k, the number of error correctable logical qubits, d, the code distance, i.e., the minimum number of errors needed to convert one code word into another, and ϵ^*, the physical error rate threshold below which the logical error rate can be suppressed by implementing the error correction code (see, e.g., [27]). Considering the experimental realization, the topological quantum error correction codes epitomized by Kitaev's toric code and surface code [22] have received broad attention, due to their high threshold and compatibility with physical platforms featuring only nearest-neighbor connectivity on a two-dimensional plane (Fig. 1.1b). In the last decade or so, the technical advancement in controlling and probing bosonic degrees of freedom with long coherence time (the time a quantum state can retain its information) has spurred the development of bosonic quantum error correction codes [28, 29]. This development has in turn led to the first few experimental achievements of the break-even point [30–32] where the logical error rate is measured to be lower than the lowest physical error rate of the constituents. While the basic quantum error correction only considers the errors happening through a quantum channel and assumes the encoding and decoding operations are perfect, this assumption is not valid for realistic physical implementations. Therefore, as the realization of quantum error correction comes within reach, the concept of fault tolerance [33, 34] is considered more important, where the entire process of encoding, error correction, logical operation, and measurement is under scrutiny and protocols are devised to control the creation and propagation of errors. In general, fault-tolerant quantum computation is the path towards building a large-scale universal quantum computer and realizing the powerful quantum algorithms mentioned above.

While achieving fault tolerance remains the ultimate yet daunting goal (lower right corner of Fig. 1.1c), current physical platforms already feature above 50 qubits with imperfect, up to individual-level controllability. It is valuable to consider what algorithms or tasks can be implemented on these noisy intermediate-scale quantum (NISQ) devices without error correction [35] (between the blue and purple region of Fig. 1.1c). One inspiration came from the well-known quote by Richard Feynman [36]: "Nature isn't classical, dammit, and if you want to make a simulation of nature, you'd better make it quantum mechanical." Within the reach of NISQ devices, variational quantum algorithms [37] and analog or hybrid analog-digital quantum simulation [38] have been implemented. Their applications cover a wide range of fields, including quantum chemistry, optimization problems, condensed matter physics, and high-energy physics. The recent development in physical platforms steadily improves the qubit number and the control fidelity, at the same time introducing higher levels of programmability and partial-system measurement in the middle of a quantum simulation. These advancements are filling the gap before we can achieve general-purpose quantum computing by showing potential quantum advantages in tackling long-standing problems that are hard to simulate classically

[38]. In addition to providing valuable information that is not readily accessible in, e.g., a condensed matter sample, the quantum simulators also construct systems beyond natural analogs [39] such as hyperbolic lattices [40] and time crystals [41, 42]. Specifically, synthesizing materials using quantum simulators, a bottom-up approach, offers a complement to the top-down condensed matter approaches. For example, ultracold atoms in optical lattices [14] offer single-site state read-out resolution to study strongly interacting fermions or bosons, the former of which is deemed to be the foundation of high-temperature superconductivity. The tunability and individual control of the trapped ion quantum simulators [13, 43] enable the exploration of non-equilibrium many-body dynamics in quantum magnets, including the non-local propagation of two-site correlations [44, 45] and various universal dynamical classes [46]. The reservoir engineering using superconducting circuits allows the study of the quantum dynamics of an open system [47] and the usage of the reservoir to stabilize many-body ground state [48]. These examples, among many experimental quantum simulation efforts, shed light on how current and future NISQ devices contribute to answering questions intractable for both experiments on natural systems and classical simulations.

1.2 Superconducting circuits

Towards the goals of quantum information science ranging from general-purpose quantum computing to NISQ-era quantum simulation, superconducting circuits [10, 11] have become one of the leading physical platforms. For quantum devices with more than 50 individually controllable qubits (see, e.g., [49–52]), the fidelity of arbitrary single-qubit control is above 99.9%, the two-qubit entangling gate fidelity is above 99.5%, and the fidelity to perform single-shot individual qubit read-out is above 95%. The entangling gate time is typically below 50 ns compared to the coherence time of tens or hundreds of micro-second. The multi-qubit devices have been used to implement quantum error correction codes, including the quantum repetition code and the surface code [50, 53–55], demonstrating modest improvement in suppressing logic error as the size of the code scales. Using these devices, various NISQ applications have also been explored, covering quantum many-body simulation and material synthesis [39, 56, 57], quantum chemistry and variational algorithms for optimizations [58–64], and machine learning [65]. Apart from the multi-qubit devices, smaller-scale superconducting circuits centered on bosonic degrees of freedom excel as the first system to achieve and go beyond the break-even point in quantum error correction [30–32].

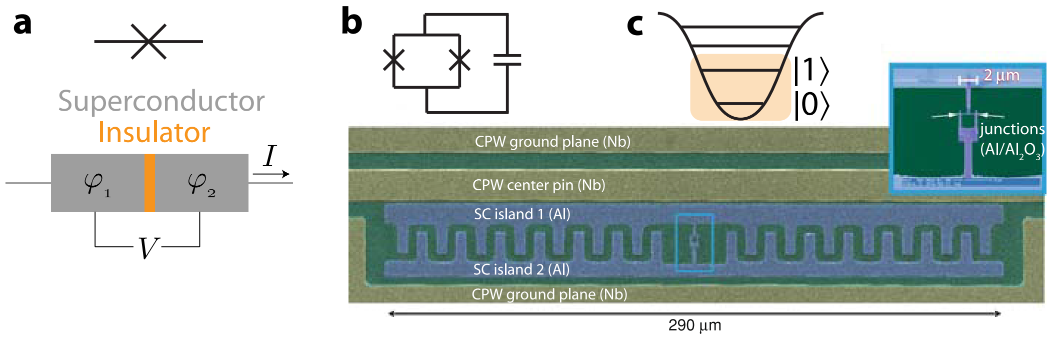

Figure 1.2: **Superconducting quantum components.** **a**, Josephson junction: circuit symbol (upper panel) and schematics of a thin layer of an insulator sandwiched by two superconductors (lower panel). The phase across the junction is $\varphi = \varphi_1 - \varphi_2$. **b**, Frequency tunable transmon qubit: circuit diagram (upper panel) and a false-colored image (lower panel). The inset shows the zoomed-in view of the loop of two parallel junctions (SQUID). The panel is adapted from [66], reprinted with permission from the copyright holder, Springer Nature. **c**, Cartoon showing the energy level structure of a transmon qubit with an anharmonic oscillator potential and eigen-energies lying on an unevenly spaced ladder. The lowest two levels ($|0\rangle$ and $|1\rangle$) shaded in orange form the qubit subspace.

The key element enabling such a quantum platform is the Josephson junction, which consists of a thin barrier or weak link connecting two superconductors (Fig. 1.2a). In this structure, the Josephson effect [67, 68] dictates that the voltage $V(t)$ and current $I(t)$ across the junction follow the relations:

$$I(t) = I_c \sin(\varphi(t)) \tag{1.1}$$

$$\frac{\partial \varphi}{\partial t} = \frac{2eV(t)}{\hbar}, \tag{1.2}$$

where I_c is a junction parameter called the critical current, φ is the superconducting phase difference across the junction, and e is the charge of an electron. This set of equations defines an effective nonlinear inductor, whose nonlinearity is so strong that together with other dissipation-less circuit elements, Josephson junctions can be used to construct mesoscopic artificial atoms. A prominent example is one of the most mature types of superconducting qubits: the transmon qubit [69] (Fig. 1.2b), which consists of a Josephson junction and its shunt capacitor. The Josephson junction makes this parallel LC circuit an *anharmonic* oscillator whose lowest two-level transition can be resolved from the higher transitions and thus can be controlled unambiguously (Fig. 1.2c). These two levels serve as the basis states $|0\rangle$ and $|1\rangle$ (also denoted as ground $|g\rangle$ and excited $|e\rangle$ states) discussed in Sec. 1.1 and form the qubit subspace. This two-level system can be prepared in an arbitrary qubit state $|\psi\rangle$ via a microwave pulse resonant to this transition (XY control). Additionally, the energy spacing of this qubit is tunable when the nonlinear inductor is composed of two parallel Josephson junctions forming a loop (a superconducting quantum interference device, also known as SQUID). In this case, the magnetic flux threading the loop changes the total effective I_c and therefore the transition frequency of this qubit (Z control). To read out the state of the qubit, the most common method is to couple the qubit with a far-detuned microwave resonator. The weak hybridization between the qubit and the resonator gives rise to a qubit-state-dependent resonator frequency. Probing the read-out resonator frequency by sending in a microwave tone allows us to deduce the state of the qubit.

Thanks to the above mature control and read-out toolkit and the long coherence time, transmon qubits have been the dominant constituents for multi-qubit superconducting quantum devices. At the architecture level, the most popular way to construct a general-purpose quantum computer keeping fault tolerance in mind is to place the transmon qubits at the vertices of a two-dimensional (2D) lattice, e.g., a square lattice (Fig. 1.3a and b). The qubits directly connected with an edge are coupled via either direct near-field coupling or a coupler, realizing 2D nearest-neighbor connectivity suitable for implementing the surface code [22]. This general architecture and its one-dimensional version, which is natural and technically easy to implement, has also been the mainstream for quantum simulation purposes.

However, the nearest-neighbor (NN) connectivity has its limitations. For example, although the surface code has exceptionally high error threshold, it is also associated with costly overhead. In fact, the family of quantum low-density parity-check (LDPC) code [34, 71], which the surface code belongs to, exhibits the trade-off between the number of logical qubits k and the code distance d introduced in Sec. 1.1 as $kd^2 \sim O(n)$ [72, 73], where n is the number of physical qubits in an locally connected architecture. This constraint makes the realization of fault-tolerant quantum computing an extremely daunting task requiring a formidable amount of physical qubits due to the low code rate k/n. The recent development of high-rate quantum LDPC codes show the potential of reducing the overhead by more than an order of magnitude compared to the surface code [70, 74]. The major obstacle to implement such high-rate codes lies in the lack of long-range connectivity (Fig. 1.3c)

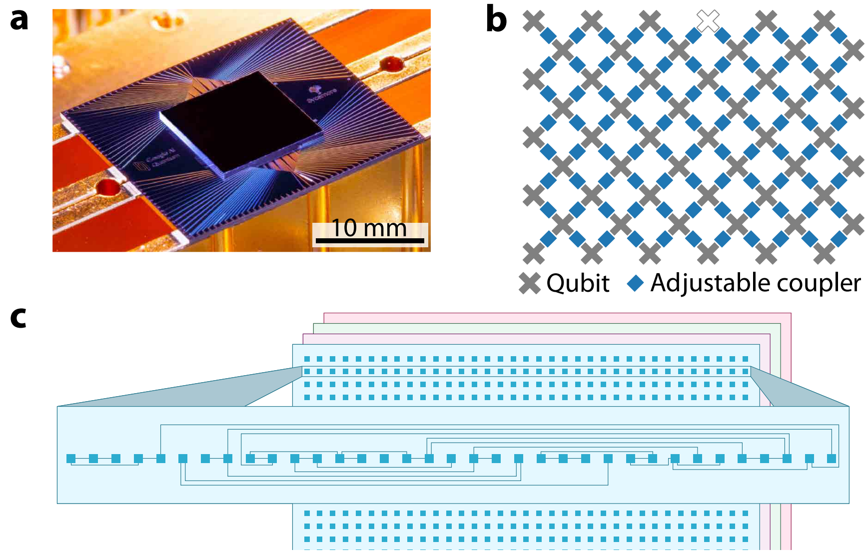

Figure 1.3: **Superconducting quantum processors and architectures. a**, Optical image of the Sycamore quantum processor from Google. **b**, The layout schematics of the Sycamore process. Panels **a** and **b** are adapted from [49], reprinted with permission from the copyright holder, Springer Nature. **c**, The schematics of a proposed architecture to implement high-rate quantum LDPC code. The qubits are still on a 2D grid with additional long-range coupling between beyond-nearest-neighbor qubits. The panel is adapted from [70], reprinted with permission from the copyright holder, APS.

in mainstream architectures.

The limitation of NN connectivity is more profound in quantum simulations. An important application of quantum technology is to simulate chemical or material structures, reactions, and even dynamics, where the electrons are the basic constituent [75, 76]. To simulate the electrons using superconducting qubits [59, 62, 77]—spin systems in nature, we need to perform the Jordan-Wigner transformation [78], which maps an electron to non-local combinations of spins. As a result, the interaction between electrons translates to non-local interaction between spins, which is inefficient to implement in an NN-connected architecture with finite error rate in every operation. Moreover, the NN connectivity directly limits the analog or analog-digital hybrid quantum simulations, where the Hamiltonian to study is emulated by the quantum simulator. The NN constraint precludes the access to a broad range of Hamiltonians, including the ones featuring fast spreading of entanglement [44, 45, 79–82], the ones with exotic ground states as a result of frustration [83–91], and the ones exhibiting non-equilibrium dynamics belonging to different universal classes [46]. Further, long-range connectivity also increases classical simulation complexity [92], enabling easier access to the regime where NISQ devices exhibit quantum simulation advantage over classical computers. These prospects in both fault-tolerant quantum computation and NISQ-era quantum simulation have being calling for a superconducting circuit architecture with beyond-NN connectivity.

1.3 Quantum light-matter interfaces

The study of light-matter interaction [93, 94] plays an essential role in major topics of physics, ranging from the laser theory [95] in AMO physics to probing or imaging techniques [96] in chemical or condensed matter physics. Especially, light-matter interaction provides an indispensable toolbox to control a quantum system, driving the experimental progress in quantum information science discussed in Sec. 1.1. A strong light field driving a two-level transition in, e.g., an atom, can be formulated by the driven two level system model and gives rise to the Rabi oscillation often used for the XY control. In the other limit, when the quantized light fields are in their ground state (i.e., the vacuum), the process of the atom starting from a higher-energy (excited) state and emitting into its surrounding light fields can be described by spontaneous emission (Fig. 1.4a). This process leads to exponential decay of the excited state population, a basic form of decoherence and an important starting point to study a quantum system in an open environment. In between the two limits where bi-directional interaction between an atom and quantized light fields take place, the key is to achieve the *strong coupling regime* where the interaction happens faster than the ubiquitous spontaneous decay. The coupling strength g exhibits the relation $g \propto |\mathbf{d}|/\sqrt{V}$ [93], where $\mathbf{d}$ is the transition dipole moment and V is the mode volume of the light field.

To enhance the light-matter interaction, a common approach is to confine the light field in a cavity such that the mode volume is small enough (Fig. 1.4b). This approach has led to the fruitful field of cavity quantum electrodynamics (QED). The experimental realization of cavity QED was pioneered in the microwave domain by the Haroche group using Rydberg atoms coupled to a superconducting cavity [97] and in the optical domain by the Kimble group using low-loss Fabry-Pérot cavities [98] and microtoroid cavities [99]. Cavity QED has enabled important techniques such as the usage of a cavity to change the environment of a quantum emitter and thus control its emission rate, as described by the Purcell effect [100]. The Purcell effect has been widely used for both cold atoms and solid-state quantum emitters in

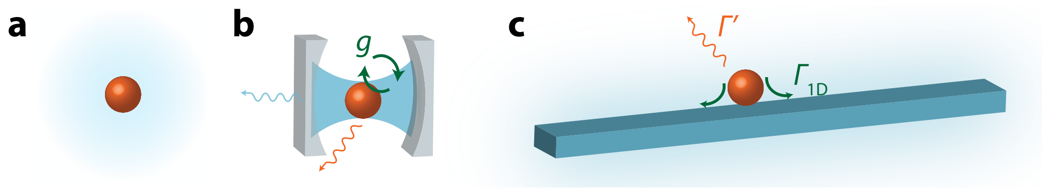

Figure 1.4: **Schematics of quantum light-matter interaction interfaces.** **a**, A quantum emitter (red ball) in free space (light blue shade). **b**, Cavity QED: a quantum emitter couples to the cavity field (blue) with rate g. The orange wavy arrow represents the spontaneous decay rate of the emitter and the blue arrow is for the cavity. **c**, Waveguide QED: a quantum emitter couples to a waveguide (blue) with the emission rate into the waveguide Γ_{1D} and spurious emission rate Γ'.

applications such as the quantum network [101] and photonic quantum computing [102]. Moreover, the cavity field shared by, e.g., atoms serves as a medium to induce all-to-all coupling between the atoms, creating highly-entangled states valuable for quantum sensing [103] and metrology [104]. For superconducting circuits, cavity QED acts as the foundation of qubit state read-out via a microwave resonator in the dispersive regime where the qubit and the resonator are far detuned [105]. Additionally, thanks to the large dipole moment $|\mathbf{d}|$ of the qubit and the confined microwave field in the resonator, the qubit-resonator coupling is so strong that the set of qubit frequencies depending on different resonator photon numbers is resolvable [106]. This so-called strong dispersive regime has enabled fast quantum control over resonators with long coherence time [107], opening up the field of bosonic quantum computing and error correction mentioned in Sec. 1.2. Similar to the atomic physics experiments, microwave resonators have also been employed to mediate all-to-all coupling between qubits, facilitating multi-qubit entanglement [108, 109] and the quantum simulation of many-body localization [110, 111] and dynamical phase transitions [112].

Another approach with enhanced light-matter interaction is to couple quantum emitters to the confined light field in a one-dimensional (1D) waveguide (Fig. 1.4c), a burgeoning research area called waveguide QED [113]. Compared to cavity QED, waveguide QED provides an intrinsically extensible degree of freedom, serving as the basis of scalable architectures. Arguably, the pioneering waveguide QED experiment with a single quantum emitter is the coupling of a quantum dot to a nanowire plasmonic waveguide in 2007 [114]. Since then, waveguide QED has been demonstrated across various platforms, including quantum dots coupled to photonic crystal waveguides [115] (Fig. 1.5a), cold atoms coupled to photonic crystal waveguides or nano fibers [116, 117] (Fig. 1.5c), superconducting qubits coupled to microwave transmission line waveguide or waveguide structures with engineered dispersion [118–120] (Fig. 1.5b), and solid-state defects coupled to nanophotonics platforms [121]. Among the platforms, superconducting circuits achieve the highest Purcell factor $P_{\mathrm{1D}} \equiv \Gamma_{\mathrm{1D}}/\Gamma'$, a key figure of merit in waveguide QED quantifying the ratio of the emitter decay rate via the waveguide Γ_{1D} versus that through other spurious channels Γ' [100, 122]. The large Purcell factor in superconducting circuits, indicating strong qubit-waveguide coupling, results from the large qubit dipole moment $|\mathbf{d}|$ and the extremely strong waveguide confinement of the microwave field perpendicular to the propagation direction (the width of a transmission line waveguide is usually smaller than 0.2% of the microwave wavelength compared to common optical feature sizes of greater than 10% wavelengths for photonic crystals or nano fibers). This strong coupling even gives access to the ultra-strong coupling regime where the qubit-waveguide coupling rate is comparable to the qubit frequency [123].

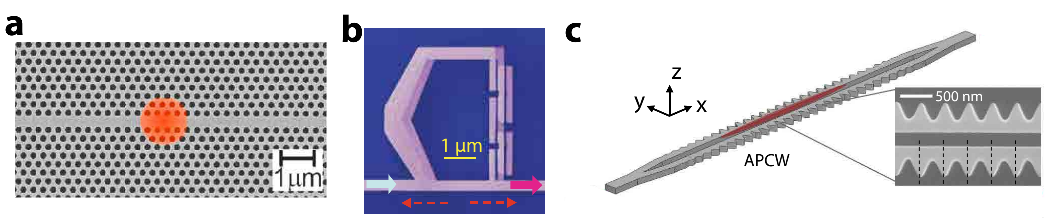

Figure 1.5: **Waveguide QED platforms.** **a**, A single quantum dot (in the orange area) coupled to the photonic crystal waveguide (unpatterned rectangle surrounded by photonic crystals forming triangular lattice), adapted from [124], reprinted with permission from the copyright holder, APS. **b**, A single superconducting flux qubit (pink pentagon ring) couples to a microwave transmission line waveguide (pink wire at the bottom). The blue and magenta arrows show the input and output waves, respectively. The dashed thin arrows show the emission from the qubit into the waveguide. This panel is adapted from [118], reprinted with permission from the copyright holder, the AAAS. **c**, A few cesium atoms (the atomic cloud shown as the elongated red ellipse) couple to the alligator photonic crystal waveguide (APCW, shown as the grey structure). The inset shows an SEM image of an APCW section. This panel is adapted from [116], reprinted with permission from the copyright holder, APS.

Although relatively nascent, waveguide QED holds the potential in numerous application regimes, which in general fall in two categories: (i) the quantum control of itinerant waveguide photons via the emitters and (ii) the interaction between quantum emitters mediated by waveguide photons. The first category [125] includes single-photon switches [122] and the creation of highly entangled photonic states [126, 127] as central resources for measurement-based quantum computing [128], where quantum entanglement is prepared beforehand and the information processing takes place by rounds of measurement on selected qubits. The second category introduces interaction between distant emitters coupled to the same waveguide, serving as the foundation of non-local entangling gates for gate-based quantum computing [129] or quantum simulation of a wide range of many-body physics models [130].

1.4 Outline of the thesis

In this thesis, we use superconducting circuits as the platform to approach the central goals of quantum information science. In particular, the thesis is centered on exploring alternative superconducting circuit architectures to introduce beyond-nearest-neighbor interaction between qubits, filling the current connectivity gap that is limiting the efficient fault-tolerant quantum computation and NISQ-era quantum simulation of a wide range of models. Here, we use the strong light-matter interaction in superconducting circuits to bring in non-local degrees of freedom. These novel circuit architectures have in turn served as the playground to study novel light-matter interactions, the ensuing non-trivial qubit-qubit interaction, and the resulting quantum many-body dynamics. The structure of the thesis is also illustrated in Fig. 1.6.

With this overview, we provide an outline of the rest of the thesis containing three parts: background and methods (Chapter 2-3), main results (Chapter 4-6), and future directions (Chapter 7).

In Chapter 2, we introduce the generic setting of quantum emitters coupled to a waveguide. We focus on the theoretical description of this waveguide QED picture and develop the formalism in two regimes categorized by the relative detuning between the quantum emitters and the itinerant waveguide photonic modes. In each regime, we study the effects of light-matter interaction and the photon-mediated interaction between multiple quantum emitters.

In Chapter 3, we provide details of the key stages in waveguide QED experiments, including design, fabrication, and measurement. Specifically, we highlight the practice beyond common superconducting qubit experiments that has enabled our work in this thesis.

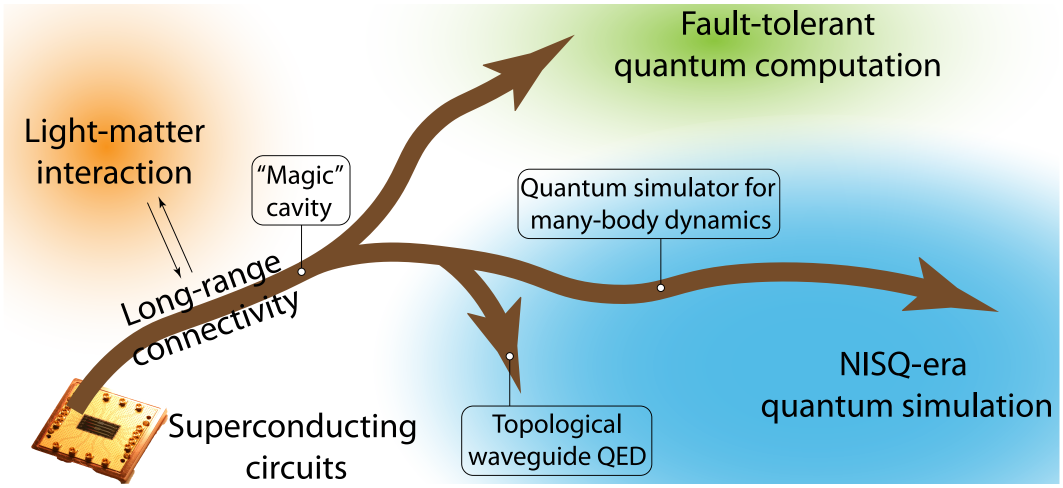

Figure 1.6: **Structure of the thesis.** Based on the platform of superconducting circuits, we use light-matter interaction to construct waveguide QED architectures featuring long-range connectivity, which serve as unique resources for NISQ-era quantum simulation and the ultimate goal of fault-tolerant quantum computation. Along the way, we have observed strong coupling and coherent dynamics in waveguide QED (labeled "Magic" cavity) [47], explored photon-mediated interaction with a topological waveguide [131], and built a quantum simulator to study many-body dynamics influenced by long-range coupling [132].

In Chapter 4, we apply the knowledge and techniques from the previous chapters to achieve strong coupling between qubits in the open environment of a waveguide. This important step of waveguide QED is enabled by the long coherence time of the sub-radiant states resulting from the collective effects of light-matter interaction. The results in this chapter are published in [47].

In Chapter 5, we explore the intersection of light-matter interaction and topological photonics using a dispersion-engineered waveguide. We observe novel qubit-qubit interaction endowed by waveguide photons with topological properties in both the passband and the bandgap. The results in this chapter are published in [133].

In Chapter 6, we move from simulating a topological photonics model in the previous chapter to simulating a quantum many-body model. Specifically, the waveguide QED architecture introduces long-range connectivity in a lattice that hosts strongly interacting microwave photons and is formed by qubits coupled to a bus waveguide. This long-range connectivity enables the study of quantum chaotic dynamics in the many-body regime. The results in this chapter are published in [132].

Finally, in Chapter 7, we provide an outlook for the novel waveguide QED architectures. We focus on a few concrete directions that can extend our results in the previous chapters and further the capabilities of the architectures towards NISQ-era quantum simulation and the grand goal of fault-tolerant quantum computation.

Chapter 2

WAVEGUIDE QUANTUM ELECTRODYNAMICS

We have given a broad overview of light-matter interaction in Chapter 1 from the perspective of spatial confinement of the light field for strong coupling. To be more quantitative, recalling the connection between the Purcell effect [100] and Fermi's golden rule [134], we can arrive at the conclusion that the key to engineering light-matter interaction is engineering the *density of states* (DOS). In addition to the resulting smaller mode volume, the spatial confinement also provides boundary conditions to shape the frequency distribution of states supported by the structure. Free space supports the whole continuum of states whereas a cavity supports a discrete set of resonances owing to the spatial confinement in all three dimensions. A waveguide can be viewed as either free space confined in two directions or a cavity elongated in 1D. Consequently, a waveguide also supports a continuum of states in the passband frequency. As a result of the cut-off frequency or dispersion engineering, a waveguide can also exhibit bandgaps, at which frequency no propagating state is supported.

A pedagogical example of a waveguide is the rectangular hollow metal waveguide with width w and height b (Fig. 2.1a). The dispersion of the $\mathrm{TM}_{m,n}$ waveguide mode is described by [135]

$$\omega = \sqrt{\left(\frac{k_{m,n}}{c}\right)^2 + \left(\frac{m\pi}{b}\right)^2 + \left(\frac{n\pi}{w}\right)^2}, \tag{2.1}$$

where $m, n = 1, 2, \cdots$, c is the speed of light, ω is the angular frequency, and $k_{m,n}$ is the wave vector. The dispersion of $\mathrm{TM}_{1,1}$ mode is shown in Fig. 2.1, exhibiting a passband of close-to-linear dispersion at large k and a bandgap.

The interaction between quantum emitters and the waveguide photons is dependent on the DOS, especially the DOS close to the transition frequency of the emitters. In the following, we provide a theoretical description of the light-matter interaction between quantum emitters and a waveguide in either the passband frequency or the bandgap frequency. This description serves as the theoretical foundation for the rest of this thesis.

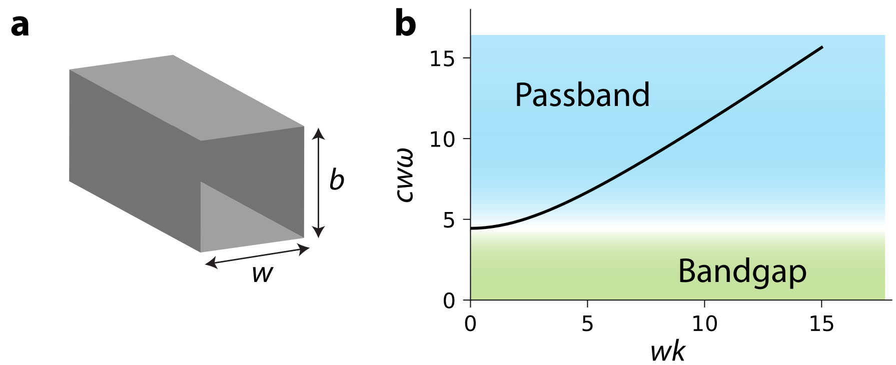

Figure 2.1: **An example of a waveguide and its dispersion relation.** **a**, Schematics of a rectangular hollow metal waveguide with width w and height b. **b**, The dispersion relation of the waveguide with $w = b$. The x and y axes are normalized. The passband and the bandgap are shaded in blue and green, respectively.

2.1 Waveguide QED with linear dispersion

A single quantum emitter in the passband frequency

A generic quantum emitter can be modeled as a two-level system (Fig. 2.2a) with transition frequency ω_q and decay rate Γ' into channels other than the waveguide, yielding the non-Hermitian Hamiltonian $H_q = \frac{1}{2}\hbar(\omega_q - i\frac{1}{2}\Gamma')\sigma_z$ where σ_z is the Pauli Z operator associated with the emitter. On the other hand, a waveguide is described by a collection of propagating photonic modes with wave vector k and corresponding frequency ω_k from the dispersion relation, giving the Hamiltonian $H_{wg} = \sum_k \hbar\omega_k a_k^\dagger a_k$ where a_k ($a_k^\dagger$) is the annihilation (creation) operator of photons in mode k. Adding the interaction between the two parts gives the full Dicke Hamiltonian [136]

$$H = \frac{1}{2}\hbar(\omega_q - i\frac{\Gamma'}{2})\sigma_z + \sum_k \hbar\omega_k a_k^\dagger a_k + \sum_k \hbar g_k(a_k^\dagger + a_k)(\sigma_+ + \sigma_-), \qquad (2.2)$$

where g_k is the coupling rate between the emitter and mode k. In this setting, the set of immediate variables to calculate includes reflection and transmission amplitude r and t. Assuming the rotating wave approximation (RWA) and that g_k is a constant g across photonic modes, we solve for the stationary solution in the single-photon manifold at input photon frequency ω [122, 137, 138] and arrive at the following results

$$r(\omega-\omega_q)=\frac{\Gamma_{1\mathrm{D}}/2}{i(\omega-\omega_q)-(\Gamma_{1\mathrm{D}}+\Gamma')/2} \tag{2.3}$$

$$t(\omega-\omega_q)=1+r(\omega-\omega_q), \tag{2.4}$$

where $\Gamma_{1\mathrm{D}}\propto g^2$ is the emitter decay rate into the waveguide.

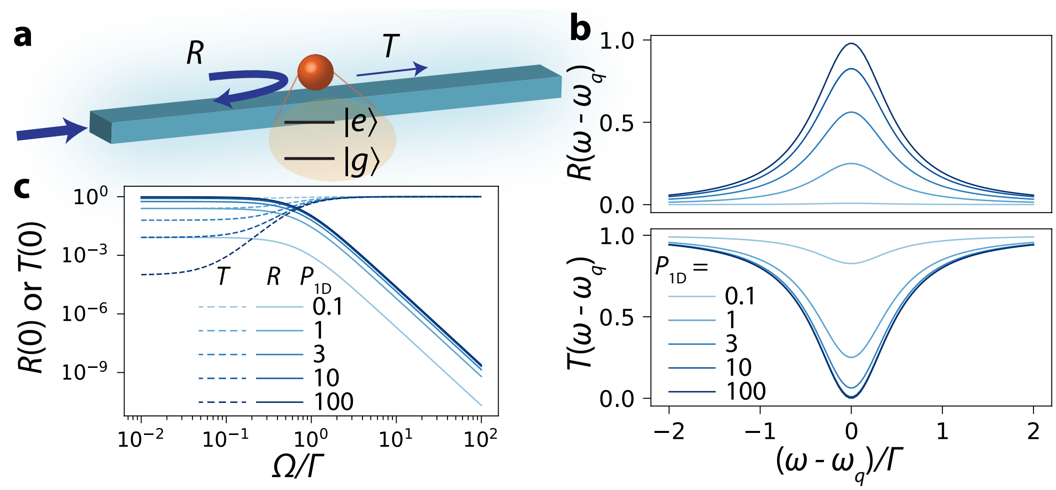

Figure 2.2: **Photon scattering from a single quantum emitter coupled to a waveguide.** **a**, Schematics of a quantum emitter coupling to a waveguide with input field, reflection (R), and transmission (T). **b**, Reflectance R and transmittance T as a function of light-emitter detuning at different $P_{1\mathrm{D}}$ with weak input field. This panel is adapted from [133]. **c**, On-resonance R (solid curves) and T (dashed curves) as a function of input field strength at different $P_{1\mathrm{D}}$.

The observables in the experiment, reflectance R (transmittance T), can be calculated using $R\equiv|r|^2$ ($T\equiv|t|^2$). The on-resonance result of R or T is determined by the Purcell factor $P_{1\mathrm{D}}\equiv\Gamma_{1\mathrm{D}}/\Gamma'$ introduced in Sec. 1.3:

$$R(\omega=\omega_q)=\left(\frac{P_{1\mathrm{D}}}{1+P_{1\mathrm{D}}}\right)^2,\ \ T(\omega=\omega_q)=\left(\frac{1}{1+P_{1\mathrm{D}}}\right)^2. \tag{2.5}$$

By performing spectroscopy measurements of these observables at low input power, we can calculate $P_{1\mathrm{D}}$. For strong coupling $P_{1\mathrm{D}}\gg1$, the on-resonance values are $R\approx1$ and $T\approx0$, meaning the input light is almost perfectly reflected by the emitter (see Fig. 2.2b for results at various $P_{1\mathrm{D}}$). Therefore, a quantum emitter can be used as an efficient mirror for a single photon, inspiring the construction of cavities from atom-like mirrors [139] and consequent cavity QED experiment detailed in Chapter 4.

The above single-photon picture involves only linear descriptions [137, 138], whereas the nature of the two-level system can be revealed by sending in a multi-photon state, yielding the nonlinear response [118, 122]

$$r(\omega-\omega_q) = -\frac{\Gamma_{1\mathrm{D}}}{2}\frac{i(\omega-\omega_q)+\Gamma/2}{(\omega-\omega_q)^2+(\Gamma/2)^2+\Omega^2/2},\;\; t(\omega-\omega_q) = 1+r(\omega-\omega_q), \quad (2.6)$$

where $\Gamma \equiv \Gamma_{1\mathrm{D}} + \Gamma'$ and Ω is the Rabi frequency treating the multi-photon input state as a classical drive. The on-resonance reflectance is modified to be (Fig. 2.2c)

$$R(\omega=\omega_q) = \left[\frac{1}{1+2(\Omega/\Gamma)^2}\right]^2 \left(\frac{P_{1\mathrm{D}}}{1+P_{1\mathrm{D}}}\right)^2. \quad (2.7)$$

We can understand the results as saturation and power-broadening of a driven two-level system. Beyond the reflection and transmission, the multi-photon states also exhibits non-trivial correlation due to the presence of a quantum emitter [122, 140, 141].

Photon-mediated coupling between quantum emitters

When multiple quantum emitters are coupled to the same waveguide, the photons in the waveguide can mediate coupling between them. Starting from a general case where N quantum emitters couple to the same waveguide at positions x_j ($j = 1, 2, \cdots, N$). The Hamiltonian H_q becomes

$$H_q = \sum_j \frac{1}{2}\hbar\omega_{q,j}\sigma_{z,j}, \quad (2.8)$$

where we have ignored the decay into other channels for simplicity. The waveguide Hamiltonian H_{wg} still contains the same set of propagating modes that we can rearrange according to $k < 0$ (left propagating) and $k > 0$ (right propagating) for the convenience of the interaction term. This gives us

$$H_{wg} = \sum_k \hbar\omega_k a_k^\dagger a_k = \sum_{k>0} \hbar\omega_k (a_{R,k}^\dagger a_{R,k} + a_{L,k}^\dagger a_{L,k}), \quad (2.9)$$

where $a_{L/R,k}^\dagger$ ($a_{L/R,k}$) is the creation (annihilation) operator for the left/right propagating mode with wave vector $\mp|k|$. When writing down the light-matter interaction term in the multi-emitter setting, it is important to keep track of the phase accumulated during the photon propagation, yielding

$$H_I = \sum_j \hbar g_j (\Xi_j^\dagger + \Xi_j)(\sigma_{+,j} + \sigma_{-,j}), \quad (2.10)$$

where Ξ_j is the total field operator at position x_j

$$\Xi_j = \sum_{k>0} (a_{L,k} e^{-ikx_j} + a_{R,k} e^{ikx_j}). \tag{2.11}$$

Here, the coupling between emitter j and each propagating mode is assumed to be equal to g_j. The multi-emitter version of Eq. 2.2 is now

$$H = H_q + H_{wg} + H_I. \tag{2.12}$$

Since we focus on the effective coupling between the emitters, we can trace out the photon modes. In this process, the most important assumption is Markov approximation, which can be intuitively understood as neglecting the retardation of light propagating between emitters. Mathematically, it requires $\omega_k(x_j - x_l)/(2\pi v_g) \ll 10$ [142] between emitters j and l, where v_g is the group velocity of light in the waveguide. An apparent indication is that the distance between emitters cannot be too large. Another important requirement is that $v_g \equiv \mathrm{d}\omega_k/\mathrm{d}k$ cannot be too small, requiring the emitter frequency to be away from the band-edge for the assumption to hold. When Markov approximation breaks down, the system properties and dynamics can still be computed using the Green function method [142, 143] or explored experimentally [144].

In the following, we stay in the Markovian regime and arrive at the effective master equation containing only the density operator ρ of quantum emitters [139, 145]

$$\frac{\mathrm{d}\rho}{\mathrm{d}t} = -\frac{i}{\hbar}[H_{\text{eff}}, \rho] + \mathcal{L}[\rho], \tag{2.13}$$

where H_{eff} is the effective Hamiltonian and $\mathcal{L}$ is the Liouvillian super-operator associated with decoherence processes. The photon-mediated coupling between emitters contains both a correlated decay term in $\mathcal{L}$ and a coherent exchange interaction term in H_{eff}.

The correlated decay term is described by

$$\mathcal{L}_c[\rho] = \sum_{j,l} \Gamma_{j,l} \left[\sigma_{-,j}\rho\sigma_{+,l} - \frac{1}{2}\{\sigma_{+,l}\sigma_{-,j}, \rho\} \right], \tag{2.14}$$

where

$$\Gamma_{j,l} = \sqrt{\Gamma_{1\text{D},j}\Gamma_{1\text{D},l}} \cos\left(k|x_j - x_l|\right) \tag{2.15}$$

and $k|x_j - x_l|$ is the phase accumulated when a photon travels between emitters j and l. Note that when $j = l$, this term captures the decay of the emitter j

into the waveguide $\Gamma_{j,j} = \Gamma_{1\mathrm{D},j}$. The correlated decay amplitude is maximized when two emitters are separated by integer multiples of $\lambda/2$, where $\lambda = 2\pi/k$ is the wavelength. As an example, we can start with two emitters separated by $x_1 - x_2 = \lambda/2$ with identical $\Gamma_{1\mathrm{D},1/2} = \Gamma_{1\mathrm{D}}$ (Fig. 2.3a-b). To diagonalize the correlated decay, we can transform the operators into a new set of basis

$$\sigma_{\pm,B} = \frac{\sigma_{\pm,1} - \sigma_{\pm,2}}{\sqrt{2}} \tag{2.16}$$

$$\sigma_{\pm,D} = \frac{\sigma_{\pm,1} + \sigma_{\pm,2}}{\sqrt{2}}, \tag{2.17}$$

which results in

$$\mathcal{L}_c[\rho] = \sum_{\mu=B,D} \Gamma_{1\mathrm{D},\mu} \left[\sigma_{-,\mu}\rho\sigma_{+,\mu} - \frac{1}{2}\{\sigma_{+,\mu}\sigma_{-,\mu}, \rho\} \right]. \tag{2.18}$$

Here, B (D) represents the bright (dark) state, as a consequence of $\Gamma_{1\mathrm{D},B} = 2\Gamma_{1\mathrm{D}}$ and $\Gamma_{1\mathrm{D},D} = 0$ (Fig. 2.3c-d). Intuitively, this can be explained by the interference of the emission from the two emitters: the relative phase in the bright (dark) state causes the light field from the two emitters to interfere constructively (destructively) such that the emission is twice as strong (completely suppressed), see Fig. 2.3a (b).

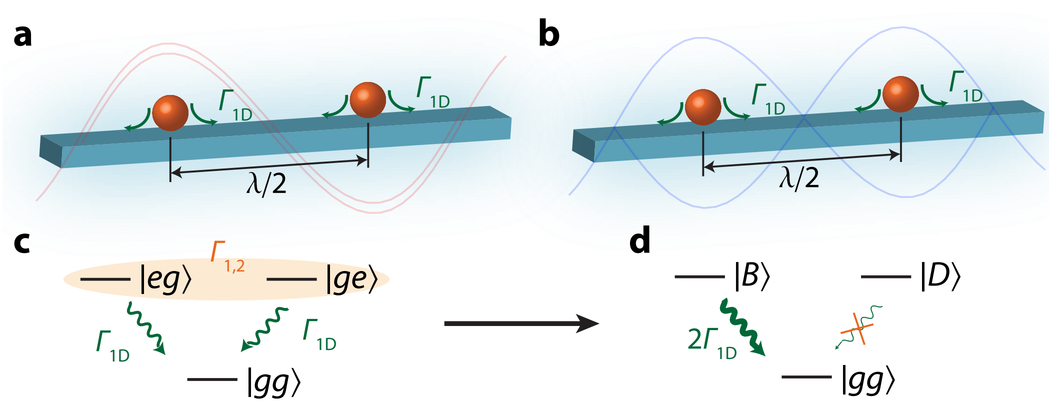

Figure 2.3: **Correlated decay of two emitters separated by half a wavelength. a** (**b**), Schematics of two emitters and their emission, shown in red (blue) sinusoidal curves, in the bright (dark) state. **c**, Energy levels and their decay rate into the waveguide of two emitters coupled to the same waveguide with correlated decay $\Gamma_{1,2}$. $|g\rangle$ ($|e\rangle$) represents the ground (excited) state of an emitter. **d**, Energy levels and their decay rate into the waveguide in the bright/dark state basis.

Note that this bright and dark emission is viewed from the far end of the waveguide. If we sit in between the two emitters on the waveguide, we would see that the electric field in this waveguide segment is enhanced for the dark state, which is the principle behind using the dark state as a cavity [139] with the experimental effort detailed in Chapter 4. In a slightly complicated case when the two emitters have unequal Γ_{1D}, the basis to diagonalize the correlated decay in Eqs. 2.16-2.17 takes different forms but the bright and dark state can always be achieved. Although the emission of the dark state is perfectly suppressed from the above derivation (rendering it a state in the decoherence-free subspace), it is truly decoherence-free only if the spurious decay Γ' and the emitter dephasing rate are both zero [145]. The latter causes the dark state population to leak into the bright state. A more detailed discussion of the decoherence of the dark state can be found in Chapter 4. Beyond two quantum emitters, the correlated decay in Eq. 2.18 in general leads to collective states with various levels of brightness, also known as sub- and superradiance, for multiple emitters [139, 146].

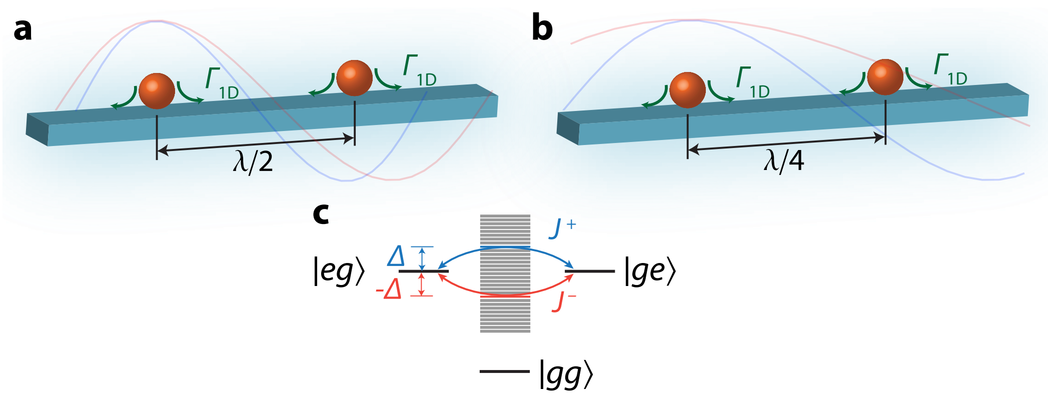

Figure 2.4: **Waveguide-mediated exchange interaction between two emitters.** **a** (**b**), Schematics of two emitters separated by $\lambda/2$ ($\lambda/4$) with the red or blue wavy curve representing the virtual photon from the left emitter below or above its frequency. **c**, Level diagram of the two emitters and a continuum of waveguide modes (gray) showing the interaction J^+ (J^-) mediated by the mode colored in blue (red) with opposite detuning Δ. This panel is inspired by [133].

Now let us turn to the exchange interaction in the coherent Hamiltonian H_{eff}. The exchange interaction has the same origin as the cavity-mediated interaction between two emitters in cavity QED [145]. In the cavity QED case, the two emitters are on resonance, both detuned from the cavity frequency by Δ. This cavity-mediated exchange interaction can be viewed as the presence of one emitter modifying the Lamb shift of the other, i.e., the emission of a virtual photon from one emitter into the cavity mode being absorbed by the other emitter. This leads to the exchange interaction $J = g_1 g_2/\Delta$ where g_j is the coupling between emitter j to the cavity. Coming back to waveguide QED, the exchange interaction is not just mediated by a single mode, but a continuum of propagating modes in the waveguide except for the ones resonant to the emitter frequency. The major difference is (i) the total exchange interaction is a sum of the contributions from all the modes, and (ii) we should take into account the field amplitude and phase when the virtual photons arriving at the other emitter. This results in the following form of exchange interaction

$$H_{ex} = \hbar \sum_{j,l} J_{j,l} \sigma_{-,j} \sigma_{+,l}, \tag{2.19}$$

where

$$J_{j,l} = \frac{1}{2}\sqrt{\Gamma_{1\mathrm{D},j}\Gamma_{1\mathrm{D},l}} \sin\left(k|x_j - x_l|\right). \tag{2.20}$$

Note that when $|x_j - x_l|$ equals integer multiples of $\lambda/2$, the exchange interaction $J_{j,l}$ vanishes. This can be explained by the cancellation of interaction mediated by modes above and below the emitter frequency with opposite signs of Δ (Fig. 2.4a, c). The cancellation is perfect because the pair of modes with opposite Δ have identical field amplitude and phase owing to the specific separation. The absence of exchange interaction allows the bright/dark states at a degenerate frequency to diagonalize the entire master equation Eq. 2.13.

The situation is different for $|x_j - x_l| = \lambda/4 + n\lambda/2$ where n is an integer. Using $x_j - x_l = \lambda/4$ as an example, the opposite-Δ mode pair now have the same field amplitude but opposite sign, flipping the sign of J from the mode once more and constructively adding up to the total $J_{j,l}$ (Fig. 2.4b, c). As a result, $J_{j,l}$ achieves the largest amplitude at this set of emitter separations. In this case, the correlated decay vanishes, and the basis set in Eqs. 2.16-2.17 still diagonalizes the master equation Eq. 2.13. However, bright/dark state is no longer a proper name as each state has the same decay rate of $(\Gamma_{1\mathrm{D},j} + \Gamma_{1\mathrm{D},l})/2$.

The exchange interaction is infinite in its range [147, 148] as long as the Markov approximation is valid. Nonetheless, the always-present decay rate, which is of comparable strength as the exchange interaction rate in Eq. 2.20, hampers the observation of coherent dynamics and strong coupling [149].

In the passband regime, we can still achieve strong coupling by using smart protocols combining decoherence-free subspace and the exchange interaction [47, 139]. Another method, which is also a novel area for waveguide QED, is by using giant atoms easily implemented using superconducting qubits [150]. This method assumes that a quantum emitter couples to the waveguide at multiple points, thus forming a decoherence-free state on its own when the coupling points are chosen wisely. Braiding or nesting giant atoms such that their waveguide sections overlap can induce coherent interaction between the giant atoms [151].

Another volume of research studying the passband regime is chiral waveguide QED [152], which can be physically implemented by, e.g., quantum dots [153]. In this case, instead of emitting into both left and right propagating modes of the waveguide, the emitter only emits into one of the direction or exhibiting asymmetric coupling $g_{L,j}$ and $g_{R,j}$ in Eqs. 2.10-2.11. This area gives rise to, e.g., photon routers in quantum network applications, as well as the driven-dissipative preparation of non-trivial many-body states.

2.2 Waveguide QED in the bandgap regime

In the end of the previous section (Sec. 2.1), we have pointed out the potential difficulty of achieving strong coupling in the passband regime. Solutions such as the atomic cavity protocol [47, 139] and giant atoms [150, 151] have been demonstrated. However, these solutions rely on the states in the decoherence-free subspace, which requires the distance between emitters to be precisely at a discrete set of values such as $n\lambda/2$. In the case of superconducting circuits where the distance between the emitters is determined in fabrication, the decoherence-free states require the qubit frequencies to be fixed at specific values, thus limiting the flexibility of quantum information processing tasks to implement. Instead of constantly combating the decay into propagating photons in the passband, another way is to place the emitter frequency inside the bandgap where DOS vanishes and radiative decay is suppressed.

In this section, we provide the derivation based on a waveguide with periodic structure (Fig. 2.5a), a common way to engineer the dispersion relation and create bandgaps, and examples include photonic crystals [154] and metamaterials [155].

A single quantum emitter in the bandgap frequency

In the bandgap frequency, there is no propagating mode for the emitter to decay into. Intuitively, the light field will be exponentially localized around the quantum emitter since the wave vector has non-zero imaginary part in the bandgap, giving $e^{ikx} = e^{ik_0x}e^{-x/\xi}$ where $\xi = i/(k - k_0)$ is the localization length and k_0 is the real part of the wave vector. The localized light field and the emitter form the *emitter-*

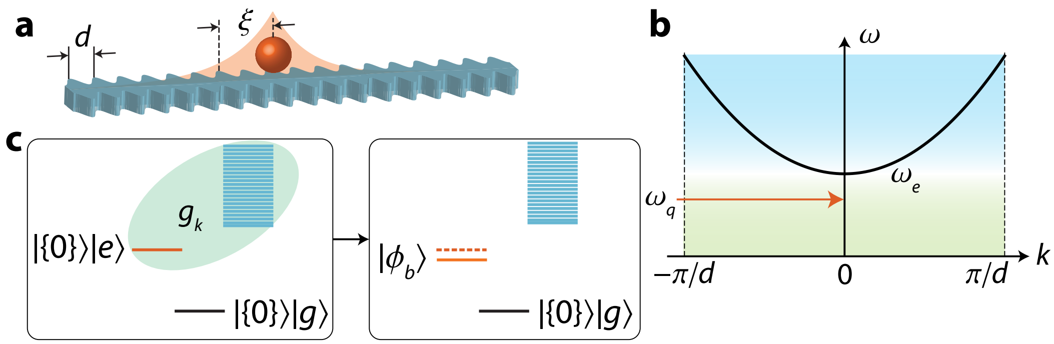

Figure 2.5: **A single emitter-photon bound state.** **a**, Schematics of a quantum emitter (red ball) coupled to a dispersion-engineered waveguide (blue wavy structure) with unit cell size d. The coupling results in an exponentially localized emitter-photon bound state (red shade) with localization length ξ. **b**, A quadratic dispersion relation in the first Brillouin zone with $k_0 = 0$. The passband is shaded blue above the bandedge frequency ω_e, and the bandgap below it is shaded in green. An example frequency of a quantum emitter in the bandgap is indicated by the red arrow. **c**, Level diagrams of the quantum emitter in the bandgap and the waveguide modes. The left part shows the bare emitter and waveguide modes, as well as the coupling g_k between them. The right part shows the dressed level diagram with the bound state $|\phi_b\rangle$ exhibiting a lower energy (solid line) than that of the bare emitter (dashed line). Panels **a-b** is inspired by [133].

photon bound state, first discussed by John and Wang in 1990 [156]. Mathematically, this picture is still captured by the Dicke Hamiltonian in Eq. 2.2 with the emitter frequency ω_q outside of possible ω_k's. In the following, we ignore the spurious decay Γ' for simplicity.

To describe the single-excitation emitter-photon bound state $|\phi_b\rangle$, we start with the superposition of single-excitation basis without loss of generosity

$$|\phi_b\rangle = \cos\theta|\{0\}\rangle|e\rangle + \sin\theta \sum_k c_k a_k^\dagger |\{0\}\rangle|g\rangle, \tag{2.21}$$

where $|\{0\}\rangle$ is the vacuum state for the photonic modes, $|g\rangle$ ($|e\rangle$) is the ground (excited) state of the quantum emitter, θ parameterizes the emitter or total photon population and c_k is the coefficient for the propagating photon mode with wave vector k satisfying $\sum_k |c_k|^2 = 1$. To solve for the parameters, we note that $|\phi_b\rangle$ is an eigenstate of the Hamiltonian in Eq. 2.2 $H|\phi_b\rangle = \hbar\omega_b|\phi_b\rangle$ with ω_b the angular frequency of the bound state. Assuming RWA, the eigenstate equation yields [120, 131, 156, 157]

$$c_k = \frac{g_k}{(\omega_b - \omega_k)\tan\theta} \tag{2.22}$$

$$\omega_b = \omega_q + \sum_k \frac{|g_k|^2}{\omega_b - \omega_k} \tag{2.23}$$

$$\tan^2\theta = \sum_k \frac{|g_k|^2}{(\omega_b - \omega_k)^2}. \tag{2.24}$$

Up to now, the result has been general with no assumption about the waveguide or its dispersion relation. Moving forward, we consider the generic quadratic dispersion relation (Fig. 2.5b) at the bandedge $\omega_k = \omega_e + \alpha(k - k_0)^2$, where ω_e is the bandedge frequency, α is the band curvature, and k_0 is the corresponding wave vector at the bandedge. This is suitable to approximate bandedge dispersion with the quadratic term as the leading order, such as the rectangular waveguide example in Eq. 2.1. For the derivation below, we assume the bandgap is below the passband with $\alpha > 0$ and the emitter frequency $\omega_q < \omega_e$. The opposite case is left as an exercise for the readers. Assuming the quadratic dispersion relation and uniform coupling to each mode k after changing the summation to integral[1] [120, 133],

$$\omega_q - \omega_b = \frac{g^2 d}{2\sqrt{\alpha(\omega_e - \omega_b)}} \tag{2.27}$$

$$\tan^2\theta = \frac{g^2 d}{4\sqrt{\alpha(\omega_e - \omega_b)^3}} = \frac{\omega_q - \omega_b}{2(\omega_e - \omega_b)}. \tag{2.28}$$

From Eq. 2.27, we can see that the bound state frequency is pushed below the bare emitter frequency because of the Lamb shift (Fig. 2.5c). The shape of the bound state can be deduced by the photonic mode coefficient in the real space, resulting in an exponentially localized shape (Fig. 2.5a)

$$c_x = \frac{1}{\sqrt{N}} \sum_k e^{ikx} c_k = -\frac{gd}{\sqrt{2\alpha(\omega_q - \omega_b)}} e^{ik_0(x - x_0)} e^{-|x - x_0|/\xi}, \tag{2.29}$$

[1] This means

$$\frac{1}{N}\sum_k \to \frac{d}{2\pi}\int \mathrm{d}k, \tag{2.25}$$

where N is the number of unit cells, d is the size of a unit cell in the waveguide exhibiting translational symmetry, and the integration covers the entire first Brillouin zone. This change from summation to integral is valid when $N \to \infty$, the thermodynamic limit. For example, the summation in Eq. 2.23 becomes

$$\frac{d}{2\pi} g^2 \int \frac{\mathrm{d}k}{\omega_b - \omega_k}, \tag{2.26}$$

where $g^2 = N g_k^2$.

where the localization length is given by

$$\xi = \sqrt{\frac{\alpha}{\omega_e - \omega_b}}. \tag{2.30}$$

This localization length is consistent with the result from the imaginary part of the wave vector at frequency ω_b

$$\omega_b = \omega_e + \alpha(k - k_0)^2, \;\; k = k_0 + \frac{i}{\xi}. \tag{2.31}$$

The properties of the bound state is determined by the detuning between the bound state and the bandedge. Decreasing the detuning results in (i) a growing photonic population in the bound state from Eq. 2.28, i.e., the bound state becoming less emitter-like and more photon-like; and (ii) the spatial extend of the bound state becoming more delocalized shown in Eq. 2.30. This tunability of the bound state properties serves as the foundation of the tunable exchange interaction discussed in the following subsection.

Exchange interaction between two bound states

Intuitively, when the two bound states spatially overlap with each other, there will be interaction between them with the interaction strength and range determined by the bound state properties. A more rigorous picture is that the virtual photons in the passband modes mediates the interactions between the two emitters, similar to the formalism in Sec. 2.1. The difference lies in the emitter frequency relative to the passband. Now let us make it more quantitative by starting from the Hamiltonian in Eq. 2.12 that still holds in this case. Additionally, the expression for the single-excitation eigenstate of the two-emitter interacting Hamiltonian can be found analytically using a similar method as the one for a single bound state. We can directly extract the interaction between the two bound states from the eigenstate equation.

Let us rewrite the Hamiltonian Eq. 2.12 in a clearer way

$$H = \sum_{j=1,2} \hbar\omega_{q,j} |e\rangle\langle e|_j + \sum_k \hbar\omega_k a_k^\dagger a_k + \sum_{j,k} \hbar \left[g_{k,j} a_k^\dagger |g\rangle\langle e|_j + h.c. \right]. \tag{2.32}$$

The two-emitter-photon bound state in the single-excitation manifold is described by

$$|\phi_b\rangle = \cos\theta |\{0\}\rangle \left(c_{q,1} |e\rangle_1 |g\rangle_2 + c_{q,2} |g\rangle_1 |e\rangle_2 \right) + \sin\theta \sum_k c_k a_k^\dagger |\{0\}\rangle |g\rangle_1 |g\rangle_2, \tag{2.33}$$

where the additional parameters $c_{q,j}$ represents the relative population of the two emitters, satisfying $\sum_j |c_{q,j}|^2 = 1$. Solving the eigenstate equation $H|\phi_b\rangle = \hbar\omega_b|\phi_b\rangle$ gives [131]

$$\omega_b \begin{pmatrix} c_{q,1} \\ c_{q,2} \end{pmatrix} = \begin{pmatrix} \omega_{q,1} + J_{1,1} & J_{1,2} \\ J_{2,1} & \omega_{q,2} + J_{2,2} \end{pmatrix} \begin{pmatrix} c_{q,1} \\ c_{q,2} \end{pmatrix}, \tag{2.34}$$

where

$$J_{j,l} = \sum_k \frac{g^*_{k,j} g_{k,l}}{\omega_b - \omega_k}. \tag{2.35}$$

For $j = l$, $J_{j,j}$ is the single-emitter Lamb shift the same as the one in Eq. 2.23. The cross-emitter term $J_{1,2}$ represents the exchange interaction between the bound states, exhibiting the form of virtual-photon-mediated interaction $g_1 g_2/\Delta$. Using similar techniques as deriving Eq. 2.29, we arrive at the expression by assuming $|g_{k,j}| = |g_{k,l}|$

$$J_{1,2} = -\frac{g^2 d}{2\sqrt{\alpha(\omega_e - \omega_b)}} e^{ik_0(x_1 - x_2)} e^{-|x_1 - x_2|/\xi}, \tag{2.36}$$

where the localization length is the same as the one in Eq. 2.30. Although the single-emitter eigenstate equation always has a bound state solution, the existence of two bound states in the two-emitter eigenstate equation is not guaranteed. Specifically, because of the interaction between the single-emitter bound states, one of the hybridized two-emitter bound state may be pushed into the passband frequency and become delocalized [157].

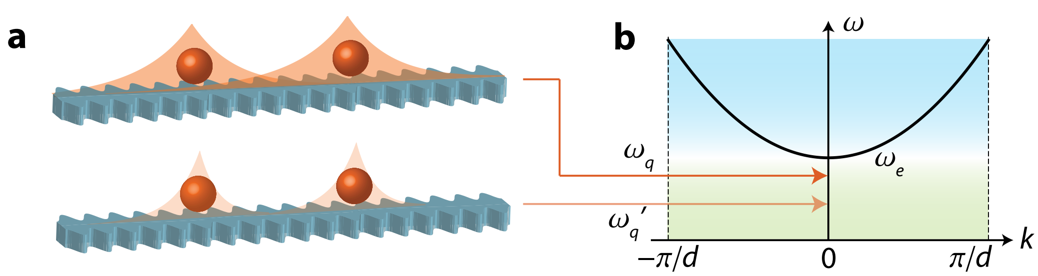

Figure 2.6: **Two quantum emitters in the bandgap frequency. a**, Schematics of two emitter-photon bound states. The upper (lower) one shows a higher (lower) emitter frequency ω_q (ω'_q), resulting in larger (smaller) population in the photonic envelope and a larger (smaller) spatial extend of the bound states. Consequently, the interaction between the bound states exhibits larger (smaller) amplitude and a longer (shorter) range. **b**, Dispersion relation showing the bandedge frequency ω_e and the different quantum emitter frequencies. This figure is adapted from [133].

The bound state interaction inherits the tunability of the bound state, exhibiting a larger amplitude and more extended range when the emitter-bandedge detuning is smaller (Fig. 2.6). Although exponentially localized interaction is not considered long range in the thermodynamic limit, the flexibility to tune the interaction range to cover the entire physical device [158] acts as the foundation of long-range connectivity in waveguide-based quantum architecture in the bandgap regime (Chapter 6). This tunable interaction also gives access to a wide range of many-body Hamiltonians [159]. Moreover, with local control or additional levels, the interaction profile can be engineered to exhibit beyond exponential decay, emulating, e.g., power-law decay or even designed connectivity [158, 160] (see also Sec. 7.2).

Beyond the single-excitation manifold, bound states consisting of a quantum emitter and multiple binding photons have also been explored showing intriguing properties in quantum optics and many-body physics [157, 161, 162]. When the quantum emitter is extended beyond a two-level system, such as the superconducting transmon qubit, higher-excitation manifold have been studied using spectroscopic tools [163]. Lastly, the dispersion relation can be engineered to exhibit, e.g., multiple bands or topological features, where the quadratic dispersion assumption no longer holds [131, 164] (an example is discussed in detail in Chapter 5).

Chapter 3

ENGINEERING AND OPERATING A SUPERCONDUCTING WAVEGUIDE QED SYSTEM

The previous chapter has provided the theoretical background for generic waveguide QED systems. We can now focus on how to implement these concepts using superconducting circuits, which achieve among the strongest emitter-waveguide coupling marked by the highest P_{1D} (above a hundred [47, 165]) among different physical platforms. It is also straightforward to control the position and the frequency of quantum emitters—superconducting transmon qubits—relative to the waveguide, which is crucial in realizing quantum information processing tasks based on waveguide QED architectures. In this chapter, we lay out a practical guide on engineering and operating a superconducting waveguide QED system. This guide is not designed to be pedagogical or comprehensive. Instead, it builds upon the basic theoretical knowledge, control and read-out principles, and measurement techniques of superconducting circuits, which are nicely reviewed in [11, 133, 166–168]. In the following, we will provide a general description of design, fabrication, and measurement, highlighting the practice that enables the waveguide QED experiments detailed in the rest of the thesis.

3.1 Circuit design

To design a circuit element to be fabricated using thin-film superconductors on a substrate, we draw the 2D geometry of the superconductor and use the electromagnetic (EM) analysis software Sonnet® to simulate key parameters such as capacitance, inductance, and resonance frequency.

Superconducting qubit

In this thesis, we use the Xmon qubit [169], a member of the transmon family with the ground acting as one of the metal island in the circuit diagram (Fig. 3.1a and b). The shape of the center capacitor of an Xmon can be designed to achieve required coupling with other elements. The XY control line is designed to capacitively couple to the Xmon qubit with a small capacitance of tens of attofarad, enabling a π-pulse on the order of 10 ns while keeping the XY-decay limited lifetime above 100 μs. The

Z control line provides the current for flux biasing the qubit frequency, where the tuning rate is determined by a combination of Z-line-qubit distance, the area of the SQUID loop, and the position of the air bridge to balance the asymmetric current. We usually use the Z line design that provide a tuning of 1 mA per frequency sweep period. Note that the qubit can also have radiative loss through the Z line if the qubit shape does not exhibit reflection symmetry with respect to the axis along the Z line [69] (Fig. 3.1c), which needs to be taken into account in the qubit design.

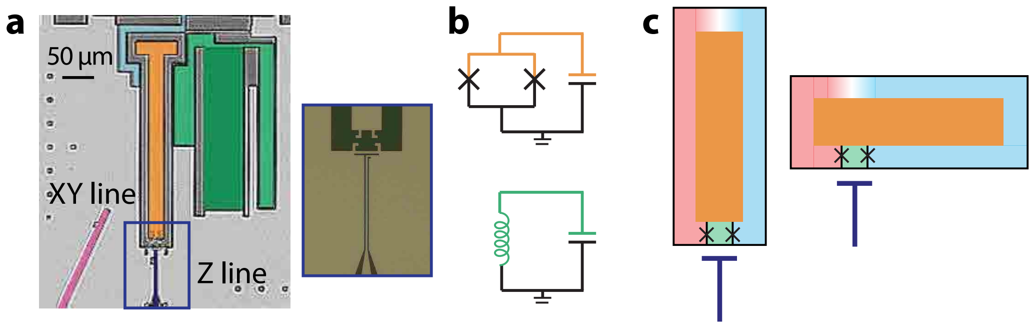

Figure 3.1: **Superconducting qubit and read-out resonator circuit design.** **a**, False colored optical image of an Xmon qubit (orange) and a lumped element read-out resonator (green) with the XY line (pink) and Z line (navy). This panel is adapted from [132] with reprint permission. The right panel shows the zoomed-in view of a Z line before the junctions and airbridges are fabricated. **b**, Circuit diagram of the Xmon qubit (upper panel) and the read-out resonator (lower panel). The metal island of the qubit and the read-out resonator is colored orange and green, respectively. **c**, Cartoon showing the inductive coupling with the Z line (represented by a "T"). The green shading represents the desired coupling between the SQUID loop and the Z line, and the red (blue) shading represents the spurious qubit coupling to the Z line with positive (negative) amplitude. The spurious coupling vanishes for the left panel, but is still present for the right panel.

Resonator

The commonly used resonator in the community is the $\lambda/4$ or $\lambda/2$ transmission line resonator, where λ is the microwave wavelength. The fundamental mode of standing-wave resonances formed by open/short-circuit boundary conditions is employed as, e.g., the read-out mode. This type of resonator is easy to design and predict its resonance frequency. The drawback of this design is the large footprint: at 6 GHz, the wavelength $\lambda \approx 15$ mm on a high-resistance silicon substrate, meaning a $\lambda/4$ resonator can take more than 600×600 μm^2.

Another design for the resonator is the lumped element inductance-capacitance (LC) resonator design, e.g., the ones used in [170]. The metal wing gives rise to the capacitance to ground, and the thin meandering wire connected to the ground provides the inductance (Fig. 3.1a and b). This design can reduce the footprint by half, whereas the resonance frequency needs to be obtained from EM simulations.

Waveguide

Coplanar waveguide (CPW), shown in Fig. 3.2a, is the basic transmission line waveguide used as on-chip control and read-out lines for superconducting circuits, which also serves as the linearly-dispersioned waveguide in Chapter 4. The theoretical modeling of a transmission line waveguide is an important subject, discussed in detail in microwave engineering textbooks such as [171]. The key parameter in design is the characteristic impedance $Z_0 = \sqrt{L_u/C_u}$, where L_u and C_u are the unit length inductance and capacitance of the waveguide. For a CPW, the impedance is controlled by the width of the center trace (colored orange in Fig. 3.2a) as well as the gap between the center trace and the ground (dark gray gap between the orange and the light gray region in Fig. 3.2a). Usually, we design the CPW to have impedance $Z_0 = 50\,\Omega$ to achieve impedance matching to external transmission lines, thus minimizing the reflection at the boundary.

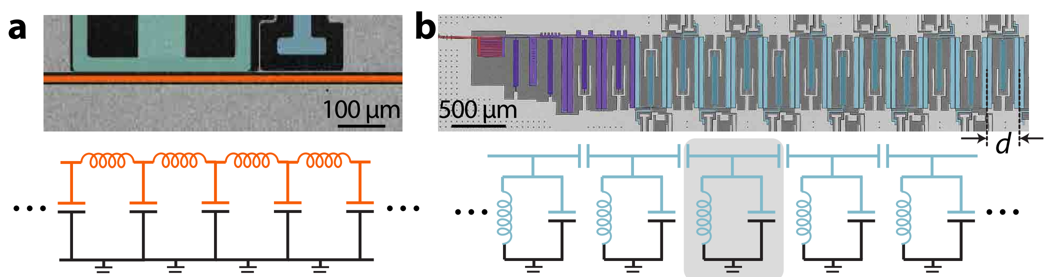

Figure 3.2: **Waveguide circuit design.** **a**, False colored optical image (upper panel) of a CPW waveguide (orange) and its circuit diagram (lower panel) showing elements representing the distributed inductance and capacitance with the unit length value of L_u and C_u. The optical image is adapted from [47] with reprint permission. **b**, False colored optical image (upper panel) of a metamaterial waveguide (blue) with the unit cell size of d connected via a tapering section (purple) to a CPW waveguide (red). The circuit diagram of the metamaterial waveguide (lower panel) shows that a unit cell (shaded in gray) consists of a lumped element LC resonator with capacitive coupling to neighboring cells. The optical image is adapted from [132] with reprint permission. In both optical images, the light grey area is the ground plane.

To engineer the dispersion of a microwave waveguide, a simple way is to start from a CPW, and periodically modulate the impedance [120], which realizes a photonic crystal [154] in the microwave domain. Another method is to create periodic cells of microwave structures much smaller than the microwave wavelength (see, e.g., Fig. 3.2b), i.e., a metamaterial [155]. For example, in [172], the metamaterial is constructed by periodically loading a CPW waveguide with resonant structures to create a waveguide with band-stop spectrum. Another example is a waveguide with band-pass spectrum, which can be built by an array of coupled lumped element resonators detailed in Chapter 5 and 6. Additionally, the metamaterial waveguide can also be used to achieve both energy and momentum matching in traveling wave amplifiers to achieve wide-band amplification gains [173, 174].

Coupling between circuit elements

The coupling between two capacitively-coupled LC resonators (Fig. 3.3a) is given by

$$g = \frac{C_g}{\sqrt{C_{1,\Sigma} C_{2,\Sigma}}} \frac{\sqrt{\omega_1 \omega_2}}{2}, \tag{3.1}$$

where C_g is the coupling capacitance between the two resonators, $C_{j,\Sigma} \equiv C_j + C_g$ with $j = 1, 2$ is the total capacitance of each resonator, and ω_j is the resonance frequency. This formula can be obtained by writing down the Hamiltonian of the circuit and performing the second quantization to extract the coupling coefficient g (see, e.g., App. D of [175]). The formula is widely used to design the coupling between a qubit and a read-out resonator, between a qubit and a waveguide resonator, and between a read-out resonator and a waveguide resonator in Chapter 5 and 6. The capacitance values can be extracted from EM simulations given the circuit geometry.

The coupling of a qubit/resonator to a waveguide can be quantified by the waveguide-induced decay rate. The open environment of the waveguide can be modeled as a $50\text{-}\Omega$ impedance on each end (Fig. 3.3b). The decay rate can be obtained from the classical external Q factor of a parallel LC circuit

$$Q_e = \omega_0 \frac{\text{average energy stored in the resonator at } \omega_0}{\text{average power lost to the external circuit}} = \frac{\omega_0 C}{\mathrm{Re}[Y(\omega_0)]}, \tag{3.2}$$

where $\omega_0 = 1/\sqrt{LC}$ is the resonance frequency and $Y(\omega)$ is the admittance seen from the external port (Fig. 3.3b). Assuming the external load can be treated as a perturbation, i.e., $Q_e \gg 1$, the decay rate into a waveguide can be deduced as

$$\Gamma_{\mathrm{1D}} = \left(\frac{C_g}{C}\right)^2 \frac{Z_0}{2L}, \tag{3.3}$$

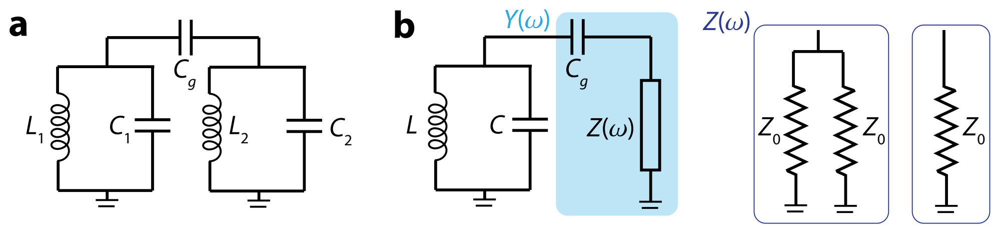

Figure 3.3: **Coupling between circuit elements. a**, Circuit diagram of two resonators with inductance L_j and capacitance C_j coupled via the coupling capacitance C_g. **b**, Left: Circuit diagram of an LC resonator capacitively (C_g) coupled to an open environment with frequency-dependent characteristic impedance $Z(\omega)$. The admittance $Y(\omega)$ seen from the resonator is shaded in blue. Right: Examples of $Z(\omega)$ showing the impedance of a double-ended waveguide (parallel Z_0) and the impedance of a single-ended waveguide (Z_0).

where the resistance associated with the waveguide is $Z_0/2$. In order to increase $\Gamma_{1\text{D}}$, we can raise the coupling capacitance by increasing the width of the waveguide center trace or eliminating the ground plane between the Xmon capacitor and the center trace, giving rise to $\Gamma_{1\text{D}}/2\pi \approx 100\,\text{MHz}$ in Chapter 4. This formula can also be used to estimate the decay rate into the XY line, in which case the associated resistance is Z_0 (Fig. 3.3b, single-ended waveguide).

System-level circuit design

Equipped with the above basic knowledge and formula, we are able to design the geometry of the metal for each element, confirming that the parameters satisfy our design goals in the EM simulation of the parts. However, it is inefficient to simulate the entire waveguide QED system with geometry spreading over a 1 cm $\times$ 1 cm (or 2 cm) substrate. Especially, this hampers the design of the metamaterial waveguide (Fig. 3.2b) where strong coupling between unit cells is assumed and the precise dispersion relation requires the simulation of an infinite structure. A solution is provided in [144]: we use the EM simulation of a single unit cell to extract the S-parameters, convert it into the dispersion relation of an infinite structure [171], and extract the lumped element inductance and capacitance values from fitting the dispersion relation.

Another challenge lies in the finite number of unit cells we can fit on a physical device, meaning the passband always consists of discrete modes instead of a continuum. This becomes a problem if we perform waveguide QED experiments in the passband

(Chapter 5) or use the passband as the feedline for reading out the qubits (Chapter 6). We overcome the challenge by designing tapering sections [144] (purple section in Fig. 3.2b), adapting the Bloch impedance of the periodic structure [171] to the $50\text{-}\Omega$ port impedance. Another way to view it is that the tapering section increases the external coupling of each mode to the ports, thus creating a quasi-flat passband by the overlap of modes with large linewidths. In the example of the waveguide in Fig. 3.2b, this intuition leads to the design principle of gradually increasing the coupling capacitance between the unit cells while maintaining the resonance frequency of the cell by decreasing the capacitance to ground. To obtain the best parameters, we start from the design of a bandpass filter (*iFilter™ Module*) in Cadence® Microwave Office® which minimizes the ripples in the passband. Using these initial values for the tapering section containing, e.g., 4 tapering cells, we simulate the transmission from the waveguide and further optimize with the target of passband transmission achieving unity. The optimization gives us the circuit parameters we can use to design individual tapering cells.

Besides designing the tapering section, we also use Microwave Office® to extract parameters involving the entire circuit, such as the decay rate into the metamaterial waveguide by simulating the real part of the admittance in Eq. 3.2.

3.2 Device fabrication and packaging

Device fabrication

All the devices in this thesis are fabricated using electron-beam evaporated Aluminum on high-resistance Silicon substrates (525 μm-thick, >10 kΩ·cm). The fabrication consists of four rounds of electron-beam lithography, defining the patterns for Niobium markers, Aluminum ground plane, Al/AlO_x/Al Josephson junctions (JJ), and Aluminum air-bridges. The bandages used to electrically connect the JJs to the ground plane are also fabricated in the air-bridge round, which includes an argon milling step before the metal evaporation. Each lithographic round includes the following steps (detailed in App. A): chip cleaning, spinning and baking the resist, electron-beam lithography, development, electron-beam metal evaporation, and lift-off.

In addition to the above common superconducting circuit fabrication practice, we add an inspection and fix step for fabricating metamaterial waveguide systems, increasing the device yield to almost 100%. The smallest feature size in the metamaterial

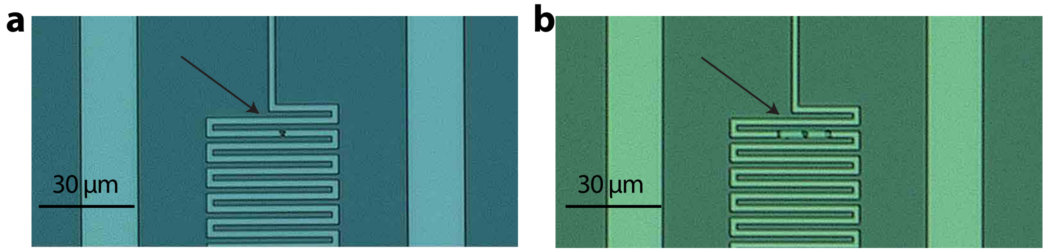

Figure 3.4: **Fixing a fabrication failure in a metamaterial waveguide.** **a** (**b**), Optical image before (after) the fix of a disconnected thin wire belonging to a metamaterial resonator. The arrows in both panels point at the fabrication failure.

waveguide is 1 μm or 2 μm, and the metamaterial covers an area of around 600 μm $\times$ 15 mm. The majority of the failures originate from dusts landing on the patterned resist before the metal evaporation, resulting in disconnected circuit wires. Any failure in, e.g., the thin-wire inductor (Fig. 3.4a), will change the resonance frequency of the waveguide resonator, thus creating defect states or even disturbing the band structure. Therefore, after the lift-off step of the ground plane round, we inspect the ground plane pattern using Keyence VHX-7000 digital microscope and generate patterns of fixing patches to use in the air-bridge round to connect the failed wires. Usually, a metamaterial waveguide of the size used in Chapter 6 have less than five critical failures (an example is shown in Fig. 3.4). After the fix, we did not find noticeable disorders in the waveguide or changes in read-out resonator frequency or coherence.

Device packaging

The packaging used in this thesis is described in detail in Sec. 3.2 of [133]. In this subsection, we report an additional recent observation.

The 26-port microwave enclosure housing a chip of 2 cm $\times$ 1 cm enables complete individual control over 10 qubits (Chapter 6). However, the stability of the connectors, especially under thermal cycling inside a dilution refrigerator, needs to be improved. The mating of the SMPM connectors (Fig. 3.5a) degrades after thermal cycling, causing the electrical connection of a few connectors to fail under cryogenic temperature. Therefore, we have added a copper piece to clamp the PCB connectors (Fig. 3.5b), which solved the electrical connection problem. We have recently found that the clamping introduces another problem: if the clamping is too tight, the SMPM connectors will be pushed into the PCB board, thus shorting the center

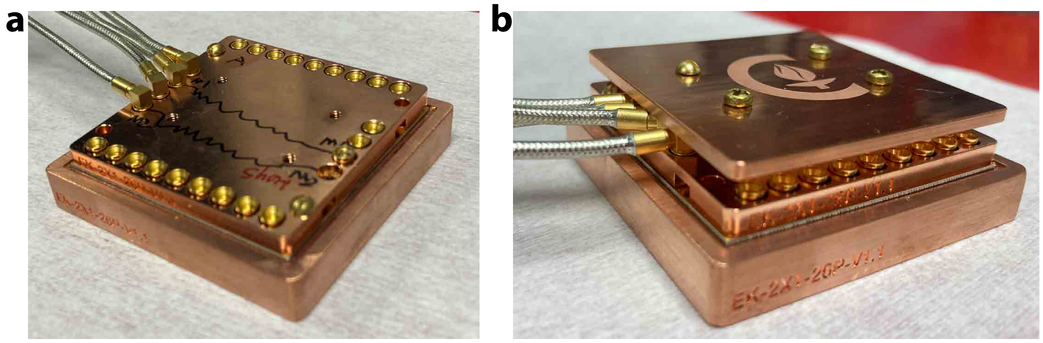

Figure 3.5: **Clamping on the connectors.** **a**, Photo showing four SMPM connectors mated to cables that are free to rotate in the plane and even tilt at a small angle. **b**, Photo showing a clamp added on top of the package to fix the position of the connectors.

pin to the ground. The clamping force is usually not harmful at room temperature, whereas during the thermal cycling, the clamp tend to be overtightened and damage the connector-PCB joint permanently. This causes short for a few connectors after warming up the device used in Chapter 6. In conclusion, we need to carefully take into account the cryogenic operation and thermal cycling when designing the packaging and choosing the connectors.

3.3 Experimental setup and operation

The experimental setup and operation used in this thesis follows common practice in superconducting qubit experiments and is detailed in App. B-D and Sec. 3.3-3.4 of [133]. In the following, we highlight a few aspects that have played an important role in improving the qubit coherence and performing multi-qubit operations.

Thermalization of the waveguide

The cryogenic setup used for experiments in this thesis follows the general rules of cryogenic engineering [176]. In addition, for waveguide QED experiments, especially the ones in the passband regime, minimizing the thermal photon number in the waveguide is crucial to prevent extra dephasing of qubits [176–179] that directly see the waveguide photons. Detailed in Chapter 4 and App. B, we have used well-thermalized attenuators to achieve better thermal anchoring of the waveguide to the mixing chamber plate. More specifically, we have used the cold attenuators from B. Palmer's group [177] or commercial attenuators[1], all of which have been anchored to their cryogenic stage directly or via thick copper pieces for good thermal conduction.

Grounding

In this subsection, we emphasize the importance of reducing the ground noise, which has been the limitation on the qubit coherence in our setup. The ability to tune the frequency of a qubit also introduces a channel for additional frequency noise, i.e., dephasing. The Z line—responsible for tuning the qubit frequency via the current—is shorted to the ground close to the SQUID (Fig. 3.1a), thus coupling the ground noise to the qubit. As pedagogically elaborated in Chapter 3 of [180], careless ground connections could result in ground noise from noisy instruments and ground loops that can pick up noisy ground current or magnetic field.

The immediate ground a qubit sees in the dilution refridgerator (DF in short) is the cryostat ground. The Bluefors LD-250 DF we use is designed to be electrically floating ($> 1\,\mathrm{M}\Omega$), isolated from the gas handling unit and the DF frame, such that it can be connected to a clean ground. During the DF installation and subsequent installations of new pieces especially on top of the DF, we need to be careful that metal pieces including bolts and nuts[2] do not make accidenta electrical connection. After making changes to the cryostat connection, we should check whether the electrical isolation is maintained. Besides connected to a clean ground, the cryostat ground is connected to the power supply of high-electron-mobility transistor (HEMT) amplifiers, in which case the use of low-noise power supply is necessary[3]. The majority of the signal lines connected to the DF only carry high frequency signals, where inner-outer DC blocks[4] can be used to break the formation of ground loops at low frequency. The DC connection to the DC voltage source for Z lines is necessary, demanding careful electrical connection design[5]. The DC connection to arbitrary waveform generator (AWG[6]) channels producing flux pulses is also unavoidable be-

[1] QMC-CRYOATT from Quantum Microwave or 4880-5523-XX-CRYO from XMA

[2] We use Polyethylene Terephthalate (PET) wraps for metal tubes and nylon bolts and nuts if necessary.

[3] We avoid using switching mode power supplies that is noisier than their linear counterparts. In out setup, we use LNF-PBA linear power block from Quantum Microwave.

[4] Inmet 8039 or CD9519 from Centric RF

[5] We mount the breakout board and the DC voltage source (QDAC from QDevil) to an instrument rack via nylon bolts and nuts. In addition, we use a USB isolator (UH401 from B&B SmartWorx) to break the electrical connection via the USB connection port.

[6] Quantum Machines OPX+

cause rejecting the DC component of the flux pulses leads to severe pulse distortion. We take care of the AWG ground by electrically isolating the instrument chassis from the rack and using EM interference filtering units[7] to connect the AWG to the power strip.

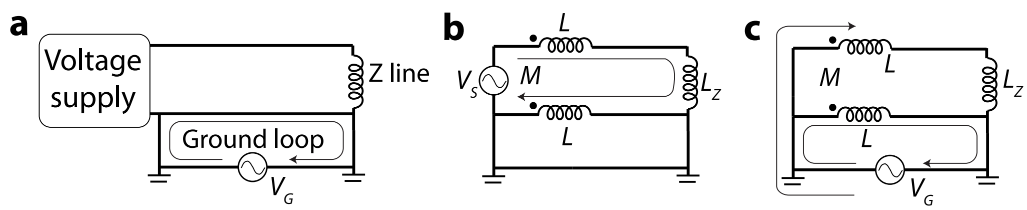

Figure 3.6: **Ground loop and common-mode choke.** **a**, Circuit diagram showing a voltage supply providing tuning current for a Z line, whereas the connection to ground at the Z line and the voltage supply creates a ground loop with the noise voltage V_G. **b**, Circuit diagram showing voltage supply V_S creating a differential mode current (arrow) to bias the Z line (L_Z), which is not affected by the common mode choke ($L = M$). **c**, Circuit diagram showing the ground noise V_G creating common mode currents (arrows) that could influence the Z line current, which sees the impedance $j\omega L$ from the common mode choke ($L = M$). This figure is inspired from [180].

From the above analysis, we see that the cryostat ground is still inevitably connected to the earth ground at multiple points, forming ground loops (Fig. 3.6a). To reduce the noise from the ground loops, we use common-mode chokes to suppress the influence from ground noise [180]. A common-mode choke introduces mutual inductance between the signal line and the return line, resulting in a large impedance for the common-mode current from the ground noise while maintaining zero impedance for the differential-mode current from the signal source (Fig. 3.6b-c). In practice, the common-mode choke can be implemented by wrapping the transmission line around a Ferrite ring or surrounding the transmission line with Ferrite snap-on beads[8].

To probe the noise level when implementing the above measures, we either measure the spectrum by connecting a transmission line from the DF to a spectrum analyzer or measuring the coherence time of a qubit. The spectrum analyzer measurement is especially quick and useful when the device is at room temperature or when the flux lines are not connected to the qubits. Using this method, we have observed

[7]AREC148FG-N515 from OnFilter

[8]We use both Mix 31 Ferrite covering 1-300 MHz and Mix 75 Ferrite covering 150 kHz-10 MHz.

that the common-mode chokes play the role of lowering the noise power. The qubit coherence is the ultimate target to optimize. For example, we have observed that adding a single Ferrite snap-on bead[9] on the flux pulse line improves the T_2^* from 733 ns to 938 ns, which is further improved to 1.1 μs with 15 beads.

Multi-qubit system operation

Calibrating and operating a multi-qubit system requires systematic approaches, involving individual-qubit-level up to system-level operations. It is not realistic to manually specifying the dependencies among the operations and assigning parameters to all the tuning knobs for every experiment. To operate a multi-qubit or even a NISQ device, we need both efficient infrastructure and strategies.

An efficient infrastructure in our case means a platform that registers and manages resources for easy access from high-level users. The resources include hardware resources, which can be categorized as classical hardware (such as the AWG and the DC voltage supply) and quantum hardware (such as a quantum simulator). The resources also include software ones such as the parameters for a control pulse. In this thesis, we build the infrastructure based on the QUA language developed by Quantum Machines that programs OPX+, which is in charge of qubit control and read-out. The compatibility of the QUA language with the Python environment allows us to register and control other hardware in a single script. The QUA language also provides the abstraction of low-level controls, e.g., wrapping the arbitrary waveform of a π-pulse operation on *Input line 1* into `play('pi', 'q1')`. The parameters, such as the ones providing details for the pulses and the physical connections are specified in the `configuration`. To achieve higher-level abstraction and include parameters specifying the status of the quantum hardware or control over other classical hardware, we construct the quantum processing unit database (`qpu_db`), which is based on the packages[10] developed by Quantum Machines.

Equipped with the above infrastructure, we can develop strategies to operate the multi-qubit system. The ultimate goal is to construct a routine that efficiently or even automatically calibrates the system and performs the experiments we have designed. Towards this goal, we use graph-based strategies [181] supported by the Quantum Machines packages. In our case, an experiment consists of multiple functional *graphs*, e.g., a graph for classical hardware calibration, a graph for

[9] Mix 75, SNO75-1/2 from Palomar Engineers

[10] `entropylab` and `entropylab_qpudb`. https://github.com/entropy-lab/entropy

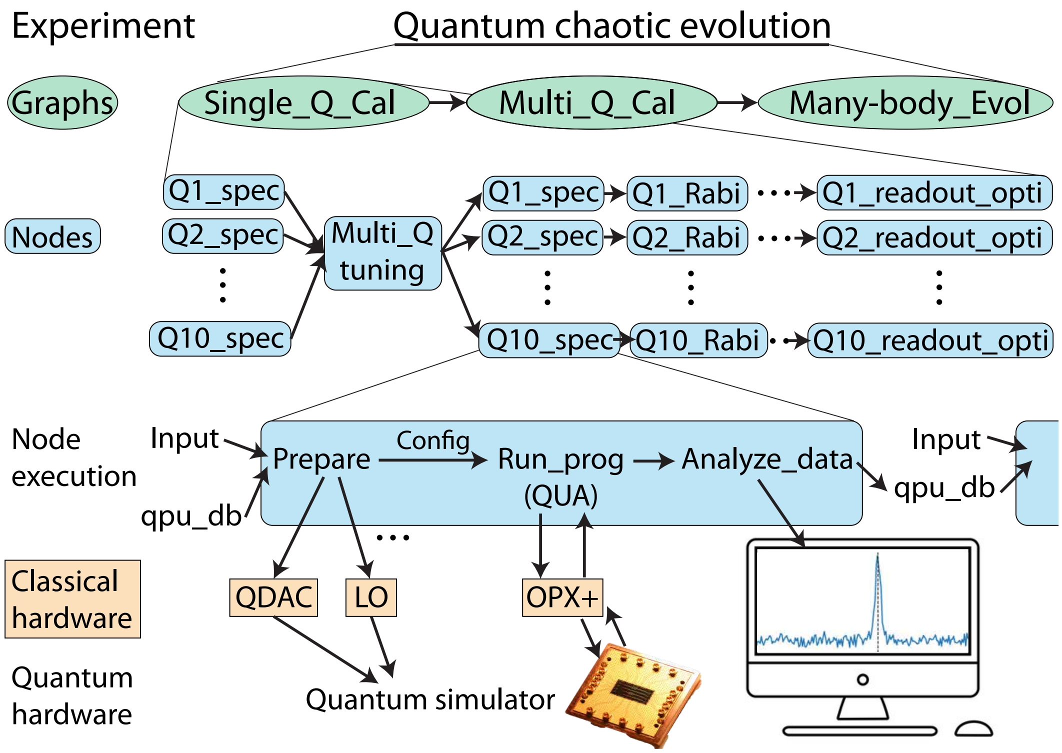

Figure 3.7: **Multi-qubit system operation.** An example experiment (Quantum chaotic evolution) consists of three graphs: single-qubit calibration graph (`Single_Q_Cal`), multi-qubit calibration graph (`Multi_Q_Cal`), and many-body evolution graph (`Many-body_Evol`). The graph `Single_Q_Cal` consists of multiple nodes with inter-dependency, including Q_j spectroscopy (`Qj_spec`), multi-qubit bias tuning (`Multi_Qtuning`), Q_j Rabi (`Qj_Rabi`), and Q_j read-out optimization (`Qj_readout_opti`). The node `Q10_spec` takes the input parameters and the `qpu_db` to prepare the control of classical hardware such as QDAC and the local oscillators (LO), and generate the `configuration` (`config`) to feed into the QUA program (`Run_prog`). The QUA program controls the OPX+, which both sends signals into and collect information from the quantum simulator. The node then analyzes and visualizes the data (`Analyze_data`), and updates the `qpu_db` for the next node.

single-qubit calibration, and a graph for multi-qubit experiment. These graphs can be run sequentially or individually depending on the users' demand. Each graph consists of multiple *nodes* which complete specific calibrations or operations such as qubit spectroscopy, optimal read-out condition calibration, or tuning all qubits on-resonance to interact under the Hamiltonian. Each node is defined in a relatively generic way such that it can be used for different elements and parameters. More specifically, when initializing a node, we pass input parameters such as the qubit label, the sweeping range, and the center frequency into a qubit spectroscopy node. By specifying these node parameters and the dependency among the nodes, we have constructed a graph. During the execution of nodes on the directed graph, it is important to keep track of the parameters renewed from the calibrations, where the infrastructure `qpu_db` plays the role of registering the most up-to-date status of the system. Within each node, the program takes the input parameters and the current `qpu_db` to update the status of classical hardware and construct the `configuration` to control the OPX+. After the operation, the node is responsible of collecting and analyzing the data, as well as updating the `qpu_db` if necessary. A structural illustration of running an experiment is shown in Fig. 3.7.

The above infrastructure and graph-based strategies have enabled the automatic experimental run starting from single-qubit calibration, multi-qubit calibration, to chaotic quantum many-body evolution described in Chapter 6. The automatic run can continue for more than 10 hours under the usual condition that the experimental system is stable. Although not yet implemented, the running strategies can be further developed to handle more complicated situations such as checking whether a calibration remains valid and running partial calibrations as needed [181].

Chapter 4

CAVITY QUANTUM ELECTRODYNAMICS WITH ATOM-LIKE MIRRORS

Equipped with the theoretical background of waveguide QED and the experimental techniques from design to measurement, we can put the pieces together and tackle experimentally one of the major challenges of waveguide QED mentioned in Sec. 2.1. This challenge—that the rapid decay of quantum emitters into the waveguide hampers the observation and usage of any coherent interaction—is rooted in the nature of waveguide-mediated interactions. Here, combining a smart protocol [139] and careful engineering, we observe, for the first time, coherent waveguide-mediated dynamics in an open environment. In this chapter, we start with an introduction placing this experiment in a rich historical context of light-matter interaction with a collective of quantum emitters. We then provide an intuitive picture of the experiments followed by measurement results in spectroscopy and time domain. Finally, we explore the higher excitation manifold and demonstrate the quantum nature of the collective effects. This chapter is adapted from [47] with a method section at the end of this chapter and the supplementary information in App. B.

4.1 Introduction

It has long been recognized that atomic emission of radiation is not an immutable property of an atom, but rather is dependent on the electromagnetic environment [100], and in the case of ensembles, also on the collective interactions between the atoms [136, 182–185]. In an open radiative environment, the hallmark of collective interactions is super-radiant spontaneous emission [136], with non-dissipative dynamics largely obscured by rapid atomic decay [186]. Here, with precise positioning of artificial atoms in the form of transmon qubits [69] along a one-dimensional waveguide, we observe dynamical exchange of excitations between a single artificial atom and an entangled collective state of an atomic array [139]. This collective state is a dark state which traps radiation, creating a form of cavity with artificial atoms acting as resonant mirrors in the otherwise open waveguide. The emergent atom-cavity system is shown to achieve a large cooperativity ($\mathcal{C} \gtrsim 100$), entering the regime of strong coupling in which coherent interactions overwhelm all dissipative and decoherence effects. Achieving strong coupling with interacting qubits in an open waveguide provides an efficient means of synthesizing multi-photon dark states, and more broadly, paves the way for exploiting correlated dissipation and decoherence-free subspaces of quantum emitter arrays at the many-body level [146, 187–189].

Collective interaction of atoms in the presence of a radiation field has been studied since the early days of quantum physics. As first studied by Dicke [136], the interaction of resonant atoms in such systems results in the formation of super- and sub-radiant states in the spontaneous emission. While Dicke utilized his central insight—that atoms interact coherently even through an open environment—to understand the radiation properties of an idealized, point-like atomic gas, the dynamical properties of ordered extended ensembles coupled to open environments exhibit similarly elegant physics. In their most essential form, such systems can be studied within the canonical waveguide quantum electrodynamics (QED) model [125]: atoms coupled to a one-dimensional (1D) continuum realized by an optical fiber or a microwave waveguide [115, 119]. Within this model, a diverse and rich set of phenomena await experimental study. For instance, one can synthesize an artificial cavity QED system [139], distill exotic many-excitation dark states with fermionic spatial correlations [146], and use classical light sources to generate entangled and quantum many-body states of light [187–189].

A central technical hurdle common to these research avenues—reaching the so-called "strong coupling" regime, in which atom-atom interactions dominate decay—is of ubiquitous import and experimental difficulty in quantum science. This hurdle is especially difficult to clear in waveguide QED, owing to the fact that while the waveguide facilitates infinite-range interactions between the atoms [147, 148], it also provides a dissipative channel [190]. Decoherence through this and other sources destroys the fragile many-body states of the system, which has limited the experimental state-of-the-art to spectroscopic probes of waveguide-mediated interactions [149, 163, 191]. However, by utilizing the collective dark states of precisely placed atoms whose overwhelming source of decoherence is emission into the waveguide, the strong coupling limit is predicted to be within reach [139]. Additionally, if the timescale of single-atom emission into the waveguide is long enough to permit measurement and manipulation of the system, the coherent dynamics can be driven and probed at the single-atom level. Here, we clear all of these hurdles with a waveguide QED system consisting of transmon qubits coupled to a common microwave waveguide, thereby unleashing the full toolbox of waveguide QED.

As a demonstration of these new tools, we construct the aforementioned emergent cavity QED system and probe its linear and non-linear dynamics. This realization features an ancillary probe qubit and a cavity-like mode formed by the dark state of two single-qubit mirrors. Using waveguide transmission and individual addressing of the probe qubit, we are able to observe spectroscopic and time-domain signatures of the collective dynamics of the qubit array, including vacuum Rabi oscillations between the probe qubit and the cavity-like mode. The latter provides direct evidence of strong coupling between these modes as well as a natural method to efficiently create and measure dark states that are inaccessible through the waveguide. In contrast to traditional cavity QED, our cavity-like mode is itself quantum nonlinear, as we show by characterizing the two-excitation dynamics of the array.

4.2 Theoretical formalism

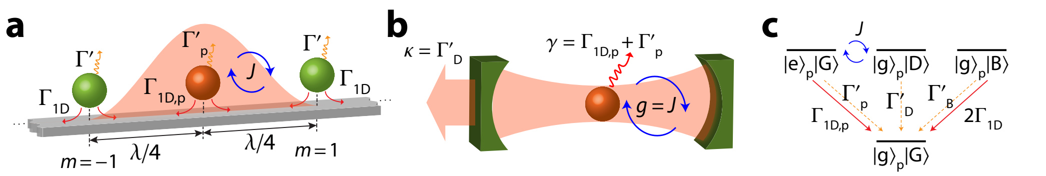

Figure 4.1: **Schematics of atomic cavity QED. a**, Schematic showing cavity configuration of waveguide-QED system consisting of an array of N mirror qubits ($N = 2$ shown; green) coupled to the waveguide with an inter-qubit separation of $\lambda_0/2$, with a probe qubit (red) at the center of the mirror array. **b**, Schematic showing analogous cavity-QED system with correspondence to waveguide parameters. **c**, Energy level diagram of the system of three qubits (2 mirror, one probe). The mirror dark state $|\mathrm{D}\rangle$ is coupled to the excited state of the probe qubit $|\mathrm{e}\rangle_{\mathrm{p}}$ at a cooperatively enhanced rate of $2J = \sqrt{2\Gamma_{\mathrm{1D}}\Gamma_{\mathrm{1D,p}}}$. The bright state is decoupled from the probe qubit. This figure is adapted from [47].

The collective evolution of an array of resonant qubits coupled to a 1D waveguide can be formally described by a master equation of the form $\dot{\hat{\rho}} = -i/\hbar[\hat{H}_{\text{eff}}, \hat{\rho}] + \sum_{m,n} \Gamma_{m,n}\hat{\sigma}^m_{\text{ge}}\hat{\rho}\hat{\sigma}^n_{\text{eg}}$ [139, 145], where $\hat{\sigma}^m_{\text{ge}} = |\mathrm{g}_m\rangle\langle\mathrm{e}_m|$, and m and n represent indices into the qubit array. Within the Born-Markov approximation, the effective Hamiltonian can be written in the interaction picture as

$$\hat{H}_{\text{eff}} = \hbar \sum_{m,n} \left(J_{m,n} - i\frac{\Gamma_{m,n}}{2} \right) \hat{\sigma}^m_{\text{eg}}\hat{\sigma}^n_{\text{ge}}. \tag{4.1}$$

Figure 4.1 depicts the waveguide-QED system considered in this work. The system consists of an array of N qubits separated by distance $d = \lambda_0/2$ and a separate probe qubit centered in the middle of the array with waveguide decay rate $\Gamma_{\text{1D,p}}$ ($\lambda_0 = c/\omega_0$ is the wavelength of a radiation field in the waveguide that is in resonance with the qubits). In this configuration, the effective Hamiltonian can be simplified in the single-excitation manifold to

$$\hat{H}_{\text{eff}} = -\frac{iN\hbar\Gamma_{\text{1D}}}{2}\hat{S}_{\text{B}}^{\dagger}\hat{S}_{\text{B}} - \frac{i\hbar\Gamma_{\text{1D,p}}}{2}\hat{\sigma}_{\text{ee}}^{(\text{p})} + \hbar J\left(\hat{\sigma}_{\text{ge}}^{(\text{p})}\hat{S}_{\text{D}}^{\dagger} + \text{h.c.}\right), \tag{4.2}$$

where $\hat{S}_{\text{B,D}} = 1/\sqrt{N}\sum_{m>0}(\hat{\sigma}_{\text{ge}}^{m} \mp \hat{\sigma}_{\text{ge}}^{-m})(-1)^m$ are the lowering operators of the bright collective state and the fully-symmetric dark collective state of the qubit array (as shown in Fig. 4.1a, $m > 0$ and $m < 0$ denote qubits to the right and left of the probe qubit, respectively). As evident by the last term in the Hamiltonian, the probe qubit is coupled to this dark state at a cooperatively enhanced rate $2J = \sqrt{N}\sqrt{\Gamma_{\text{1D}}\Gamma_{\text{1D,p}}}$. The bright state super-radiantly emits into the waveguide at a rate of $N\Gamma_{\text{1D}}$. The collective dark state has no coupling to the waveguide, and a decoherence rate Γ'_{D} which is set by parasitic damping and dephasing not captured in the simple waveguide-QED model (App. B.2). In addition to the bright and dark collective states described above, there exist an additional $N-2$ collective states of the qubit array with no coupling to either the probe qubit or the waveguide [139].

The subsystem consisting of coupled probe qubit and symmetric dark state of the mirror qubit array can be described in analogy to a cavity-QED system [139]. In this picture the probe qubit plays the role of a two-level atom and the dark state mimics a high-finesse cavity with the qubits in the $\lambda_0/2$-spaced array acting as atomic mirrors (see Fig. 4.1b). In general, provided that the fraction of excited array qubits remains small as N increases, $\hat{S}_{\text{D}}$ stays nearly bosonic and the analogy to the Jaynes-Cummings model remains valid. Mapping waveguide parameters to those of a cavity-QED system, the cooperativity between probe qubit and atomic cavity can be written as $\mathcal{C} = (2J)^2/(\Gamma_{\text{1D,p}} + \Gamma'_{\text{p}})\Gamma'_{\text{D}} \approx NP_{\text{1D}}$. Here $P_{\text{1D}} = \Gamma_{\text{1D}}/\Gamma'_{\text{D}}$ is the single qubit Purcell factor, which quantifies the ratio of waveguide emission rate to parasitic damping and dephasing rates. Attaining $\mathcal{C} > 1$ is a prerequisite for observing coherent quantum effects. Referring to the energy level diagram of Fig. 4.1c, by sufficiently reducing the waveguide coupling rate of the probe qubit one can also realize a situation in which $J > (\Gamma_{\text{1D,p}} + \Gamma'_{\text{p}}), \Gamma'_{\text{D}}$, corresponding to the strong coupling regime of cavity QED between excited state of the probe qubit ($|\text{e}\rangle_{\text{p}}|\text{G}\rangle$) and a single photon in the atomic cavity ($|\text{g}\rangle_{\text{p}}|\text{D}\rangle$). This mapping of a waveguide QED system onto a cavity QED analog therefore allows to use cavity-QED techniques to efficiently probe the dark states of the qubit array with single-photon precision.

4.3 Experimental results

Device description and spectroscopy results

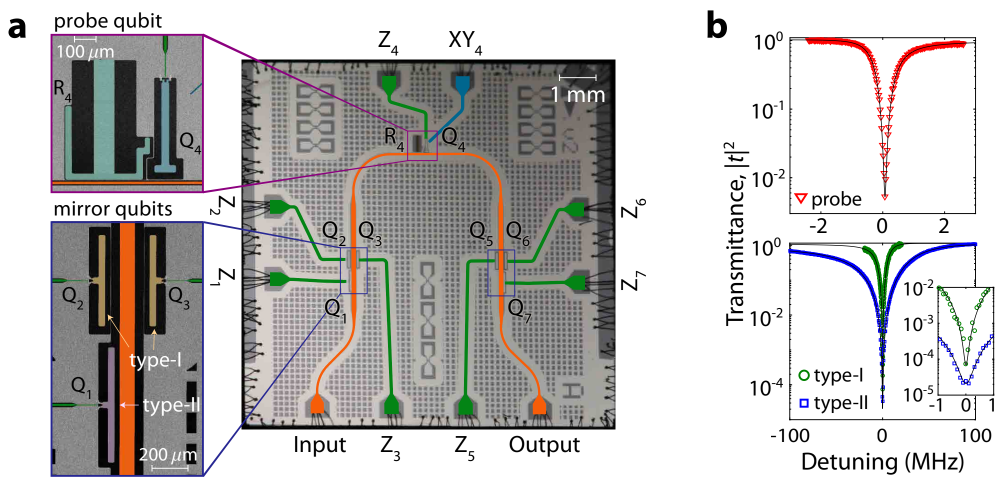

Figure 4.2: **Device and single-qubit spectroscopy.** **a**, Optical image of the fabricated waveguide-QED chip. Tunable transmon qubits interact via microwave photons in a superconducting coplanar waveguide (CPW; false-color orange trace). The CPW is used for externally exciting the system and is terminated in a 50-Ω load. Insets: Scanning electron microscope image of the different qubit designs used in our experiment. The probe qubit, designed to have $\Gamma_{\text{1D,p}}/2\pi = 1$ MHz, is accessible via a separate CPW (XY_4; false-color blue trace) for state preparation, and is also coupled to a compact microwave resonator (R_4; false-color cyan) for dispersive read-out. The mirror qubits come in two types: type-I with $\Gamma_{\text{1D}}/2\pi = 20$ MHz and type-II with $\Gamma_{\text{1D}}/2\pi = 100$ MHz. **b**, Waveguide transmission spectrum across individual qubit resonances (top: probe qubit (Q_4) ; bottom: individual type-I (Q_6, green curve) and type-II (Q_1, blue curve) mirror qubits). From Lorentzian line-shape fit of the measured waveguide transmission spectra we infer Purcell factors of $P_{\text{1D}} = 11$ for the probe qubit and $P_{\text{1D}} = 98$ (219) for the type-I (type-II) mirror qubit. This figure is adapted from [47].

The fabricated superconducting circuit used to realize the waveguide-QED system is shown in Fig. 4.2a. The circuit consists of seven transmon qubits (Q_j for $j = 1$-7), all of which are side-coupled to the same coplanar waveguide (CPW). Each qubit's transition frequency is tunable via an external flux bias port (Z_1-Z_7). We use the top-center qubit in the circuit (Q_4) as a probe qubit. This qubit can be independently excited via a weakly-coupled CPW drive line (XY_4), and is coupled to a lumped-element microwave cavity (R_4) for dispersive read-out of its state. The other six qubits are mirror qubits. The mirror qubits come in two different types (I and II), which have been designed to have different waveguide coupling rates ($\Gamma_{1D,I}/2\pi = 20$ MHz and $\Gamma_{1D,II}/2\pi = 100$ MHz) in order to provide access to a range of Purcell factors. Type-I mirror qubits also lie in pairs across the CPW waveguide and have rather large (~ 50 MHz) direct coupling. We characterize the waveguide and parasitic coupling rates of each individual qubit by measuring the phase and amplitude of microwave transmission through the waveguide (see Fig. 4.2b) [118]. In order to reduce thermal noise, measurements are performed in a dilution refrigerator at a base temperature of 8 mK (see Methods Sec. 4.5). For a sufficiently weak coherent drive the effects of qubit saturation can be neglected and the on-resonance extinction of the coherent waveguide tone relates to a lower bound on the individual qubit Purcell factor. Any residual waveguide thermal photons, however, can result in weak saturation of the qubit and a reduction of the on-resonance extinction. We find an on-resonance intensity transmittance as low as 2×10^{-5} for the type-II mirror qubits, corresponding to an upper bound on the CPW mode temperature of 43 mK and a lower bound on the Purcell factor of 200. Further details of the design, fabrication, and measured parameters of probe and each mirror qubit are provided in the section.

The transmission through the waveguide, in the presence of the probe qubit, can also be used to measure spectroscopic signatures of the collective dark state of the qubit array. As an example of this we utilize a single pair of mirror qubits (Q_2, Q_6 of type-I), which we tune to a frequency where their separation along the waveguide axis is $d = \lambda_0/2$. The remaining qubits on the chip are decoupled from the waveguide input by tuning their frequency away from the measurement point. Figure 4.3a shows the waveguide transmission spectrum for a weak coherent tone in which a broad resonance dip is evident corresponding to the bright state of the mirror qubit pair. We find a bright state waveguide coupling rate of $\Gamma_{1D,B} \approx 2\Gamma_{1D} = 2\pi \times 26.8$ MHz by fitting a Lorentzian lineshape to the spectrum. The dark state of the mirror qubits, being dark, is not observable in this waveguide spectrum. The dark state becomes observable, however, when measuring the waveguide transmission with the probe qubit tuned into resonance with the mirror qubits (see Fig. 4.3b). In addition to the broad response from the bright state, in this case there appears two spectral peaks near the center of the bright state resonance (Fig. 4.3c). This pair of highly non-Lorentzian spectral features result from the Fano interference between the broad

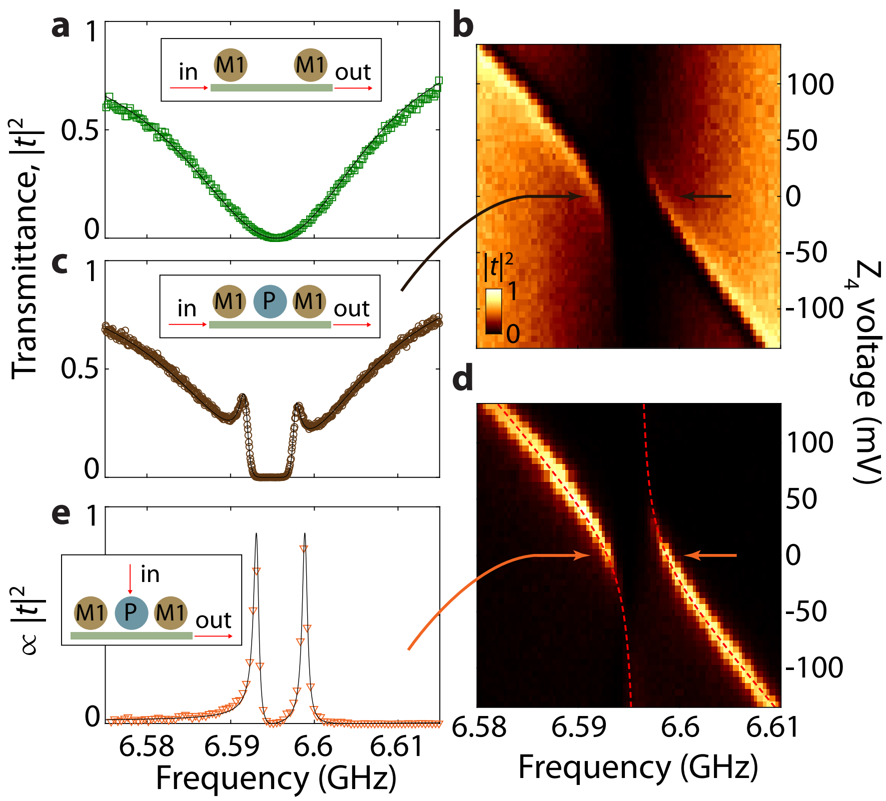

Figure 4.3: **Vacuum Rabi splitting.** **a**, Transmission through the waveguide for two mirror qubits (Q_2,Q_6) on resonance, with the remaining qubits on the chip tuned away from the measurement frequency range. **b**, Transmission through the waveguide as a function of the flux bias tuning voltage of the probe qubit (Q_4). **c**, Waveguide transmission spectrum for the three qubits tuned into resonance. **d**. Transmission spectrum as measured between the probe qubit drive line XY_4 and the waveguide output as a function of flux bias tuning of the probe qubit. **e**, XY_4-to-waveguide transmission spectrum for the three qubits tuned into resonance. The dashed red lines in (d) and solid black line in (e) show predictions of a numerical model with experimentally measured qubit parameters. The prediction in (e) includes slight power broadening effects. Legend: M1 and P denote type-I mirror qubits (Q_2,Q_6) and the probe qubit (Q_4), respectively. This figure is adapted from [47].

bright state and the hybridized polariton resonances formed between the dark state of the mirror qubits (atomic cavity photon) and the probe qubit. The hybridized probe qubit and atomic cavity eigenstates can be more clearly observed by measuring the transmission between the probe qubit drive line (XY_4) and the output port of the waveguide (see Fig. 4.3d). As the XY_4 line does not couple to the bright state due to the symmetry of its positioning along the waveguide, we observe two well-resolved resonances in Fig. 4.3e with mode splitting $2J/2\pi \approx 6$ MHz when the probe qubit is nearly resonant with the dark state. Observation of vacuum Rabi splitting in the hybridized atomic cavity-probe qubit polariton spectrum signifies operation in the strong coupling regime.

Time-domain measurements

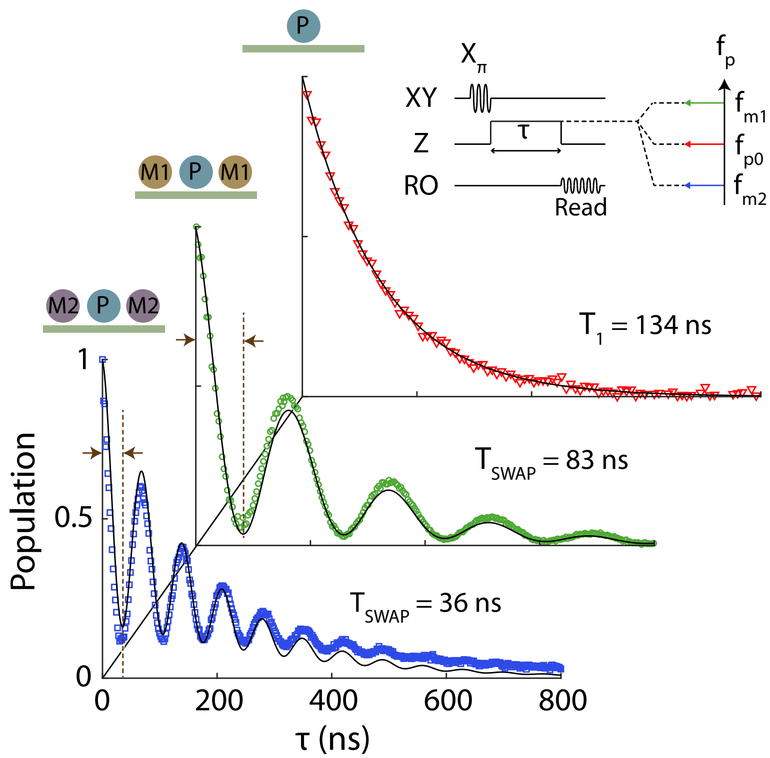

Figure 4.4: **Vacuum Rabi oscillations.** Measured population of the excited state of the probe qubit for three different scenarios. (i) Probe qubit tuned to $f_{\mathrm{p0}} = 6.55$ GHz, with all mirror qubits tuned away, corresponding to free population decay (red curve). (ii) Probe qubit tuned into resonance with a pair of type-I mirror qubits (Q_2,Q_6) at frequency $f_{\mathrm{m1}} = 6.6$ GHz corresponding to $d_{\mathrm{I}} = \lambda_0/2$ (green curve). (iii) Probe qubit tuned in resonance with type-II mirror qubits (Q_1,Q_7) at frequency $f_{\mathrm{m2}} = 5.826$ GHz corresponding to $d_{\mathrm{II}} = \lambda_0/2$ (blue curve). Inset: The sequence of pulses applied during the measurement. Legends: P, M1, and M2 denote the probe qubit, type-I, and type-II mirror qubits, respectively. This figure is adapted from [47].

To further investigate the signatures of strong coupling we perform time domain measurements in which we prepare the system in the initial state $|\mathrm{g}\rangle_{\mathrm{p}}|\mathrm{G}\rangle \rightarrow |\mathrm{e}\rangle_{\mathrm{p}}|\mathrm{G}\rangle$ using a 10 ns microwave π pulse applied at the XY_4 drive line. Following excitation of the probe qubit we use a fast (5 ns) flux bias pulse to tune the probe qubit into resonance with the collective dark state of the mirror qubits (atomic cavity) for a desired interaction time, τ. Upon returning to its initial frequency after the flux bias pulse, the excited state population of the probe qubit state is measured via the dispersively coupled read-out resonator. In Fig. 4.4 we show a timing diagram and plot three measured curves of the probe qubit's population dynamics versus τ. The top red curve corresponds to the measured probe qubit's free decay, where the probe qubit is shifted to a detuned frequency f_{p0} to eliminate mirror qubit interactions. From an exponential fit to the decay curve we find a decay rate of $1/T_1 \approx 2\pi \times 1.19$ MHz, in agreement with the result from waveguide spectroscopy at f_{p0}. In the middle green and bottom blue curves we plot the measured probe qubit population dynamics when interacting with an atomic cavity formed from type-I and type-II mirror qubit pairs, respectively. In both cases the initially prepared state $|\mathrm{e}\rangle_{\mathrm{p}}|\mathrm{G}\rangle$ undergoes vacuum Rabi oscillations with the dark state of the mirror qubits $|\mathrm{g}\rangle_{\mathrm{p}}|\mathrm{D}\rangle$. Along with the measured data we plot a theoretical model where the waveguide coupling, parasitic damping, and dephasing rate parameters of the probe qubit and dark state are taken from independent measurements, and the detuning between probe qubit and dark state is left as a free parameter (App. B.2). From the excellent agreement between measurement and model we infer an interaction rate of $2J/2\pi = 5.64$ MHz (13.0 MHz) and a cooperativity of $\mathcal{C} = 94$ (172) for the type-I (type-II) mirror system. For both mirror types we find that the system is well into the strong coupling regime ($J \gg \Gamma_{\mathrm{1D,p}} + \Gamma'_{\mathrm{p}}, \Gamma'_{\mathrm{D}}$), with the photon-mediated interactions dominating the decay and dephasing rates by roughly two orders of magnitude.

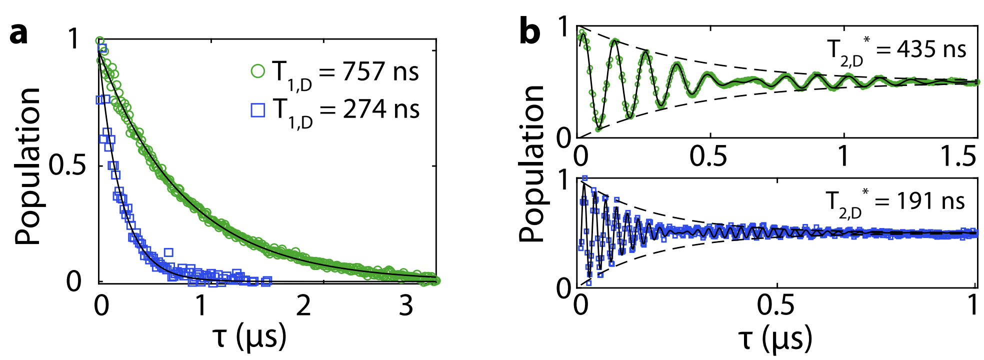

Figure 4.5: **Dark state coherence.** **a**, Measurement of the population decay time ($T_{1,\mathrm{D}}$) of the dark state of type-I (green curve) and type-II (blue curve) mirror qubits. **b**, Corresponding Ramsey coherence time ($T^*_{2,\mathrm{D}}$) of the type-I and type-II dark states. This figure is adapted from [47].

The tunable interaction time in our measurement sequence also allows for performing state transfer between the probe qubit and the dark state of the mirror qubits via an iSWAP gate. We measure the dark state's population decay in a protocol where we excite the probe qubit and transfer the excitation into the dark state (see Fig. 4.5a). From an exponential fit to the data we find a dark state decay rate of $T_{1,\mathrm{D}} = 757$ ns (274 ns) for type-I (type-II) mirror qubits, enhanced by roughly the cooperativity over the bright state lifetime. In addition to lifetime, we can measure the coherence time of the dark state with a Ramsey-like sequence (see Fig. 4.5b), yielding $T^{*}_{2,\mathrm{D}} = 435$ ns (191 ns) for type-I (type-II) mirror qubits. The collective dark state coherence time, being slightly shorter than its population decay time, hints at correlated sources of noise in the distantly entangled qubits forming the dark state (App. B.3).

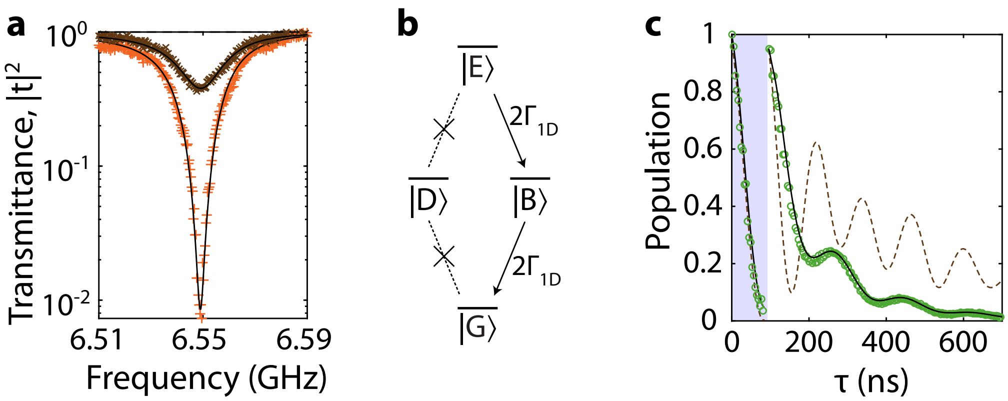

Figure 4.6: **Beyond single-excitation manifold.** **a**, Waveguide transmission spectrum through the atomic cavity without (brown data points) and with (orange data points) pre-population of the cavity. Here the atomic cavity was initialized in a single photon state by performing an iSWAP gate with the probe qubit followed by detuning of the probe qubit away from resonance. In both cases the transmission measurement is performed using coherent rectangular pulses with a duration of 260 ns and a peak power of $P \approx 0.03(\hbar\omega_0\Gamma_{1\mathrm{D}})$. Solid lines show theory fits from numerical modeling of the system. **b**, Energy level diagram of the 0 ($|\mathrm{G}\rangle$), 1 ($|\mathrm{D}\rangle$,$|\mathrm{B}\rangle$), and 2 ($|\mathrm{E}\rangle$) excitation manifolds of the atomic cavity indicating waveguide induced decay and excitation pathways. **c**, Rabi oscillation with two excitations in the system of probe qubit and atomic cavity. The shaded region shows the first iSWAP step in which an initial probe qubit excitation is transferred to the atomic cavity. Populating the probe qubit with an additional excitation at this point results in strong damping of subsequent Rabi oscillations due to the rapid decay of state $|\mathrm{E}\rangle$. Dashed brown curve is the predicted result for interaction of the probe qubit with an equivalent linear cavity. The atomic cavity is formed from type-I mirror qubits Q_2 and Q_6. This figure is adapted from [47].

Our experiments so far have probed the waveguide and multi-qubit array with a single excitation. While the cavity QED analog is helpful for understanding the response of the system in this regime, this analogy is not fully accurate for understanding multi-excitation dynamics. Driving the system beyond a single excitation, the quantum nonlinear response of the qubits leads to a number of interesting phenomena. To observe this, we populate the atomic cavity with a single photon via an iSWAP gate and then measure the waveguide transmission of weak coherent pulses through the system. Figure 4.6a shows transmission through the atomic cavity formed from type-I mirror qubits before and after adding a single photon. The sharp change in the transmissivity of the atomic cavity is a result of trapping in the long-lived dark state of the mirror qubits. The dark state has no transition dipole to the waveguide channel (see Fig. 4.6b), and thus it cannot participate in absorption or emission of photons when probed via the waveguide. As a result, populating the atomic cavity with a single photon makes it nearly transparent to incoming waveguide signals for the duration of the dark-state lifetime. This is analogous to the electron shelving phenomenon which leads to suppression of resonance fluorescence in three-level atomic systems [192]. As a further example, we use the probe qubit to attempt to prepare the cavity in the doubly excited state via two consecutive iSWAP gates. In this case, with only two mirror qubits and the rapid decay via the bright state of the two-excitation state $|\mathrm{E}\rangle$ of the mirror qubits (refer to Fig. 4.6b), the resulting probe qubit population dynamics shown in Fig. 4.6c have a strongly damped response ($\mathcal{C} < 1$) with weak oscillations occurring at the vacuum Rabi oscillation frequency. This is in contrast to the behavior of a linear cavity (dashed green curve of Fig. 4.6c), where driving the second photon transition leads to persistent Rabi oscillations with a frequency that is $\sqrt{2}$ larger than vacuum Rabi oscillations. Further analysis of the nonlinear behavior of the atomic cavity is provided in App. B.4.

The waveguide-QED chip of Fig. 4.2a can also be used to investigate the spectrum of sub-radiant states that emerge when $N > 2$ and direct interaction between mirror qubits is manifest. This situation can be realized by taking advantage of the capacitive coupling between co-localized pairs of type-I qubits (Q_2 and Q_3 or Q_5 and Q_6). Although in an idealized 1D waveguide model there is no cooperative interaction term between qubits with zero separation along the waveguide, as shown in Fig. 4.7a we observe a strong coupling ($g/2\pi = 46$ MHz) between the co-localized pair of Q_2 and Q_3 mirror qubits. This coupling results from near-field components of the electromagnetic field that are excluded in the simple waveguide model. The non-degenerate hybridized eigenstates of the qubit pair effectively

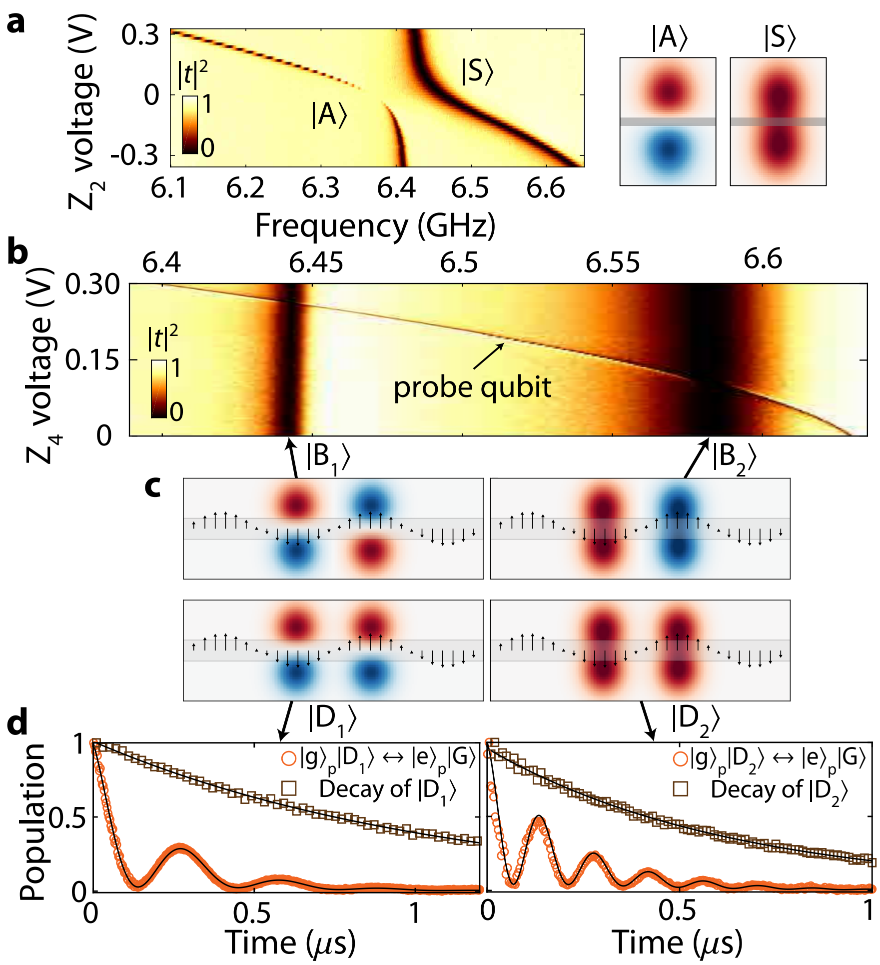

Figure 4.7: $N = 4$ **compound atomic mirrors.** **a**, Avoided mode crossing of a pair of type-I mirror qubits positioned on the opposite sides of the CPW. Near the degeneracy point, the qubits form a pair of compound eigenstates consisting of symmetric ($|\mathrm{S}\rangle$) and anti-symmetric ($|\mathrm{A}\rangle$) states with respect to the waveguide axis. **b**, Measured transmission through the waveguide with the pair of compound atomic mirrors aligned in frequency. The two broad resonances correspond to super-radiant states $|\mathrm{B}_1\rangle$ and $|\mathrm{B}_2\rangle$ as indicated. Tuning the probe qubit we observe the (avoided-crossing like) signatures of the interaction of the probe qubit with the dark states. **c**, Illustration of the single-excitation manifold of the collective states of a $N = 4$ mirror qubits forming a pair of compound atomic cavities. The bright (super-radiant) and dark (sub-radiant) states can be identified by comparing the symmetry of the compound qubit states with the resonant radiation field pattern in the waveguide. **d**, Probe qubit measurements of the two dark states, $|\mathrm{D}_1\rangle$ and $|\mathrm{D}_2\rangle$. In these measurements the frequency of each dark state is shifted to ensure $\lambda_0/2$ separation between the two compound atomic mirrors. This figure is adapted from [47].

behave as a compound atomic mirror. The emission rate of each compound mirror to the waveguide can be adjusted by setting the detuning Δ between the pair. As illustrated in Fig. 4.7b, resonantly aligning the compound atomic mirrors on both ends of the waveguide results in a hierarchy of bright and dark states involving both near-field and waveguide-mediated cooperative coupling. Probing the system with a weak tone via the waveguide, we identify the two super-radiant combinations of the compound atomic mirrors (Fig. 4.7c). Similar to the case of a two-qubit cavity, we can identify the collective dark states via the probe qubit. As evidenced by the measured Rabi oscillations shown in Fig. 4.7d, the combination of direct and waveguide-mediated interactions of mirror qubits in this geometry results in the emergence of a pair of collective entangled states of the four qubits acting as strongly-coupled atomic cavities with frequency separation of $\sqrt{4g^2 + \Delta^2}$.

4.4 Conclusion and outlook

In conclusion, we have realized a synthetic cavity QED system to observe and drive the coherent dynamics that emerge from correlated dissipation in an open waveguide. While our current work has reached single-qubit Purcell factors of 200—an order-of-magnitude increase in the experimental state-of-the-art in planar superconducting quantum circuits and on par with the values achievable in less scalable 3D architectures [165]—further improvement is possible. With better thermalization to the waveguide [177] and coherence times in line with the best planar superconducting qubits [193], Purcell factors in excess of 10^4 should be achievable. In this regime, with an already achieved system size of $N = 4$, a universal set of quantum gates with fidelity above 0.99 can theoretically be realized by encoding information in decoherence-free subspaces [129]. Even without improved Purcell factors, the demonstrated control over the sub-radiant states of an atomic chain enables studying formation of fermionic correlations between excitations, and the power-law decay dynamics associated with a critical open system in a modestly-sized array (N = 10) [146]. Further, the demonstrated ability to measure the population decay time and coherence time for the entangled states of multiple distant qubits provides a valuable experimental tool for understanding the sources of correlated decoherence in circuit QED. Finally, reducing the frequency disorder of the transmon qubits beyond the values measured in our system ($\delta f \approx 60$ MHz) and using a slow-light metamaterial waveguide [172], would allow chip-scale waveguide-QED experiments with a much larger number of qubits, in the range $N = 10$–100, where the full extent of the many-body dynamics of large quantum spin chains can be studied [187–189].

4.5 Methods

Fabrication

The device used in this work is fabricated on a 1 cm $\times$ 1 cm high resistivity 10 kΩ-cm silicon substrate. The ground plane, waveguides, resonator, and qubit capacitors are patterned by electron-beam lithography followed by electron beam evaporation of 120 nm Al at a rate of 1 nm/s. A liftoff process is performed in N-methyl-2-pyrrolidone at 80 °C for 1.5 hours. The Josephson junctions are fabricated using double-angle electron-beam evaporation on suspended Dolan bridges, following similar techniques as in Ref. [194]. The airbridges are patterned using grayscale electron-beam lithography and developed in a mixture of isopropyl alcohol and deionized water [195]. After 2 hours of resist reflow at 105 °C, electron-beam evaporation of 140 nm Al is performed at 1 nm/s rate following 5 minutes of Ar ion mill. Liftoff is done in the same fashion as in the previous steps.

Qubits

We have designed and fabricated transmon qubits in three different variants for the experiment (see Fig. 4.8a-b): type-I mirror qubits (Q_2, Q_3, Q_5, Q_6), type-II mirror qubits (Q_1, Q_7), and the probe qubit (Q_4). The qubit frequency tuning range, waveguide coupling rate (Γ_{1D}), and parasitic decoherence rate (Γ') can be extracted from waveguide spectroscopy measurements of the individual qubits. The values for all the qubits inferred in this manner are listed in Table 4.1. Note that Γ' is defined as due to damping and dephasing from channels other than the waveguide at zero temperature. The inferred value of Γ' from waveguide spectroscopy measurements is consistent with this definition in the zero temperature waveguide limit (effects of finite waveguide temperature are considered in App. B.1). The standard deviation in maximum frequencies of the four identically designed qubits (type-I) is found as 61 MHz, equivalent to $\sim 1\%$ qubit frequency disorder in our fabrication process. Asymmetric Josephson junctions are used in all qubits' superconducting quantum interference device (SQUID) loops (Fig. 4.8c) to reduce dephasing from flux noise, which limits the tuning range of qubits to $\sim$ 1.3 GHz. For Q_4, the Josephson energy of the junctions are extracted to be $(E_{J1}, E_{J2})/h = (18.4,\ 3.5)$ GHz, giving

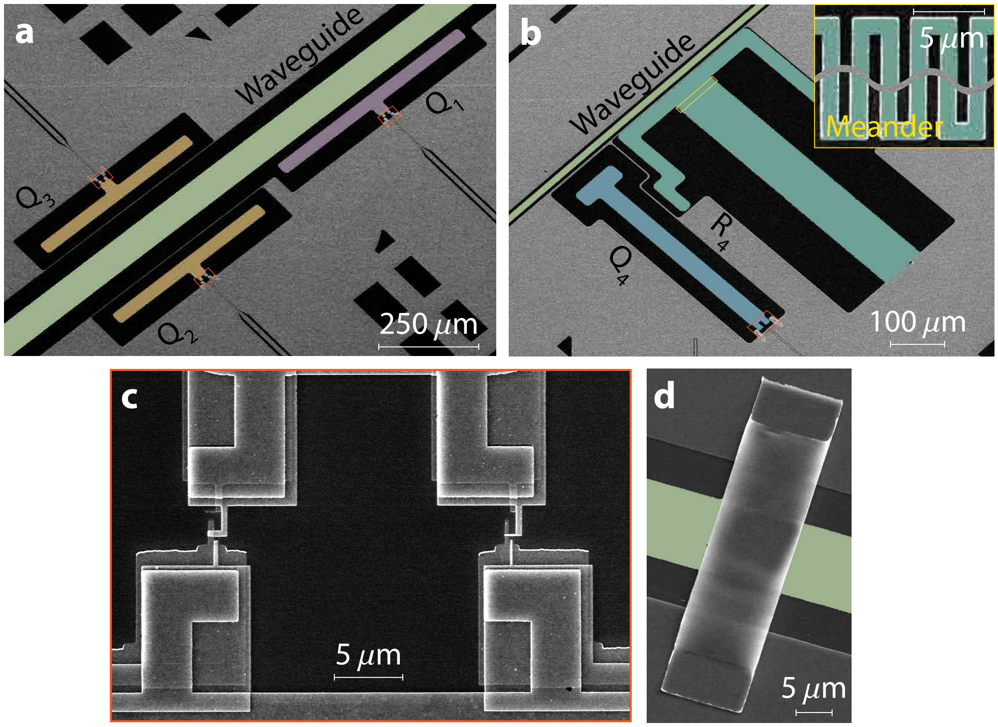

Figure 4.8: **Scanning electron microscope of the fabricated device.** **a**, Type-I (Q_2, Q_3) and type-II (Q_1) mirror qubits coupled to the coplanar waveguide (CPW). **b**, The central probe qubit (Q_4) and lumped-element read-out resonator (R_4) coupled to CPW. Inset: inductive meander of the lumped-element read-out resonator. **c**, A superconducting quantum interference device (SQUID) loop with asymmetric Josephson junctions used for qubits. **d**, An airbridge placed across the waveguide to suppress slotline mode. This figure is adapted from [47].

junction asymmetry of $d \equiv \frac{E_{J1}-E_{J2}}{E_{J1}+E_{J2}} = 0.68$. The anharmonicity was measured to be $\eta/2\pi = -272$ MHz and $E_J/E_C = 81$ at maximum frequency for Q_4.

Read-out

We have fabricated a lumped-element resonator (shown in Fig. 4.8b) to perform dispersive read-out of the state of central probe qubit (Q_4). The lumped-element resonator consists of a capacitive claw and an inductive meander of ~ 1 μm pitch, effectively acting as a quarter-wave resonator. The bare frequency of resonator and coupling to probe qubit are extracted to be $f_\mathrm{r} = 5.156$ GHz and $g/2\pi = 116$ MHz, respectively, giving dispersive frequency shift of $\chi/2\pi = -2.05$ MHz for Q_4 at maximum frequency. The resonator is loaded to the common waveguide in the

	Q_1	Q_2	Q_3	Q_4	Q_5	Q_6	Q_7
f_{max} (GHz)	6.052	6.678	6.750	6.638	6.702	6.817	6.175
f_{min} (GHz)	4.861	5.373	5.389	5.431	5.157	5.510	4.972
$\Gamma_{1D}/2\pi$ (MHz)	94.1	16.5	13.9[a,b]	0.91	18.4[b]	18.1	99.5
$\Gamma'/2\pi$ (kHz)	430	< 341	< 760[a,b]	81	375[b]	185	998

[a] Measured at 6.6 GHz
[b] Measured without the cold attenuator

Table 4.1: **Qubit characteristics.** f_{max} (f_{min}) is the maximum (minimum) frequency of the qubit, corresponding to "sweet spots" with zero first-order flux sensitivity. Γ_{1D} is the qubit's rate of decay into the waveguide channel and Γ' is its parasitic decoherence rate due to damping and dephasing from channels other than the waveguide at 0 temperature. All reported values are measured at the maximum frequency of each qubit, save for Q_3 in which case the values were measured at 6.6 GHz (marked with superscript [a]). With the exception of Q_3 and Q_5 (marked with superscript [b]), all the values are measured with the cold attenuator placed in the input line of the waveguide (App. B.1).

experiment, and its internal and external quality factors are measured to be $Q_i = 1.3 \times 10^5$ and $Q_e = 980$ below single-photon level. It should be noted that the resonator-induced Purcell decay rate of Q_4 is $\Gamma_1^{\text{Purcell}}/2\pi \sim 70$ kHz, small compared to the decay rate into the waveguide $\Gamma_{1D,p}/2\pi \sim 1$ MHz. The compact footprint of the lumped-element resonator is critical for minimizing the distributed coupling effects that may arise from interference between direct qubit decay to the waveguide and the the Purcell decay of the qubit via the resonator path.

Suppression of spurious modes

In our experiment we use a coplanar transmission line for realizing a microwave waveguide. In addition to the fundamental propagating mode of the waveguide, which has even symmetry with respect to the waveguide axis, these structures also support a set of modes with the odd symmetry, known as the slotline modes. The propagation of the slotline mode can be completely suppressed in a waveguide with perfectly symmetric boundary conditions. However, in practice perfect symmetry cannot be maintained over the full waveguide length, which unavoidably leads to presence of the slotline mode as a spurious loss channel for the qubits. Crossovers connecting ground planes across the waveguide are known to suppress propagation of slotline mode, and to this effect, aluminum airbridges have been used in superconducting circuits with negligible impedance mismatch for the desired CPW mode

[196].

In this experiment, we place airbridges (Fig. 4.8d) along the waveguide and control lines with the following considerations. Airbridges create reflecting boundary for slotline mode, and if placed by a distance d a discrete resonance corresponding to wavelength of $2d$ is formed. By placing airbridges over distances smaller than $\lambda/4$ apart from each other (λ is the wavelength of the mode resonant with the qubits), we push the slotline resonances of the waveguide sections between the airbridges to substantially higher frequencies. In this situation, the dissipation rate of qubits via the spurious channel is significantly suppressed by the off-resonance Purcell factor $\Gamma_1^{\text{Purcell}} \sim (g/\Delta)^2\kappa$, where Δ denotes detuning between the qubit transition frequency and the frequency of the odd mode in the waveguide section between the two airbridges. The parameters g and κ are the interaction rate of the qubit and the decay rate of the slot-line cavity modes. In addition, we place the airbridges before and after bends in waveguide, to ensure the fundamental waveguide mode is not converted to the slot-line mode upon propagation [197].

Crosstalk in flux biasing

We tune the frequency of each qubit by supplying a bias current to individual Z control lines, which controls the magnetic flux in the qubit's SQUID loop. The bias currents are generated via independent bias voltages generated by seven arbitrary waveform generator (AWG) channels, allowing for simultaneous tuning of all qubits. In practice, independent frequency tuning of each qubit needs to be accompanied by small changes in the flux bias of the qubits in the near physical vicinity of the qubit of interest, due to cross-talk between adjacent Z control lines.

In this experiment, we have characterized the crosstalk between bias voltage channels of the qubits in the following way. First, we tune the qubits not in use to frequencies more than 800 MHz away from the working frequency (which is set as either 5.83 GHz or 6.6 GHz). These qubits are controlled by fixed biases such that their frequencies, even in the presence of crosstalk from other qubits, remain far enough from the working frequency and hence are not considered for the rest of the analysis. Second, we tune the remaining qubits in use to relevant frequencies within $100\,\text{MHz}$ of the working frequency and record the biases $\mathbf{v}_0$ and frequencies $\mathbf{f}_0$ of these qubits. Third, we vary the bias on only a single (j-th) qubit and linearly interpolate the change in frequency (f_i) of the other (i-th) qubits with respect to bias voltage

v_j on j-th qubit, finding the cross talk matrix component $M_{ij} = (\partial f_i/\partial v_j)_{\mathbf{v}=\mathbf{v}_0}$. Repeating this step, we get the following (approximately linearized) relation between frequencies $\mathbf{f}$ and bias voltages $\mathbf{v}$ of qubits:

$$\mathbf{f} \approx \mathbf{f}_0 + M(\mathbf{v} - \mathbf{v}_0).$$

Finally, we take the inverse of the above relation to find bias voltages $\mathbf{v}$ that is required for tuning qubits to frequencies $\mathbf{f}$:

$$\mathbf{v} \approx \mathbf{v}_0 + M^{-1}(\mathbf{f} - \mathbf{f}_0).$$

An example of such crosstalk matrix between Q_2, Q_4, and Q_6 near $\mathbf{f}_0 = (6.6, 6.6, 6.6)$GHz used in the experiment is given by

$$M = \begin{pmatrix} 0.2683 & -0.0245 & -0.0033 \\ -0.0141 & -0.5310 & 0.0170 \\ 0.0016 & 0.0245 & 0.4933 \end{pmatrix} \mathrm{GHz/V}.$$

This indicates that the crosstalk level between Q_4 and either Q_2 or Q_6 is about 5%, while that between Q_2 and Q_6 is less than 1%. We have repeated similar steps for other configurations in the experiment.

Measurement setup

Fig. 4.9 illustrates the outline of the measurement chain in our dilution refrigerator. The sample is enclosed in a magnetic shield which is mounted at the mixing chamber. We have outlined four different types of input lines used in our experiment. Input lines to the waveguide and XY_4 go through a DC block at room temperature and are attenuated by 20 dB at the 4 K stage, followed by additional 40 dB of attenuation at the mixing chamber. The fast flux tuning lines (Z_3, Z_4) are attenuated by 20 dB and are filtered with a low-pass filter with corner frequency at 225 MHz to minimize thermal noise photons while maintaining short rise and fall time of pulses for fast flux control. The slow flux tuning lines (Z_1, Z_2, Z_5, Z_6, Z_7) are filtered by an additional low-pass filter with 64 kHz corner frequency at the 4K stage to further suppress noise photons. In addition, the waveguide signal output path contains a high electron mobility transistor (HEMT) amplifier at the 4K plate. Three circulators are placed in between the HEMT and the sample to ensure (> 70 dB) isolation of the sample from the amplifier noise. In addition, we have a series of low-pass and band-pass filters on the output line to suppress noise sources outside the measurement spectrum.

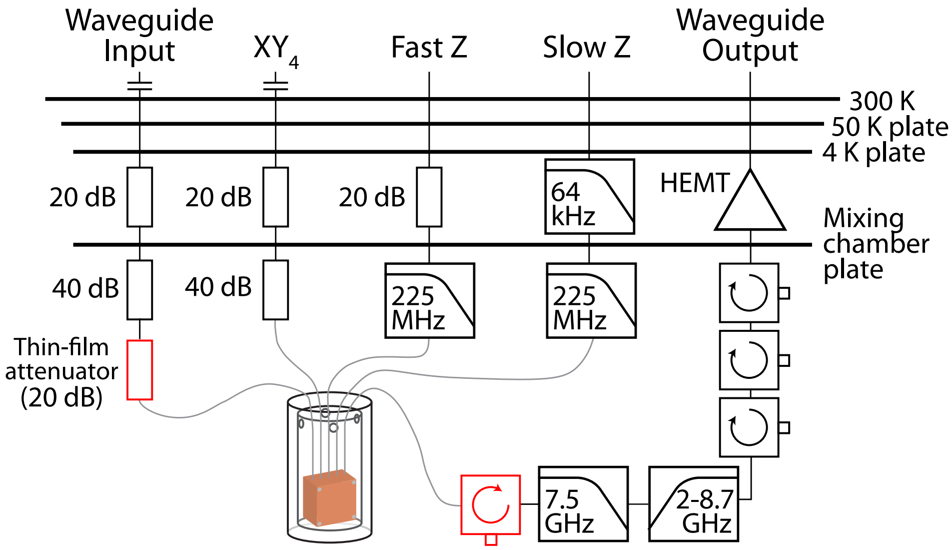

Figure 4.9: **Schematic of the measurement chain inside the dilution refrigerator.** The four types of input lines, the output line, and their connection to the device inside a magnetic shield are illustrated. Attenuators are expressed as rectangles with labeled power attenuation and capacitor symbols correspond to DC blocks. The thin-film attenuator and a circulator (colored red) are added to the waveguide input line and output line, respectively, in a second version of the setup and a second round of measurements to further protect the sample from thermal noise in the waveguide line. This figure is adapted from [47].

A thin-film "cold attenuator", developed by Palmer's group at the University of Maryland [177] is added to the measurement path in order to achieve better thermalization between the microwave coaxial line and its thermal environment. Similarly, an additional circulator is added to the waveguide measurement chain in later setups to further protect the device against thermal photons (both attenuator and circulator are highlighted in red in the schematic in Fig. 4.9). The effect of this change is discussed in App. B.1.

Dark state characterization

We characterize the collective dark state of mirror qubits with population decay time $T_{1,\mathrm{D}}$ and Ramsey coherence time $T^*_{2,\mathrm{D}}$ by utilizing the cooperative interaction with the probe qubit. For each configuration of mirror qubits, we obtain the Rabi oscillation curve (see Fig. 4.4 and Fig. 4.7d) using fast flux-bias pulse on the probe qubit as explained in the main text. The half-period T_{SWAP} of Rabi oscillation results in a complete transfer of probe qubit population to the collective dark state or vice versa, and hence defines an iSWAP gate.

To measure the population decay time $T_{1,\mathrm{D}}$ of dark state, we excite the probe qubit with a resonant microwave π-pulse, followed by an iSWAP gate. This prepares the collective dark state $|\mathrm{g}\rangle_{\mathrm{p}}|\mathrm{D}\rangle$ off-resonantly decoupled from the probe qubit. After free evolution of dark state for a variable duration τ, another iSWAP gate is applied to transfer the remaining dark state population back to the probe qubit. Finally, we measure the state of the probe qubit and perform an exponential fitting to the resulting decay curve.

Likewise, we measure Ramsey coherence time $T^*_{2,\mathrm{D}}$ of dark state as follows. First, we excite the probe qubit to a superposition $(|\mathrm{g}\rangle + |\mathrm{e}\rangle)_{\mathrm{p}}|\mathrm{G}\rangle$ of ground and excited states by applying a detuned microwave $\pi/2$-pulse. Next, application of an iSWAP gate maps this superposition to that of dark state $|\mathrm{g}\rangle_{\mathrm{p}}(|\mathrm{G}\rangle + |\mathrm{D}\rangle)$. After a varying delay time τ, another iSWAP gate is applied, followed by detuned $\pi/2$-pulse on the probe qubit. Measurement of the state of the probe qubit results in a damped oscillation curve, whose decay envelope gives the Ramsey coherence time of the dark state involved in the experiment. Note that the fast oscillation frequency in this curve is determined by detuning of dark state with respect to the frequency of the microwave pulses applied to the probe qubit.

Chapter 5

QUANTUM ELECTRODYNAMICS IN A TOPOLOGICAL WAVEGUIDE

The previous chapter enters a new regime of strong light-matter collective interaction by overcoming the rapid decay into the waveguide using subradiant states in the passband. In this chapter, we explore another territory of light-matter interaction where the light exhibits topological characteristics. Topological physics, originally employed to describe electrons in solid state materials, have played an important role in modeling and predicting exotic phases of matter, including quantum hall states [198] and topological insulators [199]. The recent realization of photons in similar periodic environment as electrons in solid state materials opened up the burgeoning field of topological photonics [200–202]. Combined with the advancement of micro- and nano-fabrication technology, topological photonics gives rise to novel phases of matter made of photons, as well as robustness in photon transport and lasing. Here, we bring topological photonics into the quantum regime by exploring the interaction between quantum emitters and topological photons in the waveguides with engineered dispersion. In this chapter, we start by explaining the construction of topological waveguides using microwave metamaterials, followed by observations of exotic properties endowed by the topology of the waveguide, including directional qubit-photon bound states in a bandgap and collective qubit passband spectroscopy that reflects the waveguide topological configuration. Lastly, we demonstrate population transfer between two distant qubits via the channel of topological edge states. This chapter is adapted from [131] and the supplementary information is in App. C.

5.1 Introduction

Harnessing the topological properties of photonic bands [200–202] is a burgeoning paradigm in the study of periodic electromagnetic structures. Topological concepts discovered in electronic systems [198, 199] have now been translated and studied as photonic analogs in various microwave and optical systems [201, 202]. In particular, symmetry-protected topological phases [203] which do not require time-reversal-symmetry breaking, have received significant attention in experimental studies of photonic topological phenomena, both in the linear and nonlinear regime [204]. One of the simplest canonical models is the Su-Schrieffer-Heeger (SSH) model [205, 206], which was initially used to describe electrons hopping along a one-dimensional dimerized chain with a staggered set of hopping amplitudes between nearest-neighbor elements. The chiral symmetry of the SSH model, corresponding to a symmetry of the electron amplitudes found on the two types of sites in the dimer chain, gives rise to two topologically distinct phases of electron propagation. The SSH model, and its various extensions, have been used in photonics to explore a variety of optical phenomena, from robust lasing in arrays of microcavities [207, 208] and photonic crystals [209], to disorder-insensitive 3rd harmonic generation in zigzag nanoparticle arrays [210].

Utilization of quantum emitters brings new opportunities in the study of topological physics with strongly interacting photons [211–213], where single-excitation dynamics [214] and topological protection of quantum many-body states [215] in the SSH model have recently been investigated. In a similar vein, a topological photonic bath can also be used as an effective substrate for endowing special properties to quantum matter. For example, a photonic waveguide which localizes and transports electromagnetic waves over large distances, can form a highly effective quantum light-matter interface [94, 115, 130] for introducing non-trivial interactions between quantum emitters. Several systems utilizing highly dispersive electromagnetic waveguide structures have been proposed for realizing quantum photonic matter exhibiting tailorable, long-range interactions between quantum emitters [120, 158, 160, 162, 163]. With the addition of non-trivial topology to such a photonic bath, exotic classes of quantum entanglement can be generated through photon-mediated interactions of a chiral [152, 216] or directional nature [164, 217].

With this motivation, here we investigate the properties of quantum emitters coupled to a topological waveguide which is a photonic analog of the SSH model, following the theoretical proposal in Ref. [164]. Our setup is realized by coupling superconducting transmon qubits [69] to an engineered superconducting metamaterial waveguide [144, 172], consisting of an array of sub-wavelength microwave resonators with SSH topology. Combining the notions from waveguide quantum electrodynamics (QED) [115, 119, 125, 130] and topological photonics [201, 202], we observe qubit-photon bound states with directional photonic envelopes inside a bandgap and cooperative radiative emission from qubits inside a passband dependent on the topological configuration of the waveguide. Coupling of qubits to the waveguide also allows for quantum control over topological edge states, enabling quantum state transfer between distant qubits via a topological channel.

5.2 Description of the topological waveguide

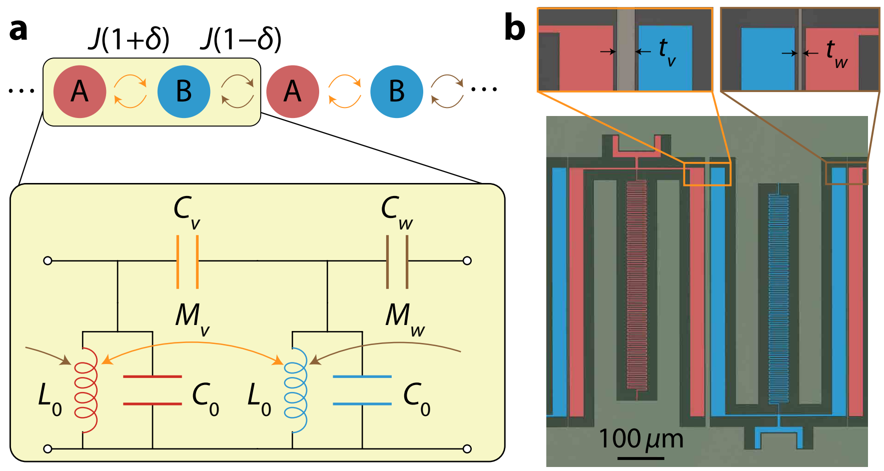

Figure 5.1: **Topological waveguide.** **a**, Top: schematic of the SSH model. Each unit cell contains two sites A and B (red and blue circles) with intra- and inter-cell coupling $J(1 \pm \delta)$ (orange and brown arrows). Bottom: an analog of this model in electrical circuits, with corresponding components color-coded. The photonic sites are mapped to LC resonators with inductance L_0 and capacitance C_0, with intra- and inter-cell coupling capacitance C_v, C_w and mutual inductance M_v, M_w between neighboring resonators, respectively (arrows). **b**, Optical micrograph (false-colored) of a unit cell (lattice constant $d = 592\,\mu$m) on a fabricated device in the topological phase. The lumped-element resonator corresponding to sublattice A (B) is colored in red (blue). The insets show zoomed-in view of the section between resonators where planar wires of thickness $(t_v, t_w) = (10, 2)\,\mu$m (indicated with black arrows) control the intra- and inter-cell distance between neighboring resonators, respectively. This figure is adapted from [131].

The SSH model describing the topological waveguide studied here is illustrated in Fig. 5.1a. Each unit cell of the waveguide consists of two photonic sites, A and B, each containing a resonator with resonant frequency ω_0. The intra-cell coupling between A and B sites is $J(1+\delta)$ and the inter-cell coupling between unit cells is $J(1-\delta)$. The discrete translational symmetry (lattice constant d) of this system allows us to write the Hamiltonian in terms of momentum-space operators, $\hat{H}/\hbar = \sum_k (\hat{\mathbf{v}}_k)^\dagger \, \mathbf{h}(k) \, \hat{\mathbf{v}}_k$, where $\hat{\mathbf{v}}_k = (\hat{a}_k, \hat{b}_k)^T$ is a vector operator consisting of a pair of A and B sublattice photonic mode operators, and the k-dependent kernel of the Hamiltonian is given by,

$$\mathbf{h}(k) = \begin{pmatrix} \omega_0 & f(k) \\ f^*(k) & \omega_0 \end{pmatrix}. \tag{5.1}$$

Here, $f(k) \equiv -J[(1+\delta)+(1-\delta)e^{-ikd}]$ is the momentum-space coupling between modes on different sublattice, which carries information about the topology of the system. The eigenstates of this Hamiltonian form two symmetric bands centered about the reference frequency ω_0 with dispersion relation

$$\omega_{\pm}(k) = \omega_0 \pm J\sqrt{2(1+\delta^2)+2(1-\delta^2)\cos(kd)},$$

where the $+$ $(-)$ branch corresponds to the upper (lower) frequency passband. While the band structure is dependent only on the magnitude of δ, and not on whether $\delta > 0$ or $\delta < 0$, deformation from one case to the other must be accompanied by the closing of the middle bandgap (MBG), defining two topologically distinct phases. For a finite system, it is well known that edge states localized on the boundary of the waveguide at a $\omega = \omega_0$ only appear in the case of $\delta < 0$, the so-called *topological* phase [202, 206]. The case for which $\delta > 0$ is the *trivial* phase with no edge states. It should be noted that for an infinite system, the topological or trivial phase in the SSH model depends on the choice of unit cell, resulting in an ambiguity in defining the bulk properties. Despite this, considering the open boundary of a finite-sized array or a particular section of the bulk, the topological character of the bands can be uniquely defined and can give rise to observable effects.

We construct a circuit analog of this canonical model using an array of inductor-capacitor (LC) resonators with alternating coupling capacitance and mutual inductance as shown in Fig. 5.1a. The topological phase of the circuit model is determined by the relative size of intra- and inter-cell coupling between neighboring resonators, including both the capacitive and inductive contributions. Strictly speaking, this circuit model breaks chiral symmetry of the original SSH Hamiltonian [202, 206], which ensures the band spectrum to be symmetric with respect to $\omega = \omega_0$. Nevertheless, the topological protection of the edge states under perturbation in the intra- and inter-cell coupling strengths remains valid as long as the bare resonant frequencies of resonators (diagonal elements of the Hamiltonian) are not perturbed, and the existence of edge states still persists due to the presence of inversion symmetry within the unit cell of the circuit analog, leading to a quantized Zak phase [218]. For detailed analysis of the modeling, symmetry, and robustness of the circuit topological waveguide see Apps. C.1 and C.2.

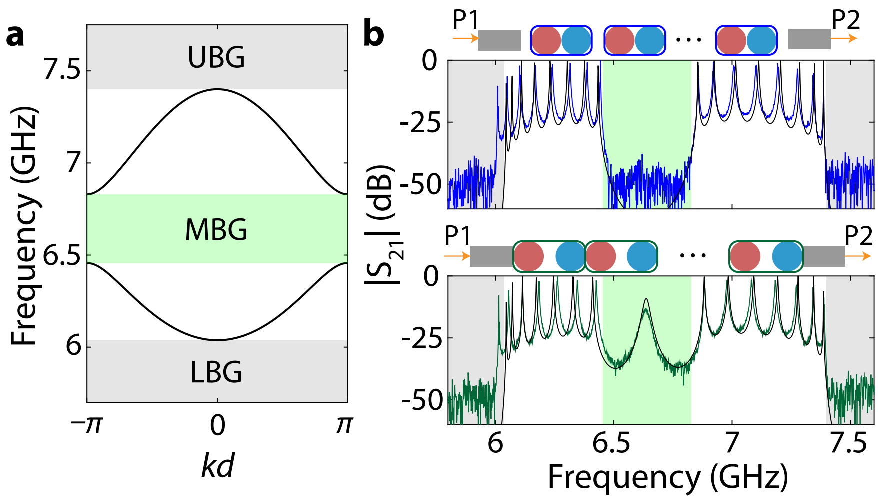

Figure 5.2: **Band structure of the topological waveguide.** **a**, Dispersion relation of the realized waveguide according to the circuit model in Fig. 5.1a. Upper bandgap (UBG) and lower bandgap (LBG) are shaded in gray, and middle bandgap (MBG) is shaded in green. **b**, Waveguide transmission spectrum $|S_{21}|$ across the test structure with 8 unit cells in the trivial ($\delta > 0$; top) and topological ($\delta < 0$; bottom) phase. The cartoons illustrate the measurement configuration of systems with external ports 1 and 2 (denoted P1 and P2), where distances between circles are used to specify relative coupling strengths between sites and blue (green) outlines enclosing two circles indicate unit cells in the trivial (topological) phase. Black solid curves are fits to the measured data (see App. C.1 for details) with parameters $L_0 = 1.9$ nH, $C_0 = 253$ fF, coupling capacitance $(C_v, C_w) = (33, 17)$ fF and mutual inductance $(M_v, M_w) = (-38, -32)$ pH in the trivial phase (the values are interchanged in the case of topological phase). The shaded regions correspond to bandgaps in the dispersion relation of panel **a**. This figure is adapted from [131].

The circuit model is realized using fabrication techniques for superconducting metamaterials discussed in Refs. [144, 172], where the coupling between sites is controlled by the physical distance between neighboring resonators. Due to the near-field nature, the coupling strength is larger (smaller) for smaller (larger) distance between resonators on a device. An example unit cell of a fabricated device in the topological phase is shown in Fig. 5.1b (the values of intra- and inter-cell distances are interchanged in the trivial phase). We find a good agreement between the measured transmission spectrum and a theoretical curve calculated from a LC lumped-element model of the test structures with 8 unit cells in both trivial and topological configurations (Fig. 5.2). For the topological configuration, the observed peak in the waveguide transmission spectrum at 6.636 GHz inside the MBG signifies the associated edge state physics in our system.

5.3 Properties of quantum emitters coupled to the topological waveguide

The non-trivial properties of the topological waveguide can be accessed by coupling quantum emitters to the engineered structure. To this end, we prepare Device I consisting of a topological waveguide in the trivial phase with 9 unit cells, whose boundary is tapered with specially designed resonators before connection to external ports (see Fig. 5.3a). The tapering sections at both ends of the array are designed to reduce the impedance mismatch to the external ports ($Z_0 = 50\,\Omega$) at frequencies in the upper passband (UPB). This is crucial for reducing ripples in the waveguide transmission spectrum in the passbands [144]. Every site of the 7 unit cells in the middle of the array is occupied by a single frequency-tunable transmon qubit [69] (the device contains in total 14 qubits labeled Q_i^α, where i =1-7 and α=A,B are the cell and sublattice indices, respectively). Properties of Device I and the tapering section are discussed in further detail in Apps. C.3 and C.4, respectively.

Directional qubit-photon bound states

For qubits lying within the middle bandgap, the topology of the waveguide manifests itself in the spatial profile of the resulting qubit-photon bound states. When the qubit transition frequency is inside the bandgap, the emission of a propagating photon from the qubit is forbidden due to the absence of photonic modes at the qubit resonant frequency. In this scenario, a stable bound state excitation forms, consisting of a qubit in its excited state and a waveguide photon with exponentially localized photonic envelope [156, 219]. Generally, bound states with a symmetric photonic envelope emerge due to the inversion symmetry of the photonic bath with respect to the qubit location [120]. In the case of the SSH photonic bath, however, a directional envelope can be realized [164] for a qubit at the centre of the MBG (ω_0), where the presence of a qubit creates a domain wall in the SSH chain and the induced photonic bound state is akin to an edge state (refer to App. C.5 for a detailed description). For example, in the trivial phase, a qubit coupled to site A (B) acts as the last site of a topological array extended to the right (left) while the subsystem consisting of the remaining sites extended to the left (right) is interpreted as a trivial array. Mimicking the topological edge state, the induced photonic envelope of the bound state faces right (left) with photon occupation only on B (A) sites (Fig. 5.3b), while

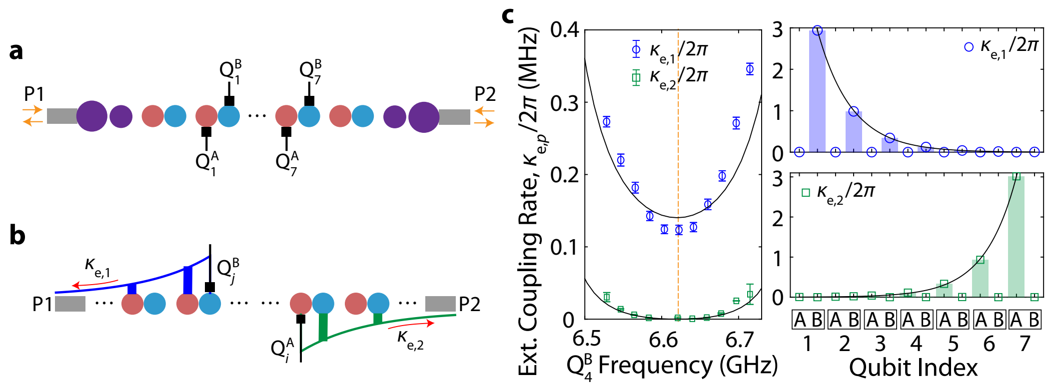

Figure 5.3: **Directionality of qubit-photon bound states.** **a**, Schematic of Device I, consisting of 9 unit cells in the trivial phase with qubits (black lines terminated with a square) coupled to every site on the 7 central unit cells. The ends of the array are tapered with additional resonators (purple) with engineered couplings designed to minimize impedance mismatch at upper passband frequencies. **b**, Theoretical photonic envelope of the directional qubit-photon bound states. At the reference frequency ω_0, the qubit coupled to site A (B) induces a photonic envelope to the right (left), colored in green (blue). The bars along the envelope indicate photon occupation on the corresponding resonator sites. **c**, Measured coupling rate $\kappa_{e,p}$ to external port numbers, $p = 1, 2$, of qubit-photon bound states. Left: external coupling rate of qubit Q_4^B to each port as a function of frequency inside the MBG. Solid black curve is a model fit to the measured external coupling curves. The frequency point of highest directionality is extracted from the fit curve, and is found to be $\omega_0/2\pi = 6.621$ GHz (vertical dashed orange line). Top (Bottom)-right: external coupling rate of all qubits tuned to $\omega = \omega_0$ measured from port P1 (P2). The solid black curves in these plots correspond to exponential fits to the measured external qubit coupling versus qubit index. This figure is adapted from [131].

across the trivial boundary on the left (right) there is no photon occupation. The opposite directional character is expected in the case of the topological phase of the waveguide. The directionality reduces away from the center of the MBG, and is effectively absent inside the upper or lower bandgaps.

We experimentally probe the directionality of qubit-photon bound states by utilizing the coupling of bound states to the external ports in the finite-length waveguide of Device I (see Fig. 5.3c). The external coupling rate $\kappa_{e,p}$ ($p = 1, 2$) is governed by the overlap of modes in the external port p with the tail of the exponentially attenuated envelope of the bound state, and therefore serves as a useful measure to characterize the localization [120, 172, 220]. To find the reference frequency ω_0 where the bound state becomes most directional, we measure the reflection spectrum S_{11} (S_{22})

of the bound state seen from port 1 (2) as a function of qubit tuning. We extract the external coupling rate $\kappa_{e,p}$ by fitting the measured reflection spectrum with a Fano lineshape [221]. For $\mathrm{Q}_4^{\mathrm{B}}$, which is located near the center of the array, we find $\kappa_{\mathrm{e},1}$ to be much larger than $\kappa_{\mathrm{e},2}$ at all frequencies inside MBG. At $\omega_0/2\pi = 6.621$ GHz, $\kappa_{\mathrm{e},2}$ completely vanishes, indicating a directionality of the $\mathrm{Q}_4^{\mathrm{B}}$ bound state to the left. Plotting the external coupling at this frequency to both ports against qubit index, we observe a decaying envelope on every other site, signifying the directionality of photonic bound states is correlated with the type of sublattice site a qubit is coupled to. Similar measurements when qubits are tuned to other frequencies near the edge of the MBG, or inside the upper bandgap (UBG), show the loss of directionality away from $\omega = \omega_0$ (App. C.6).

A remarkable consequence of the distinctive shape of bound states is direction-dependent photon-mediated interactions between qubits (Fig. 5.4). Due to the site-dependent shapes of qubit-photon bound states, the interaction between qubits becomes substantial only when a qubit on sublattice A is on the left of the other qubit on sublattice B, i.e., $j > i$ for a qubit pair ($\mathrm{Q}_i^{\mathrm{A}}$,$\mathrm{Q}_j^{\mathrm{B}}$). From the avoided crossing experiments centered at $\omega = \omega_0$, we extract the qubit-qubit coupling as a function of cell displacement $i - j$. An exponential fit of the data gives the localization length of $\xi = 1.7$ (in units of lattice constant), close to the estimated value from the circuit model of our system (see App. C.3). While theory predicts the coupling between qubits in the remaining combinations to be zero, we report that coupling of $|g_{ij}^{\mathrm{AA,BB}}|/2\pi \lesssim 0.66\,\mathrm{MHz}$ and $|g_{ij}^{\mathrm{AB}}|/2\pi \lesssim 0.48\,\mathrm{MHz}$ (for $i > j$) are observed, much smaller than the bound-state-induced coupling, e.g., $|g_{45}^{\mathrm{AB}}|/2\pi = 32.9$ MHz. We attribute such spurious couplings to the unintended near-field interaction between qubits. Note that we find consistent coupling strength of qubit pairs dependent only on their relative displacement, not on the actual location in the array, suggesting that physics inside MBG remains intact with the introduced waveguide boundaries. In total, the avoided crossing and external linewidth experiments at $\omega = \omega_0$ provide strong evidence of the shape of qubit-photon bound states, compatible with the theoretical photon occupation illustrated in Fig. 5.3b.

Topology-dependent photon scattering

In the passband regime, i.e., when the qubit frequencies lie within the upper or lower passbands, the topology of the waveguide is imprinted on cooperative interaction between qubits and the single-photon scattering response of the system.

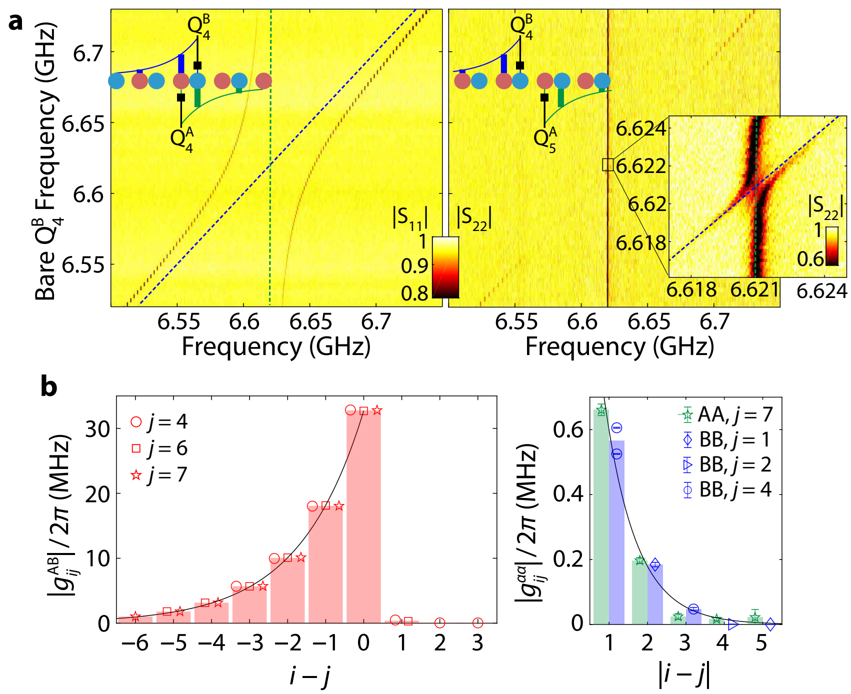

Figure 5.4: **Interaction between directional bound states.** **a**, Two-dimensional color intensity plot of the reflection spectrum under crossing between a pair of qubits with frequency centered around $\omega = \omega_0$. Left: reflection from P1 ($|S_{11}|$) while tuning $\mathrm{Q}_4^{\mathrm{B}}$ across $\mathrm{Q}_4^{\mathrm{A}}$ (fixed). An avoided crossing of $2|g_{44}^{\mathrm{AB}}|/2\pi = 65.7$ MHz is observed. Right: reflection from P2 ($|S_{22}|$) while tuning $\mathrm{Q}_4^{\mathrm{B}}$ across $\mathrm{Q}_5^{\mathrm{A}}$ (fixed), indicating the absence of appreciable coupling. Inset to the right shows a zoomed-in region where a small avoided crossing of $2|g_{54}^{\mathrm{AB}}|/2\pi = 967$ kHz is measured. The bare qubit frequencies from the fit are shown with dashed lines. **b**, Coupling $|g_{ij}^{\alpha\beta}|$ ($\alpha, \beta \in \{\mathrm{A,B}\}$) between various qubit pairs (Q_i^{α},Q_j^{β}) at $\omega = \omega_0$, extracted from the crossing experiments similar to panel (d). Solid black curves are exponential fits to the measured qubit-qubit coupling rate versus qubit index difference (spatial separation). Error bars in all figure panels indicate 95% confidence interval, and are omitted on data points whose marker size is larger than the error itself. This figure is adapted from [131].

The topology of the SSH model can be visualized by plotting the complex-valued momentum-space coupling $f(k)$ for k values in the first Brillouin zone (Fig. 5.5a). In the topological (trivial) phase, the contour of $f(k)$ encloses (excludes) the origin of the complex plane, resulting in the winding number of 1 (0) and the corresponding Zak phase of π (0) [218]. This is consistent with the earlier definition based on the sign of δ. It is known that for a regular waveguide with linear dispersion, the coherent exchange interaction J_{ij} and correlated decay Γ_{ij} between qubits at positions x_i and x_j along the waveguide take the forms $J_{ij} \propto \sin\varphi_{ij}$ and $\Gamma_{ij} \propto \cos\varphi_{ij}$ [139, 145], where $\varphi_{ij} = k|x_i - x_j|$ is the phase length.

In the case of our topological waveguide, considering a pair of qubits coupled to A/B sublattice on i/j-th unit cell, this argument additionally collects the phase $\phi(k) \equiv \arg f(k)$ [164]. This is an important difference compared to the regular waveguide case, because the zeros of equation

$$\varphi_{ij}(k) \equiv kd|i-j| - \phi(k) = 0 \mod \pi \tag{5.2}$$

determine wavevectors (and corresponding frequencies) where perfect Dicke super-radiance [136] occurs. Due to the properties of $f(k)$ introduced above, for a fixed cell-distance $\Delta n \equiv |i-j| \geq 1$ between qubits there exists exactly $\Delta n - 1$ (Δn) frequency points inside the passband where perfect super-radiance occurs in the trivial (topological) phase. An example for the $\Delta n = 2$ case is shown in Fig. 5.5b. Note that although Eq. (5.2) is satisfied at the band-edge frequencies ω_{min} and ω_{max} ($kd = \{0, \pi\}$), they are excluded from the above counting due to breakdown of the Born-Markov approximation (see App. C.7).

To experimentally probe signatures of perfect super-radiance, we tune the frequency of a pair of qubits across the UPB of Device I while keeping the two qubits resonant with each other. We measure the waveguide transmission spectrum S_{21} during this tuning, keeping track of the lineshape of the two-qubit resonance as J_{ij} and Γ_{ij} varies over the tuning. Drastic changes in the waveguide transmission spectrum occur whenever the two-qubit resonance passes through the perfectly super-radiant points, resulting in a swirl pattern in $|S_{21}|$. Such patterns arise from the disappearance of the peak in transmission associated with interference between photons scattered by imperfect super- and sub-radiant states, resembling the electromagnetically-induced transparency in a V-type atomic level structure [222]. As an example, we discuss the cases with qubit pairs ($\mathrm{Q}_2^{\mathrm{A}}$,$\mathrm{Q}_4^{\mathrm{B}}$) and ($\mathrm{Q}_2^{\mathrm{B}}$,$\mathrm{Q}_5^{\mathrm{A}}$), which are shown in Fig. 5.5c. Each qubit pair configuration encloses a three-unit-cell section of the waveguide; however for the ($\mathrm{Q}_2^{\mathrm{A}}$,$\mathrm{Q}_4^{\mathrm{B}}$) pair the waveguide section is in the trivial phase, whereas for ($\mathrm{Q}_2^{\mathrm{A}}$,$\mathrm{Q}_4^{\mathrm{B}}$) the waveguide section is in the topological phase. Both theory and measurement indicate that the qubit pair ($\mathrm{Q}_2^{\mathrm{A}}$,$\mathrm{Q}_4^{\mathrm{B}}$) has exactly one perfectly super-radiant frequency point in the UPB. For the other qubit pair ($\mathrm{Q}_2^{\mathrm{B}}$,$\mathrm{Q}_5^{\mathrm{A}}$), with waveguide section in the topological phase, two such points occur (corresponding to $\Delta n = 2$).

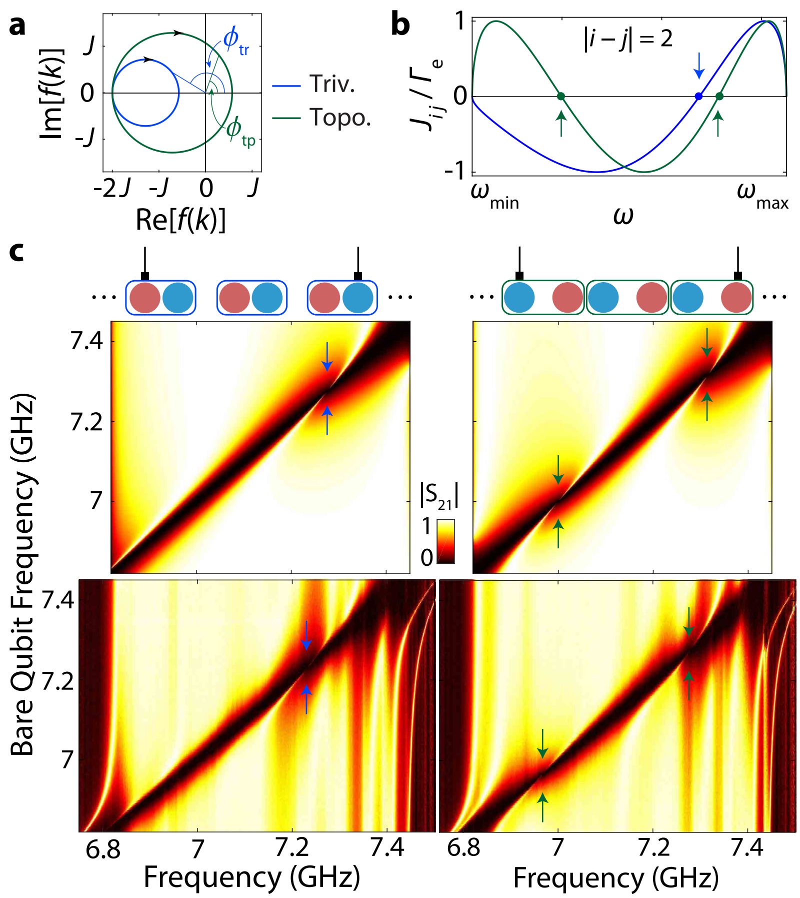

Figure 5.5: **Probing band topology using qubits.** **a**, $f(k)$ in the complex plane for k values in the first Brillouin zone. ϕ_{tr} (ϕ_{tp}) is the phase angle of $f(k)$ for a trivial (topological) section of waveguide, which changes by 0 (π) radians as kd transitions from 0 to π (arc in upper plane following black arrowheads). **b**, Coherent exchange interaction J_{ij} between a pair of coupled qubits as a function of frequency inside the passband, normalized to individual qubit decay rate Γ_{e} (only $kd \in [0, \pi)$ branch is plotted). Here, one qubit is coupled to the A sublattice of the i-th unit cell and the other qubit is coupled to the B sublattice of the j-th unit cell, where $|i - j| = 2$. Blue (green) curve corresponds to a trivial (topological) intermediate section of waveguide between qubits. The intercepts at $J_{ij} = 0$ (filled circles with arrows) correspond to points where perfect super-radiance occurs. **c**, Waveguide transmission spectrum $|S_{21}|$ as a qubit pair are resonantly tuned across the UPB of Device I [left: (Q_2^{A},Q_4^{B}), right: (Q_2^{B},Q_5^{A})]. Top: schematic illustrating system configuration during the experiment, with left (right) system corresponding to an interacting qubit pair subtending a three-unit-cell section of waveguide in the trivial (topological) phase. Middle and Bottom: two-dimensional color intensity plots of $|S_{21}|$ from theory and experiment, respectively. Swirl patterns (highlighted by arrows) are observed in the vicinity of perfectly super-radiant points, whose number of occurrences differ by one between trivial and topological waveguide sections. This figure is adapted from [131].

This observation highlights the fact that while the topological phase of the bulk in the SSH model is ambiguous, a finite section of the array can still be interpreted to have a definite topological phase. Apart from the unintended ripples near the band-edges, the observed lineshapes are in good qualitative agreement with the theoretical expectation in Ref. [164]. The frequency misalignment of swirl patterns between the theory and the experiment is due to the slight discrepancy between the realized circuit model and the ideal SSH model (see App. C.1 for details). Detailed description of the swirl pattern and similar measurement results for other qubit combinations with varying Δn are reported in App. C.7.

5.4 Quantum state transfer via topological edge states

Finally, to explore the physics associated with topological edge modes, we fabricated a second device, Device II, which realizes a closed quantum system with 7 unit cells in the topological phase (Fig. 5.6a). We denote the photonic sites in the array by (i,α), where i =1-7 is the cell index and α =A,B is the sublattice index. Due to reflection at the boundary, the passbands on this device appear as sets of discrete resonances. The system supports topological edge modes localized near the sites (1,A) and (7,B) at the boundary, labeled E_L and E_R. The edge modes are spatially distributed with exponentially attenuated tails directed toward the bulk. In a finite system, the non-vanishing overlap between the envelopes of edge states generates a coupling which depends on the localization length ξ and the system size L as $G \sim e^{-L/\xi}$. In Device II, two qubits denoted Q_L and Q_R are coupled to the topological waveguide at sites (2,A) and (6,B), respectively. Each qubit has a local drive line and a flux-bias line, which are connected to room-temperature electronics for control. The qubits are dispersively coupled to read-out resonators, which are coupled to a coplanar waveguide for time-domain measurement. The edge mode E_L (E_R) has photon occupation on sublattice A (B), inducing interaction g_L (g_R) with Q_L (Q_R). Due to the directional properties discussed earlier, bound states arising from Q_L and Q_R have photonic envelopes facing away from each other inside the MBG, and hence have no direct coupling to each other. For additional details on Device II and qubit control, refer to App. C.8.

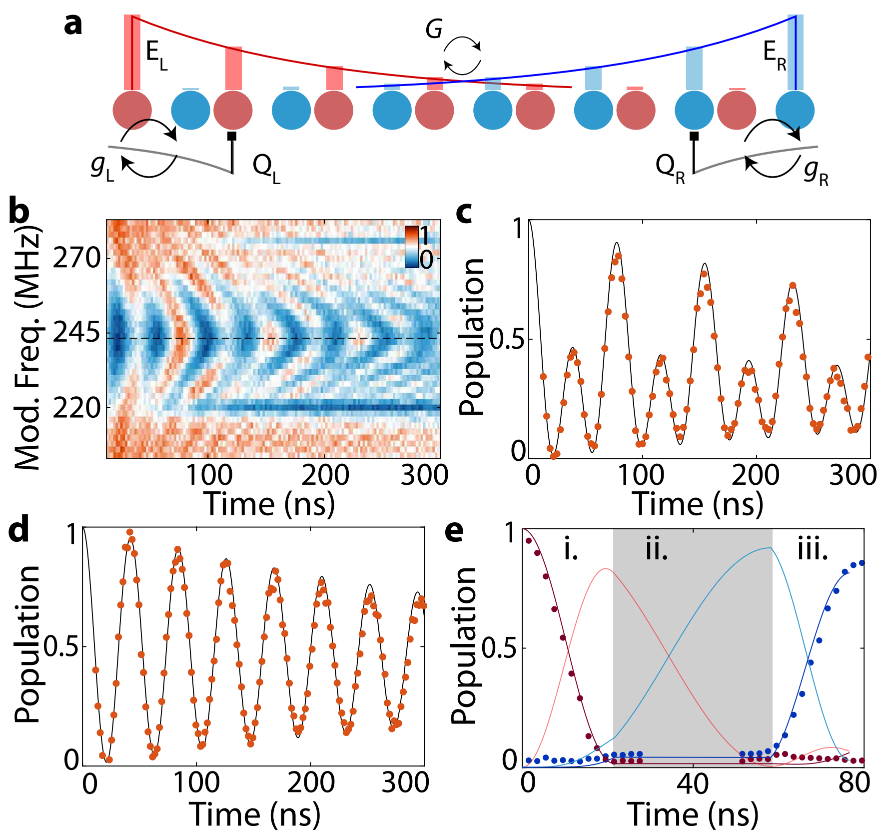

Figure 5.6: **Qubit interaction with topological edge modes.** **a**, Schematic of Device II, consisting of 7 unit cells in the topological phase with qubits $\mathrm{Q_L}= \mathrm{Q}_i^\alpha$ and $\mathrm{Q_R}= \mathrm{Q}_j^\beta$ coupled at sites $(i,\alpha) = (2,\mathrm{A})$ and $(j,\beta) = (6,\mathrm{B})$, respectively. $\mathrm{E_L}$ and $\mathrm{E_R}$ are the left-localized and right-localized edge modes which interact with each other at rate G due to their overlap in the center of the finite waveguide. **b**, Chevron-shaped oscillation of $\mathrm{Q_L}$ population arising from interaction with edge modes under variable frequency and duration of modulation pulse. The oscillation is nearly symmetric with respect to optimal modulation frequency 242.5 MHz, apart from additional features at $(219,\ 275)$ MHz due to spurious interaction of unused sidebands with modes inside the passband. **c**, Line-cut of panel b (indicated with a dashed line) at the optimal modulation frequency. A population oscillation involving two harmonics is observed due to coupling of $\mathrm{E_L}$ to $\mathrm{E_R}$. **d**, Vacuum Rabi oscillations between $\mathrm{Q_L}$ and $\mathrm{E_L}$ when $\mathrm{Q_R}$ is parked at the resonant frequency of edge modes to shift the frequency of $\mathrm{E_R}$, during the process in panel **c**. In panels **c** and **d** the filled orange circles (black solid lines) are the data from experiment (theory). **e**, Population transfer from $\mathrm{Q_L}$ to $\mathrm{Q_R}$ composed of three consecutive swap transfers $\mathrm{Q_L}\to\mathrm{E_L}\to\mathrm{E_R}\to\mathrm{Q_R}$. The population of $\mathrm{Q_L}$ ($\mathrm{Q_R}$) during the process is colored dark red (dark blue), with filled circles and solid lines showing the measured data and fit from theory, respectively. The light red (light blue) curve indicates the expected population in $\mathrm{E_L}$ ($\mathrm{E_R}$) mode, calculated from theory. This figure is adapted from [131].

We probe the topological edge modes by utilizing the interaction with the qubits. While parking Q_L at frequency $f_q = 6.835$ GHz inside MBG, we initialize the qubit into its excited state by applying a microwave π-pulse to the local drive line. Then, the frequency of the qubit is parametrically modulated [223] such that the first-order sideband of the qubit transition frequency is nearly resonant with E_L. After a variable duration of the frequency modulation pulse, the state of the qubit is read out. From this measurement, we find a chevron-shaped oscillation of the qubit population in time centered at modulation frequency 242.5 MHz (Fig. 5.6b).

We find the population oscillation at this modulation frequency to contain two harmonic components as shown in Fig. 5.6c, a general feature of a system consisting of three states with two exchange-type interactions g_1 and g_2. In such cases, three single-excitation eigenstates exist at $0, \pm g$ with respect to the bare resonant frequency of the emitters ($g \equiv \sqrt{g_1^2 + g_2^2}$), and since the only possible spacing between the eigenstates in this case is g and $2g$, the dynamics of the qubit population exhibits two frequency components with a ratio of two. From fitting the Q_L population oscillation data in Fig. 5.6c, the coupling between E_L and E_R is extracted to be $G/2\pi = 5.05$ MHz. Parking Q_R at the bare resonant frequency $\omega_E/2\pi = 6.601$ GHz of the edge modes, E_R strongly hybridizes with Q_R and is spectrally distributed at $\pm g_R$ with respect to the original frequency ($g_R/2\pi = 57.3$ MHz). As this splitting is much larger than the coupling of E_R to E_L, the interaction channel $E_L \leftrightarrow E_R$ is effectively suppressed and the vacuum Rabi oscillation only involving Q_L and E_L is recovered (Fig. 5.6d) by applying the above-mentioned pulse sequence on Q_L. The vacuum Rabi oscillation is a signature of strong coupling between the qubit and the edge state, a bosonic mode, as described by cavity QED [94]. A similar result was achieved by applying a simultaneous modulation pulse on Q_R to put its first-order sideband near-resonance with the bare edge modes (instead of parking it near resonance), which we call the *double-modulation* scheme. From the vacuum Rabi oscillation $Q_L \leftrightarrow E_L$ ($Q_R \leftrightarrow E_R$) using the double-modulation scheme, we find the effective qubit-edge mode coupling to be $\tilde{g}_L/2\pi = 23.8$ MHz ($\tilde{g}_R/2\pi = 22.5$ MHz).

The half-period of vacuum Rabi oscillation corresponds to an iSWAP gate between Q_L and E_L (or Q_R and E_R), which enables control over the edge modes with single-photon precision. As a demonstration of this tool, we perform remote population transfer between Q_L and $Q_R$through the non-local coupling of topological edge modes E_L and E_R. The qubit Q_L (Q_R) is parked at frequency 6.829 GHz (6.835 GHz) and prepared in its excited (ground) state. The transfer protocol, consisting of three steps, is implemented as follows: i) an iSWAP gate between Q_L and E_L is applied by utilizing the vacuum Rabi oscillation during the double-modulation scheme mentioned above, ii) the frequency modulation is turned off and population is exchanged from E_L to E_R using the interaction G, iii) another iSWAP gate between Q_R and E_R is applied to map the population from E_R to Q_R. The population of both qubits at any time within the transfer process is measured using multiplexed read-out [224] (Fig. 5.6e). We find the final population in Q_R after the transfer process to be 87 %. Numerical simulations suggest that (App. C.8) the infidelity in preparing the initial excited state accounts for 1.6 % of the population decrease, the leakage to the unintended edge mode due to ever-present interaction G contributes 4.9 %, and the remaining 6.5 % is ascribed to the short coherence time of qubits away from the flux-insensitive point [$T_2^* = 344\ (539)$ ns for Q_L (Q_R) at working point].

We expect that a moderate improvement on the demonstrated population transfer protocol could be achieved by careful enhancement of the excited state preparation and the iSWAP gates, i.e., optimizing the shapes of the control pulses [225–228]. The coherence-limited infidelity can be mitigated by utilizing a less flux-sensitive qubit design [229, 230] or by reducing the generic noise level of the experimental setup [180]. Further, incorporating tunable couplers [231] into the existing metamaterial architecture to control the localization length of edge states *in situ* will fully address the population leakage into unintended interaction channels, and more importantly, enable robust quantum state transfer over long distances [232]. Together with many-body protection to enhance the robustness of topological states [215], building blocks of quantum communication [101] under topological protection are also conceivable.

5.5 Discussion and outlook

Looking forward, we envision several research directions to be explored beyond the work presented here. First, the topology-dependent photon scattering in photonic bands that is imprinted in the cooperative interaction of qubits can lead to new ways of measuring topological invariants in photonic systems [233]. The directional and long-range photon-mediated interactions between qubits demonstrated in our work also opens avenues to synthesize non-trivial quantum many-body states of qubits, such as the double Néel state [164]. Even without technical advances in fabrication [234–236], a natural scale-up of the current system will allow for the construction of moderate to large-scale quantum many-body systems. Specifically, due to the on-chip wiring efficiency of a linear waveguide QED architecture, with realistic refinements involving placement of local control lines on qubits and compact read-out resonators coupled to the tapered passband (intrinsically acting as Purcell filters [237]), we expect that a fully controlled quantum many-body system consisting of 100 qubits is realizable in the near future. In such systems, protocols for preparing and stabilizing [48, 215, 238] quantum many-body states could be utilized and tested. Additionally, the flexibility of superconducting metamaterial architectures [144, 172] can be further exploited to realize other novel types of topological photonic baths [152, 164, 217]. While the present work was limited to a one-dimensional system, the state-of-the-art technologies in superconducting quantum circuits [168] utilizing flip-chip methods [235, 236] will enable integration of qubits into two-dimensional metamaterial surfaces. It also remains to be explored whether topological models with broken time-reversal symmetry, an actively pursued approach in systems consisting of arrays of three-dimensional microwave cavities [213, 239], could be realized in compact chip-based architectures. Altogether, our work sheds light on opportunities in superconducting circuits to explore quantum many-body physics originating from novel types of photon-mediated interactions in topological waveguide QED, and paves the way for creating synthetic quantum matter and performing quantum simulation [14, 39, 75, 240, 241].

Chapter 6

A SUPERCONDUCTING QUANTUM SIMULATOR BASED ON A PHOTONIC-BANDGAP METAMATERIAL

The previous two chapters have focused on exploring the light-matter interaction between superconducting qubits and microwave waveguides. In this chapter, we employ this light-matter interaction, or waveguide QED, to build a quantum simulator studying many-body dynamics. Specifically, we park the qubits in the bandgap frequencies to protect them from rapid decay into the passband (Chapter 4). At the same time, the tunable interaction between qubit-photon bound states in this regime gives rise to beyond-nearest-neighbor connectivity for the lattice hosting strongly interacting microwave photons—excitations on qubit-photon bound states. Going beyond the single-particle simulation of topological photonics (Chapter 5), we enter the many-body regime where the chaotic quantum evolution reveals the effect of lattice connectivity. In the following, we start with the context of quantum simulation, emphasizing the significance and difficulty in building a *scalable* quantum simulator with long-range connectivity. We then explain how we realize this goal using waveguide QED and how we characterize the native Hamiltonian of the quantum simulator. Lastly, we study the many-body dynamics where the beyond-nearest-neighbor connectivity enables the exploration of quantum chaos. This chapter is adapted from [132] and the supplementary information is in App. D.

6.1 Introduction

Realizing a scalable architecture for quantum computation and simulation is a central goal in the field of quantum information science. While architectures with nearest-neighbor (NN) coupling between quantum particles on a lattice are prevalent, quantum systems with long-range interactions can realize a richer set of computational tasks and physical phenomena [242–245]. For instance, in the case of gate-based quantum computation, coupling beyond the nearest-neighbor level enables non-local gate operations between qubits which can reduce the overhead of quantum algorithms and lift the restrictions on code rate and distance of local-interaction-based quantum error-correcting codes [72, 246]. In the case of analog quantum simulation, the inclusion of long-range interactions can alter the behavior of otherwise integrable many-body systems [44, 45], resulting in quantum chaotic dynamics, at the root of such topics as quantum thermalization [247] and quantum information scrambling [248]. Furthermore, control over the range of lattice connectivity grants access to different physical regimes and the crossover between them, such as in many-body quantum phase transitions [86, 249, 250] and the hydrodynamics of non-equilibrium quantum states [46].

For engineered quantum systems consisting of interacting quantum particles on a lattice, it is often challenging to scale to larger lattice sizes while maintaining a high degree of lattice connectivity and single-site control. One common approach, developed for trapped-ion and neutral-atom systems, is to use resonant modes of either vibrational [242] or optical [251] cavities as a quantum bus for mediating interactions between the internal states of atoms across the lattice. Similar schemes have been adopted in superconducting quantum circuits, realizing systems as large as 20 qubits with all-to-all coupling via a common microwave cavity [111]. Increasing the number of lattice sites in this case, however, leads to either parasitic coupling arising from dense placement of sites in a fixed-volume cavity or frequency-crowding effects stemming from the increased spectral density of cavity modes when increasing the cavity size [252].

An alternative approach for connecting quantum particles on a lattice is to construct a quantum bus from an intrinsically extensible structure, such as a waveguide. Along this direction, engineered photonic-bandgap waveguides have been proposed as a quantum bus that simultaneously protects quantum particles from radiative damping through the waveguide while allowing for extended-range lattice connectivity [158]. The waveguide-bus concept has been investigated in the context of many-body simulation with cold atoms coupled to engineered nanophotonic waveguides [130, 158], and recent experiments have explored qubit-photon bound states in superconducting quantum circuits with microwave photonic-bandgap waveguides [120, 131, 163, 172, 253]. However, the realization of a scalable many-body quantum simulator, with single-site quantum-particle control and a high level of lattice connectivity, has remained an open challenge.

We demonstrate a scalable many-body quantum simulator consisting of a one-dimensional (1D) lattice of superconducting transmon qubits coupled to a common metamaterial waveguide. This system provides both tunable-range connectivity between qubits and full single-site control and state measurement of individual qubits. The waveguide acts both as a bus for mediating exponentially decaying long-range interactions between qubits, and as a Purcell filter enabling multiplexed, rapid readout of the qubit states with high fidelity. This system realizes an extended version of the Bose-Hubbard model with tunable hopping range and on-site interaction. Utilizing our ability to efficiently collect measurement outcomes from many-body quench dynamics—enabled by the fast experimental repetition rate of our system—we perform direct analysis of outcome statistics to learn Hamiltonian parameters in situ and study the effect of hopping range on the evolution of randomness across the system. Specifically, we observe a distribution of outcome bit-string probabilities reflecting the ergodic nature of the Hamiltonian with long-range hopping. This result experimentally confirms the expectation from quantum chaos for interacting many-particle systems, highlighting the connection between ergodic unitary dynamics and its effective statistical description in terms of random matrix theory [254].

6.2 Metamaterial-based quantum simulator

The backbone of the many-body quantum simulator in this work is a metamaterial waveguide formed from a chain of lumped-element LC microwave resonators. The waveguide can be described by a generic model (Fig. 6.1a) of a 1D cavity array with NN coupling t [157, 255]. The corresponding dispersion relation (Fig. 6.1b) is given by $\omega_k = \omega_c + 2t\cos(kd)$, exhibiting a passband centered around the cavity frequency ω_c with a bandwidth of $4t$, where k is the wavevector and d is the lattice constant of the array. The bandgap at frequencies below $\omega_{e,-} = \omega_c - 2t$ (above $\omega_{e,+} = \omega_c + 2t$) is denoted as the lower (upper) bandgap, abbreviated as LBG (UBG). Inside the bandgaps, the off-resonant coupling between a bare quantum emitter and the waveguide modes gives rise to an emitter-photon bound state [156] whose photonic tail is localized around the emitter. Localization follows a spatial profile $(\mp 1)^{\Delta x} e^{-|\Delta x|/\xi}$ in the LBG/UBG [157], where Δx is the displacement in the number of unit cells from the emitter and ξ is the localization length controlled by the detuning Δ between the band-edge frequency and the transition frequency of the bound state. The overlap of two bound states results in photon-mediated coupling with a range covering multiple unit cells, i.e., long-range coupling, exhibiting a greater strength and a more extended range ξ at a smaller detuning $|\Delta|$, as displayed in Fig. 6.1e.

The metamaterial waveguide consists of a 42-unit-cell array of capacitively coupled lumped-element microwave resonators (Fig. 6.1c and Fig. 6.2), and is equipped

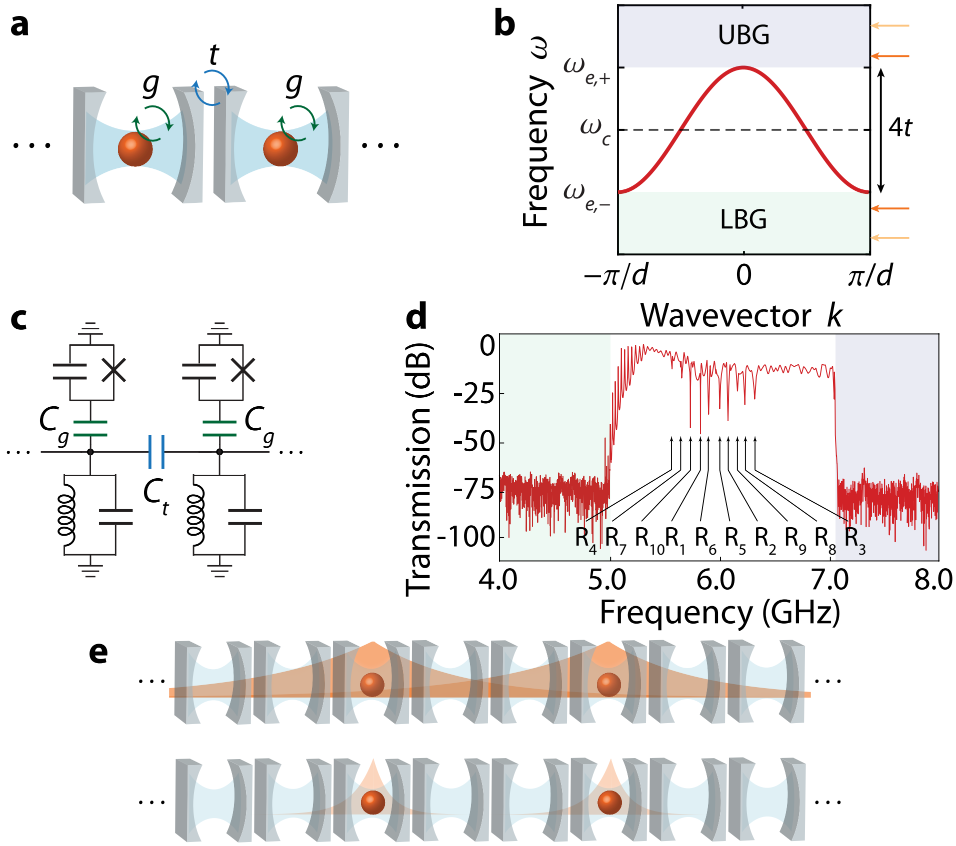

Figure 6.1: **Schematic of the metamaterial-based quantum simulator.** **a**, Schematic showing a 1D array of coupled cavities with nearest-neighbor coupling t. Each cavity is occupied by a quantum emitter (orange ball) with coupling g to the cavity. **b**, Dispersion relation of the coupled cavity array in panel **a** with a passband between $\omega_{e,\pm}$ centered at ω_c (bandwidth of $4t$). The LBG (UBG) below (above) the passband is shaded in green (purple). **c**, Electrical circuit realization of in panel **a** with capacitively coupled LC resonators and transmon qubits corresponding to the cavity array and the quantum emitters, respectively. The coupling capacitors are color coded in accordance with in panel **a**. **d**, Top (Bottom): Cartoon of two emitter-photon bound states at small (large) detuning $|\Delta|$, indicated by dark (light) orange arrows in panel **b**, exhibiting an extended (restricted) spatial range and large (small) photonic component in the bound states. **e**, Transmission spectrum through the metamaterial waveguide (red curve) with black arrows indicating the ten resonances of the read-out resonators R_i. This figure is adapted from [132].

at both ends with engineered tapering sections, designed to reduce the impedance mismatch to external 50-Ω input-output ports at frequencies lying within the passband of the waveguide [131, 144]. Each of the middle ten metamaterial resonators (unit cells labeled by i = 1–10) couples to a transmon qubit [69] serving as the quantum emitter. Individual addressing of each qubit is achieved by excitation (XY control) from a charge drive line and frequency tuning (Z control) from a flux bias line. Dispersive qubit read-out is enabled by capacitively coupling each qubit Q_i to a compact read-out resonator R_i, which itself is then coupled to the metamaterial resonator of the same unit cell. The entire metamaterial and transmon qubit system (the device) is fabricated using evaporated thin-film aluminum on a high-resistivity silicon substrate, with fabrication procedures detailed in Refs. [144, 172]. Further details of the device modelling and the experimental setup used to measure and test the device, are discussed in App. D.1 and D.2, respectively.

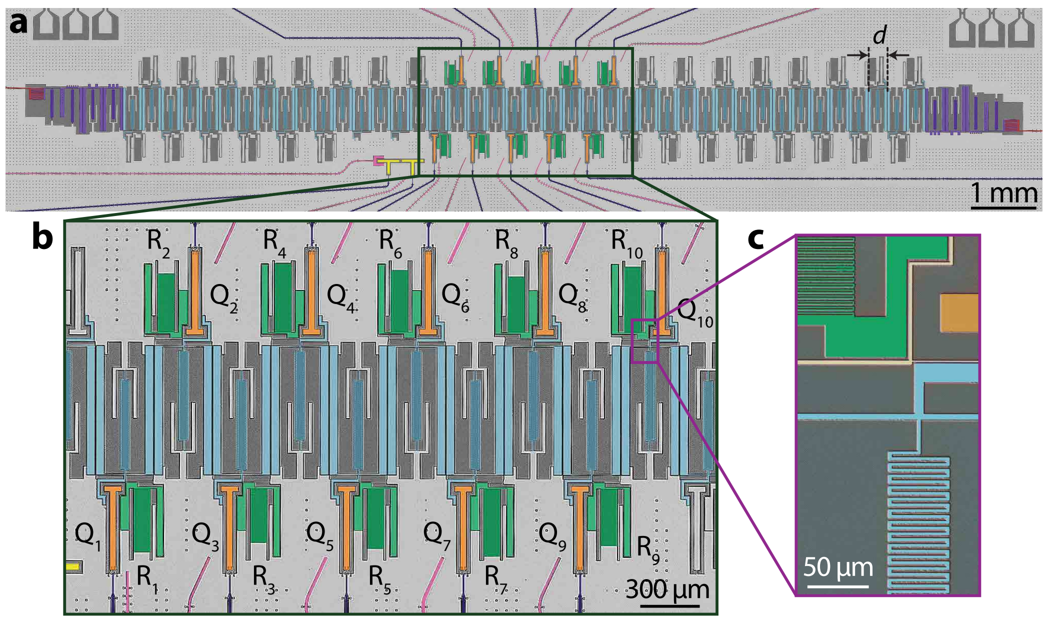

Figure 6.2: **Optical image (false colored) of the metamaterial-based quantum simulator.** **a**, The false colored optical micrograph of the fabricated quantum simulator with 42 metamaterial resonators (lattice constant $d = 292\,\mu$m) colored blue connected to input-output ports (red) via tapering sections (purple). **b**, A zoomed-in view of ten qubits (Q_i, colored orange), controlled by individual charge drive lines (pink) and flux bias lines (dark blue), and their read-out resonators (R_i, colored green) coupling to the ten inner unit cells of the metamaterial waveguide. **c**, Detailed view of the coupling region in panel **b**. Two auxiliary qubits (yellow) are not used in this experiment. This figure is adapted from [132].

This realization of the device enables qubit read-out utilizing the passband of the metamaterial waveguide with built-in protection against Purcell decay channels (App. D.3). The transmission spectrum through the waveguide, displayed in Fig. 6.1d, shows a passband ranging from $\omega_{e,-}/2\pi \approx 5.01\,\text{GHz}$ to $\omega_{e,+}/2\pi \approx$

7.08 GHz with ripples smaller than 8 dB near the center. The extinction ratio of the transmission between that measured in the passband and that measured in the bandgaps is greater than 65 dB with a sharp transition in the transmission occurring within 100 MHz of the band-edges. In the middle of the passband, resonances associated with the read-out resonators are observed between 5.574 GHz and 6.328 GHz. The average decay rate of ten read-out resonators is $\overline{\kappa_{\mathrm{R}_i}}/2\pi = 11.8$ MHz, enabling fast, high-fidelity multiplexed read-out while maintaining a low level of read-out crosstalk. For details of read-out methods and characterization, refer to App. D.4.

6.3 Bose-Hubbard model with long-range hopping

The spatially extended bound-state excitations, formed between transmon-qubit excitations and waveguide photons of the metamaterial-waveguide bus, creates a lattice of interacting microwave photons [56]. This quantum system is described by an extended version of the 1D Bose-Hubbard model with tunable long-range hopping and on-site interaction. Specifically, each bound state formed from qubit Q_i, inheriting the level structure of an anharmonic oscillator from a transmon qubit [69], serves as a bosonic site with local site energy $\epsilon_i = \omega_{01,i}$ and the on-site interaction $U_i = \omega_{12,i} - \omega_{01,i}$. Here, $\omega_{01,i}$ and $\omega_{12,i}$ are the transition frequencies of the bound state on site Q_i from its ground state $|0\rangle$ to the first excited state $|1\rangle$ and that from the first to the second excited state $|2\rangle$, respectively. In addition, the long-range hopping $J_{i,j}$ is enabled by the overlap between a pair of qubit-photon bound states on sites Q_i and Q_j. The Hamiltonian of this model that captures the basic processes mentioned above can be written as

$$\hat{H}/\hbar = \sum_{i,j} J_{i,j}\hat{b}_i^\dagger\hat{b}_j + \sum_i \frac{U_i}{2}\hat{n}_i(\hat{n}_i - 1) + \sum_i \epsilon_i\hat{n}_i, \tag{6.1}$$

where $\hat{b}_i^\dagger$ ($\hat{b}_i$) is the creation (annihilation) operator and $\hat{n}_i \equiv \hat{b}_i^\dagger\hat{b}_i$ is the number operator on site Q_i. The parameters of the Hamiltonian realized in this simulator can be learned through experiments enabled by the precise, single-site-level control over qubits.

We measure the on-site interaction U_i (Fig. 6.3a) by performing spectroscopy of ω_{12} after initializing Q_i in its first excited state $|1\rangle$. From within either bandgap, $|U_i|$ decreases as ω_{01} approaches the closest band-edge due to dressing from the passband modes of the metamaterial [163], i.e., the Lamb shift. In the UBG, a wide tuning range of $|U_i|$ is achievable from the strong hybridization between the $|1\rangle$-$|2\rangle$

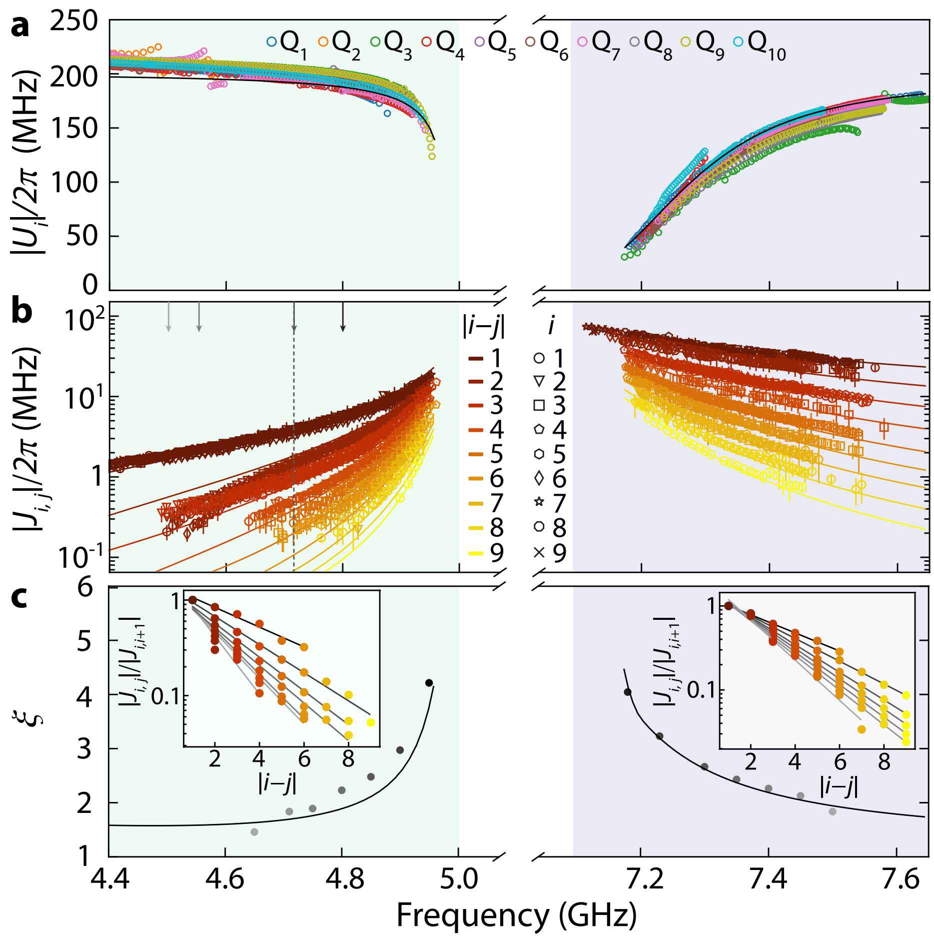

Figure 6.3: **Hamiltonian parameter characterization.** **a**, On-site interaction $|U_i|$ versus frequency ω_{01} with measured values indicated by colored circles. **b**, Hopping amplitude $|J_{i,j}|$ versus frequency with experimental data shown as markers (errorbars indicate a standard deviation). Colors represent the distance $|i-j|$ between sites. Four gray-scale arrows specify frequencies in Fig. 6.5. **c**, Localization length ξ extracted by fitting the exponential decay of measured hopping rate (results of polynomial fitting of datapoints in (B)) as a function of distance $|i-j|$ (insets) at a few different frequencies. The darkness of a marker matches a fitting curve in the inset at the same frequency. In all panels, green (purple) shading on the left (right) corresponds to LBG (UBG), and theory curves (solid) are obtained from numerical calculations using an identical circuit model. This figure is adapted from [132].

transition and the band-edge modes at $(\omega_{01}-\omega_{e,+})/2\pi < 300$ MHz. The magnitude of hopping $|J_{i,j}|$ is measured from vacuum Rabi oscillations between sites Q_i and Q_j by initializing one site with a π-pulse and tuning ω_{01} of both sites on resonance for a duration τ with fast flux pulses. As shown in Fig. 6.3b, for a fixed distance $|i-j|$, $|J_{i,j}|$ increases with a decreasing $|\Delta|$, resulting from larger photonic components of the bound states. Compared to the LBG, the UBG exhibits larger $|J_{i,j}|$ at the same $|\Delta|$, owing to a stronger coupling g of the bare qubits to the metamaterial at higher frequencies and the breakdown of the tight-binding cavity array model in the circuit realization (Fig. 6.1c; also see App. D.1). At a specific ω_{01}, $|J_{i,j}|$ decreases exponentially as a function of distance $|i-j|$, resembling the profile of the photonic tail in a qubit-photon bound state (Fig. 6.3c). From fitting the exponential decay curve we extract the localization length ξ, which ranges from $\xi = 1.4$ to 4.2, with the largest localization length occurring at the smallest achievable band-edge detunings. For even smaller detunings, the eigenstate of the two interacting bound states merges into the passband and becomes radiative to the waveguide.

6.4 Many-body Hamiltonian learning

Beyond the above single- and two-qubit measurements, we perform in situ many-body characterization of Hamiltonian parameters [256, 257] which are otherwise hard to access. For example, the sign of the hopping term $J_{i,j}$ inherits the spatial profile of the photonic component of the bound states. In the case of the bound states in the UBG, the sign of the hopping terms are all uniform (positive), whereas for bound states in the LBG the hopping terms alternate sign as the distance between lattice sites increases by one (Fig. 6.4a). This is due to the photonic component of the bound state behaving as a defect mode inside the bandgap, exhibiting a spatial profile resembling the wavevector at the nearest band-edge ($k = 0$ at the upper band-edge and $k = \pi/d$ at the lower band-edge). Although insignificant in measurements involving only two lattice sites, the sign of the hopping terms does alter the many-body dynamics of the system. Here, we utilize a many-body fidelity estimator F_d proposed in Ref. [257] to reveal this information. This fidelity estimator, which closely tracks the true many-body fidelity, is obtained for ergodic quench evolution of simple initial states (App. D.6).

We follow the sequence described in Fig. 6.4b to perform the many-body quench evolution. The sequence consists of preparing a set of five randomly chosen sites in their first excited state, followed by using flux pulses to align ω_{01} of all ten sites for time τ, and then finally performing site-resolved single-shot measurement on all lattice sites to obtain a ten-bit string $z = n_1 n_2 \cdots n_{10}$. The many-body fidelity estimator F_d is calculated by comparing bit-string statistics of repeated measurements with numerical simulation of the evolution assuming a set of Hamiltonian parameters in Eq. 6.1. The maximum F_d is achieved at the parameter values closest

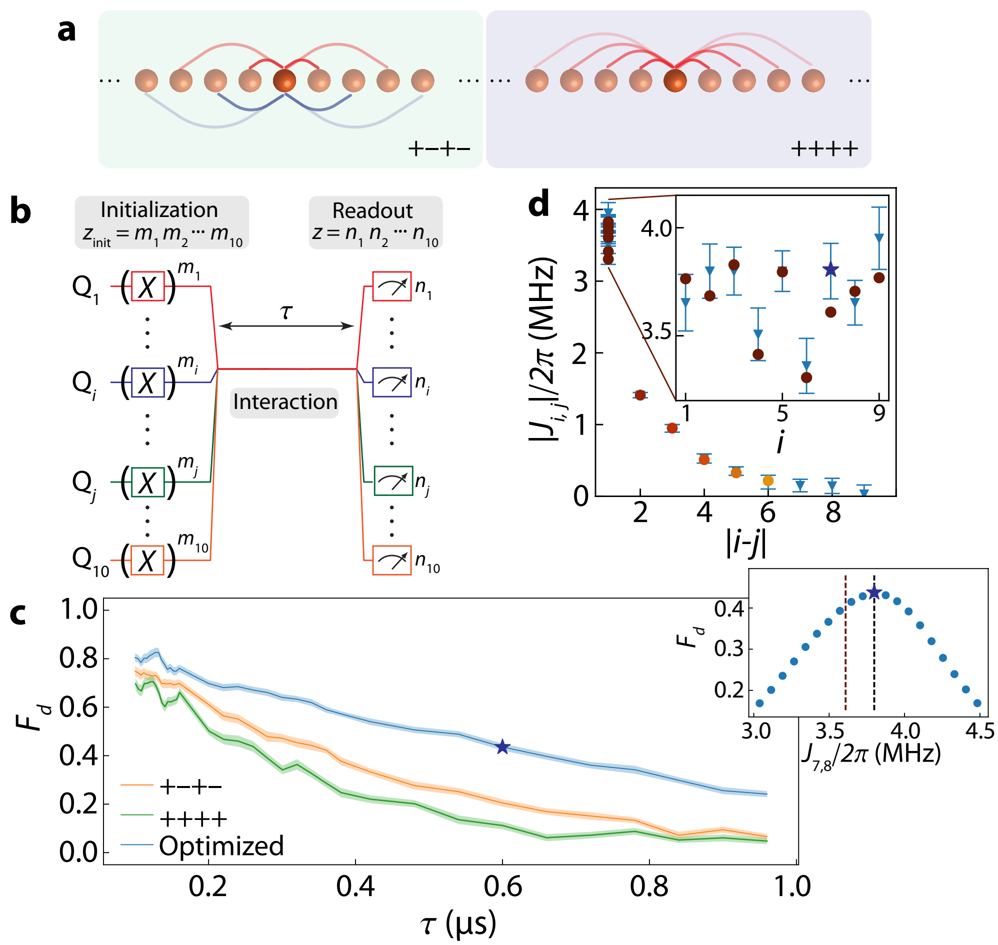

Figure 6.4: **Many-body Hamiltonian learning.** **a**, Left (Right): cartoon illustrating hopping from a site inside the LBG (UBG) with positive/negative sign represented in red/blue and the amplitude represented by opacity, with alternating (all positive) signs denoted as $+-+-$ $(++++)$. **b**, Pulse sequence for many-body evolution. Ten sites Q_1–Q_{10} are initialized (X gate) in a bit-string z_{init} at their idle frequencies, then tuned to resonance for time τ during the interaction stage, followed by a site-resolved single-shot read-out at their idle frequencies to obtain a final bit-string z. **c**, Many-body fidelity estimator F_d at $\omega_{01}/2\pi = 4.72\,\text{GHz}$ versus evolution time τ. The F_d curves assume $J_{i,j}$'s from two-qubit measurement indicated by the dashed line in Fig. 6.3b with alternating signs (orange) and all positive signs (green), and from the numerical optimization (blue). The shading corresponds to a standard deviation for 40 randomly chosen z_{init}'s in the five-excitation sector. Inset: F_d at $\tau = 0.6\,\mu\text{s}$ versus $J_{7,8}$ with optimized parameters on the remaining $J_{i,j}$'s, where the brown and the black dashed lines indicates $J_{7,8}$ extracted from Fig. 6.3b and the numerical optimization, respectively. **d**, Comparison of $|J_{i,j}|$ interpolated from two-qubit measurements (colored circles) and from numerical optimization (blue triangles with errorbars for 68% confidence interval), corresponding to the orange and the blue curves in panel **c**, respectively. All nearest-neighbor hopping $|J_{i,i+1}|$'s are shown (details in the inset), while for larger hopping distances $|i-j| > 1$ only the average values are indicated. The navy stars represent the maximum F_d at $\tau = 0.6\,\mu\text{s}$ in panel **c** and the optimized $J_{7,8}$ in the insets of panels **c** and **d**. This figure is adapted from [132].

to the Hamiltonian realized in the experiment. The fast repetition rate of this experiment enables us to perform a large number of measurements (1.6×10^5 in total), reducing statistical error and increasing sensitivity to small Hamiltonian parameter variations (see App. D.5 for details of qubit control, pulse sequence, and repetition rate).

We compare F_d at $\omega_{01}/2\pi = 4.72\,$GHz using three different parameter sets for $J_{i,j}$ in Fig. 6.4c: a first set with amplitudes derived from the two-qubit experiments in Fig. 6.3b assuming alternating signs (Fig. 6.4a, left), a second set with the same amplitudes as the first but all positive signs (Fig. 6.4a, right), and a third set of optimized parameter values that maximize F_d. The optimized hopping terms are restricted to be real-valued, with independent $J_{i,i+1}$ for each $i = 1-9$ and $J_{i,j}$ for each distance $|i-j| > 1$ (all qubit pairs of the same distance having the same $J_{i,j}$). An alternating sign of $J_{i,j}$ with distance is favored, yielding a higher many-body fidelity compared to hopping terms with all positive signs. This is further evidenced by the alternating signs of the resulting optimized parameter set. Although we find small differences between the set of optimized hopping amplitudes and those from the two-qubit experiments with alternating signs (see Fig. 6.4d), F_d of the optimized parameter set is markedly better. The sensitivity of F_d to the hopping terms is highlighted in the inset of Fig. 6.4c, where the variation of the fidelity versus $J_{7,8}$ is shown. For details of the F_d calculation and parameter optimization, refer to App. D.6.

6.5 Ergodic many-body dynamics with long-range hopping

We now utilize the platform to study the effect of long-range hopping on the many-body dynamics. Specifically, the ergodicity of the 1D Bose-Hubbard model in the hardcore limit ($|U/J| \gg 1$) depends on the range of hopping, exhibiting integrable behavior with NN hopping, and chaotic behavior with long-range hopping. We study this crossover with various hopping ranges and investigate the resulting dynamics using both conventional one- and two-site correlators, and the statistics of the global bit-strings resulting from qubit-state measurement outcomes across the lattice. This latter technique is particularly useful in identifying universal signatures of ergodicity and the effect of decoherence at long evolution times.

The crossover between integrable and ergodic dynamics can be qualitatively visualized by a two-particle quantum walk [258–260] with initial excitations on sites Q_5 and Q_6 using the sequence shown in Fig. 6.4b. The measured quantum walk at a

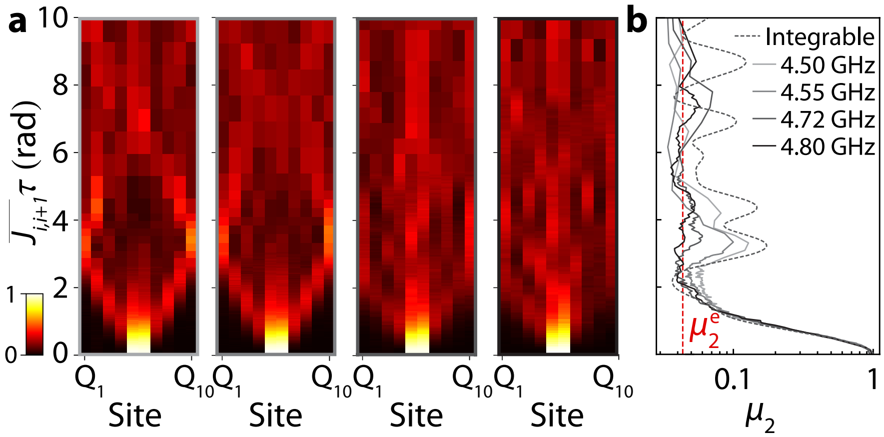

Figure 6.5: **Two-particle quantum walk with increasing hopping range.** **a**, Evolution of the population $\langle \hat{n}_i \rangle$ on sites Q_1–Q_{10} as a function of normalized evolution time $\overline{J_{i,i+1}}\tau$. The system is initialized in $z_{\text{init}} = 0000110000$ and the evolution occurs at $\omega_{01}/2\pi = 4.50$ GHz, 4.55 GHz, 4.72 GHz, and 4.80 GHz with the longest evolution times of 904 ns, 781 ns, 430 ns, and 200 ns from left to right. **b**, The second moment μ_2 as a function of normalized evolution time $\overline{J_{i,i+1}}\tau$. Results calculated from the data in panel **a** are shown in solid curves with gray scales corresponding to frames in panel **a** and arrows in Fig. 6.3b. Result from numerical simulation of the integrable Hamiltonian is shown as the dotted curve and μ_2^{e} for a generic ergodic system is indicated by the red dashed line. This figure is adapted from [132].

few different ω_{01}'s indicated by arrows in Fig. 6.3b is shown (Fig. 6.5a) as a function of normalized evolution time $\overline{J_{i,i+1}}\tau$, where $\overline{J_{i,i+1}}$ is the average NN hopping rate (the corresponding numerical simulations are provided in App. D.7, showing that the quantum walk patterns are not visibly affected by decoherence). The excitation wave packets smear over the system when ω_{01} is close to the band-edge frequency. More quantitatively, this trend can be probed by computing the probability p_z of measuring a certain bit-string z in the two-excitation sector at evolution time τ. For a generic ergodic Hamiltonian, the second moment $\mu_2 \equiv \sum_z p_z^2$ [254], which reflects the probability fluctuations, converges to $\mu_2^{\text{e}} = 2/(D+1)$ after initial evolution [257] due to the chaotic nature of its quantum dynamics ($D = 45$ is the dimension of the two-excitation Hilbert space). No such convergence is expected in an integrable Hamiltonian due to revivals associated with ballistic propagation of wave packets. As an example, we show in Fig. 6.5b the results from the spin-$1/2$ XY model obtained from modifying the Hamiltonian in Eq. 6.1 by keeping only NN hopping terms in the hardcore limit. When ω_{01} is closer to the band-edge, the measured second moment deviates from the simulated integrable result and converges to μ_2^{e} at an earlier normalized evolution time $\overline{J_{i,i+1}}\tau$ consistent with the breaking of integrability due to the extended hopping range. We note that with $|U/J| > 36$ for all the measurements illustrated in Fig. 6.5, finite on-site interactions of the Bose-Hubbard model play a negligible role in the breaking of integrability (App. D.8).

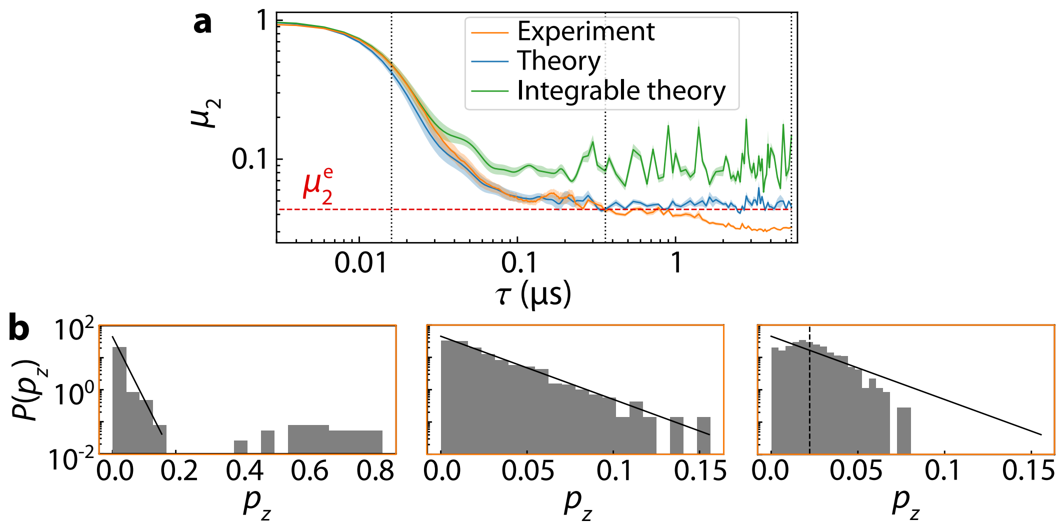

Figure 6.6: **Ergodic many-body dynamics with long-range hopping at 4.72 GHz.** **a**, Second moment μ_2 as a function of evolution time τ in our system from the experiment (orange) and the theory with the optimized parameter set in Fig. 6.4c (blue), compared to theoretical predictions of the integrable model (green). The shading on each curve corresponds to a standard deviation of the mean second moment for 20 randomly chosen initial bit-strings z_{init} in the two-particle sector, and the red dashed line represents the ergodic value μ_2^{e}. **b**, Density histogram $P(p_z)$ of the distribution of experimental bit-string probabilities $\{p_z\}$ with the 20 initializations z_{init}'s at evolution times $\tau = 16\,\mathrm{ns}$, 360 ns, and 5.4 μs from left to right (indicated by the dotted lines in (A)). The solid lines show the PT distribution and the dashed line in the right plot shows the value $p_z = 1/D$ of a classical uniform distribution. This figure is adapted from [132].

To further probe this ergodic nature of Hamiltonian with long-range hopping, we use the experimental evolution at $\omega_{01}/2\pi = 4.72\,\mathrm{GHz}$ as an example. At a short time ($\tau = 16\,\mathrm{ns}$), the excitations remain in their initial sites. This is visualized for a quantum walk with initial excitations on sites Q_5 and Q_6 in the left panel of Fig. 6.7a (evolution of population $\langle \hat{n}_i \rangle$) and in the bottom left panel of Fig. 6.7b (two-site correlator $\langle \hat{n}_i \hat{n}_j \rangle$). The histogram $P(p_z)$ of experimentally measured bit-string probabilities $\{p_z\}$ at this early evolution stage (Fig. 6.6b, left) shows a distribution with a tail of large p_z values, giving a large μ_2 (Experiment curve in Fig. 6.6a). This is associated with an insufficient scrambling of the initially localized quantum information. At an intermediate time ($\tau = 360\,\mathrm{ns}$), the excitations are more spread out over the entire 1D lattice (middle left panel of Fig. 6.7a), forming a "speckle" pattern with site-to-site fluctuation associated with quantum interference. The quantitative signatures of this speckle pattern manifest in the histogram $P(p_z)$ following the Porter-Thomas (PT) distribution [261] (Fig. 6.6b, middle) and in the second moment μ_2 settling to the ergodic value μ_2^{e}. The PT distribution results from the randomness in the distribution of wavefunction magnitudes, which is predicted by Berry's conjecture [262] stating that the single-particle eigenstates of a chaotic system behave like random superpositions of plane waves. Similarly, in the many-body settings, the distribution of wavefunction magnitudes across basis states also follow the PT distribution. Our observation is the first experimental verification of this many-body version of Berry's conjecture in a Bose-Hubbard system, whose extension in the thermodynamic limit provides the modern theory of quantum thermalization such as eigenstate thermalization hypothesis [263, 264]. This draws connection between quantum many-body chaos and random matrix theory, leading to a deeper understanding of the randomness in many-body dynamics [256]. Note that the randomness in our case originates from the ergodicity of the time-independent Hamiltonian instead of the randomness inherent in random circuits [49, 254]. In contrast to the experimental results, theoretical calculations at the same evolution time using the integrable Hamiltonian shows aggregated excitations on a few sites (Fig. 6.7c, middle) and the resulting larger value of μ_2 (Integrable theory curve in Fig. 6.6a). This comparison highlights the effect of long-range hopping in probing the ergodic regime.

Finally, we study the impact of decoherence by juxtaposing the measurement results and the decoherence-free theoretical calculation using the optimal learned Hamiltonian with long-range hopping. Before the evolution time of $\tau \approx 1\,\mu\mathrm{s}$, the two cases agree in the second moment μ_2 (Experiment and Theory curves in Fig. 6.6a), the quantum walk population (Fig. 6.7a, left and middle), and the two-site correlator (middle panels of Fig. 6.7b), suggesting these results are not affected by decoherence. After a long evolution time ($\tau = 5.4\,\mu\mathrm{s}$, larger than the averaged Ramsey coherence time $\overline{T_{2,i}^{*}} = 1.16\,\mu\mathrm{s}$), the second moment of the two cases deviates from one another, and the experimental speckle pattern begins to wash out compared to the theoretical modeling (top panels of Fig. 6.7b). Another probe of the decoherence is the histogram $P(p_z)$ of the measured bit-string probabilities (Fig. 6.6b, right).

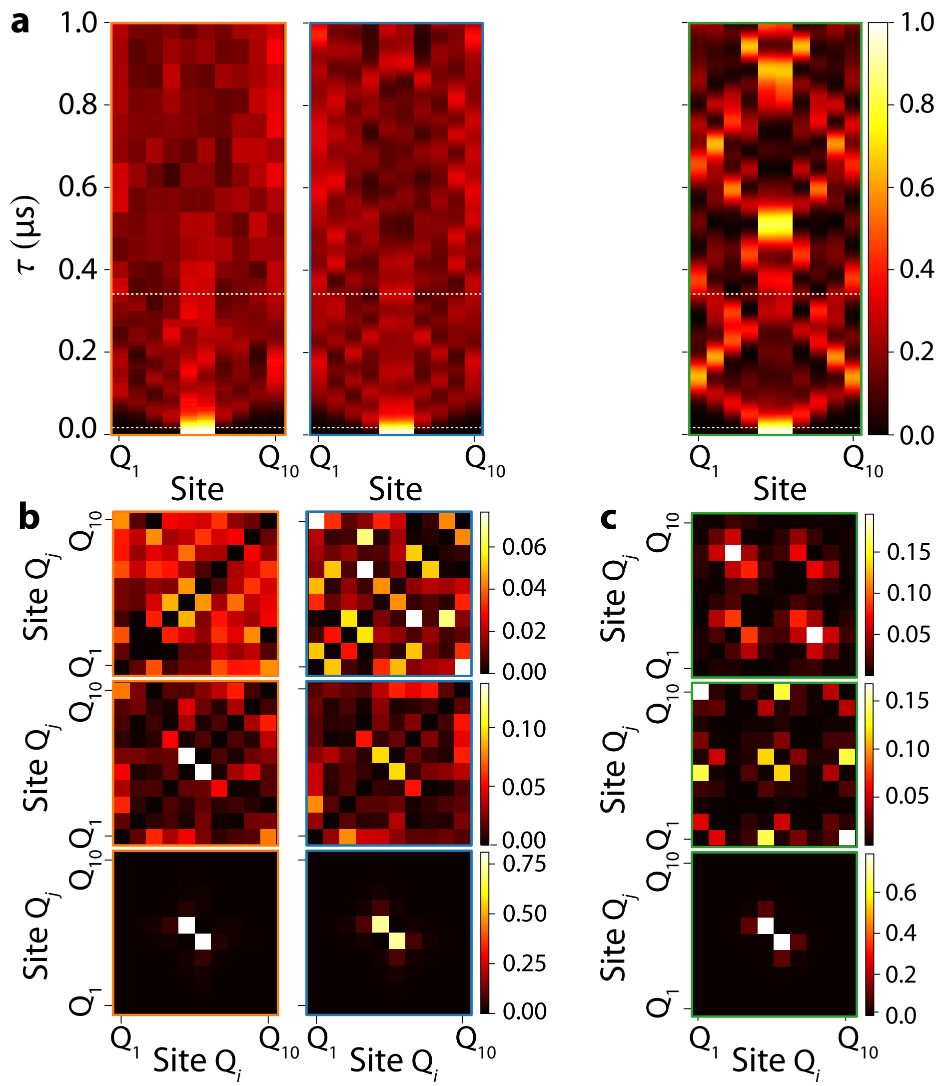

Figure 6.7: **Quantum walk under ergodic many-body dynamics.** **a**, Evolution of the population $\langle \hat{n}_i \rangle$ on sites Q_1–Q_{10} as a function of time τ with $z_{\text{init}} = 0000110000$ in the cases of experiment, theory, and integrable theory from left to right. The white dashed lines at the bottom (in the middle) indicates $\tau = 16\,\text{ns}$ (360 ns). **b–c**, Two-site correlator $\langle \hat{n}_i \hat{n}_j \rangle$ with $z_{\text{init}} = 0000110000$ at evolution times $\tau = 16\,\text{ns}$, 360 ns, and 5.4 μs from bottom to top in the cases of experiment (left column of panel **b**), theory (right column of panel **b**), and integrable theory in panel **c**. This figure is adapted from [132].

Here, the histogram deviates from the PT distribution, narrows substantially, and approaches a uniform distribution corresponding to a completely decohered, maximally mixed state. Additional numerical simulations of μ_2 and $P(p_z)$ for ergodic and integrable systems can be found in App. D.8.

6.6 Conclusion and outlook

Our many-body quantum simulator is based on a one-dimensional lattice of transmon qubits connected together using a superconducting metamaterial, which exhibits photonic bandgaps that protect qubit-photon bound states from decay and a transmission passband used for high-fidelity multiplexed qubit-state read-out. Furthermore, the metamaterial plays the role of a scalable photonic bus to mediate tunable long-range coupling between qubit-photon bound states. This system of interacting bound states realizes a Bose-Hubbard model with long-range hopping. We characterize the system using conventional single- and two-qubit measurements along with a sample-efficient many-body Hamiltonian learning protocol. Lastly, we study the many-body quench dynamics of the system versus the range of the lattice hopping, revealing the ergodic nature of the extended Bose-Hubbard model, distinct from its nearest-neighbor-coupling counterpart. The major challenge in probing long-time quantum evolution in our experiment is the short Ramsey coherence time $\overline{T_{2,i}^{*}} = 1.16\,\mu$s, limited by flux-noise-induced dephasing. Incorporating a single refocusing pulse has shown to increase the coherence time to $\overline{T_{2E,i}} = 5.64\,\mu$s at the single-qubit level (see App. D.2). The extended quantum evolution times enabled by further dynamical decoupling, combined with the tunable-range coupling investigated in this work, provide unique opportunities to explore non-equilibrium dynamics with or without coupling to an environment and quantum phases of matter in the presence of frustration.

Chapter 7

FUTURE DIRECTIONS

The previous three chapters have presented the development of superconducting circuit architectures based on waveguide QED and their applications in studying light-matter interactions and many-body physics. In this final chapter, we bring up future directions for these architectures, especially the one detailed in Chapter 6 exhibiting the best controllability and coherence over multiple qubits. These future directions are aligned with the grand goals of quantum information science and engineering. For example, the programmability of the simulators is increasingly emphasized [38, 43, 244, 250] in order to expand the realm of accessible Hamiltonians towards NISQ-era quantum simulations. The programmability covers not only the amplitude and phase of the Hamiltonian parameters such as the interaction strength, but also the connectivity and even the dimensionality of the lattice that hosts interacting particles. Moreover, for both NISQ applications and fault-tolerant quantum computing, scaling up to a large system size is the key to entering the regime where classical computation becomes difficult. In the following, we detail future directions starting from the quantum simulation of ground state properties of the extended version of the Bose-Hubbard model (Chapter 6), followed by discussions on increasing the programmability of the quantum simulators and scaling up the systems based on waveguide QED architectures.

7.1 The extended version of the Bose-Hubbard model: ground state properties

The Bose-Hubbard (BH) model describes interacting bosons on a lattice, captured by the Hamiltonian (similar to Eq. 6.1)

$$\hat{H}/\hbar = \sum_{i,j} J_{i,j}\hat{b}_i^\dagger \hat{b}_j + \frac{U}{2}\sum_i \hat{n}_i(\hat{n}_i - 1) + \mu \sum_i \hat{n}_i, \tag{7.1}$$

where $\hat{b}_i^\dagger$ ($\hat{b}_i$) is the bosonic creation (annihilation) operator and $\hat{n}_i \equiv \hat{b}_i^\dagger \hat{b}_i$ is the number operator on site i. As described in Sec. 6.3, the first two terms represent the hopping between sites i-j and the on-site interaction (assuming uniform U over sites), respectively. The third term, adapted from the site energy term $\sum_i \epsilon_i \hat{n}_i$

in Eq. 6.1, assumes a uniform site energy that is parameterized by the chemical potential μ.

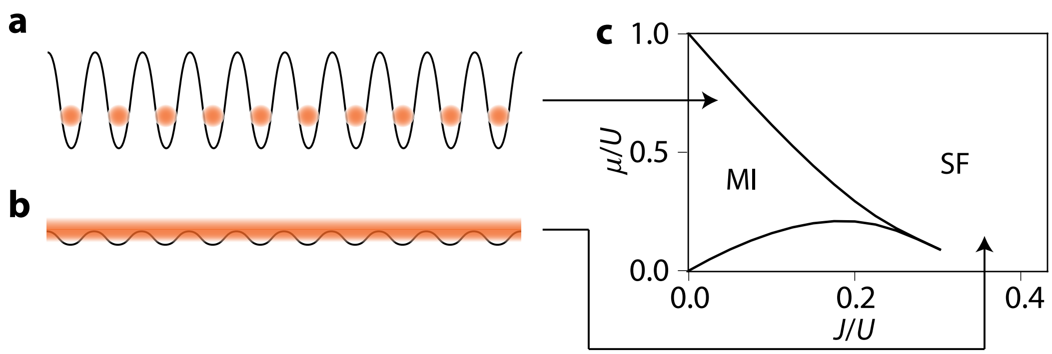

Figure 7.1: **Ground states of the 1D standard BH model.** **a**, Cartoon showing a unity-filling Mott insulator (MI) phase with one boson (orange circle) occupying each site (cosine-shaped well). **b**, Cartoon showing a superfluid (SF) phase with the bosons delocalizing over the entire system. **c**, The ground state phase diagram of the 1D standard BH model as a function of the normalized chemical potential μ/U and the normalized hopping J/U.

The standard BH model considers nearest-neighbor (NN) hopping $J_{i,j} = J$ (i, j are NN sites) between sites and has been extensively studied theoretically and experimentally, especially using transport measurements in Josephson junction arrays and quantum gas microscope of ultracold atoms [14, 265, 266]. In these experiments, the on-site interaction U is usually positive as a result of the repulsive interaction of two particles on the same site.

The zero-temperature ground state of the standard BH model depends on the parameter regimes. Consider the unity filling (the particle number N is the same as the number of lattice sites L), in the limit of $|J/U| \to 0$, the energy penalty of particles overlapping on the same site is so large that the particles are frozen at their individual sites, forming the Mott insulator (MI) phase (Fig. 7.1a). In the opposite limit of $|J/U| \to \infty$, the kinetic energy associated with particle hopping dominates and the particles tend to delocalize over the entire system in the ground state, forming the superfluid (SF) phase (Fig. 7.1b). In between the limits, a critical value $(J/U)_c$ marks the quantum phase transition. Away from the unity filling, changing the chemical potential can add (subtract) a particle, thus creating a free particle (hole) to hop in the system and resulting in the SF phase. Combining the above analysis gives us the ground state phase diagram (shown in Fig. 7.1c is the 1D standard BH model phase diagram) featuring MI lobes surrounded by SF. In the MI phase at a fixed J/U, overcoming the on-site interaction penalty requires a significant raise in the chemical potential μ represented by the MI gap (the height of the MI lobe). Whereas in the SF phase, there is no energy penalty associated with changing the particle number since all the particles are delocalized, meaning the SF phase is *compressible*. The early experiments have explored both the MI and the SF regime using site-resolved measurements that captures site-to-site correlations and non-local order parameters, as well as exploring the quantum phase transition described by an effectively relativistic theory [267–269].

However, the extended version of the BH model, where the beyond-nearest-neighbor hopping is included, still remains to be explored largely due to the lack of experimental controllability over the beyond-NN hopping. The quantum simulator with individual site control and read-out detailed in Chapter 6 provides the playground in this frontier. In this quantum simulator, the on-site interaction is negative as a result of the transmon level structure (Fig. 7.2a). Therefore, the many-body ground state of this BH model with attractive interaction is the superposition of aggregation of all the particles on a single site [270, 271]. To regain the competition between the hopping and the on-site interaction in repulsive BH models, we can study the highest energy state instead, which corresponds to the ground state of $-\hat{H}$ (referred to as the “ground state” below). The study of this extended version of the BH model may provide insights into the effect of frustration from beyond NN hopping in quantum phase transition and nontrivial correlations.

Numerical simulation

To access the unity-filling ground state of 10 or more sites efficiently, we use the *iTensor* Julia package [272] that implements the density matrix renormalization group (DMRG) technique[1] [273, 274]. We simulate the 1D Hamiltonian $-\hat{H}$ where $\hat{H}$ is specified in Eq. 7.1 with U normalized to -1 and $J_{i,j}$ assuming the exponential form $|J_{i,j}| = Je^{-(|i-j|-1)/\xi}(|i-j| \geq 1)$ with the NN hopping rate J and localization length ξ. The signs of the hopping terms are consistent with Sec. 6.4. We specify the particle number in the initial state that is conserved during the simulation, which effectively takes care of the chemical potential μ.

[1]We construct a spinless boson class containing 5 levels (enough for the ground state study) and use the DMRG solver that conserves the total particle number to solve for the ground state energy and wave function.

Ground state phase diagram

We obtain the phase diagram at a certain localization length ξ following the methods in [275]. More specifically, the boundary of the phase diagram corresponds to the chemical potential $\mu_{p(m)}$ or energy needed to add (subtract) one particle, which can be obtained from the ground state energy difference between the particle number $N = L$ and $L + 1$ $(L - 1)$ in the system where L is the system size. The value of $\mu_{p(m)}$ is always affected by finite system effect, which we overcome by simulating $L = 32, 64, 128, 256$ and extrapolate the value to $L \to \infty$ (or equivalently, $1/L \to 0$) to find the value in the thermodynamical limit. From this process, we find the phase diagram for the standard BH model that is consistent with earlier results [275]. Moreover, the phase diagrams for $\xi = 1$ in the UBG and LBG are drastically different: the MI lobe is more restricted (extended) in the UBG (LBG) compared to the standard BH model with NN hopping (Fig. 7.2b).

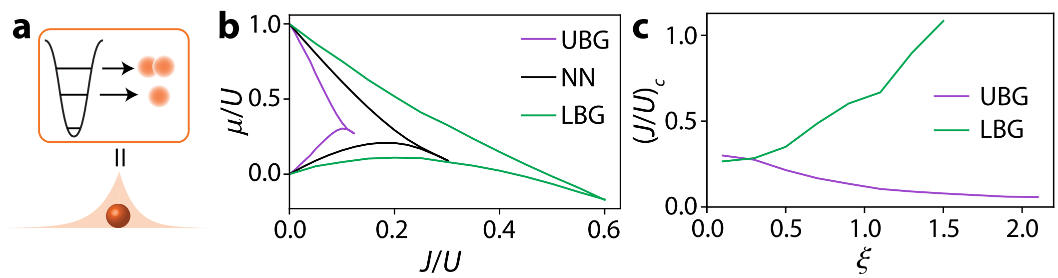

Figure 7.2: **Phase diagram and critical values of the extended version of the 1D BH model.** **a**, Cartoon showing a single lattice site realized by the qubit-photon bound state introduced in Chapter 6. **b**, The ground state phase diagram of the 1D extended BH model as a function of the normalized chemical potential μ/U and the normalized hopping J/U for localization length $\xi = 1$ in the upper bandgap (UBG) and the lower bandgap (LBG). The standard BH model phase diagram (nearest-neighbor, or NN, coupling) is shown as a reference. **c**, The critical value $(J/U)_c$ as a function of localization length ξ in the UBG and LBG.

This difference originates in the sign of hopping in the two bandgaps. In the standard BH model, the sign of J is not important since the effect of $J \to -J$ is equivalent to redefining $\hat{b}_i \to -\hat{b}_i$ where i is even. However, the sign of beyond-NN hopping can not be gauged out in this way especially when $|i - j|$ is an even number. The all positive (alternating) sign in the UBG (LBG) further lowers (raises) the SF ground state energy of $-\hat{H}$, effectively stabilizing (creating frustration) for the SF phase and causing the MI lobe to shrink (extend).

Although the critical value $(J/U)_c$ is where the upper and lower boundaries of the MI lobe overlap (the MI gap closes), it is hard to find the accurate critical value in this way since the gap closes slowly, introducing large uncertainty in the critical value. Following [275], we use the characteristic parameter K for a Luttinger liquid[2] [276–278], which describes the low-energy properties of 1D SF phase, to determine the critical value. The parameter K can be extracted from the correlation decay $\langle \hat{b}_d^\dagger \hat{b}_0 \rangle \sim d^{-K/2}$. The parameter $K = K_c = 1/2$ represents the unity-filling critical point of the constant-particle-number phase transition, the Kosterlitz-Thouless transition [279–282], which we use to determine $(J/U)_c$. Using this method, we obtain the critical value as a function of ξ in the two bandgaps[3] (Fig. 7.2c).

Correlation functions

In addition to the ground state energy, we also obtain the ground state wave function from the DMRG simulations. Using the wave function, we can extract information such as correlation function and non-local string-order parameters [283–285]. As an example, we show the two-site number correlation function in the UBG for a system with $L = 64$, $C(d) = \langle \hat{n}_i \hat{n}_{i+d} \rangle - \langle \hat{n}_i \rangle \langle \hat{n}_{i+d} \rangle$ (Fig. 7.3). The on-site fluctuation reflected in $C(0)$ rises at a smaller J/U for smaller ξ as a result of entering the SF phase. The correlation $C(d)$ also exhibits a larger value for $d > 2$ at large ξ.

Plans for the experimental exploration

Parameter regimes

To see what ground state phase we can realize using, e.g., the quantum simulator in Chapter 6, we can compare the result of $(J/U)_c$ versus ξ above (Fig. 7.2c) and

---

[2] The Hamiltonian can be written as

$$\hat{H}_L = \frac{1}{2\pi} \int dx \left\{ (vK)[\hat{\Pi}(x)]^2 + \left(\frac{v}{K}\right) [\partial_x \hat{\Phi}(x)]^2 \right\},$$

where $\hat{\Pi}(x)$ and $\hat{\Phi}(x)$ represent the density and phase fluctuations, respectively, in the relation $b^\dagger(x) = \sqrt{\rho(x)} e^{i\Phi(x)}$, v is the second sound velocity, and K describes the decay of the correlation function $\langle \hat{b}_d^\dagger \hat{b}_0 \rangle \sim d^{-K/2}$.

[3] To reduce the finite-size effect, K obtained from two largest system sizes are used [275]. The simulation for UBG ends at small (J/U) and the largest system sizes are $L = 128, 256$ whereas LBG simulation covers very large J/U value, making the simulation much harder, and thus the largest system sizes are only $L = 32, 64$. This could cause error in the critical value and explain the smaller value of $(J/U)_c$ at $\xi = 0.1$.

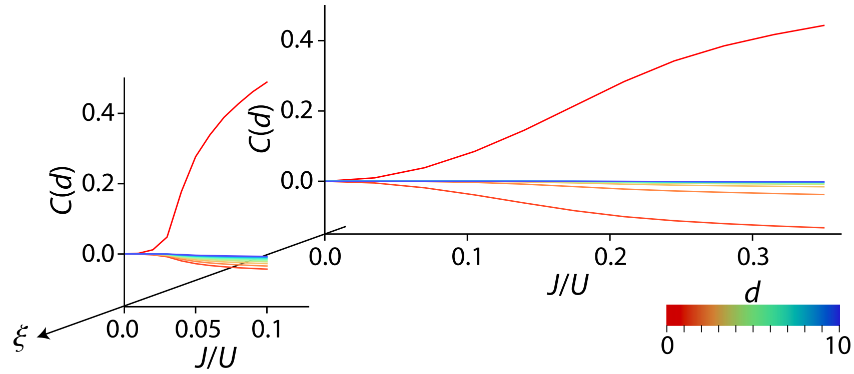

Figure 7.3: **Two-site correlations in the extended version of the BH model.** The two-site correlations in the UBG at different site separations (colored) as a function of normalized J/U at $\xi = 2.9$ (the front panel) and $\xi = 0.1$ (the back panel). The axes are of the same scale for both panels.

the experimental characterization (Fig. 6.3). In the LBG, the quantum simulator exhibits ξ of 1.4 to 4.2 and (J/U) of 0.013 to 0.067, which is deep inside the MI phase. In the UBG, ξ ranges from 1.8 to 4.1 with (J/U) of 0.188 to 1.33, which is inside the SF phase. Therefore, this quantum simulator allows us to study the MI and SF phase separately in the two bandgaps but the phase transition is not accessible. It is difficult to approach the phase transition point in the LBG since increasing (J/U) at smaller detuning also raises ξ, which drives $(J/U)_c$ to a higher value. Changing parameters in the circuit design could help, whereas the qubit-waveguide coupling needs to be comparable to the strength of the coupling between waveguide resonators, which is challenging to realize. In contrast, the parameter trend in the UBG is in favor of accessing the phase transition, and we can enter the MI phase at large qubit-bandedge detuning[4]. On the design side, lowering the qubit-waveguide coupling also helps to approach the MI phase in the UBG. For example, reducing the qubit-waveguide coupling by half will lower J to 1/4 of its original value (Eq. D.21), thus placing (J/U) below the critical value.

Accessing the ground states

In general, it is challenging to prepare an entangled many-body ground state. A common method is the adiabatic preparation, where an easy-to-prepare ground state

[4]In the quantum simulator in Chapter 6, this is limited by the low upper sweet spot frequency of about 7.5 GHz. The upper sweet spot frequency can be designed to be higher by changing the Josephson junction parameters.

such as a product state can be adiabatically transformed into the target ground state by tuning the parameters of the Hamiltonian. This method is applicable in preparing the ground state for the extended version of the BH model. The MI phase in the limit of $(J/U) \to 0$ is a product state $|n = 1\rangle^{\otimes L}$ in the position basis that we can prepare using the sequence in Fig. 6.4b. We can first prepare the product state at the smallest (J/U) accessible and ramp up this parameter (by reducing the qubit-bandedge detuning) to the target value where the entangled MI state can be prepared. Using this method, we can even ramp through the phase transition and access the SF phase if we keep a small ramping rate compared to the many-body gap that remains finite for an experimental system [286]. The fidelity of this preparation protocol depends on how close the initial ground state is to the product state, which exhibits an error $\sim O(J/U)$ in the wave function [287]. This error may influence the observation of small correlations.

To overcome this error, we can use an adiabatic driving protocol [215] starting from no excitation in the system, a true ground state of $-\hat{H}$ when the chemical potential is negative. A drive term

$$\hat{H}_d/\hbar = \frac{\Omega_d}{2}\sum_i(\hat{b}_i^\dagger + \hat{b}_i) \tag{7.2}$$

can be added to the Hamiltonian such that in the rotating frame of the driving frequency, the detuning between the drive and the qubit controls the chemical potential μ. In addition, the drive term also couples different particle-number sectors of the original particle-number-conserving Hamiltonian to allow an adiabatic path from a vacuum state to the unity-filling MI state.

Another ground-state preparation method is dissipative preparation [48], which can also be used to stabilize a many-body state. This method relies on the incompressibility of, e.g., the MI phase and achieves the balance between drive and dissipation to stabilize the particle number to unity filling. We have designed two extra qubits in the quantum simulator in Chapter 6 (Fig. 6.2a), which can act as stabilizer sites to perform this preparation.

7.2 Engineering the coupling profile

The waveguide QED architectures open the door to beyond nearest-neighbor connectivity for superconducting qubits. However, the architecture that provides wide-band coherence protection only supports the native coupling profile of exponential decay in strength [288] (see also Chapter 6), which limits the realm of Hamiltonians to implement and still belongs to short-range coupling in the thermodynamic limit. Further engineering of the coupling profile and even the connectivity graph is valuable for both quantum simulation and computation.

Flux modulation of the qubit frequency

The tunability in the localization length allows us to combine the coupling profile of different exponents to emulate new classes of coupling profiles [289], especially in a physical device with a finite size. In [158], the authors proposed to use two sets of Raman drives to generate an approximate power-law decay profile composed of the summation of two exponentials. Although the transmon qubits do not support the level structure to realize this proposal, we can combine multiple exponentials using flux modulation of the qubit frequency.

The flux modulation creates sidebands around the major qubit frequency, usually used to bridge the energy gap between two parties that are off-resonant [290–293]. In our case, we start from qubits that are on-resonant with each other, which gives rise to a single exponential decay profile. Additionally, we can flux modulate each qubit to create sidebands that are resonant to each other. These sidebands, exhibiting different detunings from the original qubit frequency, lead to decay profiles with different exponents (Fig. 7.4). The strength of a sideband, controlled by the modulation frequency and strength, determines the strength of the corresponding exponential profile in the combination. Therefore, we can use the flux modulation to engineer the coupling profiles.

More concretely, we start from the Hamiltonian describing multiple qubits coupled to a waveguide, similar to Eq. D.13,

$$\begin{aligned}\hat{H}/\hbar = \sum_k \omega_k \hat{a}_k^\dagger \hat{a}_k + \sum_n \frac{\omega_{q_n}(t)}{2}\hat{\sigma}_n^z \\ + \sum_{n,k}\left(g_{k,n}\hat{a}_k^\dagger\hat{\sigma}_n^- + g_{k,n}^*\hat{a}_k\hat{\sigma}_n^+\right),\end{aligned} \tag{7.3}$$

where ω_k is the frequency of the waveguide mode with wave vector k and creation (annihilation) operator $\hat{a}_k^\dagger$ ($\hat{a}_k$), $\omega_{q_n}(t)$ is the flux modulated n-th qubit frequency, and $g_{k,n}$ is the coupling strength between the n-th qubit and mode k. We assume that the flux modulation leads to the same time-dependent frequency for all the qubits

$$\omega_{q_n}(t) = \omega_0 + \epsilon\cos(\Omega t + \phi), \tag{7.4}$$

where ω_0 is the averaged qubit frequency during the modulation, ϵ is the modulation strength, Ω and ϕ represents the modulation frequency and phase, respectively (a $\phi = 0$ example is shown in Fig. 7.4a). By transforming the Hamiltonian in Eq. 7.3 into the interaction picture and back to the lab frame, we obtain the effective sideband-enabled interaction

$$\begin{aligned} \hat{H}/\hbar = &\sum_k \omega_k \hat{a}_k^\dagger \hat{a}_k + \sum_n \frac{\omega_0}{2} \hat{\sigma}_n^z \\ &+ \sum_{n,k} \sum_j \left(g_{k,n} \mathcal{J}_j(\frac{\epsilon}{\Omega}) e^{-ij(\Omega t + \phi)} \hat{a}_k^\dagger \hat{\sigma}_n^- + h.c. \right), \end{aligned} \tag{7.5}$$

where $\mathcal{J}_j(x)$ is the j-th order Bessel function of the first kind. For simplicity, we define $h_{k,n,j} \equiv g_{k,n} \mathcal{J}_j(\frac{\epsilon}{\Omega}) e^{-ij\phi}$. To address the time-dependent coupling terms from the sidebands, we iteratively (i) apply the Schrieffer-Wolff transformation to obtain the photon-mediated qubit-qubit interaction by the non-rotating coupling[5] and (ii) transform to the frame where the next sideband-photon coupling is static. By repeating the procedure for each sideband and keeping up to first order in g/Δ, where Δ is the detuning between the sideband and a photonic mode, we arrive at the photon-mediated interaction

$$\hat{H}_I/\hbar = \sum_{n,m} \sum_j \left(\sum_k \frac{h_{k,n,j}^* h_{k,m,j}}{\Delta_k - j\Omega} \hat{\sigma}_n^+ \hat{\sigma}_m^- + h.c. \right). \tag{7.6}$$

In the following, we show an example of using the flux modulation to emulate the power-law profile $J_{n,m} \propto 1/|n-m|$ (Fig. 7.4b). Although the flux modulation creates an infinite series of sidebands, the strength of higher-order sidebands is small at weak modulation amplitude. The major contribution comes from the zeroth-order (averaged qubit frequency) and the first-order sideband. Using the parameters from Fig. 6.3, we choose the averaged qubit frequency to be $\omega_0/2\pi = 4.7\,\mathrm{GHz}$ (localization length $\xi \sim 1.4$), the modulation frequency $\Omega/2\pi = 258\,\mathrm{MHz}$, the modulation amplitude $\epsilon/2\pi = 96\,\mathrm{MHz}$, and the modulation phase $\phi = 0$. With the formulas in App. D.1, we can calculate the localization length and coupling strength associated with the sideband $\omega_0 - \Omega$, ω_0, and $\omega_0 + \Omega$, resulting in the approximate power-law profile $J_{n,m} \propto 1/|n-m|$ (Fig. 7.4c). The weak second order sideband $\omega_0 + 2\Omega$ lands in the passband frequency, resulting in a radiative-decay-limited qubit lifetime of about 11 μs[6].

[5]The fast-rotating qubit-qubit coupling proportional to $\frac{h_{k,n,j} h_{k,m,l}^*}{\Delta_k} e^{-i(j-l)\Omega t}$ is ignored assum-

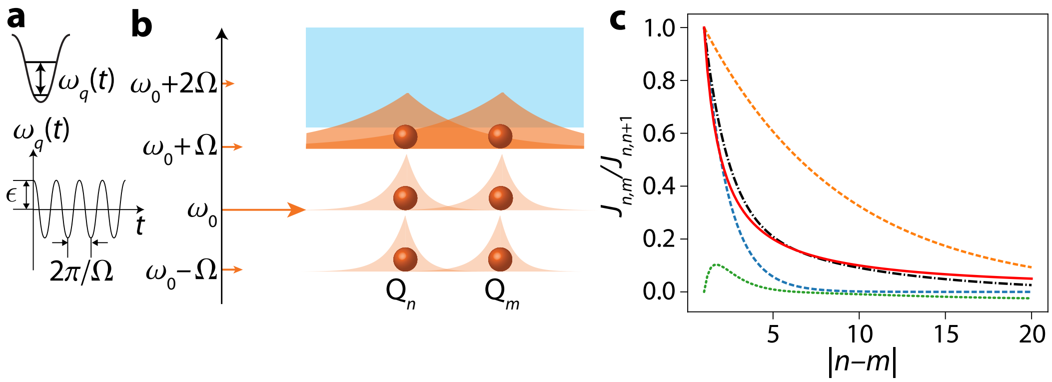

Figure 7.4: **Engineering the coupling profile using flux modulation.** **a**, Time-dependent qubit frequency $\omega_q(t)$ in Eq. 7.4 resulting from the flux modulation with the modulation amplitude ϵ, modulation frequency Ω, and the modulation phase in this example $\phi = 0$. **b**, Cartoon showing the qubit-photon bound states Q_n and Q_m after flux modulation with the vertical (horizontal) direction representing the frequency (position) space. The dominant component is the zeroth order sideband or the average qubit frequency at ω_0 (large orange arrow). The first-order sideband at $\omega_0+\Omega$ ($\omega_0-\Omega$) locates closer (farther) from the passband (the blue band), resulting in a more extended (localized) bound state. The second-order sideband $\omega_0+2\Omega$ lands inside the passband. The orange arrows and the photonic envelope reflects qualitative relations, which are not exact in scale. **c**, An example of emulating the power-law profile $J_{n,m} \propto 1/|n-m|$ (red solid curve) using the zeroth order sideband (blue dashed curve) and the first order sideband (orange dashed curve). The combination gives the black dash-dotted curve with the error from the power-law profile shown in the green dotted curve. The $\omega_0-\Omega$ sideband makes a small contribution from its weak coupling strength with a profile similar to the blue dashed curve.

In addition to engineering the coupling profile in 1D, the flux modulation also enables synthetic higher-dimensional connectivity and magnetic field, which is the basic building block for fractional quantum Hall states [294, 295]. We can realize the higher-dimensional connectivity using the frequency space as synthetic dimensions. To illustrate, we use the construction of a four-qubit plaquette as an example (Fig. 7.5). At the averaged qubit frequencies, Q_1 and Q_2 (Q_3 and Q_4) are on resonance at ω_A (ω_B) and $\omega_A \neq \omega_B$. We modulate the qubits to create the first-order sideband for Q_1 and Q_3 (Q_2 and Q_4) at ω_C (ω_D) with all ω_i ($i =$

ing $|(j-l)\Omega| \gg \frac{h_{k,n,j}h^*_{k,m,l}}{\Delta_k}$, where $\Delta_k = \omega_0 - \omega_k$ is the detuning between the averaged qubit frequency and the mode k.

[6]The decay rate of $\Gamma_{1D}/2\pi = 46\,\text{MHz}$ calculated from the circuit design values is used to estimate the sideband qubit decay. The second order sideband is proportional to $\mathcal{J}_2(\epsilon/\Omega) < 0.018$.

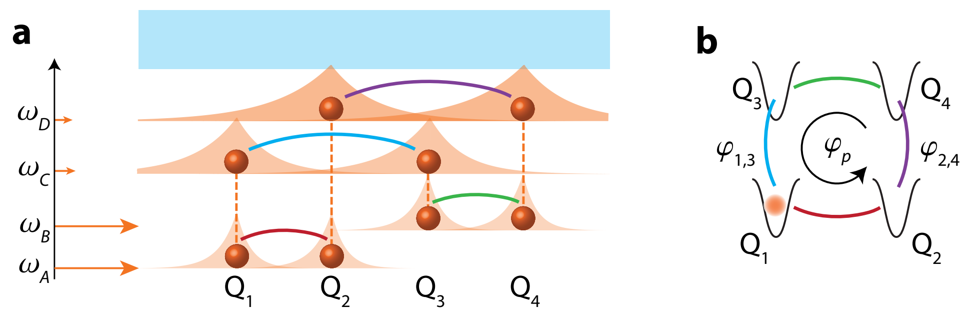

Figure 7.5: **Synthetic higher-dimensional connectivity and magnetic field. a**, Schematic showing an example of four-qubit plaquette constructed from flux modulation. The vertical direction represents the frequency dimension and the horizontal direction is the position space. The dashed orange line connects different sidebands of the same bound state and the colored curves represent photon-mediated bound state coupling. The passband of the waveguide is represented by the blue band. **b**, The plaquette for microwave photons with a synthetic magnetic field and a total accumulated hopping phase φ_p resulting from the flux modulation in panel **a**.

A, B, C, D) of distinct values. In this way, we employ the beyond-NN coupling and the frequency dimension to create a 2D plaquette out of a 1D structure. Moreover, the photon-mediated qubit exchange interaction exhibits a phase determined by the flux modulation phase $\varphi_{n,m} = \phi_n - \phi_m$ from Eq. 7.6 where ϕ_n is the flux modulation phase of the n-th qubit. By setting the modulation phase of the four qubits such that the total plaquette phase $\varphi_p = \varphi_{1,3} - \varphi_{2,4} \neq 0$, we can introduce a synthetic magnetic field for microwave photons hopping around the plaquette [212] (Fig. 7.5b). This method can be extended to even higher dimensions with more flux modulation tones. The drawback of this method is the ultimate limit of the number of modulation tones for a single qubit before we run into the frequency crowding problem. As we see from the above example, each link connecting a qubit to another qubit occupies a distinct frequency with a bandwidth proportional to the coupling strength of this link. Two links without a common qubit may use the same frequency only if the four qubits involved in the links are sufficiently separated on the waveguide.

When using the flux modulation, it is important to take into account higher order sidebands even if we only use the first order ones. The higher order sidebands may land in the passband or other unwanted frequencies to introduce spurious decay or interaction, especially when we use a large modulation strength ϵ. This problem may be overcome by engineering the time-dependent qubit frequency in Eq. 7.4 to take more sophisticated forms [127, 296].

Waveguide dispersion engineering

Engineering the dispersion of the waveguide can also change the coupling profile with an example of the topological waveguide described in Chapter 5. In addition, left-handed metamaterials [297, 298] and waveguides with flat dispersions [299] can also introduce intruiguing waveguide QED phenomena. The construction of 2D metamaterials [300] will open the door to a richer set of physics, including the hyperbolic space [40] and anisotropic coupling profiles [143]. Coupling qubits to such metamaterials is also within reach by using standard flip-chip technique [235, 236].

7.3 Scaling up to a large system size

Scalability is an important motivation to move from cavity-QED-based architectures to waveguide-QED-based architectures. The waveguide itself is intrinsically extensible, i.e., its dispersion relation remains unchanged by adding extra length or unit cells to the waveguide. Here, we discuss the scaling considerations when coupling qubits to a waveguide.

In the passband regime, scaling to a large number of qubits will not change the collective effects and protocols [129, 139, 145] assuming that the Markov approximation remains valid (discussed in Sec. 2.1). This translates to the separation between qubits $\Delta x \ll 10\lambda$ [142], i.e., about 20 qubits given the separation of $\lambda/2$. Beyond this limit, the theoretical modeling, including numerical simulation, is more challenging and the formulas in Sec. 2.1 are not longer valid. Nonetheless, this regime presents exciting opportunities for experimental exploration of collective non-Markovian effects [143].

In the bandgap regime, we can scale up the system size without worrying about frequency crowding thanks to the tunable range and strength of the photon-mediated interactions. By choosing the qubit idle frequency to be away from the bandgap, we can suppress the coupling between unwanted qubit pairs. Using the quantum simulator in Chapter 6 as an example, the nearest-neighbor coupling is smaller than 1 MHz when the qubit frequency is below 4.3 GHz. With the localization length of $\xi = 1.4$, the coupling strength decays below 1 kHz for qubit-qubit separation of 10 sites. This illustrates that the required bandwidth for qubit idle frequencies does not grow with the number of qubits coupled to the waveguide.

The scaling of the number of read-out resonators in the passband is different. Owing to the infinite-range interacting nature of the passband and the requirement to prevent read-out crosstalk by separating the frequencies of different read-out resonators, the metamaterial waveguide Purcell filter cannot be simply extended to host a large number of read-out resonators. Therefore, we propose a truly scalable waveguide QED architecture by separating the quantum bus as the interaction media from the metamaterial Purcell filter (Fig. 7.6). The quantum bus is shared among all qubits to mediate long-range interactions while multiple metamaterial Purcell filters are incorporated, each of which can host around 10 read-out resonators.

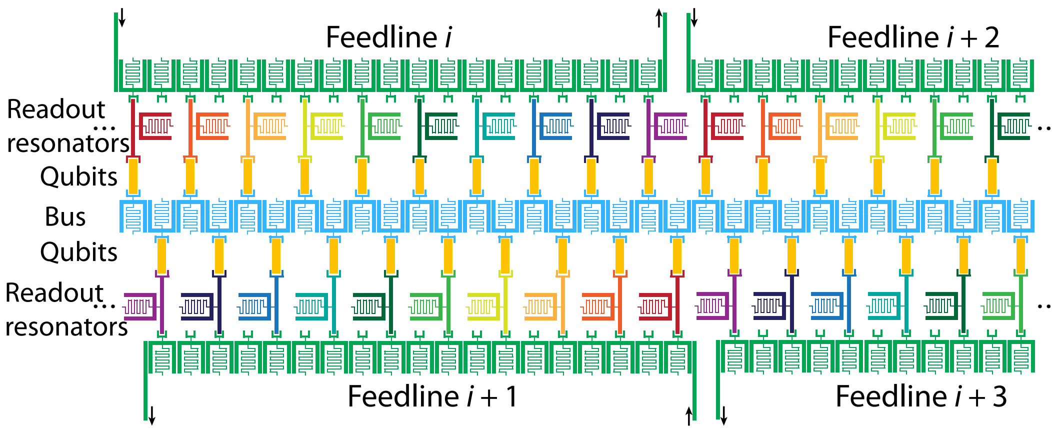

Figure 7.6: **Waveguide QED architecture for scaling up to large system sizes.** Cartoon showing a truly scalable waveguide QED architecture where the middle blue structure represents the waveguide bus to mediate qubit-qubit interaction, the orange rectangles represent the qubits, the colors of the read-out resonators represents different frequencies, and the green structures are the read-out feedlines hosting 10 read-out resonators on a single feedline.

Beyond analog quantum simulation, we also consider using this architecture to construct long-range gates that are valuable for low-overhead quantum error correction [34, 70, 72–74] and fermionic quantum simulation [59, 62, 77]. The important factor is the gate speed in the long-range limit, where the passband modes approaches continuum in frequency and the gate is mediated by a collection of the passband modes. The interaction strength described in, e.g., Eq. 2.36 for the quadratic dispersion predicts that large qubit-waveguide coupling g and small qubit-bandedge detuning $|\Delta|$ gives a large interaction strength $J_{i,j}$. While the specific expression is dependent on the exact dispersion relation, $J_{i,j}$ usually diverges when $|\Delta| \to 0$. However, this limit is beyond the perturbative regime where Schrieffer-Wolff transformation, which assumes $|g/\Delta| \ll 1$, is valid[7]. To calculate the interaction strength in this limit, we need to use the Green function formalism, which gives a finite interaction strength close to the bandedge [143, 164] as expected. In addition, to mediate the interaction between distant qubits, the bound state needs to be extended in space, which requires special care in the preparation process. Directly exciting the qubit itself close to the bandedge is not effective since the wave-function overlap between the bare qubit and the extended qubit-photon bound state is smaller at smaller qubit-bandedge detunings [143, 301]. A viable solution is to excite the qubit at large $|\Delta|$ and tune it close to the bandedge adiabatically, which may slow down the entire long-range-gate protocol. Therefore, when very-long-range gates are considered, it may be beneficial to employ a hybrid protocol where shorter-range interaction is performed in the bandgap with interaction meditaed by virtual photons and the very-long-range gate is achieved using the pitch-and-catch method in the passband [127, 252, 302, 303]. This protocol is ultimately limited by the loss of the waveguide or the Anderson localization from the waveguide disorder, the former of which is found to be the limiting factor of microwave propagation in the passband of a metamaterial waveguide [127, 144]. The waveguide loss can be reduced by more than two orders of magnitude via improved fabrication processes [304].

[7] Alternatively, the handling of the perturbation can also be viewed as the Born-Markov approximation where the photonic degrees of freedom are traced out, leaving the effective qubit-qubit interaction [143].

BIBLIOGRAPHY

[1] Lord Kelvin. “Nineteenth century clouds over the dynamical theory of heat and light”. In: *The London, Edinburgh, and Dublin Philosophical Magazine and Journal of Science* 2.7 (1901), pp. 1–40.

[2] Max Planck. *The theory of heat radiation*. Blakiston, 1914.

[3] Albert Einstein. “On a heuristic point of view concerning the production and transformation of light”. In: *Annalen der Physik* (1905), pp. 1–18.

[4] John S Bell. “On the Einstein Podolsky Rosen paradox”. In: *Physics Physique Fizika* 1.3 (1964), p. 195.

[5] John F Clauser, Michael A Horne, Abner Shimony, and Richard A Holt. “Proposed experiment to test local hidden-variable theories”. In: *Phys. Rev. Lett.* 23.15 (1969), p. 880. DOI: 10.1103/PhysRevLett.23.880.

[6] Stuart J Freedman and John F Clauser. “Experimental test of local hidden-variable theories”. In: *Phys. Rev. Lett.* 28.14 (1972), p. 938. DOI: 10.1103/PhysRevLett.28.938.

[7] Alain Aspect, Jean Dalibard, and Gérard Roger. “Experimental test of Bell’s inequalities using time-varying analyzers”. In: *Phys. Rev. Lett.* 49.25 (1982), p. 1804. DOI: 10.1103/PhysRevLett.49.1804.

[8] Jian-Wei Pan, Dik Bouwmeester, Harald Weinfurter, and Anton Zeilinger. “Experimental entanglement swapping: entangling photons that never interacted”. In: *Phys. Rev. Lett.* 80.18 (1998), p. 3891. DOI: 10.1103/PhysRevLett.80.3891.

[9] Michael A Nielsen and Isaac L Chuang. “Quantum information and quantum computation”. In: *Cambridge: Cambridge University Press* 2.8 (2000), p. 23.

[10] Michel H Devoret and Robert J Schoelkopf. “Superconducting circuits for quantum information: an outlook”. In: *Science* 339.6124 (2013), pp. 1169–1174. DOI: 10.1126/science.1231930.

[11] Morten Kjaergaard, Mollie E Schwartz, Jochen Braumüller, Philip Krantz, Joel I-J Wang, Simon Gustavsson, and William D Oliver. “Superconducting qubits: Current state of play”. In: *Annu. Rev. Condens. Matter Phys.* 11 (2020), pp. 369–395. DOI: 10.1146/annurev-conmatphys-031119-050605.

[12] Gary Wolfowicz, F Joseph Heremans, Christopher P Anderson, Shun Kanai, Hosung Seo, Adam Gali, Giulia Galli, and David D Awschalom. “Quantum guidelines for solid-state spin defects”. In: *Nat. Rev. Mater.* 6.10 (2021), pp. 906–925. DOI: 10.1038/s41578-021-00393-x.

[13] Colin D Bruzewicz, John Chiaverini, Robert McConnell, and Jeremy M Sage. "Trapped-ion quantum computing: Progress and challenges". In: *Appl. Phys. Rev.* 6.2 (2019), p. 021314. DOI: 10.1063/1.5088164.

[14] Christian Gross and Immanuel Bloch. "Quantum simulations with ultracold atoms in optical lattices". In: *Science* 357.6355 (2017), pp. 995–1001. DOI: 10.1126/science.aal3837.

[15] John L Bohn, Ana Maria Rey, and Jun Ye. "Cold molecules: Progress in quantum engineering of chemistry and quantum matter". In: *Science* 357.6355 (2017), pp. 1002–1010. DOI: 10.1126/science.aam6299.

[16] Antoine Browaeys and Thierry Lahaye. "Many-body physics with individually controlled Rydberg atoms". In: *Nat. Phys.* 16.2 (2020), pp. 132–142. DOI: 10.1038/s41567-019-0733-z.

[17] Sergei Slussarenko and Geoff J Pryde. "Photonic quantum information processing: A concise review". In: *Appl. Phys. Rev.* 6.4 (2019), p. 041303. DOI: 10.1063/1.5115814.

[18] Peter W Shor. "Algorithms for quantum computation: discrete logarithms and factoring". In: *Proceedings 35th annual symposium on foundations of computer science*. Ieee. 1994, pp. 124–134. DOI: 10.1109/SFCS.1994.365700.

[19] Lov K Grover. "Quantum mechanics helps in searching for a needle in a haystack". In: *Phys. Rev. Lett.* 79.2 (1997), p. 325. DOI: 10.1103/PhysRevLett.79.325.

[20] Stephen Jordan. *Quantum Algorithm Zoo*. https://quantumalgorithmzoo.org/. Updated: 2022-10-14.

[21] J Robert Johansson, Paul D Nation, and Franco Nori. "QuTiP: An open-source Python framework for the dynamics of open quantum systems". In: *Comp. Phys. Comm.* 183.8 (2012), pp. 1760–1772. DOI: 10.1016/j.cpc.2012.11.019.

[22] A Yu Kitaev. "Fault-tolerant quantum computation by anyons". In: *Ann. Phys.* 303.1 (2003), pp. 2–30. DOI: 10.1016/S0003-4916(02)00018-0.

[23] Austin G Fowler, Matteo Mariantoni, John M Martinis, and Andrew N Cleland. "Surface codes: Towards practical large-scale quantum computation". In: *Phys. Rev. A* 86.3 (2012), p. 032324. DOI: 10.1103/PhysRevA.86.032324.

[24] Martin Bossert. *Channel coding for telecommunications*. John Wiley & Sons, Inc., 1999.

[25] Asher Peres. "Reversible logic and quantum computers". In: *Phys. Rev. A* 32.6 (1985), p. 3266. DOI: 10.1103/PhysRevA.32.3266.

[26] Peter W Shor. "Scheme for reducing decoherence in quantum computer memory". In: *Phys. Rev. A* 52.4 (1995), R2493. DOI: 10.1103/PhysRevA.52.R2493.

[27] Daniel Gottesman. "An introduction to quantum error correction and fault-tolerant quantum computation". In: *Quantum information science and its contributions to mathematics, Proceedings of Symposia in Applied Mathematics*. Vol. 68. 2010, pp. 13–58.

[28] Weizhou Cai, Yuwei Ma, Weiting Wang, Chang-Ling Zou, and Luyan Sun. "Bosonic quantum error correction codes in superconducting quantum circuits". In: *Fundam. Res.* 1.1 (2021), pp. 50–67. DOI: 10.1016/j.fmre.2020.12.006.

[29] Victor V Albert. "Bosonic coding: introduction and use cases". In: *arXiv preprint arXiv:2211.05714* (2022). DOI: 10.48550/arXiv.2211.05714.

[30] Nissim Ofek, Andrei Petrenko, Reinier Heeres, Philip Reinhold, Zaki Leghtas, Brian Vlastakis, Yehan Liu, Luigi Frunzio, SM Girvin, Liang Jiang, et al. "Extending the lifetime of a quantum bit with error correction in superconducting circuits". In: *Nature* 536.7617 (2016), pp. 441–445. DOI: 10.1038/nature18949.

[31] VV Sivak, A Eickbusch, B Royer, S Singh, I Tsioutsios, S Ganjam, A Miano, BL Brock, AZ Ding, L Frunzio, et al. "Real-time quantum error correction beyond break-even". In: *arXiv preprint arXiv:2211.09116* (2022). DOI: 10.48550/arXiv.2211.09116.

[32] Zhongchu Ni, Sai Li, Xiaowei Deng, Yanyan Cai, Libo Zhang, Weiting Wang, Zhen-Biao Yang, Haifeng Yu, Fei Yan, Song Liu, et al. "Beating the break-even point with a discrete-variable-encoded logical qubit". In: *arXiv preprint arXiv:2211.09319* (2022). DOI: 10.48550/arXiv.2211.09319.

[33] Peter W Shor. "Fault-tolerant quantum computation". In: *Proceedings of 37th conference on foundations of computer science*. IEEE. 1996, pp. 56–65.

[34] Daniel Gottesman. "Opportunities and Challenges in Fault-Tolerant Quantum Computation". In: *arXiv preprint arXiv:2210.15844* (2022). DOI: 10.48550/arXiv.2210.15844.

[35] John Preskill. "Quantum computing in the NISQ era and beyond". In: *Quantum* 2 (2018), p. 79. DOI: 10.22331/q-2018-08-06-79.

[36] Richard P Feynman. "Simulating physics with computers". In: *Feynman and computation*. CRC Press, 2018, pp. 133–153.

[37] Marco Cerezo, Andrew Arrasmith, Ryan Babbush, Simon C Benjamin, Suguru Endo, Keisuke Fujii, Jarrod R McClean, Kosuke Mitarai, Xiao Yuan, Lukasz Cincio, et al. "Variational quantum algorithms". In: *Nat. Rev. Phys.* 3.9 (2021), pp. 625–644. DOI: 10.1038/s42254-021-00348-9.

[38] Andrew J Daley, Immanuel Bloch, Christian Kokail, Stuart Flannigan, Natalie Pearson, Matthias Troyer, and Peter Zoller. "Practical quantum advantage in quantum simulation". In: *Nature* 607.7920 (2022), pp. 667–676. DOI: 10.1038/s41586-022-04940-6.

[39] Iacopo Carusotto, Andrew A Houck, Alicia J Kollár, Pedram Roushan, David I Schuster, and Jonathan Simon. "Photonic materials in circuit quantum electrodynamics". In: *Nat. Phys.* 16.3 (2020), pp. 268–279. DOI: 10.1038/s41567-020-0815-y.

[40] Alicia J Kollár, Mattias Fitzpatrick, and Andrew A Houck. "Hyperbolic lattices in circuit quantum electrodynamics". In: *Nature* 571.7763 (2019), pp. 45–50. DOI: 10.1038/s41586-019-1348-3.

[41] Jiehang Zhang, Paul W Hess, A Kyprianidis, Petra Becker, A Lee, J Smith, Gaetano Pagano, I-D Potirniche, Andrew C Potter, Ashvin Vishwanath, et al. "Observation of a discrete time crystal". In: *Nature* 543.7644 (2017), pp. 217–220. DOI: 10.1038/nature21413.

[42] Dominic V Else, Christopher Monroe, Chetan Nayak, and Norman Y Yao. "Discrete time crystals". In: *Annu. Rev. Condens. Matter Phys.* 11 (2020), pp. 467–499. DOI: 10.1146/annurev-conmatphys-031119-050658.

[43] Christopher Monroe, Wes C Campbell, L-M Duan, Z-X Gong, Alexey V Gorshkov, PW Hess, R Islam, K Kim, Norbert M Linke, Guido Pagano, et al. "Programmable quantum simulations of spin systems with trapped ions". In: *Rev. Mod. Phys.* 93.2 (2021), p. 025001. DOI: 10.1103/RevModPhys.93.025001.

[44] Petar Jurcevic, Ben P Lanyon, Philipp Hauke, Cornelius Hempel, Peter Zoller, Rainer Blatt, and Christian F Roos. "Quasiparticle engineering and entanglement propagation in a quantum many-body system". In: *Nature* 511.7508 (2014), pp. 202–205. DOI: 10.1038/nature13461.

[45] Philip Richerme, Zhe-Xuan Gong, Aaron Lee, Crystal Senko, Jacob Smith, Michael Foss-Feig, Spyridon Michalakis, Alexey V Gorshkov, and Christopher Monroe. "Non-local propagation of correlations in quantum systems with long-range interactions". In: *Nature* 511.7508 (2014), pp. 198–201. DOI: 10.1038/nature13450.

[46] Manoj K Joshi, Florian Kranzl, Alexander Schuckert, Izabella Lovas, Christine Maier, Rainer Blatt, Michael Knap, and Christian F Roos. "Observing emergent hydrodynamics in a long-range quantum magnet". In: *Science* 376.6594 (2022), pp. 720–724. DOI: 10.1126/science.abk2400.

[47] Mohammad Mirhosseini, Eunjong Kim, Xueyue Zhang, Alp Sipahigil, Paul B Dieterle, Andrew J Keller, Ana Asenjo-Garcia, Darrick E Chang, and Oskar Painter. "Cavity quantum electrodynamics with atom-like mirrors". In: *Nature* 569.7758 (2019), pp. 692–697. DOI: 10.1038/s41586-019-1196-1.

[48] Ruichao Ma, Brendan Saxberg, Clai Owens, Nelson Leung, Yao Lu, Jonathan Simon, and David I Schuster. “A dissipatively stabilized Mott insulator of photons”. In: *Nature* 566.7742 (2019), pp. 51–57. DOI: 10.1038/s41586-019-0897-9.

[49] Frank Arute, Kunal Arya, Ryan Babbush, Dave Bacon, Joseph C Bardin, Rami Barends, Rupak Biswas, Sergio Boixo, Fernando GSL Brandao, David A Buell, et al. “Quantum supremacy using a programmable superconducting processor”. In: *Nature* 574.7779 (2019), pp. 505–510. DOI: 10.1038/s41586-019-1666-5.

[50] Zijun Chen, Kevin J Satzinger, Juan Atalaya, Alexander N Korotkov, Andrew Dunsworth, Daniel Sank, Chris Quintana, Matt McEwen, Rami Barends, Paul V Klimov, et al. “Exponential suppression of bit or phase errors with cyclic error correction”. In: *Nature* 595.7867 (2021), pp. 383–387. DOI: 10.1038/s41586-021-03588-y.

[51] Qingling Zhu, Sirui Cao, Fusheng Chen, Ming-Cheng Chen, Xiawei Chen, Tung-Hsun Chung, Hui Deng, Yajie Du, Daojin Fan, Ming Gong, et al. “Quantum computational advantage via 60-qubit 24-cycle random circuit sampling”. In: *Science bulletin* 67.3 (2022), pp. 240–245. DOI: 10.1016/j.scib.2021.10.017.

[52] Shibo Xu, Zheng-Zhi Sun, Ke Wang, Liang Xiang, Zehang Bao, Zitian Zhu, Fanhao Shen, Zixuan Song, Pengfei Zhang, Wenhui Ren, et al. “Digital simulation of non-Abelian anyons with 68 programmable superconducting qubits”. In: *arXiv preprint arXiv:2211.09802* (2022). DOI: 10.48550/arXiv.2211.09802.

[53] Sebastian Krinner, Nathan Lacroix, Ants Remm, Agustin Di Paolo, Elie Genois, Catherine Leroux, Christoph Hellings, Stefania Lazar, Francois Swiadek, Johannes Herrmann, et al. “Realizing repeated quantum error correction in a distance-three surface code”. In: *Nature* 605.7911 (2022), pp. 669–674. DOI: 10.1038/s41586-022-04566-8.

[54] Youwei Zhao, Yangsen Ye, He-Liang Huang, Yiming Zhang, Dachao Wu, Huijie Guan, Qingling Zhu, Zuolin Wei, Tan He, Sirui Cao, et al. “Realization of an error-correcting surface code with superconducting qubits”. In: *Phys. Rev. Lett.* 129.3 (2022), p. 030501. DOI: 10.1103/PhysRevLett.129.030501.

[55] Rajeev Acharya, Igor Aleiner, Richard Allen, Trond I Andersen, Markus Ansmann, Frank Arute, Kunal Arya, Abraham Asfaw, Juan Atalaya, Ryan Babbush, et al. “Suppressing quantum errors by scaling a surface code logical qubit”. In: *arXiv preprint arXiv:2207.06431* (2022). DOI: 10.48550/arXiv.2207.06431.

[56] Andrew A Houck, Hakan E Türeci, and Jens Koch. "On-chip quantum simulation with superconducting circuits". In: *Nat. Phys.* 8.4 (2012), pp. 292–299. DOI: 10.1038/nphys2251.

[57] Samuel A Wilkinson and Michael J Hartmann. "Superconducting quantum many-body circuits for quantum simulation and computing". In: *Appl. Phys. Lett.* 116.23 (2020), p. 230501. DOI: 10.1063/5.0008202.

[58] Peter JJ O'Malley, Ryan Babbush, Ian D Kivlichan, Jonathan Romero, Jarrod R McClean, Rami Barends, Julian Kelly, Pedram Roushan, Andrew Tranter, Nan Ding, et al. "Scalable quantum simulation of molecular energies". In: *Phys. Rev. X* 6.3 (2016), p. 031007. DOI: 10.1103/PhysRevX.6.031007.

[59] Abhinav Kandala, Antonio Mezzacapo, Kristan Temme, Maika Takita, Markus Brink, Jerry M Chow, and Jay M Gambetta. "Hardware-efficient variational quantum eigensolver for small molecules and quantum magnets". In: *Nature* 549.7671 (2017), pp. 242–246. DOI: 10.1038/nature23879.

[60] Nikolaj Moll, Panagiotis Barkoutsos, Lev S Bishop, Jerry M Chow, Andrew Cross, Daniel J Egger, Stefan Filipp, Andreas Fuhrer, Jay M Gambetta, Marc Ganzhorn, et al. "Quantum optimization using variational algorithms on near-term quantum devices". In: *Quantum Sci. Technol.* 3.3 (2018), p. 030503. DOI: 10.1088/2058-9565/aab822.

[61] Alexander J McCaskey, Zachary P Parks, Jacek Jakowski, Shirley V Moore, Titus D Morris, Travis S Humble, and Raphael C Pooser. "Quantum chemistry as a benchmark for near-term quantum computers". In: *npj Quantum Inf* 5.1 (2019), pp. 1–8. DOI: 10.1038/s41534-019-0209-0.

[62] Google AI Quantum, Collaborators*†, Frank Arute, Kunal Arya, Ryan Babbush, Dave Bacon, Joseph C Bardin, Rami Barends, Sergio Boixo, Michael Broughton, Bob B Buckley, et al. "Hartree-Fock on a superconducting qubit quantum computer". In: *Science* 369.6507 (2020), pp. 1084–1089. DOI: 10.1126/science.abb9811.

[63] Nathan Lacroix, Christoph Hellings, Christian Kraglund Andersen, Agustin Di Paolo, Ants Remm, Stefania Lazar, Sebastian Krinner, Graham J Norris, Mihai Gabureac, Johannes Heinsoo, et al. "Improving the performance of deep quantum optimization algorithms with continuous gate sets". In: *PRX Quantum* 1.2 (2020), p. 110304. DOI: 10.1103/PRXQuantum.1.020304.

[64] Mario Motta, Gavin O Jones, Julia E Rice, Tanvi P Gujarati, Rei Sakuma, Ieva Liepuoniute, Jeannette M Garcia, and Yu-ya Ohnishi. "Quantum chemistry simulation of ground-and excited-state properties of the sulfonium cation on a superconducting quantum processor". In: *arXiv preprint arXiv:2208.02414* (2022). DOI: 10.48550/arXiv.2208.02414.

[65] Jacob Biamonte, Peter Wittek, Nicola Pancotti, Patrick Rebentrost, Nathan Wiebe, and Seth Lloyd. "Quantum machine learning". In: *Nature* 549.7671 (2017), pp. 195–202. DOI: 10.1038/nature23474.

[66] Andrew A Houck, Jens Koch, Michel H Devoret, Steven M Girvin, and Robert J Schoelkopf. "Life after charge noise: recent results with transmon qubits". In: *Quantum Inf. Process.* 8.2 (2009), pp. 105–115. DOI: 10.1007/s11128-009-0100-6.

[67] Brian D. Josephson. "Possible new effects in superconductive tunnelling". In: *Phys. Lett.* 1.7 (1962), pp. 251–253. DOI: 10.1016/0031-9163(62)91369-0.

[68] Brian D. Josephson. "The discovery of tunnelling supercurrents". In: *Rev. Mod. Phys.* 46.2 (1974), p. 251. DOI: 10.1103/RevModPhys.46.251.

[69] Jens Koch, M Yu Terri, Jay Gambetta, Andrew A Houck, David I Schuster, Johannes Majer, Alexandre Blais, Michel H Devoret, Steven M Girvin, and Robert J Schoelkopf. "Charge-insensitive qubit design derived from the Cooper pair box". In: *Phys. Rev. A* 76.4 (2007), p. 042319. DOI: 10.1103/PhysRevA.76.042319.

[70] Maxime A Tremblay, Nicolas Delfosse, and Michael E Beverland. "Constant-overhead quantum error correction with thin planar connectivity". In: *Phys. Rev. Lett.* 129.5 (2022), p. 050504. DOI: 10.1103/PhysRevLett.129.050504.

[71] Daniel Gottesman. "Fault-tolerant quantum computation with constant overhead". In: *arXiv preprint arXiv:1310.2984* (2013). DOI: 10.48550/arXiv.1310.2984.

[72] Sergey Bravyi, David Poulin, and Barbara Terhal. "Tradeoffs for reliable quantum information storage in 2D systems". In: *Phys. Rev. Lett.* 104.5 (2010), p. 050503. DOI: 10.1103/PhysRevLett.104.050503.

[73] Nouédyn Baspin and Anirudh Krishna. "Quantifying nonlocality: How outperforming local quantum codes is expensive". In: *Phys. Rev. Lett.* 129.5 (2022), p. 050505. DOI: 10.1103/PhysRevLett.129.050505.

[74] Lawrence Z Cohen, Isaac H Kim, Stephen D Bartlett, and Benjamin J Brown. "Low-overhead fault-tolerant quantum computing using long-range connectivity". In: *Sci. Adv.* 8.20 (2022), eabn1717. DOI: 10.1126/sciadv.abn1717.

[75] I. M. Georgescu, S. Ashhab, and Franco Nori. "Quantum simulation". In: *Rev. Mod. Phys.* 86.1 (2014), pp. 153–185. ISSN: 0034-6861. DOI: 10.1103/revmodphys.86.153.

[76] Bela Bauer, Sergey Bravyi, Mario Motta, and Garnet Kin-Lic Chan. "Quantum algorithms for quantum chemistry and quantum materials science". In: *Chem. Rev.* 120.22 (2020), pp. 12685–12717. DOI: 10.1021/acs.chemrev.9b00829.

[77] Rami Barends, L Lamata, Julian Kelly, L Garcıa-Álvarez, Austin G Fowler, A Megrant, Evan Jeffrey, Ted C White, Daniel Sank, Josh Y Mutus, et al. "Digital quantum simulation of fermionic models with a superconducting circuit". In: *Nat. Commun.* 6.1 (2015), pp. 1–7. DOI: 10.1038/ncomms8654.

[78] Pascual Jordan and Eugene Paul Wigner. *Über das paulische äquivalenzverbot*. Springer, 1993.

[79] Philipp Hauke and Luca Tagliacozzo. "Spread of correlations in long-range interacting quantum systems". In: *Phys. Rev. Lett.* 111.20 (2013), p. 207202. DOI: 10.1103/PhysRevLett.111.207202.

[80] Johannes Jünemann, Andrea Cadarso, David Pérez-Garcıa, Alejandro Bermudez, and Juan José Garcıa-Ripoll. "Lieb-Robinson bounds for spin-boson lattice models and trapped ions". In: *Phys. Rev. Lett.* 111.23 (2013), p. 230404. DOI: 10.1103/PhysRevLett.111.230404.

[81] Zhe-Xuan Gong, Michael Foss-Feig, Spyridon Michalakis, and Alexey V Gorshkov. "Persistence of locality in systems with power-law interactions". In: *Phys. Rev. Lett.* 113.3 (2014), p. 030602. DOI: 10.1103/PhysRevLett.113.030602.

[82] Michael Foss-Feig, Zhe-Xuan Gong, Charles W Clark, and Alexey V Gorshkov. "Nearly linear light cones in long-range interacting quantum systems". In: *Phys. Rev. Lett.* 114.15 (2015), p. 157201. DOI: 10.1103/PhysRevLett.114.157201.

[83] Kristian Baumann, Christine Guerlin, Ferdinand Brennecke, and Tilman Esslinger. "Dicke quantum phase transition with a superfluid gas in an optical cavity". In: *Nature* 464.7293 (2010), pp. 1301–1306. DOI: 10.1038/nature09009.

[84] Anders W Sandvik. "Ground states of a frustrated quantum spin chain with long-range interactions". In: *Phys. Rev. Lett.* 104.13 (2010), p. 137204. DOI: 10.1103/PhysRevLett.104.137204.

[85] Rafael Mottl, Ferdinand Brennecke, Kristian Baumann, Renate Landig, T Donner, and Tilman Esslinger. "Roton-type mode softening in a quantum gas with cavity-mediated long-range interactions". In: *Science* 336.6088 (2012), pp. 1570–1573. DOI: 10.1126/science.1220314.

[86] R Islam, Crystal Senko, Wes C Campbell, S Korenblit, J Smith, A Lee, EE Edwards, C-CJ Wang, JK Freericks, and C Monroe. "Emergence and frustration of magnetism with variable-range interactions in a quantum simulator". In: *Science* 340.6132 (2013), pp. 583–587. DOI: 10.1126/science.1232296.

[87] Z-X Gong, Mohammad F Maghrebi, Anzi Hu, Michael L Wall, Michael Foss-Feig, and Alexey V Gorshkov. "Topological phases with long-range interactions". In: *Phys. Rev. B* 93.4 (2016), p. 041102. DOI: 10.1103/PhysRevB.93.041102.

[88] Z-X Gong, Mohammad F Maghrebi, Anzi Hu, Michael Foss-Feig, Phillip Richerme, Christopher Monroe, and Alexey V Gorshkov. "Kaleidoscope of quantum phases in a long-range interacting spin-1 chain". In: *Phys. Rev. B* 93.20 (2016), p. 205115. DOI: 10.1103/PhysRevB.93.205115.

[89] Mohammad F Maghrebi, Zhe-Xuan Gong, and Alexey V Gorshkov. "Continuous symmetry breaking in 1D long-range interacting quantum systems". In: *Phys. Rev. Lett.* 119.2 (2017), p. 023001. DOI: 10.1103/PhysRevLett.119.023001.

[90] Bojan Žunkovič, Markus Heyl, Michael Knap, and Alessandro Silva. "Dynamical quantum phase transitions in spin chains with long-range interactions: Merging different concepts of nonequilibrium criticality". In: *Phys. Rev. Lett.* 120.13 (2018), p. 130601. DOI: 10.1103/PhysRevLett.120.130601.

[91] Giulia Semeghini, Harry Levine, Alexander Keesling, Sepehr Ebadi, Tout T Wang, Dolev Bluvstein, Ruben Verresen, Hannes Pichler, Marcin Kalinowski, Rhine Samajdar, et al. "Probing topological spin liquids on a programmable quantum simulator". In: *Science* 374.6572 (2021), pp. 1242–1247. DOI: 10.1126/science.abi8794.

[92] Nishad Maskara, Abhinav Deshpande, Adam Ehrenberg, Minh C Tran, Bill Fefferman, and Alexey V Gorshkov. "Complexity phase diagram for interacting and long-range bosonic Hamiltonians". In: *Phys. Rev. Lett.* 129.15 (2022), p. 150604. DOI: 10.1103/PhysRevLett.129.150604.

[93] Claude Cohen-Tannoudji, Jacques Dupont-Roc, and Gilbert Grynberg. *Atom-photon interactions: basic processes and applications*. John Wiley & Sons, 1998.

[94] Serge Haroche and J-M Raimond. *Exploring the quantum: atoms, cavities, and photons*. Oxford University Press, 2006.

[95] Hermann Haken. "Laser theory". In: *Light and Matter Ic/Licht und Materie Ic*. Springer, 1970, pp. 1–304.

[96] Martin C Fischer, Jesse W Wilson, Francisco E Robles, and Warren S Warren. "Invited review article: pump-probe microscopy". In: *Rev. Sci. Instrum.* 87.3 (2016), p. 031101. DOI: 10.1063/1.4943211.

[97] Serge Haroche. "Nobel Lecture: Controlling photons in a box and exploring the quantum to classical boundary". In: *Rev. Mod. Phys.* 85.3 (2013), p. 1083. DOI: 10.1103/RevModPhys.85.1083.

[98] G Rempe, RJ Thompson, H Jeffrey Kimble, and Ramin Lalezari. "Measurement of ultralow losses in an optical interferometer". In: *Opt. Lett.* 17.5 (1992), pp. 363–365. DOI: 10.1364/OL.17.000363.

[99] Takao Aoki, Barak Dayan, Elizabeth Wilcut, Warwick P Bowen, A Scott Parkins, TJ Kippenberg, KJ Vahala, and HJ Kimble. "Observation of strong coupling between one atom and a monolithic microresonator". In: *Nature* 443.7112 (2006), pp. 671–674. DOI: 10.1038/nature05147.

[100] Edward Mills Purcell. "Spontaneous emission probabilities at radio frequencies". In: *Confined Electrons and Photons*. Springer, 1995, pp. 839–839.

[101] H Jeff Kimble. "The quantum internet". In: *Nature* 453.7198 (2008), pp. 1023–1030. DOI: 10.1038/nature07127.

[102] Philip Thomas, Leonardo Ruscio, Olivier Morin, and Gerhard Rempe. "Efficient generation of entangled multiphoton graph states from a single atom". In: *Nature* 608.7924 (2022), pp. 677–681. DOI: 10.1038/s41586-022-04987-5.

[103] Christian L Degen, Friedemann Reinhard, and Paola Cappellaro. "Quantum sensing". In: *Rev. Mod. Phys.* 89.3 (2017), p. 035002. DOI: 10.1103/RevModPhys.89.035002.

[104] Vittorio Giovannetti, Seth Lloyd, and Lorenzo Maccone. "Advances in quantum metrology". In: *Nat. Photon* 5.4 (2011), pp. 222–229. DOI: 10.1038/nphoton.2011.35.

[105] Andreas Wallraff, David I Schuster, Alexandre Blais, Luigi Frunzio, Johannes Majer, Michel H Devoret, Steven M Girvin, and Robert J Schoelkopf. "Approaching unit visibility for control of a superconducting qubit with dispersive readout". In: *Phys. Rev. Lett.* 95.6 (2005), p. 060501. DOI: 10.1103/PhysRevLett.95.060501.

[106] D. I. Schuster, A. A. Houck, J. A. Schreier, A. Wallraff, J. M. Gambetta, A. Blais, L. Frunzio, J. Majer, B. Johnson, M. H. Devoret, et al. "Resolving photon number states in a superconducting circuit". In: *Nature* 445.7127 (2007), pp. 515–518. DOI: 10.1038/nature05461.

[107] Wen-Long Ma, Shruti Puri, Robert J Schoelkopf, Michel H Devoret, Steven M Girvin, and Liang Jiang. "Quantum control of bosonic modes with superconducting circuits". In: *Sci. Bull.* 66.17 (2021), pp. 1789–1805. DOI: 10.1016/j.scib.2021.05.024.

[108] Chao Song, Kai Xu, Wuxin Liu, Chui-ping Yang, Shi-Biao Zheng, Hui Deng, Qiwei Xie, Keqiang Huang, Qiujiang Guo, Libo Zhang, et al. "10-qubit entanglement and parallel logic operations with a superconducting circuit". In: *Phys. Rev. Lett.* 119.18 (2017), p. 180511. DOI: 10.1103/PhysRevLett.119.180511.

[109] Chao Song, Shi-Biao Zheng, Pengfei Zhang, Kai Xu, Libo Zhang, Qiujiang Guo, Wuxin Liu, Da Xu, Hui Deng, Keqiang Huang, et al. "Continuous-variable geometric phase and its manipulation for quantum computation in a superconducting circuit". In: *Nat. Commun.* 8.1 (2017), pp. 1–7. DOI: 10.1038/s41467-017-01156-5.

[110] Kai Xu, Jin-Jun Chen, Yu Zeng, Yu-Ran Zhang, Chao Song, Wuxin Liu, Qiujiang Guo, Pengfei Zhang, Da Xu, Hui Deng, et al. "Emulating many-body localization with a superconducting quantum processor". In: *Phys. Rev. Lett.* 120.5 (2018), p. 050507. DOI: 10.1103/PhysRevLett.120.050507.

[111] Qiujiang Guo, Chen Cheng, Zheng-Hang Sun, Zixuan Song, Hekang Li, Zhen Wang, Wenhui Ren, Hang Dong, Dongning Zheng, Yu-Ran Zhang, et al. "Observation of energy-resolved many-body localization". In: *Nat. Phys.* 17.2 (2021), pp. 234–239. DOI: 10.1038/s41567-020-1035-1.

[112] Kai Xu, Zheng-Hang Sun, Wuxin Liu, Yu-Ran Zhang, Hekang Li, Hang Dong, Wenhui Ren, Pengfei Zhang, Franco Nori, Dongning Zheng, et al. "Probing dynamical phase transitions with a superconducting quantum simulator". In: *Sci. Adv.* 6.25 (2020), eaba4935. DOI: 10.1126/sciadv.aba4935.

[113] Alexandra S Sheremet, Mihail I Petrov, Ivan V Iorsh, Alexander V Poshakinskiy, and Alexander N Poddubny. "Waveguide quantum electrodynamics: collective radiance and photon-photon correlations". In: *arXiv preprint arXiv:2103.06824* (2021). DOI: 10.48550/arXiv.2103.06824.

[114] AV Akimov, A Mukherjee, CL Yu, DE Chang, AS Zibrov, PR Hemmer, H Park, and MD Lukin. "Generation of single optical plasmons in metallic nanowires coupled to quantum dots". In: *Nature* 450.7168 (2007), pp. 402–406. DOI: 10.1038/nature06230.

[115] Peter Lodahl, Sahand Mahmoodian, and Søren Stobbe. "Interfacing single photons and single quantum dots with photonic nanostructures". In: *Rev. Mod. Phys.* 87.2 (2015), p. 347. DOI: 10.1103/RevModPhys.87.347.

[116] A Goban, C-L Hung, JD Hood, S-P Yu, JA Muniz, O Painter, and HJ Kimble. "Superradiance for atoms trapped along a photonic crystal waveguide". In: *Phys. Rev. Lett.* 115.6 (2015), p. 063601.

[117] E Vetsch, D Reitz, G Sagué, R Schmidt, ST Dawkins, and A Rauschenbeutel. "Optical interface created by laser-cooled atoms trapped in the evanescent field surrounding an optical nanofiber". In: *Phys. Rev. Lett.* 104.20 (2010), p. 203603. DOI: 10.1103/PhysRevLett.104.203603.

[118] O Astafiev, Alexandre M Zagoskin, AA Abdumalikov Jr, Yu A Pashkin, T Yamamoto, K Inomata, Y Nakamura, and Jaw Shen Tsai. "Resonance fluorescence of a single artificial atom". In: *Science* 327.5967 (2010), pp. 840–843. DOI: 10.1126/science.1181918.

[119] Xiu Gu, Anton Frisk Kockum, Adam Miranowicz, Yu-xi Liu, and Franco Nori. "Microwave photonics with superconducting quantum circuits". In: *Phys. Rep.* 718 (2017), pp. 1–102. DOI: 10.1016/j.physrep.2017.10.002.

[120] Yanbing Liu and Andrew A Houck. "Quantum electrodynamics near a photonic bandgap". In: *Nat. Phys.* 13.1 (2017), pp. 48–52. DOI: 10.1038/nphys3834.

[121] Alp Sipahigil, Ruffin E Evans, Denis D Sukachev, Michael J Burek, Johannes Borregaard, Mihir K Bhaskar, Christian T Nguyen, Jose L Pacheco, Haig A Atikian, Charles Meuwly, et al. "An integrated diamond nanophotonics platform for quantum-optical networks". In: *Science* 354.6314 (2016), pp. 847–850. DOI: 10.1126/science.aah6875.

[122] Darrick E Chang, Anders S Sørensen, Eugene A Demler, and Mikhail D Lukin. "A single-photon transistor using nanoscale surface plasmons". In: *Nat. Phys.* 3.11 (2007), pp. 807–812. DOI: 10.1038/nphys708.

[123] P Forn-Dıaz, J José Garcıa-Ripoll, Borja Peropadre, J-L Orgiazzi, MA Yurtalan, R Belyansky, Christopher M Wilson, and A Lupascu. "Ultrastrong coupling of a single artificial atom to an electromagnetic continuum in the nonperturbative regime". In: *Nat. Phys.* 13.1 (2017), pp. 39–43. DOI: 10.1038/nphys3905.

[124] Toke Lund-Hansen, Søren Stobbe, Brian Julsgaard, H Thyrrestrup, T Sünner, M Kamp, A Forchel, and Peter Lodahl. "Experimental realization of highly efficient broadband coupling of single quantum dots to a photonic crystal waveguide". In: *Phys. Rev. Lett.* 101.11 (2008), p. 113903. DOI: 10.1103/PhysRevLett.101.113903.

[125] D Roy, C M Wilson, and O Firstenberg. "Colloquium: Strongly interacting photons in one-dimensional continuum". In: *Rev. Mod. Phys.* 89.2 (2017), p. 021001. DOI: 10.1103/RevModPhys.89.021001.

[126] Jean-Claude Besse, Kevin Reuer, Michele C Collodo, Arne Wulff, Lucien Wernli, Adrian Copetudo, Daniel Malz, Paul Magnard, Abdulkadir Akin, Mihai Gabureac, et al. "Realizing a deterministic source of multipartite-entangled photonic qubits". In: *Nat. Commun.* 11.1 (2020), pp. 1–6. DOI: 10.1038/s41467-020-18635-x.

[127] Vinicius S Ferreira, Gihwan Kim, Andreas Butler, Hannes Pichler, and Oskar Painter. "Deterministic Generation of Multidimensional Photonic Cluster States with a Single Quantum Emitter". In: *arXiv preprint arXiv:2206.10076* (2022). DOI: 10.48550/arXiv.2206.10076.

[128] Hans J Briegel, David E Browne, Wolfgang Dür, Robert Raussendorf, and Maarten Van den Nest. "Measurement-based quantum computation". In: *Nat. Phys.* 5.1 (2009), pp. 19–26. DOI: 10.1038/nphys1157.

[129] Vanessa Paulisch, HJ Kimble, and Alejandro González-Tudela. "Universal quantum computation in waveguide QED using decoherence free subspaces". In: *New J. Phys.* 18.4 (2016), p. 043041. DOI: 10.1088/1367-2630/18/4/043041.

[130] DE Chang, JS Douglas, Alejandro González-Tudela, C-L Hung, and HJ Kimble. "Colloquium: Quantum matter built from nanoscopic lattices of atoms and photons". In: *Rev. Mod. Phys.* 90.3 (2018), p. 031002. DOI: 10.1103/RevModPhys.90.031002.

[131] Eunjong Kim, Xueyue Zhang, Vinicius S Ferreira, Jash Banker, Joseph K Iverson, Alp Sipahigil, Miguel Bello, Alejandro González-Tudela, Mohammad Mirhosseini, and Oskar Painter. "Quantum electrodynamics in a topological waveguide". In: *Phys. Rev. X* 11.1 (2021), p. 011015. DOI: 10.1103/PhysRevX.11.011015.

[132] Xueyue Zhang, Eunjong Kim, Daniel K Mark, Soonwon Choi, and Oskar Painter. "A superconducting quantum simulator based on a photonic-bandgap metamaterial". In: *Science* 379.6629 (2023), pp. 278–283. DOI: 10.1126/science.ade7651.

[133] Eun Jong Kim. "Waveguide Quantum Electrodynamics in Superconducting Circuits". PhD thesis. California Institute of Technology, 2022.

[134] Enrico Fermi. *Nuclear physics: a course given by Enrico Fermi at the University of Chicago*. University of Chicago Press, 1950.

[135] David J Griffiths. *Introduction to electrodynamics*. 2005.

[136] Robert H Dicke. "Coherence in spontaneous radiation processes". In: *Phys. Rev.* 93.1 (1954), p. 99. DOI: 10.1103/PhysRev.93.99.

[137] Jung-tsung Shen and Shanhui Fan. "Coherent photon transport from spontaneous emission in one-dimensional waveguides". In: *Opt. Lett.* 30.15 (2005), pp. 2001–2003. DOI: 10.1364/OL.30.002001.

[138] Jung-Tsung Shen and Shanhui Fan. "Coherent single photon transport in a one-dimensional waveguide coupled with superconducting quantum bits". In: *Phys. Rev. Lett.* 95.21 (2005), p. 213001. DOI: 10.1103/PhysRevLett.95.213001.

[139] Darrick E Chang, L Jiang, AV Gorshkov, and HJ Kimble. "Cavity QED with atomic mirrors". In: *New J. Phys.* 14.6 (2012), p. 063003. DOI: 10.1088/1367-2630/14/6/063003.

[140] Jung-Tsung Shen and Shanhui Fan. "Strongly correlated two-photon transport in a one-dimensional waveguide coupled to a two-level system". In: *Phys. Rev. Lett.* 98.15 (2007), p. 153003. DOI: 10.1103/PhysRevLett.98.153003.

[141] Jung-Tsung Shen and Shanhui Fan. "Strongly correlated multiparticle transport in one dimension through a quantum impurity". In: *Phys. Rev. A* 76.6 (2007), p. 062709. DOI: 10.1103/PhysRevA.76.062709.

[142] Huaixiu Zheng and Harold U Baranger. “Persistent quantum beats and long-distance entanglement from waveguide-mediated interactions”. In: *Phys. Rev. Lett.* 110.11 (2013), p. 113601. DOI: 10.1103/PhysRevLett.110.113601.

[143] Alejandro González-Tudela and J Ignacio Cirac. “Markovian and non-Markovian dynamics of quantum emitters coupled to two-dimensional structured reservoirs”. In: *Phys. Rev. A* 96.4 (2017), p. 043811. DOI: 10.1103/PhysRevA.96.043811.

[144] Vinicius S Ferreira, Jash Banker, Alp Sipahigil, Matthew H Matheny, Andrew J Keller, Eunjong Kim, Mohammad Mirhosseini, and Oskar Painter. “Collapse and revival of an artificial atom coupled to a structured photonic reservoir”. In: *Phys. Rev. X* 11.4 (2021), p. 041043. DOI: 10.1103/PhysRevX.11.041043.

[145] Kevin Lalumiere, Barry C Sanders, Arjan F van Loo, Arkady Fedorov, Andreas Wallraff, and Alexandre Blais. “Input-output theory for waveguide QED with an ensemble of inhomogeneous atoms”. In: *Phys. Rev. A* 88.4 (2013), p. 043806. DOI: 10.1103/PhysRevA.88.043806.

[146] Andreas Albrecht, Loıc Henriet, Ana Asenjo-Garcia, Paul B Dieterle, Oskar Painter, and Darrick E Chang. “Subradiant states of quantum bits coupled to a one-dimensional waveguide”. In: *New J. Phys.* 21.2 (2019), p. 025003. DOI: 10.1088/1367-2630/ab0134.

[147] David Dzsotjan, Anders S Sørensen, and Michael Fleischhauer. “Quantum emitters coupled to surface plasmons of a nanowire: A Green’s function approach”. In: *Phys. Rev. B* 82.7 (2010), p. 075427. DOI: 10.1103/PhysRevB.82.075427.

[148] A Asenjo-Garcia, J D Hood, D E Chang, and H J Kimble. “Atom-light interactions in quasi-one-dimensional nanostructures: A Green’s-function perspective”. In: *Phys. Rev. A* 95.3 (Mar. 2017), p. 033818. DOI: 10.1103/PhysRevA.95.033818.

[149] Arjan F Van Loo, Arkady Fedorov, Kevin Lalumiere, Barry C Sanders, Alexandre Blais, and Andreas Wallraff. “Photon-mediated interactions between distant artificial atoms”. In: *Science* 342.6165 (2013), pp. 1494–1496. DOI: 10.1126/science.1244324.

[150] Anton Frisk Kockum. “Quantum optics with giant atoms—the first five years”. In: *International Symposium on Mathematics, Quantum Theory, and Cryptography*. Springer Singapore. 2021, pp. 125–146. DOI: 10.1007/978-981-15-5191-8_12.

[151] Bharath Kannan, Max J Ruckriegel, Daniel L Campbell, Anton Frisk Kockum, Jochen Braumüller, David K Kim, Morten Kjaergaard, Philip Krantz, Alexander Melville, Bethany M Niedzielski, et al. “Waveguide quantum electrody-

namics with superconducting artificial giant atoms". In: *Nature* 583.7818 (2020), pp. 775–779. DOI: 10.1038/s41586-020-2529-9.

[152] Peter Lodahl, Sahand Mahmoodian, Søren Stobbe, Arno Rauschenbeutel, Philipp Schneeweiss, Jürgen Volz, Hannes Pichler, and Peter Zoller. "Chiral quantum optics". In: *Nature* 541.7638 (2017), pp. 473–480. DOI: 10.1038/nature21037.

[153] Immo Söllner, Sahand Mahmoodian, Sofie Lindskov Hansen, Leonardo Midolo, Alisa Javadi, Gabija Kiršanskė, Tommaso Pregnolato, Haitham El-Ella, Eun Hye Lee, Jin Dong Song, et al. "Deterministic photon–emitter coupling in chiral photonic circuits". In: *Nature Nanotech.* 10.9 (2015), pp. 775–778. DOI: 10.1038/nnano.2015.159.

[154] John D Joannopoulos, Pierre R Villeneuve, and Shanhui Fan. "Photonic crystals". In: *Solid State Commun.* 102.2-3 (1997), pp. 165–173. DOI: 10.1016/S0038-1098(96)00716-8.

[155] Yongmin Liu and Xiang Zhang. "Metamaterials: a new frontier of science and technology". In: *Chem. Soc. Rev.* 40.5 (2011), pp. 2494–2507. DOI: 10.1039/C0CS00184H.

[156] Sajeev John and Jian Wang. "Quantum electrodynamics near a photonic band gap: Photon bound states and dressed atoms". In: *Phys. Rev. Lett.* 64.20 (1990), p. 2418. DOI: 10.1103/PhysRevLett.64.2418.

[157] Giuseppe Calajó, Francesco Ciccarello, Darrick Chang, and Peter Rabl. "Atom-field dressed states in slow-light waveguide QED". In: *Phys. Rev. A* 93.3 (2016), p. 033833. DOI: 10.1103/PhysRevA.93.033833.

[158] James S Douglas, Hessam Habibian, C-L Hung, Alexey V Gorshkov, H Jeff Kimble, and Darrick E Chang. "Quantum many-body models with cold atoms coupled to photonic crystals". In: *Nature Photon.* 9.5 (2015), pp. 326–331. DOI: 10.1038/nphoton.2015.57.

[159] Miguel Bello, Gloria Platero, and Alejandro González-Tudela. "Spin Many-Body Phases in Standard-and Topological-Waveguide QED Simulators". In: *PRX Quantum* 3.1 (2022), p. 010336. DOI: 10.1103/PRXQuantum.3.010336.

[160] C-L Hung, Alejandro González-Tudela, J Ignacio Cirac, and HJ Kimble. "Quantum spin dynamics with pairwise-tunable, long-range interactions". In: *PNAS* 113.34 (2016), E4946–E4955. DOI: 10.1073/pnas.1603777113.

[161] Tao Shi, Ying-Hai Wu, Alejandro González-Tudela, and J Ignacio Cirac. "Bound states in boson impurity models". In: *Phys. Rev. X* 6.2 (2016), p. 021027. DOI: 10.1103/PhysRevX.6.021027.

[162] Tao Shi, Ying Hai Wu, Alejandro González-Tudela, and J Ignacio Cirac. "Effective many-body Hamiltonians of qubit-photon bound states". In: *New J. Phys.* 20.10 (2018), p. 105005. DOI: 10.1088/1367-2630/aae4a9.

[163] Neereja M Sundaresan, Rex Lundgren, Guanyu Zhu, Alexey V Gorshkov, and Andrew A Houck. "Interacting qubit-photon bound states with superconducting circuits". In: *Phys. Rev. X* 9.1 (2019), p. 011021. DOI: 10.1103/PhysRevX.9.011021.

[164] Miguel Bello, Gloria Platero, Juan Ignacio Cirac, and Alejandro González-Tudela. "Unconventional quantum optics in topological waveguide QED". In: *Sci. Adv.* 5.7 (2019), eaaw0297. DOI: 10.1126/sciadv.aaw0297.

[165] Andrés Rosario Hamann, Clemens Müller, Markus Jerger, Maximilian Zanner, Joshua Combes, Mikhail Pletyukhov, Martin Weides, Thomas M Stace, and Arkady Fedorov. "Nonreciprocity realized with quantum nonlinearity". In: *Phys. Rev. Lett.* 121.12 (2018), p. 123601. DOI: 10.1103/PhysRevLett.121.123601.

[166] Yvonne Y Gao, M Adriaan Rol, Steven Touzard, and Chen Wang. "Practical guide for building superconducting quantum devices". In: *PRX Quantum* 2.4 (2021), p. 040202. DOI: 10.1103/PRXQuantum.2.040202.

[167] Alexandre Blais, Arne L Grimsmo, Steven M Girvin, and Andreas Wallraff. "Circuit quantum electrodynamics". In: *Rev. Mod. Phys.* 93.2 (2021), p. 025005. DOI: 10.1103/RevModPhys.93.025005.

[168] Philip Krantz, Morten Kjaergaard, Fei Yan, Terry P Orlando, Simon Gustavsson, and William D Oliver. "A quantum engineer's guide to superconducting qubits". In: *App. Phys. Rev.* 6.2 (2019), p. 021318. DOI: 10.1063/1.5089550.

[169] Rami Barends, Julian Kelly, Anthony Megrant, Daniel Sank, Evan Jeffrey, Yu Chen, Yi Yin, Ben Chiaro, Josh Mutus, Charles Neill, et al. "Coherent Josephson qubit suitable for scalable quantum integrated circuits". In: *Phys. Rev. Lett.* 111.8 (2013), p. 080502. DOI: 10.1103/PhysRevLett.111.080502.

[170] N Leung, Y Lu, S Chakram, RK Naik, N Earnest, R Ma, K Jacobs, AN Cleland, and DI Schuster. "Deterministic bidirectional communication and remote entanglement generation between superconducting qubits". In: *npj Quantum Inf* 5.1 (2019), pp. 1–5. DOI: 10.1038/s41534-019-0128-0.

[171] David M Pozar. *Microwave engineering*. John wiley & sons, 2011.

[172] Mohammad Mirhosseini, Eunjong Kim, Vinicius S Ferreira, Mahmoud Kalaee, Alp Sipahigil, Andrew J Keller, and Oskar Painter. "Superconducting metamaterials for waveguide quantum electrodynamics". In: *Nature Commun* 9.1 (2018), pp. 1–7. DOI: 10.1038/s41467-018-06142-z.

[173] Kevin O'Brien, Chris Macklin, Irfan Siddiqi, and Xiang Zhang. "Resonant phase matching of Josephson junction traveling wave parametric amplifiers". In: *Phys. Rev. Lett.* 113.15 (2014), p. 157001. DOI: 10.1103/PhysRevLett.113.157001.

[174] Chris Macklin, K O'brien, D Hover, ME Schwartz, V Bolkhovsky, X Zhang, WD Oliver, and I Siddiqi. "A near–quantum-limited Josephson traveling-wave parametric amplifier". In: *Science* 350.6258 (2015), pp. 307–310. DOI: 10.1126/science.aaa8525.

[175] Daniel T. Sank. "Fast, Accurate State Measurement in Superconducting Qubits". PhD thesis. University of California, Santa Barbara, 2014.

[176] Sebastian Krinner, Simon Storz, Philipp Kurpiers, Paul Magnard, Johannes Heinsoo, Raphael Keller, Janis Luetolf, Christopher Eichler, and Andreas Wallraff. "Engineering cryogenic setups for 100-qubit scale superconducting circuit systems". In: *EPJ Quantum Technol.* 6.1 (2019), p. 2. DOI: 10.1140/epjqt/s40507-019-0072-0.

[177] Jen-Hao Yeh, Jay LeFebvre, Shavindra Premaratne, FC Wellstood, and BS Palmer. "Microwave attenuators for use with quantum devices below 100 mK". In: *J. Appl. Phys.* 121.22 (2017), p. 224501. DOI: 10.1063/1.4984894.

[178] Jen-Hao Yeh, Yizhou Huang, Rui Zhang, Shavindra Premaratne, Jay LeFebvre, FC Wellstood, and BS Palmer. "Hot electron heatsinks for microwave attenuators below 100 mK". In: *Appl. Phys. Lett.* 114.15 (2019), p. 152602. DOI: 10.1063/1.5097369.

[179] Z Wang, S Shankar, ZK Minev, P Campagne-Ibarcq, A Narla, and Michel H Devoret. "Cavity attenuators for superconducting qubits". In: *Phys. Rev. Applied* 11.1 (2019), p. 014031. DOI: 10.1103/PhysRevApplied.11.014031.

[180] Henry W Ott. *Electromagnetic compatibility engineering*. John Wiley & Sons, 2011.

[181] Julian Kelly, Peter O'Malley, Matthew Neeley, Hartmut Neven, and John M Martinis. "Physical qubit calibration on a directed acyclic graph". In: *arXiv preprint arXiv:1803.03226* (2018). DOI: 10.48550/arXiv.1803.03226.

[182] M Gross and S Haroche. "Superradiance: An essay on the theory of collective spontaneous emission". In: *Phys. Rep.* 93.5 (Dec. 1982), pp. 301–396. DOI: 10.1016/0370-1573(82)90102-8. URL: https://doi.org/10.1016/0370-1573(82)90102-8.

[183] S Osnaghi, P Bertet, A Auffeves, P Maioli, M Brune, J M Raimond, and S Haroche. "Coherent Control of an Atomic Collision in a Cavity". In: *Phys. Rev. Lett.* 87.3 (June 2001), p. 037902. DOI: 10.1103/PhysRevLett.87.037902.

[184] J Majer et al. "Coupling superconducting qubits via a cavity bus". In: *Nature* 449.7161 (Sept. 2007), pp. 443–447. DOI: 10.1038/nature06184.

[185] Ralf Röhlsberger, Kai Schlage, Balaram Sahoo, Sebastien Couet, and Rudolf Rüffer. "Collective Lamb Shift in Single-Photon Superradiance". In: *Science* 328.5983 (June 2010), pp. 1248–1251. DOI: 10.1126/science.1187770.

[186] Marlan O Scully. "Collective Lamb Shift in Single Photon Dicke Superradiance". In: *Phys. Rev. Lett.* 102.14 (Apr. 2009), p. 143601. DOI: 10.1103/PhysRevLett.102.143601. URL: https://link.aps.org/doi/10.1103/PhysRevLett.102.143601.

[187] Tomás Ramos, Hannes Pichler, Andrew J. Daley, and Peter Zoller. "Quantum Spin Dimers from Chiral Dissipation in Cold-Atom Chains". In: *Phys. Rev. Lett.* 113 (Dec. 2014), p. 237203. DOI: 10.1103/PhysRevLett.113.237203.

[188] Sahand Mahmoodian, Mantas Čepulkovskis, Sumanta Das, Peter Lodahl, Klemens Hammerer, and Anders S Sørensen. "Strongly correlated photon transport in waveguide quantum electrodynamics with weakly coupled emitters". In: *Phys. Rev. Lett.* 121.14 (2018), p. 143601. DOI: 10.1103/PhysRevLett.121.143601.

[189] A González-Tudela, V Paulisch, D E Chang, H J Kimble, and J I Cirac. "Deterministic Generation of Arbitrary Photonic States Assisted by Dissipation". In: *Phys. Rev. Lett.* 115.16 (Oct. 2015), p. 163603. DOI: 10.1103/PhysRevLett.115.163603.

[190] Anton Frisk Kockum, Göran Johansson, and Franco Nori. "Decoherence-Free Interaction between Giant Atoms in Waveguide Quantum Electrodynamics". In: *Phys. Rev. Lett.* 120.14 (2018). DOI: 10.1103/PhysRevLett.120.140404.

[191] Jonathan D Hood, Akihisa Goban, Ana Asenjo-Garcia, Mingwu Lu, Su-Peng Yu, Darrick E Chang, and HJ Kimble. "Atom–atom interactions around the band edge of a photonic crystal waveguide". In: *PNAS* 113.38 (2016), pp. 10507–10512. DOI: 10.1073/pnas.1603788113.

[192] Richard J Cook and H J Kimble. "Possibility of Direct Observation of Quantum Jumps". In: *Phys. Rev. Lett.* 54.10 (Mar. 1985), pp. 1023–1026. DOI: 10.1103/PhysRevLett.54.1023.

[193] Nicholas T Bronn, Vivekananda P Adiga, Salvatore B Olivadese, Xian Wu, Jerry M Chow, and David P Pappas. "High coherence plane breaking packaging for superconducting qubits". In: *Quantum Sci. Technol.* 3.2 (Apr. 2018), p. 024007. DOI: 10.1088/2058-9565/aaa645.

[194] Andrew J. Keller, Paul B. Dieterle, Michael Fang, Brett Berger, Johannes M. Fink, and Oskar Painter. "Al transmon qubits on silicon-on-insulator for quantum device integration". In: *Appl. Phys. Lett.* 111.4 (July 2017),

p. 042603. ISSN: 0003-6951. DOI: 10.1063/1.4994661. URL: http://aip.scitation.org/doi/10.1063/1.4994661.

[195] M. J. Rooks, E. Kratschmer, R. Viswanathan, J. Katine, R. E. Fontana, and S. A. MacDonald. "Low stress development of poly(methylmethacrylate) for high aspect ratio structures". In: *J. Vac. Sci. Technol. B* 20.6 (Dec. 2002), p. 2937. ISSN: 0734211X. DOI: 10.1116/1.1524971. URL: http://scitation.aip.org/content/avs/journal/jvstb/20/6/10.1116/1.1524971.

[196] Zijun Chen et al. "Fabrication and Characterization of Aluminum Airbridges for Superconducting Microwave Circuits". In: *Appl. Phys. Lett.* 104.5 (Oct. 2013), p. 052602. ISSN: 0003-6951. DOI: 10.1063/1.4863745. URL: http://aip.scitation.org/doi/10.1063/1.4863745.

[197] Ming-Dong Wu, Sheng-Ming Deng, Ruey-Beei Wu, and Powen Hsu. "Full-wave characterization of the mode conversion in a coplanar waveguide right-angled bend". In: *IEEE Trans. Microwave Theory Tech.* 43.11 (1995), pp. 2532–2538. ISSN: 00189480. DOI: 10.1109/22.473174. URL: http://ieeexplore.ieee.org/document/473174/.

[198] Klaus von Klitzing. "The quantized Hall effect". In: *Rev. Mod. Phys.* 58.3 (July 1986), pp. 519–531. ISSN: 0034-6861. DOI: 10.1103/RevModPhys.58.519.

[199] M. Z. Hasan and C. L. Kane. "Colloquium: Topological insulators". In: *Rev. Mod. Phys.* 82.4 (2010), pp. 3045–3067. ISSN: 0034-6861. DOI: 10.1103/revmodphys.82.3045.

[200] FDM Haldane and S Raghu. "Possible realization of directional optical waveguides in photonic crystals with broken time-reversal symmetry". In: *Phys. Rev. Lett.* 100.1 (2008), p. 013904. DOI: 10.1103/PhysRevLett.100.013904.

[201] Ling Lu, John D Joannopoulos, and Marin Soljačić. "Topological photonics". In: *Nat. Photonics* 8.11 (2014), pp. 821–829. DOI: 10.1038/nphoton.2014.248.

[202] Tomoki Ozawa, Hannah M Price, Alberto Amo, Nathan Goldman, Mohammad Hafezi, Ling Lu, Mikael C Rechtsman, David Schuster, Jonathan Simon, Oded Zilberberg, and Iacopo Carusotto. "Topological photonics". In: *Rev. Mod. Phys.* 91.1 (Jan. 2019), p. 015006. ISSN: 0034-6861. DOI: 10.1103/RevModPhys.91.015006.

[203] Xie Chen, Zheng-Cheng Gu, Zheng-Xin Liu, and Xiao-Gang Wen. "Symmetry protected topological orders and the group cohomology of their symmetry group". In: *Phys. Rev. B* 87.15 (2013), p. 155114. ISSN: 1098-0121. DOI: 10.1103/physrevb.87.155114.

[204] Daria Smirnova, Daniel Leykam, Yidong Chong, and Yuri Kivshar. "Nonlinear topological photonics". In: *Appl. Phys. Rev.* 7.2 (2020), p. 021306. DOI: 10.1063/1.5142397.

[205] W P Su, J R Schrieffer, and A J Heeger. "Solitons in Polyacetylene". In: *Phys. Rev. Lett.* 42.25 (1979), pp. 1698–1701. ISSN: 0031-9007. DOI: 10.1103/physrevlett.42.1698.

[206] János K. Asbóth, László Oroszlány, and András Pályi. *A Short Course on Topological Insulators*. Lecture Notes in Physics. Springer, 2016. DOI: 10.1007/978-3-319-25607-8.

[207] P. St-Jean, V. Goblot, E. Galopin, A. Lemaître, T. Ozawa, L. Le Gratiet, I. Sagnes, J. Bloch, and A. Amo. "Lasing in topological edge states of a one-dimensional lattice". In: *Nat. Photonics* 11.10 (2017), pp. 651–656. ISSN: 1749-4885. DOI: 10.1038/s41566-017-0006-2.

[208] Han Zhao, Pei Miao, Mohammad H. Teimourpour, Simon Malzard, Ramy El-Ganainy, Henning Schomerus, and Liang Feng. "Topological hybrid silicon microlasers". In: *Nat. Commun.* 9 (Mar. 2018), p. 981. DOI: 10.1038/s41467-018-03434-2.

[209] Yasutomo Ota, Ryota Katsumi, Katsuyuki Watanabe, Satoshi Iwamoto, and Yasuhiko Arakawa. "Topological photonic crystal nanocavity laser". In: *Commun. Phys.* 1 (Nov. 2018), p. 86. DOI: 10.1038/s42005-018-0083-7.

[210] Sergey Kruk, Alexander Poddubny, Daria Smirnova, Lei Wang, Alexey Slobozhanyuk, Alexander Shorokhov, Ivan Kravchenko, Barry Luther-Davies, and Yuri Kivshar. "Nonlinear light generation in topological nanostructures". In: *Nat. Nanotechnol.* 14 (Feb. 2019), pp. 126–130. DOI: 10.1038/s41565-018-0324-7.

[211] Iacopo Carusotto and Cristiano Ciuti. "Quantum fluids of light". In: *Rev. Mod. Phys.* 85.1 (2013), p. 299. DOI: 10.1103/RevModPhys.85.299.

[212] P. Roushan et al. "Chiral ground-state currents of interacting photons in a synthetic magnetic field". In: *Nat. Phys.* 13.2 (2017), p. 146. ISSN: 1745-2481. DOI: 10.1038/nphys3930.

[213] Brandon M. Anderson, Ruichao Ma, Clai Owens, David I. Schuster, and Jonathan Simon. "Engineering Topological Many-Body Materials in Microwave Cavity Arrays". In: *Phys. Rev. X* 6.4 (2016), p. 041043. ISSN: 2160-3308. DOI: 10.1103/physrevx.6.041043.

[214] Weizhou Cai, Jiaxiu Han, Feng Mei, Yuan Xu, Yuwei Ma, Xuegang Li, Haiyan Wang, YP Song, Zheng-Yuan Xue, Zhang-qi Yin, et al. "Observation of topological magnon insulator states in a superconducting circuit". In: *Phys. Rev. Lett.* 123.8 (2019), p. 080501. DOI: 10.1103/PhysRevLett.123.080501.

[215] Sylvain de Léséleuc, Vincent Lienhard, Pascal Scholl, Daniel Barredo, Sebastian Weber, Nicolai Lang, Hans Peter Büchler, Thierry Lahaye, and Antoine Browaeys. "Observation of a symmetry-protected topological phase of interacting bosons with Rydberg atoms". In: *Science* 365.6455 (2019), pp. 775–780. ISSN: 0036-8075. DOI: 10.1126/science.aav9105.

[216] Sabyasachi Barik, Aziz Karasahin, Christopher Flower, Tao Cai, Hirokazu Miyake, Wade DeGottardi, Mohammad Hafezi, and Edo Waks. "A topological quantum optics interface". In: *Science* 359.6376 (2018), pp. 666–668. DOI: 10.1126/science.aaq0327.

[217] Iñaki Garcıa-Elcano, Alejandro González-Tudela, and Jorge Bravo-Abad. "Tunable and Robust Long-Range Coherent Interactions between Quantum Emitters Mediated by Weyl Bound States". In: *Phys. Rev. Lett.* 125 (16 Oct. 2020), p. 163602. DOI: 10.1103/PhysRevLett.125.163602. URL: https://link.aps.org/doi/10.1103/PhysRevLett.125.163602.

[218] J Zak. "Berry's phase for energy bands in solids". In: *Phys. Rev. Lett.* 62.23 (1989), pp. 2747–2750. ISSN: 0031-9007. DOI: 10.1103/physrevlett.62.2747.

[219] Gershon Kurizki. "Two-atom resonant radiative coupling in photonic band structures". In: *Phys. Rev. A* 42.5 (1990), pp. 2915–2924. ISSN: 1050-2947. DOI: 10.1103/physreva.42.2915.

[220] Matteo Biondi, Sebastian Schmidt, Gianni Blatter, and Hakan E. Türeci. "Self-protected polariton states in photonic quantum metamaterials". In: *Phys. Rev. A* 89.2 (2014), p. 025801. ISSN: 1050-2947. DOI: 10.1103/physreva.89.025801.

[221] M S Khalil, M J A Stoutimore, F C Wellstood, and K D Osborn. "An analysis method for asymmetric resonator transmission applied to superconducting devices". In: *J. Appl. Phys.* 111.5 (2012), p. 054510. ISSN: 0021-8979. DOI: 10.1063/1.3692073.

[222] D Witthaut and A S Sorensen. "Photon scattering by a three-level emitter in a one-dimensional waveguide". In: *New J. Phys.* 12.4 (2010), p. 043052. ISSN: 1367-2630. DOI: 10.1088/1367-2630/12/4/043052.

[223] R. K. Naik, N. Leung, S. Chakram, Peter Groszkowski, Y. Lu, N. Earnest, D. C. McKay, Jens Koch, and D. I. Schuster. "Random access quantum information processors using multimode circuit quantum electrodynamics". In: *Nat. Commun.* 8.1 (2017), p. 1904. DOI: 10.1038/s41467-017-02046-6.

[224] Yu Chen et al. "Multiplexed dispersive readout of superconducting phase qubits". In: *Appl. Phys. Lett.* 101.18 (2012), p. 182601. ISSN: 0003-6951. DOI: 10.1063/1.4764940.

[225] Navin Khaneja, Timo Reiss, Cindie Kehlet, Thomas Schulte-Herbrüggen, and Steffen J. Glaser. "Optimal control of coupled spin dynamics: design of NMR pulse sequences by gradient ascent algorithms". In: *J. Magn. Reson.* 172.2 (2005), pp. 296–305. ISSN: 1090-7807. DOI: 10.1016/j.jmr.2004.11.004.

[226] F. Motzoi, J. M. Gambetta, P. Rebentrost, and F. K. Wilhelm. "Simple Pulses for Elimination of Leakage in Weakly Nonlinear Qubits". In: *Phys. Rev. Lett.* 103.11 (2009), p. 110501. ISSN: 0031-9007. DOI: 10.1103/physrevlett.103.110501.

[227] Nicolas Didier, Eyob A Sete, Joshua Combes, and Marcus P da Silva. "AC flux sweet spots in parametrically-modulated superconducting qubits". In: *Phys. Rev. Appl.* 12.5 (2018), p. 054015. DOI: 10.1103/physrevapplied.12.054015.

[228] Sabrina S Hong, Alexander T Papageorge, Prasahnt Sivarajah, Genya Crossman, Nicolas Didier, Anthony M Polloreno, Eyob A Sete, Stefan W Turkowski, Marcus P da Silva, and Blake R Johnson. "Demonstration of a parametrically activated entangling gate protected from flux noise". In: *Phys. Rev. A* 101.1 (2020), p. 012302. ISSN: 2469-9926. DOI: 10.1103/physreva.101.012302.

[229] Eyob A. Sete, Matthew J. Reagor, Nicolas Didier, and Chad T. Rigetti. "Charge- and Flux-Insensitive Tunable Superconducting Qubit". In: *Phys. Rev. Appl.* 8.2 (Jan. 2017), p. 024004. DOI: 10.1103/PhysRevApplied.8.024004.

[230] M. D. Hutchings, J. B. Hertzberg, Y. Liu, N. T. Bronn, G. A. Keefe, Markus Brink, Jerry M. Chow, and B. L. T. Plourde. "Tunable Superconducting Qubits with Flux-Independent Coherence". In: *Phys. Rev. Appl.* 8.4 (2017), p. 044003. DOI: 10.1103/physrevapplied.8.044003.

[231] Yu Chen et al. "Qubit Architecture with High Coherence and Fast Tunable Coupling". In: *Phys. Rev. Lett.* 113.22 (2014), p. 220502. ISSN: 0031-9007. DOI: 10.1103/physrevlett.113.220502.

[232] Nicolai Lang and Hans Peter Büchler. "Topological networks for quantum communication between distant qubits". In: *npj Quantum Inf.* 3.1 (2017), p. 47. ISSN: 2056-6387. DOI: 10.1038/s41534-017-0047-x.

[233] Duc Thanh Tran, Alexandre Dauphin, Adolfo G. Grushin, Peter Zoller, and Nathan Goldman. "Probing topology by "heating": Quantized circular dichroism in ultracold atoms". In: *Sci. Adv.* 3.8 (2017), e1701207. ISSN: 2375-2548. DOI: 10.1126/sciadv.1701207.

[234] A Dunsworth et al. "A method for building low loss multi-layer wiring for superconducting microwave devices". In: *Appl. Phys. Lett.* 112.6 (2018), p. 063502. ISSN: 0003-6951. DOI: 10.1063/1.5014033.

[235] D Rosenberg et al. “3D integrated superconducting qubits”. In: *npj Quantum Inf.* 3.1 (2017), p. 42. DOI: 10.1038/s41534-017-0044-0.

[236] B Foxen et al. “Qubit compatible superconducting interconnects”. In: *Quantum Sci. Technol.* 3.1 (2017), p. 014005. ISSN: 2058-9565. DOI: 10.1088/2058-9565/aa94fc.

[237] Evan Jeffrey et al. “Fast Accurate State Measurement with Superconducting Qubits”. In: *Phys. Rev. Lett.* 112.19 (2014), p. 190504. ISSN: 0031-9007. DOI: 10.1103/physrevlett.112.190504.

[238] Ruichao Ma, Clai Owens, Andrew Houck, David I. Schuster, and Jonathan Simon. “Autonomous stabilizer for incompressible photon fluids and solids”. In: *Phys. Rev. A* 95.4 (2017), p. 043811. ISSN: 2469-9926. DOI: 10.1103/physreva.95.043811.

[239] Clai Owens, Aman LaChapelle, Brendan Saxberg, Brandon M Anderson, Ruichao Ma, Jonathan Simon, and David I Schuster. “Quarter-flux Hofstadter lattice in a qubit-compatible microwave cavity array”. In: *Phys. Rev. A* 97.1 (2018), p. 013818. ISSN: 2469-9926. DOI: 10.1103/physreva.97.013818.

[240] R Blatt and C F Roos. “Quantum simulations with trapped ions”. In: *Nat. Phys.* 8.4 (2012), pp. 277–284. ISSN: 1745-2473. DOI: 10.1038/nphys2252.

[241] R J Lewis-Swan, A Safavi-Naini, A M Kaufman, and A M Rey. “Dynamics of quantum information”. In: *Nat. Rev. Phys.* 1.10 (2019), pp. 627–634. ISSN: 2522-5820. DOI: 10.1038/s42254-019-0090-y.

[242] Klaus Mølmer and Anders Sørensen. “Multiparticle entanglement of hot trapped ions”. In: *Phys. Rev. Lett.* 82.9 (1999), p. 1835. DOI: 10.1103/PhysRevLett.82.1835.

[243] Varun D. Vaidya, Yudan Guo, Ronen M. Kroeze, Kyle E. Ballantine, Alicia J. Kollár, Jonathan Keeling, and Benjamin L. Lev. “Tunable-Range, Photon-Mediated Atomic Interactions in Multimode Cavity QED”. In: *Phys. Rev. X* 8 (1 Jan. 2018), p. 011002. DOI: 10.1103/PhysRevX.8.011002.

[244] Avikar Periwal, Eric S Cooper, Philipp Kunkel, Julian F Wienand, Emily J Davis, and Monika Schleier-Smith. “Programmable interactions and emergent geometry in an array of atom clouds”. In: *Nature* 600.7890 (2021), pp. 630–635. DOI: 10.1038/s41586-021-04156-0.

[245] Dolev Bluvstein et al. “A quantum processor based on coherent transport of entangled atom arrays”. In: *Nature* 604.7906 (2022), pp. 451–456. DOI: 10.1038/s41586-022-04592-6.

[246] Nicolas Delfosse, Michael E Beverland, and Maxime A Tremblay. “Bounds on stabilizer measurement circuits and obstructions to local implementations of quantum LDPC codes”. In: *arXiv:2109.14599* (2021). DOI: 10.48550/arXiv.2109.14599.

[247] Rahul Nandkishore and David A. Huse. “Many-body Localization and Thermalization in Quantum Statistical Mechanics”. In: *Annu. Rev. Condens. Matter Phys.* 6 (2015), pp. 15–38. DOI: 10.1146/annurev-conmatphys-031214-014726.

[248] Manoj K Joshi, Andreas Elben, Benoıt Vermersch, Tiff Brydges, Christine Maier, Peter Zoller, Rainer Blatt, and Christian F Roos. “Quantum information scrambling in a trapped-ion quantum simulator with tunable range interactions”. In: *Phys. Rev. Lett.* 124.24 (2020), p. 240505. DOI: 10.1103/PhysRevLett.124.240505.

[249] Renate Landig, Lorenz Hruby, Nishant Dogra, Manuele Landini, Rafael Mottl, Tobias Donner, and Tilman Esslinger. “Quantum phases from competing short- and long-range interactions in an optical lattice”. In: *Nature* 532.7600 (2016), pp. 476–479. DOI: 10.1038/nature17409.

[250] Sepehr Ebadi et al. “Quantum phases of matter on a 256-atom programmable quantum simulator”. In: *Nature* 595.7866 (2021), pp. 227–232. DOI: 10.1038/s41586-021-03582-4.

[251] Shi-Biao Zheng and Guang-Can Guo. “Efficient Scheme for Two-Atom Entanglement and Quantum Information Processing in Cavity QED”. In: *Phys. Rev. Lett.* 85 (11 Sept. 2000), pp. 2392–2395. DOI: 10.1103/PhysRevLett.85.2392.

[252] Y. P. Zhong et al. “Violating Bell’s inequality with remotely connected superconducting qubits”. In: *Nat. Phys.* 15.8 (2019), pp. 741–744. DOI: 10.1038/s41567-019-0507-7.

[253] Marco Scigliuzzo, Giuseppe Calajò, Francesco Ciccarello, Daniel Perez Lozano, Andreas Bengtsson, Pasquale Scarlino, Andreas Wallraff, Darrick Chang, Per Delsing, and Simone Gasparinetti. “Controlling Atom-Photon Bound States in an Array of Josephson-Junction Resonators”. In: *Phys. Rev. X* 12 (3 Sept. 2022), p. 031036. DOI: 10.1103/PhysRevX.12.031036.

[254] Sergio Boixo, Sergei V. Isakov, Vadim N. Smelyanskiy, Ryan Babbush, Nan Ding, Zhang Jiang, Michael J. Bremner, John M. Martinis, and Hartmut Neven. “Characterizing quantum supremacy in near-term devices”. In: *Nat. Phys.* 14.6 (2018), pp. 595–600. DOI: 10.1038/s41567-018-0124-x.

[255] Michael J. Hartmann, Fernando G. S. L. Brandão, and Martin B. Plenio. “Strongly interacting polaritons in coupled arrays of cavities”. In: *Nat. Phys.* 2.12 (2006), pp. 849–855. DOI: 10.1038/nphys462.

[256] Joonhee Choi et al. “Emergent randomness and benchmarking from many-body quantum chaos”. In: *arXiv:2103.03535* (2021). URL: https://arxiv.org/abs/2103.03535.

[257] Daniel K Mark, Joonhee Choi, Adam L Shaw, Manuel Endres, and Soonwon Choi. “Benchmarking Quantum Simulators using Quantum Chaos”. In: *arXiv:2205.12211* (2022). URL: https://arxiv.org/abs/2205.12211.

[258] Alberto Peruzzo et al. “Quantum Walks of Correlated Photons”. In: *Science* 329.5998 (2010), pp. 1500–1503. DOI: 10.1126/science.1193515.

[259] Philipp M Preiss, Ruichao Ma, M Eric Tai, Alexander Lukin, Matthew Rispoli, Philip Zupancic, Yoav Lahini, Rajibul Islam, and Markus Greiner. “Strongly correlated quantum walks in optical lattices”. In: *Science* 347.6227 (2015), pp. 1229–1233. DOI: 10.1126/science.1260364.

[260] Zhiguang Yan, Yu-Ran Zhang, Ming Gong, Yulin Wu, Yarui Zheng, Shaowei Li, Can Wang, Futian Liang, Jin Lin, Yu Xu, et al. “Strongly correlated quantum walks with a 12-qubit superconducting processor”. In: *Science* 364.6442 (2019), pp. 753–756. DOI: 10.1126/science.aaw1611.

[261] C. E. Porter and R. G. Thomas. “Fluctuations of Nuclear Reaction Widths”. In: *Phys. Rev.* 104 (2 Oct. 1956), pp. 483–491. DOI: 10.1103/PhysRev.104.483.

[262] Michael V Berry. “Regular and irregular semiclassical wavefunctions”. In: *J. Phys. A: Math. Gen.* 10.12 (1977), p. 2083. DOI: 10.1088/0305-4470/10/12/016.

[263] Josh M Deutsch. “Quantum statistical mechanics in a closed system”. In: *Phys. Rev. A* 43.4 (1991), p. 2046. DOI: 10.1103/PhysRevA.43.2046.

[264] Mark Srednicki. “Chaos and quantum thermalization”. In: *Phys. Rev. E* 50.2 (1994), p. 888. DOI: 10.1103/PhysRevE.50.888.

[265] JE Mooij and GB Schon. “Coherence in superconducting networks”. In: *Physica B* 152 (1988), pp. 1–302.

[266] Christof Bruder, Rosario Fazio, and Gerd Schon. “The Bose-Hubbard model: from Josephson junction arrays to optical lattices”. In: *Annalen der Physik* 14.9-10 (2005), pp. 566–577.

[267] Markus Greiner, Olaf Mandel, Tilman Esslinger, Theodor W Hänsch, and Immanuel Bloch. “Quantum phase transition from a superfluid to a Mott insulator in a gas of ultracold atoms”. In: *Nature* 415.6867 (2002), pp. 39–44. DOI: 10.1038/415039a.

[268] Manuel Endres, Marc Cheneau, Takeshi Fukuhara, Christof Weitenberg, Peter Schauss, Christian Gross, Leonardo Mazza, Mari Carmen Banuls, L Pollet, Immanuel Bloch, et al. “Observation of correlated particle-hole pairs and string order in low-dimensional Mott insulators”. In: *Science* 334.6053 (2011), pp. 200–203. DOI: 10.1126/science.1209284.

[269] Manuel Endres, Takeshi Fukuhara, David Pekker, Marc Cheneau, Peter Schauβ, Christian Gross, Eugene Demler, Stefan Kuhr, and Immanuel Bloch. “The ‘Higgs’ amplitude mode at the two-dimensional superfluid/Mott insulator transition”. In: *Nature* 487.7408 (2012), pp. 454–458. DOI: 10.1038/nature11255.

[270] Michael W Jack and Makoto Yamashita. “Bose-Hubbard model with attractive interactions”. In: *Phys. Rev. A* 71.2 (2005), p. 023610. DOI: 10.1103/PhysRevA.71.023610.

[271] Norman Oelkers and Jon Links. “Ground-state properties of the attractive one-dimensional Bose-Hubbard model”. In: *Phys. Rev. B* 75.11 (2007), p. 115119. DOI: 10.1103/PhysRevB.75.115119.

[272] Matthew Fishman, Steven R. White, and E. Miles Stoudenmire. “The ITensor Software Library for Tensor Network Calculations”. In: *SciPost Phys. Codebases* (2022), p. 4. DOI: 10.21468/SciPostPhysCodeb.4.

[273] Steven R White. “Density matrix formulation for quantum renormalization groups”. In: *Phys. Rev. Lett.* 69.19 (1992), p. 2863. DOI: 10.1103/PhysRevLett.69.2863.

[274] Steven R White. “Density-matrix algorithms for quantum renormalization groups”. In: *Phys. Rev. B* 48.14 (1993), p. 10345. DOI: 10.1103/PhysRevB.48.10345.

[275] Till D Kühner, Steven R White, and Hartmut Monien. “One-dimensional Bose-Hubbard model with nearest-neighbor interaction”. In: *Phys. Rev. B* 61.18 (2000), p. 12474. DOI: 10.1103/PhysRevB.61.12474.

[276] Matthew PA Fisher, Peter B Weichman, Geoffrey Grinstein, and Daniel S Fisher. “Boson localization and the superfluid-insulator transition”. In: *Phys. Rev. B* 40.1 (1989), p. 546. DOI: 10.1103/PhysRevB.40.546.

[277] FDM Haldane. “Effective harmonic-fluid approach to low-energy properties of one-dimensional quantum fluids”. In: *Phys. Rev. Lett.* 47.25 (1981), p. 1840. DOI: 10.1103/PhysRevLett.47.1840.

[278] T Giamarchi. “Resistivity of a one-dimensional interacting quantum fluid”. In: *Phys. Rev. B* 46.1 (1992), p. 342. DOI: 10.1103/PhysRevB.46.342.

[279] VL Berezinskii. “Destruction of long-range order in one-dimensional and two-dimensional systems possessing a continuous symmetry group. II. Quantum systems”. In: *Sov. Phys. JETP* 34.3 (1972), pp. 610–616.

[280] John Michael Kosterlitz and David James Thouless. “Ordering, metastability and phase transitions in two-dimensional systems”. In: *J. Phys. C: Solid State Phys.* 6.7 (1973), p. 1181. DOI: 10.1088/0022-3719/6/7/010.

[281] JM Kosterlitz. “The critical properties of the two-dimensional XY model”. In: *J. Phys. C: Solid State Phys.* 7.6 (1974), p. 1046. DOI: 10.1088/0022-3719/7/6/005.

[282] RM Bradley and S Doniach. “Quantum fluctuations in chains of Josephson junctions”. In: *Phys. Rev. B* 30.3 (1984), p. 1138. DOI: 10.1103/PhysRevB.30.1138.

[283] Eliot Kapit and Erich Mueller. "Even-odd correlation functions on an optical lattice". In: *Phys. Rev. A* 82.1 (2010), p. 013644. DOI: 10.1103/PhysRevA.82.013644.

[284] Emanuele G Dalla Torre, Erez Berg, and Ehud Altman. "Hidden order in 1D Bose insulators". In: *Phys. Rev. Lett.* 97.26 (2006), p. 260401. DOI: 10.1103/PhysRevLett.97.260401.

[285] Erez Berg, Emanuele G Dalla Torre, Thierry Giamarchi, and Ehud Altman. "Rise and fall of hidden string order of lattice bosons". In: *Phys. Rev. B* 77.24 (2008), p. 245119. DOI: 10.1103/PhysRevB.77.245119.

[286] Brendan Saxberg, Andrei Vrajitoarea, Gabrielle Roberts, Margaret G Panetta, Jonathan Simon, and David I Schuster. "Disorder-assisted assembly of strongly correlated fluids of light". In: *Nature* 612.7940 (2022), pp. 435–441. DOI: 10.1038/s41586-022-05357-x.

[287] Manuel Endres. *Probing correlated quantum many-body systems at the single-particle level*. Springer Science & Business, 2014. DOI: 10.1007/978-3-319-05753-8_5.

[288] Eduardo Sánchez-Burillo, Diego Porras, and Alejandro González-Tudela. "Limits of photon-mediated interactions in one-dimensional photonic baths". In: *Phys. Rev. A* 102.1 (2020), p. 013709. DOI: 10.1103/PhysRevA.102.013709.

[289] Thierry Bochud and Damien Challet. "Optimal approximations of power-laws with exponentials". In: *arXiv preprint physics/0605149* (2006). DOI: 10.48550/arXiv.physics/0605149.

[290] Félix Beaudoin, Marcus P da Silva, Zachary Dutton, and Alexandre Blais. "First-order sidebands in circuit QED using qubit frequency modulation". In: *Phys. Rev. A* 86.2 (2012), p. 022305. DOI: 10.1103/PhysRevA.86.022305.

[291] JD Strand, Matthew Ware, Félix Beaudoin, TA Ohki, BR Johnson, Alexandre Blais, and BLT Plourde. "First-order sideband transitions with flux-driven asymmetric transmon qubits". In: *Phys. Rev. B* 87.22 (2013), p. 220505. DOI: 10.1103/PhysRevB.87.220505.

[292] Matthew Reagor, Christopher B Osborn, Nikolas Tezak, Alexa Staley, Guenevere Prawiroatmodjo, Michael Scheer, Nasser Alidoust, Eyob A Sete, Nicolas Didier, Marcus P da Silva, et al. "Demonstration of universal parametric entangling gates on a multi-qubit lattice". In: *Sci. Adv.* 4.2 (2018), eaao3603. DOI: 10.1126/sciadv.aao3603.

[293] SA Caldwell, N Didier, CA Ryan, EA Sete, A Hudson, P Karalekas, R Manenti, MP da Silva, R Sinclair, E Acala, et al. "Parametrically activated entangling gates using transmon qubits". In: *Phys. Rev. Applied* 10.3 (2018), p. 034050. DOI: 10.1103/PhysRevApplied.10.034050.

[294] Daniel C Tsui, Horst L Stormer, and Arthur C Gossard. "Two-dimensional magnetotransport in the extreme quantum limit". In: *Phys. Rev. Lett.* 48.22 (1982), p. 1559. DOI: 10.1103/PhysRevLett.48.1559.

[295] Robert B Laughlin. "Anomalous quantum Hall effect: an incompressible quantum fluid with fractionally charged excitations". In: *Phys. Rev. Lett.* 50.18 (1983), p. 1395. DOI: 10.1103/PhysRevLett.50.1395.

[296] Daniil M Lukin, Alexander D White, Rahul Trivedi, Melissa A Guidry, Naoya Morioka, Charles Babin, Öney O Soykal, Jawad Ul-Hassan, Nguyen Tien Son, Takeshi Ohshima, et al. "Spectrally reconfigurable quantum emitters enabled by optimized fast modulation". In: *npj Quantum Inf.* 6.1 (2020), pp. 1–9. DOI: 10.1038/s41534-020-00310-0.

[297] H Wang, AP Zhuravel, S Indrajeet, Bruno G Taketani, MD Hutchings, Y Hao, F Rouxinol, FK Wilhelm, MD LaHaye, AV Ustinov, et al. "Mode structure in superconducting metamaterial transmission-line resonators". In: *Phys. Rev. Applied* 11.5 (2019), p. 054062. DOI: 10.1103/PhysRevApplied.11.054062.

[298] S Indrajeet, H Wang, MD Hutchings, BG Taketani, Frank K Wilhelm, MD LaHaye, and BLT Plourde. "Coupling a superconducting qubit to a left-handed metamaterial resonator". In: *Phys. Rev. Applied* 14.6 (2020), p. 064033. DOI: 10.1103/PhysRevApplied.14.064033.

[299] Markku Hyrkäs, Vesa Apaja, and Matti Manninen. "Many-particle dynamics of bosons and fermions in quasi-one-dimensional flat-band lattices". In: *Phys. Rev. A* 87.2 (2013), p. 023614. DOI: 10.1103/PhysRevA.87.023614.

[300] Alejandro González-Tudela, C-L Hung, Darrick E Chang, J Ignacio Cirac, and HJ Kimble. "Subwavelength vacuum lattices and atom–atom interactions in two-dimensional photonic crystals". In: *Nat. Photon* 9.5 (2015), pp. 320–325. DOI: https://doi.org/10.1038/nphoton.2015.54.

[301] Sajeev John and Tran Quang. "Spontaneous emission near the edge of a photonic band gap". In: *Phys. Rev. A* 50.2 (1994), p. 1764. DOI: 10.1103/PhysRevA.50.1764.

[302] Philipp Kurpiers, Paul Magnard, Theo Walter, Baptiste Royer, Marek Pechal, Johannes Heinsoo, Yves Salathé, Abdulkadir Akin, Simon Storz, J-C Besse, et al. "Deterministic quantum state transfer and remote entanglement using microwave photons". In: *Nature* 558.7709 (2018), pp. 264–267. DOI: 10.1038/s41586-018-0195-y.

[303] Youpeng Zhong, Hung-Shen Chang, Audrey Bienfait, Étienne Dumur, Ming-Han Chou, Christopher R Conner, Joel Grebel, Rhys G Povey, Haoxiong Yan, David I Schuster, et al. "Deterministic multi-qubit entanglement in a quantum network". In: *Nature* 590.7847 (2021), pp. 571–575. DOI: 10.1038/s41586-021-03288-7.

[304] Anthony Megrant, Charles Neill, Rami Barends, Ben Chiaro, Yu Chen, Ludwig Feigl, Julian Kelly, Erik Lucero, Matteo Mariantoni, Peter JJ O'Malley, et al. "Planar superconducting resonators with internal quality factors above one million". In: *Appl. Phys. Lett.* 100.11 (2012), p. 113510. DOI: 10.1063/1.3693409.

[305] Crispin Gardiner and Peter Zoller. *Quantum Noise*. Springer, 2004.

[306] B Peropadre, J Lindkvist, I.-C. Hoi, C. M. Wilson, J J Garcia-Ripoll, P Delsing, and G Johansson. "Scattering of coherent states on a single artificial atom". In: *New J. Phys.* 15.3 (Mar. 2013), p. 035009. ISSN: 1367-2630. DOI: 10.1088/1367-2630/15/3/035009. URL: http://stacks.iop.org/1367-2630/15/i=3/a=035009?key=crossref.b678584ad37dd80820e11fc4e80303f8.

[307] Lu-Ming Duan and Guang-Can Guo. "Reducing spatially correlated noise and decoherence with quantum error correcting codes". In: *arXiv:quant-ph/9811058* (1998). DOI: 10.48550/arXiv.quant-ph/9811058. URL: https://arxiv.org/abs/quant-ph/9811058.

[308] John M Martinis, S Nam, J Aumentado, KM Lang, and C Urbina. "Decoherence of a superconducting qubit due to bias noise". In: *Phys. Rev. B* 67.9 (2003), p. 094510. DOI: 10.1103/PhysRevB.67.094510.

[309] G Ithier, E Collin, P Joyez, P. J. Meeson, D Vion, D Esteve, F Chiarello, A Shnirman, Yu Makhlin, Josef Schriefl, and G Schön. "Decoherence in a superconducting quantum bit circuit". In: *Phys. Rev. B* 72.13 (2005), p. 134519. DOI: 10.1103/PhysRevB.72.134519.

[310] Tal Goren, Kirill Plekhanov, Félicien Appas, and Karyn Le Hur. "Topological Zak phase in strongly coupled LC circuits". In: *Phys. Rev. B* 97.4 (2018), p. 041106. ISSN: 2469-9950. DOI: 10.1103/physrevb.97.041106.

[311] Anton Frisk Kockum, Adam Miranowicz, Simone De Liberato, Salvatore Savasta, and Franco Nori. "Ultrastrong coupling between light and matter". In: *Nat. Rev. Phys.* 1.1 (2019), pp. 19–40. ISSN: 2522-5820. DOI: 10.1038/s42254-018-0006-2.

[312] Beatriz Pérez-González, Miguel Bello, Alvaro Gómez-León, and Gloria Platero. "SSH model with long-range hoppings: topology, driving and disorder". In: *arXiv:1802.03973v3* (2018).

[313] S. Longhi. "Probing one-dimensional topological phases in waveguide lattices with broken chiral symmetry". In: *Opt. Lett.* 43.19 (Oct. 2018), pp. 4639–4642. DOI: 10.1364/OL.43.004639.

[314] Arjan Ferdinand van Loo. "Interactions in waveguide quantum electrodynamics". PhD thesis. ETH Zurich, 2014.

[315] Herbert Goldstein, Charles Poole, and John Safko. *Classical Mechanics*. 3rd ed. Addison–Wesley, 2002.

[316] Dimitris G. Angelakis, Marcelo Franca Santos, and Sougato Bose. "Photon-blockade-induced Mott transitions and XY spin models in coupled cavity arrays". In: *Phys. Rev. A* 76 (3 Sept. 2007), p. 031805. DOI: 10.1103/PhysRevA.76.031805.

[317] John M. Martinis, Rami Barends, and Alex Korotkov. "Calculation of Coupling Capacitance in Planar Electrodes". In: *arXiv:1410.3458* (2014). URL: https://arxiv.org/abs/1410.3458.

[318] Edward Bennett Rosa. *The self and mutual inductances of linear conductors*. 80. US Department of Commerce and Labor, Bureau of Standards, 1908.

[319] Alexandre Blais, Ren-Shou Huang, Andreas Wallraff, S. M. Girvin, and R. J. Schoelkopf. "Cavity quantum electrodynamics for superconducting electrical circuits: An architecture for quantum computation". In: *Phys. Rev. A* 69 (6 June 2004), p. 062320. DOI: 10.1103/PhysRevA.69.062320.

[320] D. I. Schuster, A. Wallraff, A. Blais, L. Frunzio, R.-S. Huang, J. Majer, S. M. Girvin, and R. J. Schoelkopf. "ac Stark Shift and Dephasing of a Superconducting Qubit Strongly Coupled to a Cavity Field". In: *Phys. Rev. Lett.* 94 (12 Mar. 2005), p. 123602. DOI: 10.1103/PhysRevLett.94.123602.

[321] A. A. Houck, J. A. Schreier, B. R. Johnson, J. M. Chow, Jens Koch, J. M. Gambetta, D. I. Schuster, L. Frunzio, M. H. Devoret, S. M. Girvin, and R. J. Schoelkopf. "Controlling the Spontaneous Emission of a Superconducting Transmon Qubit". In: *Phys. Rev. Lett.* 101 (8 Aug. 2008), p. 080502. DOI: 10.1103/PhysRevLett.101.080502.

[322] M. D. Reed, B. R. Johnson, A. A. Houck, L. DiCarlo, J. M. Chow, D. I. Schuster, L. Frunzio, and R. J. Schoelkopf. "Fast reset and suppressing spontaneous emission of a superconducting qubit". In: *Appl. Phys. Lett.* 96.20 (2010), p. 203110. DOI: 10.1063/1.3435463.

[323] Agnetta Y Cleland, Marek Pechal, Pieter-Jan C Stas, Christopher J Sarabalis, E Alex Wollack, and Amir H Safavi-Naeini. "Mechanical Purcell filters for microwave quantum machines". In: *Appl. Phys. Lett.* 115.26 (2019), p. 263504. ISSN: 0003-6951. DOI: 10.1063/1.5111151.

[324] Eyob A. Sete, John M. Martinis, and Alexander N. Korotkov. "Quantum theory of a bandpass Purcell filter for qubit readout". In: *Phys. Rev. A* 92 (1 July 2015), p. 012325. DOI: 10.1103/PhysRevA.92.012325.

[325] Colm A. Ryan, Blake R. Johnson, Jay M. Gambetta, Jerry M. Chow, Marcus P. da Silva, Oliver E. Dial, and Thomas A. Ohki. "Tomography via correlation of noisy measurement records". In: *Phys. Rev. A* 91 (2 Feb. 2015), p. 022118. DOI: 10.1103/PhysRevA.91.022118.

[326] Easwar Magesan, Jay M. Gambetta, A. D. Córcoles, and Jerry M. Chow. "Machine Learning for Discriminating Quantum Measurement Trajectories and Improving Readout". In: *Phys. Rev. Lett.* 114 (20 May 2015), p. 200501. DOI: 10.1103/PhysRevLett.114.200501.

[327] R. A. Fisher. "THE USE OF MULTIPLE MEASUREMENTS IN TAXONOMIC PROBLEMS". In: *Ann. Eugen.* 7.2 (1936), pp. 179–188. DOI: 10.1111/j.1469-1809.1936.tb02137.x.

[328] F. Pedregosa et al. "Scikit-learn: Machine Learning in Python". In: *J. Mach. Learn. Res.* 12 (2011), pp. 2825–2830. DOI: 10.5555/1953048.2078195.

[329] Zhiling Wang, Zenghui Bao, Yukai Wu, Yan Li, Cheng Ma, Tianqi Cai, Yipu Song, Hongyi Zhang, and Luming Duan. "Improved Superconducting Qubit State Readout by Path Interference". In: *Chin. Phys. Lett.* 38.11, 110303 (2021), p. 110303. DOI: 10.1088/0256-307X/38/11/110303.

[330] D. H. Slichter, R. Vijay, S. J. Weber, S. Boutin, M. Boissonneault, J. M. Gambetta, A. Blais, and I. Siddiqi. "Measurement-Induced Qubit State Mixing in Circuit QED from Up-Converted Dephasing Noise". In: *Phys. Rev. Lett.* 109 (15 Oct. 2012), p. 153601. DOI: 10.1103/PhysRevLett.109.153601.

[331] Daniel Sank, Zijun Chen, Mostafa Khezri, J. Kelly, R. Barends, B. Campbell, Y. Chen, B. Chiaro, A. Dunsworth, A. Fowler, et al. "Measurement-Induced State Transitions in a Superconducting Qubit: Beyond the Rotating Wave Approximation". In: *Phys. Rev. Lett.* 117 (19 Nov. 2016), p. 190503. DOI: 10.1103/PhysRevLett.117.190503.

[332] Jay Gambetta, Alexandre Blais, D. I. Schuster, A. Wallraff, L. Frunzio, J. Majer, M. H. Devoret, S. M. Girvin, and R. J. Schoelkopf. "Qubit-photon interactions in a cavity: Measurement-induced dephasing and number splitting". In: *Phys. Rev. A* 74 (4 Oct. 2006), p. 042318. DOI: 10.1103/PhysRevA.74.042318. URL: https://link.aps.org/doi/10.1103/PhysRevA.74.042318.

[333] Zijun Chen. "Metrology of Quantum Control and Measurement in Superconducting Qubits". PhD thesis. University of California, Santa Barbara, 2018.

[334] Yaser S Abu-Mostafa, Malik Magdon-Ismail, and Hsuan-Tien Lin. *Learning from data*. Vol. 4. AMLBook, 2012.

[335] D. T. McClure, Hanhee Paik, L. S. Bishop, M. Steffen, Jerry M. Chow, and Jay M. Gambetta. "Rapid Driven Reset of a Qubit Readout Resonator". In: *Phys. Rev. Applied* 5 (1 Jan. 2016), p. 011001. DOI: 10.1103/PhysRevApplied.5.011001.

[336] T. Walter, P. Kurpiers, S. Gasparinetti, P. Magnard, A. Poto čnik, Y. Salathé, M. Pechal, M. Mondal, M. Oppliger, C. Eichler, and A. Wallraff. "Rapid High-Fidelity Single-Shot Dispersive Readout of Superconducting Qubits".

In: *Phys. Rev. Applied* 7 (5 May 2017), p. 054020. DOI: 10.1103/PhysRevApplied.7.054020.

[337] Johannes Heinsoo, Christian Kraglund Andersen, Ants Remm, Sebastian Krinner, Theodore Walter, Yves Salathé, Simone Gasparinetti, Jean-Claude Besse, Anton Poto čnik, Andreas Wallraff, and Christopher Eichler. "Rapid High-fidelity Multiplexed Readout of Superconducting Qubits". In: *Phys. Rev. Applied* 10 (3 Sept. 2018), p. 034040. DOI: 10.1103/PhysRevApplied.10.034040.

[338] Michiel A Rol, Livio Ciorciaro, Filip K Malinowski, Brian M Tarasinski, Ramiro E Sagastizabal, Cornelis Christiaan Bultink, Yves Salathe, Niels Haandbæk, Jan Sedivy, and Leonardo DiCarlo. "Time-domain characterization and correction of on-chip distortion of control pulses in a quantum processor". In: *Appl. Phys. Lett.* 116.5 (2020), p. 054001. DOI: 10.1063/1.5133894.

[339] D. Ristè, C. C. Bultink, K. W. Lehnert, and L. DiCarlo. "Feedback Control of a Solid-State Qubit Using High-Fidelity Projective Measurement". In: *Phys. Rev. Lett.* 109 (24 Dec. 2012), p. 240502. DOI: 10.1103/PhysRevLett.109.240502.

[340] Nathan Wiebe, Christopher Granade, Christopher Ferrie, and David G Cory. "Hamiltonian learning and certification using quantum resources". In: *Phys. Rev. Lett.* 112.19 (2014), p. 190501. DOI: 10.1103/PhysRevLett.112.190501.

[341] Harry Buhrman, Richard Cleve, John Watrous, and Ronald De Wolf. "Quantum fingerprinting". In: *Phys. Rev. Lett.* 87.16 (2001), p. 167902. DOI: 10.1103/PhysRevLett.87.167902.

[342] Steven T Flammia and Yi-Kai Liu. "Direct fidelity estimation from few Pauli measurements". In: *Phys. Rev. Lett.* 106.23 (2011), p. 230501. DOI: 10.1103/PhysRevLett.106.230501.

[343] Lukasz Cincio, Yiğit Subaşı, Andrew T Sornborger, and Patrick J Coles. "Learning the quantum algorithm for state overlap". In: *New J. Phys.* 20.11 (2018), p. 113022. DOI: 10.1088/1367-2630/aae94a.

[344] Matthias Steffen, Markus Ansmann, Radoslaw C Bialczak, Nadav Katz, Erik Lucero, Robert McDermott, Matthew Neeley, Eva Maria Weig, Andrew N Cleland, and John M Martinis. "Measurement of the entanglement of two superconducting qubits via state tomography". In: *Science* 313.5792 (2006), pp. 1423–1425. DOI: 10.1126/science.1130886.

[345] Jean Dalibard, Yvan Castin, and Klaus Mølmer. "Wave-function approach to dissipative processes in quantum optics". In: *Phys. Rev. Lett.* 68.5 (1992), p. 580. DOI: 10.1103/PhysRevLett.68.580.

[346] Martin B Plenio and Peter L Knight. "The quantum-jump approach to dissipative dynamics in quantum optics". In: *Rev. Mod. Phys.* 70.1 (1998), p. 101. DOI: 10.1103/RevModPhys.70.101.

[347] Naoto Nagaosa. *Quantum field theory in strongly correlated electronic systems*. Springer Science & Business Media, 1999.

[348] C. Neill, P. Roushan, K. Kechedzhi, S. Boixo, S. V. Isakov, V. Smelyanskiy, A. Megrant, B. Chiaro, A. Dunsworth, K. Arya, et al. "A blueprint for demonstrating quantum supremacy with superconducting qubits". In: *Science* 360.6385 (2018), pp. 195–199. DOI: 10.1126/science.aao4309.

[349] Christian Gogolin and Jens Eisert. "Equilibration, thermalisation, and the emergence of statistical mechanics in closed quantum systems". In: *Rep. Prog. Phys.* 79.5 (2016), p. 056001. DOI: 10.1088/0034-4885/79/5/056001.

[350] Alexander M Dalzell, Nicholas Hunter-Jones, and Fernando GSL Brandão. "Random quantum circuits transform local noise into global white noise". In: *arXiv:2111.14907* (2021). URL: https://arxiv.org/abs/2111.14907.

Appendix A

DEVICE FABRICATION DETAILS

In this appendix, we provide details of each fabrication step mentioned in Sec. 3.2. The majority of the description is the same as App. A in [133] with minor updates. The key parameters are summarized in Table A.1 with the footnotes providing detailed information. The sequence of each step appearing in the table dictates the sequence of performing each step in the fabrication.

[1] Trichloroethylene

[2] With sonication

[3] Isopropyl alcohol, with sonication

[4] PIE Tergeo Plus. Before running the recipe, clean the chamber for 5 min and condition the chamber for another 10 min. This procedure is the same for all the O_2 plasma processes.

[5] Buffered Oxide Etch: 15 sec in BOE, rinse with deionized water for 10 sec in beaker I, rinse with deionized water for 10 sec in beaker II.

[6] SPTS uEtch

[7] Bilayer resist. Bake after each layer.

[8] Trilayer resist. Bake after each layer.

[9] (Spin speed in unit of rpm, acceleration in unit of rpm/s)

[10] Baking time: 3 min. There is a prebake before spinning any resist.

[11] Methyl isobutyl ketone

[12] Volume ratio 3:1

[13] Development temperature: 1.5°C

[14] The plasma power is reduced by half.

[15] Before evaporating the metal, Titanium is first evaporated (0.2 nm/s for 3 min) to further lower the chamber pressure. The device is not exposed at this point.

[16] This is double-angle evaporation. The first evaporation has tilt of 60° and rotation of 90°, followed by a 20-min oxidation at 5 mbar and the second evaporation with tilt of 20° and rotation of 180°.

[17] The lift-off is always performed with two NMP (N-Methyl-2-pyrrolidone) beakers, both of which are heated to 150°C. Unless stated, the chip stays in beaker I for 1 hour, transferred to beaker II, sonicated for 5 min, transferred to Acetone and sonicated for 2 min, transferred to IPA and sonicated for 1 min. The process is described in detail in App. A.8 of [133]

E-beam round	Marker	Ground	JJ	Air-bridge
Chip cleaning				
TCE[1]	10 min, 80°C	-	-	-
Acetone [2]	5 min	3 min	-	-
IPA[3]	3 min	2 min	-	-
O_2 plasma[4]	2 min	2 min	2 min	2 min
BOE[5]	Yes	Yes	-	-
Vapor HF[6]	-	-	Yes	Yes
Spin/bake				
Resist	ZEP 520A	ZEP 520A	MMA(8.5)MAA EL11, 950PMMA A4[7]	950PMMA A9, MMA(8.5)MAA EL11, 950PMMA A9[8]
Spinner parameters[9]	(3k, 1.5k)	(3k, 1.5k)	(2.2k, 1.5k)	(4k, 1.5k)
Baking temperature[10]	180°C	180°C	170°C	170°C
Beamwrite				
Current	10 nA	10 or 100 nA	0.18 nA	4 nA
Aperture	300 μm	300 μm	200 μm	300 μm
Dose (μC/cm^2)	245	245	990	480
Development				
(Developer, Rinser)	(ZED-N50, MIBK[11])	(ZED-N50, MIBK)	(IPA/DI water[12], IPA)[13]	(IPA/DI water, IPA)
Time	(2.5 min, 30 sec)	(2.5 min, 30 sec)	(10 min, 10 sec)	(> 90 sec, 10 sec)
Resist reflow	-	-	-	105°C, 2 hr
O_2 plasma	2 min	1 min	1 min[14]	2 min
BOE	-	Yes	-	-
Vapor HF	-	-	Yes	-
Evaporation[15]				
Ar milling	-	-	-	400 V, 21 mA, 6 min
Metal	Nb	Al	Al	Al
Rate	0.4 nm/s	1 nm/s	1 nm/s	0.2 nm/s
Thickness	150 nm	120 nm	60 nm, 120 nm[16]	200 nm
Oxidation	-	10 mbar, 2 min	5 mbar for 20 min, 10 mbar for 2 min	10 mbar, 2 min
Lift-off[17]		3 hr in beaker I		Gentle lift-off

Table A.1: Key parameters in device fabrication

Appendix B

SUPPLEMENTARY INFORMATION FOR CHAPTER 4

B.1 Spectroscopic measurement of individual qubits

The master equation of a qubit in a thermal bath at temperature T, driven by a classical field is given by $\dot{\hat{\rho}} = -i[\hat{H}/\hbar, \hat{\rho}] + \mathcal{L}[\hat{\rho}]$, where the Hamiltonian $\hat{H}$ and the Liouvillian $\mathcal{L}$ is written as [305]

$$\hat{H}/\hbar = -\frac{\omega_\mathrm{p} - \omega_\mathrm{q}}{2}\,\hat{\sigma}_z + \frac{\Omega_\mathrm{p}}{2}\,\hat{\sigma}_x, \tag{B.1}$$

$$\mathcal{L}[\hat{\rho}] = (\bar{n}_\mathrm{th} + 1)\Gamma_1\mathcal{D}[\hat{\sigma}_-]\hat{\rho} + \bar{n}_\mathrm{th}\Gamma_1\mathcal{D}[\hat{\sigma}_+]\hat{\rho} + \frac{\Gamma_\varphi}{2}\mathcal{D}[\hat{\sigma}_z]\hat{\rho}. \tag{B.2}$$

Here, ω_p (ω_q) is the frequency of the drive (qubit), Ω_p is the Rabi frequency of the drive, $\bar{n}_\mathrm{th} = 1/(e^{\hbar\omega_\mathrm{q}/k_\mathrm{B}T} - 1)$ is the thermal occupation of photons in the bath, Γ_1 and Γ_φ are relaxation rate and pure dephasing rates of the qubit, respectively. The superoperator

$$\mathcal{D}[\hat{A}]\hat{\rho} = \hat{A}\hat{\rho}\hat{A}^\dagger - \frac{1}{2}\{\hat{A}^\dagger\hat{A}, \hat{\rho}\} \tag{B.3}$$

denotes the Lindblad dissipator. The master equation can be rewritten in terms of density matrix elements $\rho_{a,b} \equiv \langle a|\hat{\rho}|b\rangle$ as

$$\dot{\rho}_\mathrm{e,e} = \frac{i\Omega_\mathrm{p}}{2}(\rho_\mathrm{e,g} - \rho_\mathrm{g,e}) - (\bar{n}_\mathrm{th} + 1)\Gamma_1\rho_\mathrm{e,e} + \bar{n}_\mathrm{th}\Gamma_1\rho_\mathrm{g,g} \tag{B.4}$$

$$\dot{\rho}_\mathrm{e,g} = \left[i(\omega_\mathrm{p} - \omega_\mathrm{q}) - \frac{(2\bar{n}_\mathrm{th} + 1)\Gamma_1 + 2\Gamma_\varphi}{2}\right]\rho_\mathrm{e,g} + \frac{i\Omega_\mathrm{p}}{2}(\rho_\mathrm{e,e} - \rho_\mathrm{g,g}) \tag{B.5}$$

$$\dot{\rho}_\mathrm{g,e} = \dot{\rho}^*_\mathrm{e,g}; \quad \dot{\rho}_\mathrm{g,g} = -\dot{\rho}_\mathrm{e,e} \tag{B.6}$$

With $\rho_\mathrm{e,e} + \rho_\mathrm{g,g} = 1$, the steady-state solution ($\dot{\hat{\rho}} = 0$) to the master equation can be expressed as

$$\rho^\mathrm{ss}_\mathrm{e,e} = \frac{\bar{n}_\mathrm{th}}{2\bar{n}_\mathrm{th} + 1}\frac{1 + (\delta\omega/\Gamma^\mathrm{th}_2)^2}{1 + (\delta\omega/\Gamma^\mathrm{th}_2)^2 + \Omega^2_\mathrm{p}/(\Gamma^\mathrm{th}_1\Gamma^\mathrm{th}_2)} + \frac{1}{2}\frac{\Omega^2_\mathrm{p}/(\Gamma^\mathrm{th}_1\Gamma^\mathrm{th}_2)}{1 + (\delta\omega/\Gamma^\mathrm{th}_2)^2 + \Omega^2_\mathrm{p}/(\Gamma^\mathrm{th}_1\Gamma^\mathrm{th}_2)}, \tag{B.7}$$

$$\rho^\mathrm{ss}_\mathrm{e,g} = -i\frac{\Omega_\mathrm{p}}{2\Gamma^\mathrm{th}_2(2\bar{n}_\mathrm{th} + 1)}\frac{1 + i\,\delta\omega/\Gamma^\mathrm{th}_2}{1 + (\delta\omega/\Gamma^\mathrm{th}_2)^2 + \Omega^2_\mathrm{p}/(\Gamma^\mathrm{th}_1\Gamma^\mathrm{th}_2)}, \tag{B.8}$$

where $\delta\omega = \omega_\mathrm{p} - \omega_\mathrm{q}$ is the detuning of the drive from qubit frequency, $\Gamma^\mathrm{th}_1 = (2\bar{n}_\mathrm{th} + 1)\Gamma_1$ and $\Gamma^\mathrm{th}_2 = \Gamma^\mathrm{th}_1/2 + \Gamma_\varphi$ are the thermally enhanced decay rate and dephasing rate of the qubit.

Now, let us consider the case where a qubit is coupled to the waveguide with decay rate of $\Gamma_{\rm 1D}$. If we send in a probe field $\hat{a}_{\rm in}$ from left to right along the waveguide, the right-propagating output field $\hat{a}_{\rm out}$ after interaction with the qubit is written as [145]

$$\hat{a}_{\rm out} = \hat{a}_{\rm in} + \sqrt{\frac{\Gamma_{\rm 1D}}{2}}\hat{\sigma}_{-}.$$

The probe field creates a classical drive on the qubit with the rate of $\Omega_{\rm p}/2 = -i\langle\hat{a}_{\rm in}\rangle\sqrt{\Gamma_{\rm 1D}/2}$. With the steady-state solution of master equation (B.8) the transmission amplitude $t = \langle\hat{a}_{\rm out}\rangle/\langle\hat{a}_{\rm in}\rangle$ can be written as

$$t(\delta\omega) = 1 - \frac{\Gamma_{\rm 1D}}{2\Gamma_2^{\rm th}(2\bar{n}_{\rm th}+1)}\frac{1+i\,\delta\omega/\Gamma_2^{\rm th}}{1+(\delta\omega/\Gamma_2^{\rm th})^2+\Omega_{\rm p}^2/(\Gamma_1^{\rm th}\Gamma_2^{\rm th})}. \tag{B.9}$$

At zero temperature ($\bar{n}_{\rm th} = 0$) Eq. (B.9) reduces to [118, 306]

$$t(\delta\omega) = 1 - \frac{\Gamma_{\rm 1D}}{2\Gamma_2}\frac{1+i\,\delta\omega/\Gamma_2}{1+(\delta\omega/\Gamma_2)^2+\Omega_{\rm p}^2/(\Gamma_1\Gamma_2)}. \tag{B.10}$$

Here, $\Gamma_2 = \Gamma_\varphi + \Gamma_1/2$ is the dephasing rate of the qubit in the absence of thermal occupancy. In the following, we define the parasitic decoherence rate of the qubit as $\Gamma' = 2\Gamma_2 - \Gamma_{\rm 1D} = \Gamma_{\rm loss} + 2\Gamma_\varphi$, where $\Gamma_{\rm loss}$ denotes the decay rate of qubit induced by channels other than the waveguide. Examples of $\Gamma_{\rm loss}$ in superconducting qubits include dielectric loss, decay into slotline mode, and loss from coupling to two-level system (TLS) defects.

Effect of saturation

To discuss the effect of saturation on the extinction in transmission, we start with the zero temperature case of Eq. (B.10). We introduce the saturation parameter $s \equiv \Omega_{\rm p}^2/\Gamma_1\Gamma_2$ to rewrite the on-resonance transmittivity as

$$t(0) = 1 - \frac{\Gamma_{\rm 1D}}{2\Gamma_2}\frac{1}{1+s} \approx 1 - \frac{\Gamma_{\rm 1D}}{2\Gamma_2}(1-s) = \left(1+s\frac{\Gamma_{\rm 1D}}{\Gamma'}\right)\left(\frac{\Gamma'}{\Gamma'+\Gamma_{\rm 1D}}\right), \tag{B.11}$$

where the low-power assumption $s \ll 1$ has been made in the last step. For the extinction to get negligible effect from saturation, the power-dependent part in Eq. (B.11) should be small compared to the power-independent part. This is equivalent to $s < \Gamma'/\Gamma_{\rm 1D}$. Using the relation

$$\Omega_{\rm p} = \sqrt{\frac{2\Gamma_{\rm 1D}P_{\rm p}}{\hbar\omega_{\rm q}}}$$

between the driven Rabi frequency and the power P_p of the probe and assuming $\Gamma' \ll \Gamma_\mathrm{1D}$, this reduces to

$$P_\mathrm{p} \lesssim \frac{\hbar\omega_\mathrm{q}\Gamma'}{4}. \tag{B.12}$$

In the experiment, the probe power used to resolve the extinction was -150 dBm (10^{-18} W), which gives a limit to the observable Γ' due to our coherent drive of $\Gamma'/2\pi \approx 150\,\mathrm{kHz}$.

Effect of thermal occupation

To take into account the effect of thermal occupancy, we take the limit where the saturation is very small ($\Omega_\mathrm{p} \approx 0$). On resonance, the transmission amplitude is expressed as

$$t(0) = 1 - \frac{\Gamma_\mathrm{1D}}{[(2\bar{n}_\mathrm{th}+1)\Gamma_1 + 2\Gamma_\varphi](2\bar{n}_\mathrm{th}+1)} \approx 1 - \frac{\Gamma_\mathrm{1D}}{2\Gamma_2} + \frac{(\Gamma_1+\Gamma_\varphi)\Gamma_\mathrm{1D}}{\Gamma_2^2}\bar{n}_\mathrm{th}, \tag{B.13}$$

where we have assumed the thermal occupation is very small, $\bar{n}_\mathrm{th} \ll 1$. In the limit where Γ_1D is dominating spurious loss and pure dephasing rates ($\Gamma_2 \approx \Gamma_\mathrm{1D}/2$), this reduces to

$$t(0) \approx t(0)|_{T=0} + 4\bar{n}_\mathrm{th} \tag{B.14}$$

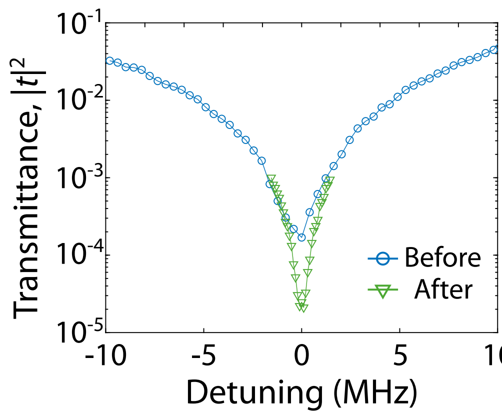

Figure B.1: **Effect of thermal occupancy on extinction.** The transmittance of Q_1 is measured at the flux-insensitive point before and after installation of customized microwave attenuator. We observe an order-of-magnitude enhancement in extinction after the installation, indicating a better thermalization of input signals to the chip. This figure is adapted from [47].

and hence the thermal contribution dominates the transmission amplitude unless $\bar{n}_{\text{th}} < \Gamma'/4\Gamma_{\text{1D}}$.

Using this relation, we can estimate the upper bound on the temperature of the environment based on our measurement of extinction. We have measured the transmittance of Q_1 at its maximum frequency (Fig. B.1) before and after installing a thin-film microwave attenuator, which is customized for proper thermalization of the input signals sent into the waveguide with the mixing chamber plate of the dilution refrigerator [177]. The minimum transmittance was measured to be $|t|^2 \approx 1.7 \times 10^{-4}$ (2.1×10^{-5}) before (after) installation of the attenuator, corresponding to the upper bound on thermal photon number of $\bar{n}_{\text{th}} \lesssim 3.3 \times 10^{-3}$ (1.1×10^{-3}). With the attenuator, this corresponds to temperature of 43 mK, close to the temperature values reported in Ref. [177].

B.2 Detailed modeling of the atomic cavity

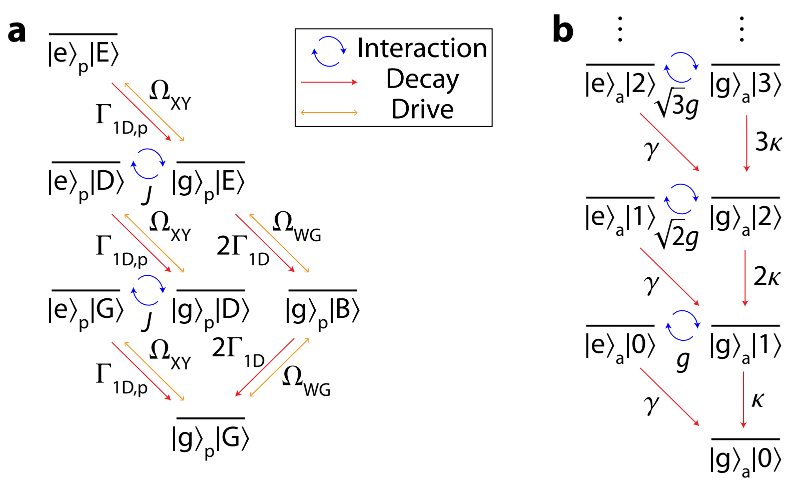

Figure B.2: **Level structure of the atomic cavity and linear cavity.** **a**, Level structure of the three-qubit system of probe qubit and atomic cavity. $\Gamma_{\text{1D,p}}$ and $2\Gamma_{\text{1D}}$ denotes the decay rates into the waveguide channel, Ω_{XY} is the local drive on the probe qubit, and Ω_{WG} is the drive from the waveguide. The coupling strength J is the same for the first excitation and second excitation levels, **b**, Level structure of an atom coupled to a linear cavity. $|e\rangle_{\text{a}}$ $(|g\rangle_{\text{a}})$ denotes the excited state (ground state) of the atom, while $|n\rangle$ is the n-photon Fock state of the cavity field. g is the coupling, γ is the decay rate of the atom, and κ is the photon loss rate of the cavity. This figure is adapted from [47].

In this section, we analyze the atomic cavity discussed in the main text in more detail, taking into account its higher excitation levels. The atomic cavity is formed by two identical *mirror* qubits [frequency ω_{q}, decay rate Γ_{1D} (Γ') to waveguide (spurious loss) channel placed at $\lambda/2$ distance along the waveguide (Fig. 4.1a). From the $\lambda/2$ spacing, the correlated decay of the two qubits is maximized to $-\Gamma_{\mathrm{1D}}$, while the exchange interaction is zero. This results in formation of dark state $|\mathrm{D}\rangle$ and bright state $|\mathrm{B}\rangle$

$$|\mathrm{D}\rangle = \frac{|\mathrm{eg}\rangle + |\mathrm{ge}\rangle}{\sqrt{2}}, \quad |\mathrm{B}\rangle = \frac{|\mathrm{eg}\rangle - |\mathrm{ge}\rangle}{\sqrt{2}}, \tag{B.15}$$

which are single-excitation states of two qubits with suppressed and enhanced waveguide decay rates $\Gamma_{\mathrm{1D,D}} = 0$, $\Gamma_{\mathrm{1D,B}} = 2\Gamma_{\mathrm{1D}}$ to the waveguide. Here, g (e) denotes the ground (excited) state of each qubit. Other than the ground state $|\mathrm{G}\rangle \equiv |\mathrm{gg}\rangle$, there also exists a second excited state $|\mathrm{E}\rangle \equiv |\mathrm{ee}\rangle$ of two qubits, completing $2^2 = 4$ eigenstates in the Hilbert space of two qubits. We can alternatively define $|\mathrm{D}\rangle$ and $|\mathrm{B}\rangle$ in terms of collective annihilation operators

$$\hat{S}_{\mathrm{D}} = \frac{1}{\sqrt{2}}\left(\hat{\sigma}_{-}^{(1)} + \hat{\sigma}_{-}^{(2)}\right), \quad \hat{S}_{\mathrm{B}} = \frac{1}{\sqrt{2}}\left(\hat{\sigma}_{-}^{(1)} - \hat{\sigma}_{-}^{(2)}\right) \tag{B.16}$$

as $|\mathrm{D}\rangle = \hat{S}_{\mathrm{D}}^{\dagger}|\mathrm{G}\rangle$ and $|\mathrm{B}\rangle = \hat{S}_{\mathrm{B}}^{\dagger}|\mathrm{G}\rangle$. Here, $\hat{\sigma}_{-}^{(i)}$ de-excites the state of i-th mirror qubit. Note that the doubly-excited state $|\mathrm{E}\rangle$ can be obtained by successive application of either $\hat{S}_{\mathrm{D}}^{\dagger}$ or $\hat{S}_{\mathrm{B}}^{\dagger}$ twice on the ground state $|\mathrm{G}\rangle$.

The interaction of qubits with the field in the waveguide is written in the form of $\hat{H}_{\mathrm{WG}} \propto (\hat{S}_{\mathrm{B}} + \hat{S}_{\mathrm{B}}^{\dagger})$, and hence the state transfer via classical drive on the waveguide can be achieved only between states of non-vanishing transition dipole $\langle f|\hat{S}_{\mathrm{B}}|i\rangle$. In the present case, only $|\mathrm{G}\rangle \leftrightarrow |\mathrm{B}\rangle$ and $|\mathrm{B}\rangle \leftrightarrow |\mathrm{E}\rangle$ transitions are available via the waveguide with the same transition dipole. This implies that the waveguide decay rate of $|\mathrm{E}\rangle$ is equal to that of $|\mathrm{B}\rangle$, $\Gamma_{\mathrm{1D,E}} = 2\Gamma_{\mathrm{1D}}$.

To investigate the level structure of the dark state, which is not accessible via the waveguide channel, we introduce an ancilla *probe* qubit [frequency ω_{q}, decay rate $\Gamma_{\mathrm{1D,p}}$ (Γ'_{p}) to waveguide (loss) channel] at the center of mirror qubits. The probe qubit is separated by $\lambda/4$ from mirror qubits, maximizing the exchange interaction to $\sqrt{\Gamma_{\mathrm{1D,p}}\Gamma_{\mathrm{1D}}}/2$ with zero correlated decay. This creates an interaction of excited state of probe qubit to the dark state of mirror qubits $|\mathrm{e}\rangle_{\mathrm{p}}|\mathrm{G}\rangle \leftrightarrow |\mathrm{g}\rangle_{\mathrm{p}}|\mathrm{D}\rangle$, while the bright state remains decoupled from this dynamics.

The master equation of the three-qubit system reads $\dot{\hat{\rho}} = -i[\hat{H}/\hbar, \hat{\rho}] + \mathcal{L}[\hat{\rho}]$, where the Hamiltonian $\hat{H}$ and the Liouvillian $\mathcal{L}$ are given by

$$\hat{H} = \hbar J \left[\hat{\sigma}_-^{(\mathrm{p})}\hat{S}_\mathrm{D}^\dagger + \hat{\sigma}_+^{(\mathrm{p})}\hat{S}_\mathrm{D}\right] \tag{B.17}$$

$$\mathcal{L}[\hat{\rho}] = (\Gamma_{1\mathrm{D,p}} + \Gamma'_\mathrm{p})\,\mathcal{D}\left[\hat{\sigma}_-^{(\mathrm{p})}\right]\hat{\rho} + (2\Gamma_{1\mathrm{D}} + \Gamma')\,\mathcal{D}\left[\hat{S}_\mathrm{B}\right]\hat{\rho} + \Gamma'\,\mathcal{D}\left[\hat{S}_\mathrm{D}\right]\hat{\rho} \tag{B.18}$$

Here, $\hat{\sigma}_\pm^{(\mathrm{p})}$ are the Pauli operators for the probe qubit, $2J = \sqrt{2\Gamma_{1\mathrm{D,p}}\Gamma_{1\mathrm{D}}}$ is the interaction between probe qubit and dark state, and $\mathcal{D}[\cdot]$ is the Lindblad dissipator defined in Eq. (B.3). The full level structure of the $2^3 = 8$ states of three qubits and the rates in the system are summarized in Fig. B.2a. Note that the effective (non-Hermitian) Hamiltonian $\hat{H}_\mathrm{eff}$ in the main text can be obtained from absorbing part of the Liouvillian in Eq. (B.18) excluding terms associated with quantum jumps.

To reach the dark state of the atomic cavity, we first apply a local gate $|\mathrm{g}\rangle_\mathrm{p}|\mathrm{G}\rangle \to |\mathrm{e}\rangle_\mathrm{p}|\mathrm{G}\rangle$ on the probe qubit (Ω_XY in Fig. B.2a) to prepare the state in the first-excitation manifold. Then, the Rabi oscillation $|\mathrm{e}\rangle_\mathrm{p}|\mathrm{G}\rangle \leftrightarrow |\mathrm{g}\rangle_\mathrm{p}|\mathrm{D}\rangle$ takes place with the rate of J. We can identify $g = J$, $\gamma = \Gamma_{1\mathrm{D,p}} + \Gamma'_\mathrm{p}$, $\kappa = \Gamma'$ in analogy to cavity QED (Fig. 4.1 and Fig. B.2b) and calculate cooperativity as

$$\mathcal{C} = \frac{(2J)^2}{\Gamma_{1,\mathrm{p}}\Gamma_{1,\mathrm{D}}} = \frac{2\Gamma_{1\mathrm{D,p}}\Gamma_{1\mathrm{D}}}{(\Gamma_{1\mathrm{D,p}} + \Gamma'_\mathrm{p})\Gamma'} \approx \frac{2\Gamma_{1\mathrm{D}}}{\Gamma'},$$

when the spurious loss rate Γ' is small. A high cooperativity can be achieved in this case due to collective suppression of radiation in atomic cavity and cooperative enhancement in the interaction, scaling linearly with the Purcell factor $P_{1\mathrm{D}} = \Gamma_{1\mathrm{D}}/\Gamma'$. Thus, we can successfully map the population from the excited state of probe qubit to dark state of mirror qubits with the interaction time of $(2J/\pi)^{-1}$.

Going further, we attempt to reach the second-excited state $|\mathrm{E}\rangle = (\hat{S}_\mathrm{D}^\dagger)^2|\mathrm{G}\rangle$ of atomic cavity. After the state preparation of $|\mathrm{g}\rangle_\mathrm{p}|\mathrm{D}\rangle$ mentioned above, we apply another local gate $|\mathrm{g}\rangle_\mathrm{p}|\mathrm{D}\rangle \to |\mathrm{e}\rangle_\mathrm{p}|\mathrm{D}\rangle$ on the probe qubit and prepare the state in the second-excitation manifold. In this case, the second excited states $|\mathrm{e}\rangle_\mathrm{p}|\mathrm{D}\rangle \leftrightarrow |\mathrm{g}\rangle_\mathrm{p}|\mathrm{E}\rangle$ have interaction strength J, same as the first excitation, while the $|\mathrm{E}\rangle$ state becomes highly radiative to waveguide channel. The cooperativity $\mathcal{C}$ is calculated as

$$\mathcal{C} = \frac{(2J)^2}{\Gamma_{1,\mathrm{p}}\Gamma_{1,\mathrm{E}}} = \frac{2\Gamma_{1\mathrm{D,p}}\Gamma_{1\mathrm{D}}}{(\Gamma_{1\mathrm{D,p}} + \Gamma'_\mathrm{p})(2\Gamma_{1\mathrm{D}} + \Gamma')} < 1,$$

which is always smaller than unity. Therefore, the state $|\mathrm{g}\rangle_\mathrm{p}|\mathrm{E}\rangle$ is only virtually populated and the interaction maps the population in $|\mathrm{e}\rangle_\mathrm{p}|\mathrm{D}\rangle$ to $|\mathrm{g}\rangle_\mathrm{p}|\mathrm{B}\rangle$ with the rate of $(2J)^2/(2\Gamma_{1\mathrm{D}}) = \Gamma_{1\mathrm{D,p}}$. This process competes with radiative decay (at a rate of $\Gamma_{1\mathrm{D,p}}$) of probe qubit $|\mathrm{e}\rangle_\mathrm{p}|\mathrm{D}\rangle \to |\mathrm{g}\rangle_\mathrm{p}|\mathrm{D}\rangle$ followed by the Rabi oscillation in the first-excitation manifold, giving rise to damped Rabi oscillation in Fig. 4.6c.

Effect of phase length mismatch

Deviation of phase length between mirror qubits from $\lambda/2$ along the waveguide can act as a non-ideal contribution in the dynamics of atomic cavity. The waveguide decay rate of dark state can be written as $\Gamma_{\mathrm{1D,D}} = \Gamma_{\mathrm{1D}}(1-|\cos\phi|)$, where $\phi = k_{\mathrm{1D}}d$ is the phase separation between mirror qubits [145]. Here, k_{1D} is the wavenumber and d is the distance between mirror qubits.

We consider the case where the phase mismatch $\Delta\phi = \phi - \pi$ of mirror qubits is small. The decay rate of the dark state scales as $\Gamma_{\mathrm{1D,D}} \approx \Gamma_{\mathrm{1D}}(\Delta\phi)^2/2$ only adding a small contribution to the decay rate of dark state. Based on the decay rate of dark states from time-domain measurement in Table B.2, we estimate the upper bound on the phase mismatch $\Delta\phi/\pi$ to be 5% for type-I and 3.5% for type-II.

Effect of asymmetry in Γ_{1D}

So far we have assumed that the waveguide decay rate Γ_{1D} of mirror qubits are identical and neglected the asymmetry. If the waveguide decay rates of mirror qubits are given by $\Gamma_{\mathrm{1D,1}} \neq \Gamma_{\mathrm{1D,2}}$, the dark state and bright state are redefined as

$$|\mathrm{D}\rangle = \frac{\sqrt{\Gamma_{\mathrm{1D,2}}}|\mathrm{eg}\rangle + \sqrt{\Gamma_{\mathrm{1D,1}}}|\mathrm{ge}\rangle}{\sqrt{\Gamma_{\mathrm{1D,1}}+\Gamma_{\mathrm{1D,2}}}}, \quad |\mathrm{B}\rangle = \frac{\sqrt{\Gamma_{\mathrm{1D,1}}}|\mathrm{eg}\rangle - \sqrt{\Gamma_{\mathrm{1D,2}}}|\mathrm{ge}\rangle}{\sqrt{\Gamma_{\mathrm{1D,1}}+\Gamma_{\mathrm{1D,2}}}}, \tag{B.19}$$

with collectively suppressed and enhanced waveguide decay rates of $\Gamma_{\mathrm{1D,D}} = 0$, $\Gamma_{\mathrm{1D,B}} = \Gamma_{\mathrm{1D,1}} + \Gamma_{\mathrm{1D,2}}$, remaining fully dark and fully bright even in the presence of asymmetry. We also generalize Eq. (B.16) as

$$\hat{S}_{\mathrm{D}} = \frac{\sqrt{\Gamma_{\mathrm{1D,2}}}\hat{\sigma}_-^{(1)} + \sqrt{\Gamma_{\mathrm{1D,1}}}\hat{\sigma}_-^{(2)}}{\sqrt{\Gamma_{\mathrm{1D,1}}+\Gamma_{\mathrm{1D,2}}}}, \quad \hat{S}_{\mathrm{B}} = \frac{\sqrt{\Gamma_{\mathrm{1D,1}}}\hat{\sigma}_-^{(1)} - \sqrt{\Gamma_{\mathrm{1D,2}}}\hat{\sigma}_-^{(2)}}{\sqrt{\Gamma_{\mathrm{1D,1}}+\Gamma_{\mathrm{1D,2}}}}. \tag{B.20}$$

With this basis, the Hamiltonian can be written as

$$\hat{H} = \hbar J_{\mathrm{D}}\left(\hat{\sigma}_-^{(\mathrm{p})}\hat{S}_{\mathrm{D}}^\dagger + \hat{\sigma}_+^{(\mathrm{p})}\hat{S}_{\mathrm{D}}\right) + \hbar J_{\mathrm{B}}\left(\hat{\sigma}_-^{(\mathrm{p})}\hat{S}_{\mathrm{B}}^\dagger + \hat{\sigma}_+^{(\mathrm{p})}\hat{S}_{\mathrm{B}}\right), \tag{B.21}$$

where

$$J_{\mathrm{D}} = \frac{\sqrt{\Gamma_{\mathrm{1D,p}}\Gamma_{\mathrm{1D,1}}\Gamma_{\mathrm{1D,2}}}}{\sqrt{\Gamma_{\mathrm{1D,1}}+\Gamma_{\mathrm{1D,2}}}}, \quad J_{\mathrm{B}} = \frac{\sqrt{\Gamma_{\mathrm{1D,p}}}(\Gamma_{\mathrm{1D,1}}-\Gamma_{\mathrm{1D,2}})}{2\sqrt{\Gamma_{\mathrm{1D,1}}+\Gamma_{\mathrm{1D,2}}}}.$$

Thus, the probe qubit interacts with both the dark state and bright state with the ratio of $J_{\mathrm{D}} : J_{\mathrm{B}} = 2\sqrt{\Gamma_{\mathrm{1D,1}}\Gamma_{\mathrm{1D,2}}} : (\Gamma_{\mathrm{1D,1}} - \Gamma_{\mathrm{1D,2}})$, and thus for a small asymmetry in the waveguide decay rate, the coupling to the dark state dominates the dynamics. In addition, we note that the bright state superradiantly decays to the waveguide, and it follows that coupling of probe qubit to the bright state manifest only as contribution of

$$\frac{(2J_{\mathrm{B}})^2}{\Gamma_{\mathrm{1D},1}+\Gamma_{\mathrm{1D},2}} = \Gamma_{\mathrm{1D,p}}\left(\frac{\Gamma_{\mathrm{1D},1}-\Gamma_{\mathrm{1D},2}}{\Gamma_{\mathrm{1D},1}+\Gamma_{\mathrm{1D},2}}\right)^2$$

to the probe qubit decay rate into spurious loss channel. In our experiment, the maximum asymmetry $d = \frac{|\Gamma_{\mathrm{1D},1}-\Gamma_{\mathrm{1D},2}|}{\Gamma_{\mathrm{1D},1}+\Gamma_{\mathrm{1D},2}}$ in waveguide decay rate between qubits is 0.14 (0.03) for type-I (type-II) from Table B.1, and this affects the decay rate of probe qubit by at most $\sim 2\%$.

Fitting of Rabi oscillation curves

The Rabi oscillation curves in Fig. 4.4 and Fig. 4.7d are modeled using a numerical master equation solver [21]. The qubit parameters used for fitting the Rabi oscillation curves are summarized in Table B.1. For all the qubits, Γ_{1D} was found from spectroscopy. In addition, we have done a time-domain population decay measurement on the probe qubit to find the total decay rate of $\Gamma_1/2\pi = 1.1946$ MHz (95% confidence interval $[1.1644, 1.2263]$ MHz, measured at 6.55 GHz). Using the value of $\Gamma_{\mathrm{1D}}/2\pi = 1.1881$ MHz (95% confidence interval $[1.1550, 1.2211]$ MHz, measured at 6.6 GHz) from spectroscopy, we find the spurious population decay rate $\Gamma_{\mathrm{loss}}/2\pi = \Gamma_1/2\pi - \Gamma_{\mathrm{1D}}/2\pi = 6.5$ kHz (with uncertainty of 45.3 kHz) for the probe qubit. The value of spurious population decay rate is assumed to be identical for all the qubits in the experiment. Note that the decaying rate of the envelope in the Rabi oscillation curve is primarily set by the waveguide decay rate of the probe qubit $\Gamma_{\mathrm{1D,p}}$, and the large relative uncertainty in Γ_{loss} does not substantially affect the fit curve.

The dephasing rate of the probe qubit is derived from time-domain population decay and Ramsey sequence measurements $\Gamma_\varphi = \Gamma_2 - \Gamma_1/2$. In the case of the mirror qubits, the table shows effective single qubit parameters inferred from measurements of the dark state lifetime. We calculate single mirror qubit dephasing rates that theoretically yield the corresponding measured collective value. Assuming an uncorrelated Markovian dephasing for the mirror qubits forming the cavity we find $\Gamma_{\varphi,\mathrm{m}} = \Gamma_{\varphi,\mathrm{D}}$ (App. B.3). Similarly, the waveguide decay rate of the mirror qubits is found from the spectroscopy of the bright collective state as $\Gamma_{\mathrm{1D,m}} = \Gamma_{\mathrm{1D,B}}/2$. The detuning between probe qubit and the atomic cavity (Δ) is treated as the only free parameter in our model. The value of Δ sets the visibility and frequency of the Rabi oscillation, and is found from the the fitting algorithm.

Type	Qubits involved	$\Gamma_{1D,p}/2\pi$ (MHz)	$\Gamma_{1D,m}/2\pi$ (MHz)	$\Gamma_{\varphi,p}/2\pi$ (kHz)	$\Gamma_{\varphi,m}/2\pi$ (kHz)	$\Delta/2\pi$ (MHz)
I	Q_2, Q_6	1.19	13.4	191	210	1.0
II	Q_1, Q_7	0.87	96.7	332	581	5.9
Dark compound	Q_2Q_3, Q_5Q_6	1.19	4.3	191	146	0.9
Bright compound	Q_2Q_3, Q_5Q_6	1.19	20.2	191	253	1.4

Table B.1: **Parameters used for fitting Rabi oscillation curves.** The first and second row are the data for 2-qubit dark states, the third and fourth row are the data for 4-qubit dark states made of compound mirrors. Here, $\Gamma_{1D,p}$ ($\Gamma_{1D,m}$) is the waveguide decay rate and $\Gamma_{\varphi,p}$ ($\Gamma_{\varphi,m}$) is the pure dephasing rate of probe (mirror) qubit, Δ is the detuning between probe qubit and mirror qubits used for fitting the data.

B.3 Lifetime (T_1) and coherence time (T_2^*) of dark state

The dark state of mirror qubits belongs to the decoherence-free subspace in the system due to its collectively suppressed radiation to the waveguide channel. However, there exists non-ideal channels that each qubit is coupled to, and such channels contribute to the finite lifetime (T_1) and coherence time (T_2^*) of the dark state (See Table B.2). In the experiment, we have measured the decoherence rate $\Gamma_{2,D}$ of the dark state to be always larger than the decay rate $\Gamma_{1,D}$, which cannot be explained by simple Markovian model of two qubits subject to their own independent noise. We discuss possible scenarios that can give rise to this situation of $\Gamma_{2,D} > \Gamma_{1,D}$, with distinction of the Markovian and non-Markovian noise contributions.

Type	Qubits involved	$\Gamma_{1,D}/2\pi$ (kHz)	$\Gamma_{2,D}/2\pi$ (kHz)
I	Q_2, Q_6	210	366
II	Q_1, Q_7	581	838
Dark compound	Q_2Q_3, Q_5Q_6	146	215
Bright compound	Q_2Q_3, Q_5Q_6	253	376

Table B.2: **Decay rate and decoherence rate of dark states.** The first and second row are the data for 2-qubit dark states, the third and fourth row are the data for 4-qubit dark states made of compound mirrors. Here, $\Gamma_{1,D}$ ($\Gamma_{2,D}$) is the decay (decoherence) rate of the dark state.

There are two major channels that can affect the coherence of the dark state. First, coupling of a qubit to dissipative channels other than the waveguide can give rise to additional decay rate $\Gamma_{\text{loss}} = \Gamma_1 - \Gamma_{\text{1D}}$ (so-called non-radiative decay rate). This type of decoherence is uncorrelated between qubits and is well understood in terms of the Lindblad form of master equation, whose contribution to lifetime and coherence time of dark state is similar as in individual qubit case. Another type of contribution that severely affects the dark state coherence arises from fluctuations in qubit frequency, which manifest as pure dephasing rate Γ_φ in the individual qubit case. This can affect the decoherence of the dark state in two ways: (i) By accumulating a relative phase between different qubit states, this act as a channel to map the dark state into the bright state with short lifetime, and hence contributes to loss of population in the dark state; (ii) fluctuations in qubit frequency also induces the frequency jitter of the dark state and therefore contributes to the dephasing of dark state.

In the following, we model the aforementioned contributions to the decoherence of dark state. Let us consider two qubits separated by $\lambda/2$ along the waveguide on resonance, in the presence of fluctuations $\tilde{\Delta}_j(t)$ in the qubit frequency. The master equation can be written as $\dot{\hat{\rho}} = -i[\hat{H}/\hbar, \hat{\rho}] + \mathcal{L}[\hat{\rho}]$, where the Hamiltonian $\hat{H}$ and the Liouvillian $\mathcal{L}$ are given by

$$\hat{H}(t) = \hbar \sum_{j=1,2} \tilde{\Delta}_j(t)\hat{\sigma}_+^{(j)}\hat{\sigma}_-^{(j)}, \tag{B.22}$$

$$\mathcal{L}[\rho] = \sum_{j,k=1,2} \left[(-1)^{j-k}\Gamma_{\text{1D}} + \delta_{jk}\Gamma_{\text{loss}}\right] \left(\hat{\sigma}_-^{(j)}\hat{\rho}\hat{\sigma}_+^{(k)} - \frac{1}{2}\{\hat{\sigma}_+^{(k)}\hat{\sigma}_-^{(j)}, \hat{\rho}\}\right). \tag{B.23}$$

Here, Γ_{1D} (Γ_{loss}) is the decay rate of qubits into waveguide (spurious loss) channel. Note that we have assumed the magnitude of fluctuation $\tilde{\Delta}_j(t)$ in qubit frequency is small and neglected its effect on exchange interaction and correlated decay. We investigate two scenarios in the following subsections depending on the correlation of noise that gives rise to qubit frequency fluctuations.

Markovian noise

If the frequency fluctuations of the individual qubits satisfy the conditions for Born and Markov approximations, i.e. the noise is weakly coupled to the qubit and has short correlation time, the frequency jitter can be described in terms of the standard Lindblad form of dephasing [305].

More generally, we also consider the correlation between frequency jitter of different qubits. Such contribution can arise when different qubits are coupled to a single fluctuating noise source. For instance, if two qubits in a system couple to a magnetic field $B_0+\tilde{B}(t)$ that is global to the chip with $D_j \equiv \partial\tilde{\Delta}_j/\partial\tilde{B}$, the correlation between detuning of different qubits follows correlation of the fluctuations in magnetic field, giving $\langle\tilde{\Delta}_1(t)\tilde{\Delta}_2(t+\tau)\rangle = D_1 D_2\langle\tilde{B}(t)\tilde{B}(t+\tau)\rangle \neq 0$. The Liouvillian associated with dephasing can be written as [307]

$$\mathcal{L}_{\varphi,jk}[\hat{\rho}] = \frac{\Gamma_{\varphi,jk}}{2}\left(\hat{\sigma}_z^{(j)}\hat{\rho}\hat{\sigma}_z^{(k)} - \frac{1}{2}\left\{\hat{\sigma}_z^{(k)}\hat{\sigma}_z^{(j)},\hat{\rho}\right\}\right), \tag{B.24}$$

where the dephasing rate $\Gamma_{\varphi,jk}$ between qubit j and qubit k ($j = k$ denotes individual qubit dephasing and $j \neq k$ is the correlated dephasing) is given by

$$\Gamma_{\varphi,jk} \equiv \frac{1}{2}\int_{-\infty}^{+\infty} \mathrm{d}\tau\, \langle\tilde{\Delta}_j(0)\tilde{\Delta}_k(\tau)\rangle. \tag{B.25}$$

Here, the average $\langle\cdot\rangle$ is taken over an ensemble of fluctuators in the environment. Note that the correlated dephasing rate $\Gamma_{\varphi,jk}$ can be either positive or negative depending on the sign of noise correlation, while the individual pure dephasing rate $\Gamma_{\varphi,jj}$ is always positive.

After we incorporate the frequency jitter as the dephasing contributions to the Liouvillian, the master equation takes the form

$$\begin{aligned}\dot{\hat{\rho}} = \sum_{j,k=1,2}\Bigg\{&\left[(-1)^{j-k}\Gamma_{1\mathrm{D}} + \delta_{jk}\Gamma_{\mathrm{loss}}\right]\left(\hat{\sigma}_-^{(j)}\hat{\rho}\hat{\sigma}_+^{(k)} - \frac{1}{2}\{\hat{\sigma}_+^{(k)}\hat{\sigma}_-^{(j)},\hat{\rho}\}\right)\\ &+\frac{\Gamma_{\varphi,jk}}{2}\left(\hat{\sigma}_z^{(j)}\hat{\rho}\hat{\sigma}_z^{(k)} - \frac{1}{2}\left\{\hat{\sigma}_z^{(k)}\hat{\sigma}_z^{(j)},\hat{\rho}\right\}\right)\Bigg\},\end{aligned} \tag{B.26}$$

We diagonalize the correlated decay part of the Liouvillian describe the two-qubit system in terms of bright and dark states defined in Eq. (B.15). From now on, we assume the pure dephasing rate and the correlated dephasing rate are identical for the two qubits, and write $\Gamma_\varphi \equiv \Gamma_{\varphi,11} = \Gamma_{\varphi,22}$, $\Gamma_{\varphi,\mathrm{c}} \equiv \Gamma_{\varphi,12} = \Gamma_{\varphi,21}$. For qubits with a large Purcell factor ($\Gamma_{1\mathrm{D}} \gg \Gamma_\varphi, |\Gamma_{\varphi,\mathrm{c}}|, \Gamma_{\mathrm{loss}}$), we can assume that the superradiant states $|\mathrm{B}\rangle$ and $|\mathrm{E}\rangle$ are only virtually populated [129] and neglect the density matrix elements associated with $|\mathrm{B}\rangle$ and $|\mathrm{E}\rangle$. Rewriting Eq. (B.26) in the basis of $\{|\mathrm{G}\rangle, |\mathrm{B}\rangle, |\mathrm{D}\rangle, |\mathrm{E}\rangle\}$, the dynamics related to dark state can be expressed as $\dot{\rho}_{\mathrm{D,D}} \approx -\Gamma_{1,\mathrm{D}}\rho_{\mathrm{D,D}}$ and $\dot{\rho}_{\mathrm{D,G}} \approx -\Gamma_{2,\mathrm{D}}\rho_{\mathrm{D,G}}$, where

$$\Gamma_{1,\mathrm{D}} = \Gamma_{\mathrm{loss}} + \Gamma_\varphi - \Gamma_{\varphi,\mathrm{c}}, \quad \Gamma_{2,\mathrm{D}} = \frac{\Gamma_{\mathrm{loss}}}{2} + \Gamma_\varphi. \tag{B.27}$$

Note that if the correlated dephasing rate $\Gamma_{\varphi,\mathrm{c}}$ is zero, $\Gamma_{1,\mathrm{D}}$ is always larger than $\Gamma_{2,\mathrm{D}}$, which is in contradiction to our measurement result.

We estimate the decay rate into non-ideal channels to be $\Gamma_{\mathrm{loss}}/2\pi = 6.5\,\mathrm{kHz}$ from the difference in Γ_1 and $\Gamma_{1\mathrm{D}}$ of the probe qubit, and assume Γ_{loss} to be similar for all the qubits. Applying Eq. (B.27) to measured values of $\Gamma_{2,\mathrm{D}}$ listed in Table B.2, we expect that the pure dephasing of the individual qubit is the dominant decay and decoherence source for the dark state. In addition, we compare the decay rate $\Gamma_{1,\mathrm{D}}$ and decoherence rate $\Gamma_{2,\mathrm{D}}$ of dark states in the Markovian noise model and infer that the correlated dephasing rate $\Gamma_{\varphi,\mathrm{c}}$ is positive and is around a third of the individual dephasing rate Γ_{φ} for all types of mirror qubits.

Non-Markovian noise

In a realistic experimental setup, there also exists non-Markovian noise sources contributing to the dephasing of the qubits, e.g. $1/f$-noise or quasi-static noise [69, 308, 309]. In such cases, the frequency jitter cannot be simply put into the Lindblad form as described above. In this subsection, we consider how the individual qubit dephasing induced by non-Markovian noise influences the decoherence of dark state. As shown below, we find that a non-Markovian noise source can lead to a shorter coherence time to lifetime ratio for the dark states, in a similar fashion to correlated dephasing. However, we find that the functional form of the visibility of Ramsey fringes is not necessarily an exponential for a non-Markovian noise source.

We start from the master equation introduced in Eqs. (B.22)-(B.23) can be written in terms of the basis of $\{|\mathrm{G}\rangle, |\mathrm{B}\rangle, |\mathrm{D}\rangle, |\mathrm{E}\rangle\}$,

$$\dot{\hat{\rho}} = -\frac{i}{\hbar}[\hat{H}, \hat{\rho}] + (2\Gamma_{1\mathrm{D}} + \Gamma_{\mathrm{loss}})\,\mathcal{D}[\hat{S}_{\mathrm{B}}]\hat{\rho} + \Gamma_{\mathrm{loss}}\mathcal{D}[\hat{S}_{\mathrm{D}}]\hat{\rho}, \tag{B.28}$$

where the Hamiltonian is written using the common frequency jitter $\tilde{\Delta}_c(t) \equiv [\tilde{\Delta}_1(t) + \tilde{\Delta}_2(t)]/2$ and differential frequency jitter $\tilde{\Delta}_d(t) \equiv [\tilde{\Delta}_1(t) - \tilde{\Delta}_2(t)]/2$

$$\hat{H}(t)/\hbar = \tilde{\Delta}_c(t)\left(2|\mathrm{E}\rangle\langle\mathrm{E}| + |\mathrm{D}\rangle\langle\mathrm{D}| + |\mathrm{B}\rangle\langle\mathrm{B}|\right) + \tilde{\Delta}_d(t)\left(|\mathrm{B}\rangle\langle\mathrm{D}| + |\mathrm{D}\rangle\langle\mathrm{B}|\right). \tag{B.29}$$

Here, $\hat{S}_{\mathrm{B}}$ and $\hat{S}_{\mathrm{D}}$ are defined in Eq. (B.16). From the Hamiltonian in Eq. (B.29), we see that the common part of frequency fluctuation $\tilde{\Delta}_c(t)$ results in the frequency jitter of the dark state while the differential part of frequency fluctuation $\tilde{\Delta}_d(t)$ drives the transition between $|\mathrm{D}\rangle$ and $|\mathrm{B}\rangle$, which acts as a decay channel for the dark state.

For uncorrelated low-frequency noise on the two qubits, the decoherence rate is approximately the standard deviation of the common frequency jitter $\sqrt{\langle\tilde{\Delta}_c(t)^2\rangle}$. The decay rate in this model can be found by modeling the bright state as a cavity in the Purcell regime, and calculate the damping rate of the dark state using the Purcell factor as $\langle 4\tilde{\Delta}_d(t)^2/\Gamma_\mathrm{B}\rangle$. As evident, in this model the dark state's population decay rate is strongly suppressed by the large damping rate of bright state Γ_B, while the dark state's coherence time can be sharply reduced due to dephasing.

B.4 Shelving

We consider the case of two identical mirror qubits of frequency ω_q, separated by distance $\lambda/2$ along the waveguide. In addition to free evolution of qubits, we include a coherent probe signal from the waveguide in the analysis. In the absence of pure dephasing ($\Gamma_\varphi = 0$) and thermal occupancy ($\bar{n}_\mathrm{th} = 0$), the master equation in the rotating frame of the probe signal takes the same form as Eq. (B.28), where the Hamiltonian containing the drive from the probe signal is written as

$$\hat{H}/\hbar = \sum_{\mu=\mathrm{B,D}} \left[-\delta\omega\, \hat{S}_\mu^\dagger \hat{S}_\mu + \frac{\Omega_\mu}{2}\left(\hat{S}_\mu + \hat{S}_\mu^\dagger\right)\right], \tag{B.30}$$

where $\hat{S}_\mathrm{B}$ and $\hat{S}_\mathrm{D}$ are defined in Eq. (B.16), $\delta\omega = \omega_\mathrm{p} - \omega_\mathrm{q}$ is the detuning of the probe signal from the mirror qubit frequency, Ω_μ is the corresponding driven Rabi frequency. Note that due to the symmetry of the excitations with respect to the waveguide, we see that $\Omega_\mathrm{D} = 0$ and $\Omega_\mathrm{B} = \sqrt{2}\Omega_1$, where Ω_1 is the Rabi frequency of one of the mirror qubits from the probe signal along the waveguide.

Let us consider the limit where the Purcell factor $P_\mathrm{1D} = \Gamma_\mathrm{1D}/\Gamma'$ of qubits is much larger than unity (equivalent to $\Gamma_\mathrm{D} = \Gamma' \ll \Gamma_\mathrm{B} = 2\Gamma_\mathrm{1D} + \Gamma'$) and the drive applied to the qubits is weak $\Omega_\mathrm{B} \ll \Gamma_\mathrm{B}$. Then, we can effectively remove some of the density matrix elements [1],

$$\rho_\mathrm{E,E},\ \rho_\mathrm{B,E},\ \rho_\mathrm{E,B},\ \rho_\mathrm{G,E},\ \rho_\mathrm{E,G} \approx 0$$

[1] From the master equation, the time-evolution of part of the density matrix elements are approximately written as

$$\begin{aligned}
\dot{\rho}_\mathrm{E,E} &= -(\Gamma_\mathrm{B} + \Gamma_\mathrm{D})\rho_\mathrm{E,E} + \frac{i\Omega_\mathrm{B}}{2}(\rho_\mathrm{B,E} - \rho_\mathrm{E,B}),\\
\dot{\rho}_\mathrm{E,B} &= \left[i\delta\omega - \left(\Gamma_\mathrm{B} + \frac{\Gamma_\mathrm{D}}{2}\right)\right]\rho_\mathrm{E,B} + \frac{i\Omega_\mathrm{B}}{2}(\rho_\mathrm{B,B} - \rho_\mathrm{E,E} + \rho_\mathrm{E,G}),\\
\dot{\rho}_\mathrm{E,G} &= \left(2i\delta\omega - \frac{\Gamma_\mathrm{B} + \Gamma_\mathrm{D}}{2}\right)\rho_\mathrm{E,G} + \frac{i\Omega_\mathrm{B}}{2}(\rho_\mathrm{B,G} + \rho_\mathrm{E,B}),\\
\dot{\rho}_\mathrm{E,B} &= \dot{\rho}^*_\mathrm{B,E}; \quad \dot{\rho}_\mathrm{E,G} = \dot{\rho}^*_\mathrm{G,E}.
\end{aligned}$$

and restrict the analysis to ones involved with three levels $\{|\mathrm{G}\rangle, |\mathrm{D}\rangle, |\mathrm{B}\rangle\}$. In addition, the dark state $|\mathrm{D}\rangle$ is effectively decoupled from $|\mathrm{G}\rangle$ and $|\mathrm{B}\rangle$, acting as a metastable state. Therefore, we only consider the following set of the master equation:

$$\dot{\rho}_{\mathrm{B,B}} \approx -\Gamma_{\mathrm{B}}\, \rho_{\mathrm{B,B}} + \frac{i\Omega_{\mathrm{B}}}{2}(\rho_{\mathrm{B,G}} - \rho_{\mathrm{G,B}}) \tag{B.31}$$

$$\dot{\rho}_{\mathrm{B,G}} \approx \left(i\delta\omega - \frac{\Gamma_{\mathrm{B}}}{2}\right)\rho_{\mathrm{B,G}} + \frac{i\Omega_{\mathrm{B}}}{2}(\rho_{\mathrm{B,B}} - \rho_{\mathrm{G,G}}) \tag{B.32}$$

$$\dot{\rho}_{\mathrm{G,G}} \approx -\dot{\rho}_{\mathrm{B,B}}; \quad \dot{\rho}_{\mathrm{G,B}} = \dot{\rho}^*_{\mathrm{B,G}} \tag{B.33}$$

Using the normalization of total population $\rho_{\mathrm{G,G}} + \rho_{\mathrm{D,D}} + \rho_{\mathrm{B,B}} \approx 1$ with Eqs. (B.31)-(B.33), we obtain the approximate steady-state solution

$$\langle \hat{S}_{\mathrm{B}} \rangle \approx \rho_{\mathrm{B,G}} \approx -\frac{i\Omega_{\mathrm{B}}(1-\rho_{\mathrm{D,D}})}{\Gamma_{\mathrm{B}} - 2i\delta\omega}. \tag{B.34}$$

The input-output relation [145] is given as

$$\hat{a}_{\mathrm{out}} = \hat{a}_{\mathrm{in}} + \sqrt{\frac{\Gamma_{\mathrm{1D}}}{2}}\hat{\sigma}_-^{(1)} - \sqrt{\frac{\Gamma_{\mathrm{1D}}}{2}}\hat{\sigma}_-^{(2)} = \hat{a}_{\mathrm{in}} + \sqrt{\Gamma_{\mathrm{1D}}}\hat{S}_{\mathrm{B}}, \tag{B.35}$$

where $\hat{a}_{\mathrm{in}}$ is the input field operator and $\hat{a}_{\mathrm{out}}$ is the operator for output field propagating in the same direction as the input field (here, the input field is assumed to be incident from only one direction). The transmission amplitude is calculated as

$$t = \frac{\langle \hat{a}_{\mathrm{out}} \rangle}{\langle \hat{a}_{\mathrm{in}} \rangle} = 1 - \frac{(1-\rho_{\mathrm{D,D}})\Gamma_{\mathrm{1D}}}{-i\delta\omega + \Gamma_{\mathrm{B}}/2} \tag{B.36}$$

where the relation $\Omega_1/2 = -i\langle \hat{a}_{\mathrm{in}} \rangle \sqrt{\Gamma_{\mathrm{1D}}/2}$ has been used.

In the measurement, we use the state transfer protocol to transfer part of the ground state population into the dark state. Following this, we drive the $|\mathrm{G}\rangle \leftrightarrow |\mathrm{B}\rangle$ transition by sending a weak coherent pulse with a duration 260 ns into the waveguide, and recording the transmission spectrum. As a comparison, we also measure

In the steady state, it can be shown that

$$\begin{aligned}
\rho_{\mathrm{E,E}} &\sim \mathcal{O}(x^2)\rho_{\mathrm{B,B}} + \mathcal{O}(x^3)(\rho_{\mathrm{B,G}} - \rho_{\mathrm{G,B}}) \\
\rho_{\mathrm{B,E}} &\sim \mathcal{O}(x)\rho_{\mathrm{B,B}} + \mathcal{O}(x^2)\rho_{\mathrm{G,B}} \\
\rho_{\mathrm{G,E}} &\sim \mathcal{O}(x^2)\rho_{\mathrm{B,B}} + \mathcal{O}(x)\rho_{\mathrm{G,B}}
\end{aligned}$$

to leading order in $x \equiv \Omega_{\mathrm{B}}/\Gamma_{\mathrm{B}} < 1$, and hence we can neglect the contributions from $\rho_{\mathrm{E,E}}$, $\rho_{\mathrm{B,E}}$, $\rho_{\mathrm{E,B}}$, $\rho_{\mathrm{G,E}}$, $\rho_{\mathrm{E,G}}$ from the analysis in the weak driving limit. The probe power we have used in the experiment corresponds to $x \sim 0.15$, which makes this approximation valid.

the transmission spectrum when the mirror qubits are in the ground state, which corresponds to having $\rho_{\mathrm{D,D}} = 0$. The transmittance in the two cases (Fig. 4.6a) are fitted with identical parameters for Γ_{1D} and Γ_{B}. The dark state population $\rho_{\mathrm{D,D}}$ following the iSWAP gate is extracted from the data as 0.58, which is lower than the value (0.68) found from the Rabi oscillation peaks (Fig. 4.4). The lower value of the dark state population can be understood considering the finite lifetime of dark state ($757\,\mathrm{ns}$), which leads to a partial population decay during the measurement time (the single-shot measurement time is set by the duration of the input pulse). It should be noted that the input pulse has a transform-limited bandwidth of ~ 3.8 MHz, which results in frequency averaging of the spectral response over this bandwidth. For this reason, the on-resonance transmission extinction measured in the pulsed scheme is lower than the value found from continuous wave (CW) measurement (Fig. 4.2b).

Appendix C

SUPPLEMENTARY INFORMATION FOR CHAPTER 5

C.1 Modeling of the topological waveguide

In this section we provide a theoretical description of the topological waveguide discussed in the main text, an analog to the Su-Schrieffer-Heeger model [205]. An approximate form of the physically realized waveguide is given by an array of coupled LC resonators, a unit cell of which is illustrated in Fig. C.1. Each unit cell of the topological waveguide has two sites A and B whose intra- and inter-cell coupling capacitance (mutual inductance) are given by C_v (M_v) and C_w (M_w). We denote the flux variable of each node as $\Phi_n^\alpha(t) \equiv \int_{-\infty}^{t} \mathrm{d}t' \, V_n^\alpha(t')$ and the current going through each inductor as i_n^α ($\alpha = \{\mathrm{A}, \mathrm{B}\}$). The Lagrangian in position space reads

$$\mathcal{L} = \sum_n \Bigg\{ \frac{C_v}{2}\left(\dot{\Phi}_n^{\mathrm{B}} - \dot{\Phi}_n^{\mathrm{A}}\right)^2 + \frac{C_w}{2}\left(\dot{\Phi}_{n+1}^{\mathrm{A}} - \dot{\Phi}_n^{\mathrm{B}}\right)^2 + \frac{C_0}{2}\left[\left(\dot{\Phi}_n^{\mathrm{A}}\right)^2 + \left(\dot{\Phi}_n^{\mathrm{B}}\right)^2\right] - \frac{L_0}{2}\left[\left(i_n^{\mathrm{A}}\right)^2 + \left(i_n^{\mathrm{B}}\right)^2\right] - M_v i_n^{\mathrm{A}} i_n^{\mathrm{B}} - M_w i_n^{\mathrm{B}} i_{n+1}^{\mathrm{A}} \Bigg\}. \tag{C.1}$$

The node flux variables are written in terms of current through the inductors as

$$\Phi_n^{\mathrm{A}} = L_0 i_n^{\mathrm{A}} + M_v i_n^{\mathrm{B}} + M_w i_{n-1}^{\mathrm{B}}, \quad \Phi_n^{\mathrm{B}} = L_0 i_n^{\mathrm{B}} + M_v i_n^{\mathrm{A}} + M_w i_{n+1}^{\mathrm{A}}. \tag{C.2}$$

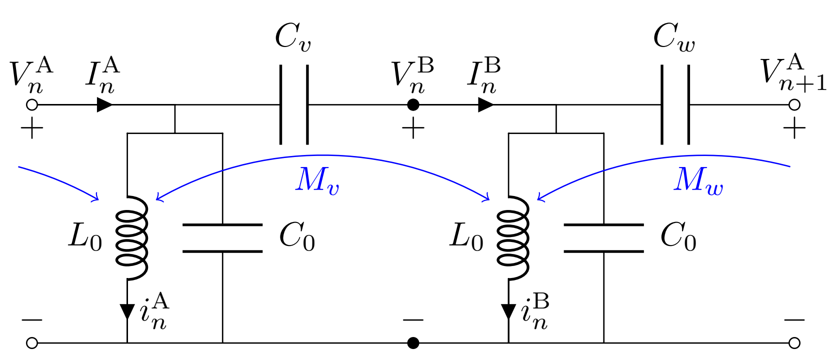

Figure C.1: LC resonators of inductance L_0 and capacitance C_0 are coupled with alternating coupling capacitance C_v, C_w and mutual inductance M_v, M_w. The voltage and current at each resonator node A (B) are denoted as V_n^{A}, I_n^{A} (V_n^{B}, I_n^{B}).

Considering the discrete translational symmetry in our system, we can rewrite the variables in terms of Fourier components as

$$\Phi_n^\alpha = \frac{1}{\sqrt{N}} \sum_k e^{inkd} \Phi_k^\alpha, \quad i_n^\alpha = \frac{1}{\sqrt{N}} \sum_k e^{inkd} i_k^\alpha, \tag{C.3}$$

where $\alpha = \mathrm{A}, \mathrm{B}$, N is the number of unit cells, and $k = \frac{2\pi m}{Nd}$ ($m = -N/2, \cdots, N/2-1$) are points in the first Brillouin zone. Equation (C.2) is written as

$$\sum_{k'} e^{ink'd} \Phi_{k'}^{\mathrm{A}} = \sum_{k'} e^{ink'd} \left(L_0 i_{k'}^{\mathrm{A}} + M_v i_{k'}^{\mathrm{B}} + e^{-ik'd} M_w i_{k'}^{\mathrm{B}} \right)$$

under this transform. Multiplying the above equation with e^{-inkd} and summing over all n, we get a linear relation between Φ_k^α and i_k^α:

$$\begin{pmatrix} \Phi_k^{\mathrm{A}} \\ \Phi_k^{\mathrm{B}} \end{pmatrix} = \begin{pmatrix} L_0 & M_v + M_w e^{-ikd} \\ M_v + M_w e^{ikd} & L_0 \end{pmatrix} \begin{pmatrix} i_k^{\mathrm{A}} \\ i_k^{\mathrm{B}} \end{pmatrix}.$$

By calculating the inverse of this relation, the Lagrangian of the system (C.1) can be rewritten in k-space as

$$\begin{aligned} \mathcal{L} = \sum_k \Bigg[& \frac{C_0 + C_v + C_w}{2} \left(\dot{\Phi}_{-k}^{\mathrm{A}} \dot{\Phi}_k^{\mathrm{A}} + \dot{\Phi}_{-k}^{\mathrm{B}} \dot{\Phi}_k^{\mathrm{B}} \right) - C_g(k)\, \dot{\Phi}_{-k}^{\mathrm{A}} \dot{\Phi}_k^{\mathrm{B}} \\ & - \frac{L_0}{2} \left(i_{-k}^{\mathrm{A}} i_k^{\mathrm{A}} + i_{-k}^{\mathrm{B}} i_k^{\mathrm{B}} \right) - M_g(k)\, i_{-k}^{\mathrm{A}} i_k^{\mathrm{B}} \Bigg] \\ = \sum_k \Bigg[& \frac{C_0 + C_v + C_w}{2} \left(\dot{\Phi}_{-k}^{\mathrm{A}} \dot{\Phi}_k^{\mathrm{A}} + \dot{\Phi}_{-k}^{\mathrm{B}} \dot{\Phi}_k^{\mathrm{B}} \right) - C_g(k)\, \dot{\Phi}_{-k}^{\mathrm{A}} \dot{\Phi}_k^{\mathrm{B}} \\ & - \frac{\frac{L_0}{2} \left(\Phi_{-k}^{\mathrm{A}} \Phi_k^{\mathrm{A}} + \Phi_{-k}^{\mathrm{B}} \Phi_k^{\mathrm{B}} \right) - M_g(k) \Phi_{-k}^{\mathrm{A}} \Phi_k^{\mathrm{B}}}{L_0^2 - M_g(-k) M_g(k)} \Bigg] \end{aligned} \tag{C.4}$$

where $C_g(k) \equiv C_v + C_w e^{-ikd}$ and $M_g(k) \equiv M_v + M_w e^{-ikd}$. The node charge variables $Q_k^\alpha \equiv \partial \mathcal{L} / \partial \dot{\Phi}_k^\alpha$ canonically conjugate to node flux Φ_k^α are

$$\begin{pmatrix} Q_k^{\mathrm{A}} \\ Q_k^{\mathrm{B}} \end{pmatrix} = \begin{pmatrix} C_0 + C_v + C_w & -C_g(-k) \\ -C_g(k) & C_0 + C_v + C_w \end{pmatrix} \begin{pmatrix} \dot{\Phi}_{-k}^{\mathrm{A}} \\ \dot{\Phi}_{-k}^{\mathrm{B}} \end{pmatrix}.$$

Note that due to the Fourier transform implemented on flux variables, the canonical charge in momentum space is related to that in real space by

$$Q_n^\alpha = \frac{\partial \mathcal{L}}{\partial \dot{\Phi}_n^\alpha} = \sum_k \frac{\partial \mathcal{L}}{\partial \dot{\Phi}_k^\alpha} \frac{\partial \dot{\Phi}_k^\alpha}{\partial \dot{\Phi}_n^\alpha} = \frac{1}{\sqrt{N}} \sum_k e^{-inkd} Q_k^\alpha,$$

which is in the opposite sense of regular Fourier transform in Eq. (C.3). Also, due to the Fourier-transform properties, the constraint that Φ_n^α and Q_n^α are real reduces to $(\Phi_k^\alpha)^* = \Phi_{-k}^\alpha$ and $(Q_k^\alpha)^* = Q_{-k}^\alpha$. Applying the Legendre transformation $H = \sum_{k,\alpha} Q_k^\alpha \dot{\Phi}_k^\alpha - \mathcal{L}$, the Hamiltonian takes the form

$$H = \sum_k \left[\frac{C_\Sigma(Q_{-k}^{\mathrm{A}}Q_k^{\mathrm{A}} + Q_{-k}^{\mathrm{B}}Q_k^{\mathrm{B}}) + C_g(-k)Q_{-k}^{\mathrm{A}}Q_k^{\mathrm{B}} + C_g(k)Q_{-k}^{\mathrm{B}}Q_k^{\mathrm{A}}}{2C_d^2(k)} \right.$$
$$\left. + \frac{L_0(\Phi_{-k}^{\mathrm{A}}\Phi_k^{\mathrm{A}} + \Phi_{-k}^{\mathrm{B}}\Phi_k^{\mathrm{B}}) - M_g(k)\Phi_{-k}^{\mathrm{A}}\Phi_k^{\mathrm{B}} - M_g(-k)\Phi_{-k}^{\mathrm{B}}\Phi_k^{\mathrm{A}}}{2L_d^2(k)} \right],$$

where

$$C_\Sigma \equiv C_0 + C_v + C_w, \quad C_d^2(k) \equiv C_\Sigma^2 - C_g(-k)C_g(k), \quad L_d^2(k) \equiv L_0^2 - M_g(-k)M_g(k).$$

Note that $C_d^2(k)$ and $L_d^2(k)$ are real and even function in k. We impose the canonical commutation relation between real-space conjugate variables $[\hat{\Phi}_n^\alpha, \hat{Q}_{n'}^\beta] = i\hbar\delta_{\alpha,\beta}\delta_{n,n'}$ to promote the flux and charge variables to quantum operators. This reduces to $[\hat{\Phi}_k^\alpha, \hat{Q}_{k'}^\beta] = i\hbar\delta_{\alpha,\beta}\delta_{k,k'}$ in the momentum space [Note that due to the Fourier transform, $(\hat{\Phi}_k^\alpha)^\dagger = \hat{\Phi}_{-k}^\alpha$ and $(\hat{Q}_k^\alpha)^\dagger = \hat{Q}_{-k}^\alpha$, meaning flux and charge operators in momentum space are *non-Hermitian* since the Hermitian conjugate flips the sign of k]. The Hamiltonian can be written as a sum $\hat{H} = \hat{H}_0 + \hat{V}$, where the "uncoupled" part $\hat{H}_0$ and coupling terms $\hat{V}$ are written as

$$\hat{H}_0 = \sum_{k,\alpha} \left[\frac{\hat{Q}_{-k}^\alpha \hat{Q}_k^\alpha}{2C_0^{\mathrm{eff}}(k)} + \frac{\hat{\Phi}_{-k}^\alpha \hat{\Phi}_k^\alpha}{2L_0^{\mathrm{eff}}(k)} \right], \quad \hat{V} = \sum_k \left[\frac{\hat{Q}_{-k}^{\mathrm{A}} \hat{Q}_k^{\mathrm{B}}}{2C_g^{\mathrm{eff}}(k)} + \frac{\hat{\Phi}_{-k}^{\mathrm{A}} \hat{\Phi}_k^{\mathrm{B}}}{2L_g^{\mathrm{eff}}(k)} + \mathrm{H.c.} \right], \tag{C.5}$$

with the effective self-capacitance $C_0^{\mathrm{eff}}(k)$, self-inductance $L_0^{\mathrm{eff}}(k)$, coupling capacitance $C_g^{\mathrm{eff}}(k)$, and coupling inductance $L_g^{\mathrm{eff}}(k)$ given by

$$C_0^{\mathrm{eff}}(k) = \frac{C_d^2(k)}{C_\Sigma}, \quad L_0^{\mathrm{eff}}(k) = \frac{L_d^2(k)}{L_0}, \quad C_g^{\mathrm{eff}}(k) = \frac{C_d^2(k)}{C_g(-k)}, \quad L_g^{\mathrm{eff}}(k) = -\frac{L_d^2(k)}{M_g(k)}. \tag{C.6}$$

The diagonal part $\hat{H}_0$ of the Hamiltonian can be written in a second-quantized form by introducing annihilation operators $\hat{a}_k$ and $\hat{b}_k$, which are operators of the Bloch waves on A and B sublattice, respectively:

$$\hat{a}_k \equiv \frac{1}{\sqrt{2\hbar}} \left[\frac{\hat{\Phi}_k^{\mathrm{A}}}{\sqrt{Z_0^{\mathrm{eff}}(k)}} + i\sqrt{Z_0^{\mathrm{eff}}(k)}\hat{Q}_{-k}^{\mathrm{A}} \right], \quad \hat{b}_k \equiv \frac{1}{\sqrt{2\hbar}} \left[\frac{\hat{\Phi}_k^{\mathrm{B}}}{\sqrt{Z_0^{\mathrm{eff}}(k)}} + i\sqrt{Z_0^{\mathrm{eff}}(k)}\hat{Q}_{-k}^{\mathrm{B}} \right].$$

Here, $Z_0^{\mathrm{eff}}(k) \equiv \sqrt{L_0^{\mathrm{eff}}(k)/C_0^{\mathrm{eff}}(k)}$ is the effective impedance of the oscillator at wavevector k. Unlike the Fourier transform notation, for bosonic modes $\hat{a}_k$ and

$\hat{b}_k$, we use the notation $(\hat{a}_k)^\dagger \equiv \hat{a}_k^\dagger$ and $(\hat{b}_k)^\dagger \equiv \hat{b}_k^\dagger$. Under this definition, the commutation relation is rewritten as $[\hat{a}_k, \hat{a}_{k'}^\dagger] = [\hat{b}_k, \hat{b}_{k'}^\dagger] = \delta_{k,k'}$. Note that the flux and charge operators are written in terms of mode operators as

$$\hat{\Phi}_k^{\mathrm{A}} = \sqrt{\frac{\hbar Z_0^{\mathrm{eff}}(k)}{2}}\left(\hat{a}_k + \hat{a}_{-k}^\dagger\right), \quad \hat{Q}_k^{\mathrm{A}} = \frac{1}{i}\sqrt{\frac{\hbar}{2Z_0^{\mathrm{eff}}(k)}}\left(\hat{a}_{-k} - \hat{a}_k^\dagger\right),$$
$$\hat{\Phi}_k^{\mathrm{B}} = \sqrt{\frac{\hbar Z_0^{\mathrm{eff}}(k)}{2}}\left(\hat{b}_k + \hat{b}_{-k}^\dagger\right), \quad \hat{Q}_k^{\mathrm{B}} = \frac{1}{i}\sqrt{\frac{\hbar}{2Z_0^{\mathrm{eff}}(k)}}\left(\hat{b}_{-k} - \hat{b}_k^\dagger\right).$$

The uncoupled Hamiltonian is written as

$$\hat{H}_0 = \sum_k \frac{\hbar\omega_0(k)}{2}\left(\hat{a}_k^\dagger \hat{a}_k + \hat{a}_{-k}\hat{a}_{-k}^\dagger + \hat{b}_k^\dagger \hat{b}_k + \hat{b}_{-k}\hat{b}_{-k}^\dagger\right), \tag{C.7}$$

where the "uncoupled" oscillator frequency is given by $\omega_0(k) \equiv [L_0^{\mathrm{eff}}(k)C_0^{\mathrm{eff}}(k)]^{-1/2}$, which ranges between values

$$\omega_0(k=0) = \sqrt{\frac{L_0 C_\Sigma}{[L_0^2 - (M_v + M_w)^2][C_\Sigma^2 - (C_v + C_w)^2]}},$$
$$\omega_0\left(k = \frac{\pi}{d}\right) = \sqrt{\frac{L_0 C_\Sigma}{(L_0^2 - |M_v - M_w|^2)(C_\Sigma^2 - |C_v - C_w|^2)}}.$$

The coupling Hamiltonian $\hat{V}$ is rewritten as

$$\hat{V} = -\sum_k \left[\frac{\hbar g_C(k)}{2}\left(\hat{a}_{-k}\hat{b}_k - \hat{a}_{-k}\hat{b}_{-k}^\dagger - \hat{a}_k^\dagger \hat{b}_k + \hat{a}_k^\dagger \hat{b}_{-k}^\dagger\right)\right.$$
$$\left. + \frac{\hbar g_L(k)}{2}\left(\hat{a}_{-k}\hat{b}_k + \hat{a}_{-k}\hat{b}_{-k}^\dagger + \hat{a}_k^\dagger \hat{b}_k + \hat{a}_k^\dagger \hat{b}_{-k}^\dagger\right) + h.c.\right], \tag{C.8}$$

where the capacitive coupling $g_C(k)$ and inductive coupling $g_L(k)$ are simply written as

$$g_C(k) = \frac{\omega_0(k) C_g(k)}{2C_\Sigma}, \quad g_L(k) = \frac{\omega_0(k) M_g(k)}{2L_0}, \tag{C.9}$$

respectively. Note that $g_C^*(k) = g_C(-k)$ and $g_L^*(k) = g_L(-k)$. In the following, we discuss the diagonalization of this Hamiltonian to explain the dispersion relation and band topology.

Band structure within the rotating-wave approximation

We first consider the band structure of the system within the rotating-wave approximation (RWA), where we discard the counter-rotating terms $\hat{a}\hat{b}$ and $\hat{a}^\dagger\hat{b}^\dagger$ in the

Hamiltonian. This assumption is known to be valid when the strength of the couplings $|g_L(k)|$, $|g_C(k)|$ are small compared to the uncoupled oscillator frequency $\omega_0(k)$. Under this approximation, the Hamiltonian in Eqs. (C.7)-(C.8) reduces to a simple form $\hat{H} = \hbar \sum_k (\hat{\mathbf{v}}_k)^\dagger \mathbf{h}(k) \hat{\mathbf{v}}_k$, where the single-particle kernel of the Hamiltonian is,

$$\mathbf{h}(k) = \begin{pmatrix} \omega_0(k) & f(k) \\ f^*(k) & \omega_0(k) \end{pmatrix}. \tag{C.10}$$

Here, $\hat{\mathbf{v}}_k = (\hat{a}_k, \hat{b}_k)^T$ is the vector of annihilation operators at wavevector k and $f(k) \equiv g_C(k) - g_L(k)$. In this case, the Hamiltonian is diagonalized to the form

$$\hat{H} = \hbar \sum_k \left[\omega_+(k)\, \hat{a}^\dagger_{+,k} \hat{a}_{+,k} + \omega_-(k)\, \hat{a}^\dagger_{-,k} \hat{a}_{-,k} \right], \tag{C.11}$$

where two bands $\omega_\pm(k) = \omega_0(k) \pm |f(k)|$ symmetric with respect to $\omega_0(k)$ at each wavevector k appear [here, note that $\hat{a}^\dagger_{\pm,k} \equiv (\hat{a}_{\pm,k})^\dagger$]. The supermodes $\hat{a}_{\pm,k}$ are written as

$$\hat{a}_{\pm,k} = \frac{\pm e^{-i\phi(k)} \hat{a}_k + \hat{b}_k}{\sqrt{2}},$$

where $\phi(k) \equiv \arg f(k)$ is the phase of coupling term. The Bloch states in the single-excitation bands are written as

$$|\psi_{k,\pm}\rangle = \hat{a}^\dagger_{\pm,k} |0\rangle = \frac{1}{\sqrt{2}} \left(\pm e^{i\phi(k)} |1_k, 0_k\rangle + |0_k, 1_k\rangle \right),$$

where $|n_k, n'_k\rangle$ denotes a state with n (n') photons in mode $\hat{a}_k$ ($\hat{b}_k$).

As discussed below in App. C.2, the kernel of the Hamiltonian in Eq. (C.10) has an inversion symmetry in the sublattice unit cell which is known to result in bands with quantized Zak phase [218]. In our system the Zak phase of the two bands are evaluated as

$$\begin{aligned} \mathcal{Z} &= i \oint_{\text{B.Z.}} \mathrm{d}k\, \frac{1}{\sqrt{2}} \begin{pmatrix} \pm e^{-i\phi(k)} & 1 \end{pmatrix} \frac{\partial}{\partial k} \left[\frac{1}{\sqrt{2}} \begin{pmatrix} \pm e^{i\phi(k)} \\ 1 \end{pmatrix} \right] \\ &= -\frac{1}{2} \oint_{\text{B.Z.}} \mathrm{d}k\, \frac{\partial \phi(k)}{\partial k}. \end{aligned}$$

The Zak phase of photonic bands is determined by the behavior of $f(k)$ in the complex plane. If the contour of $f(k)$ for k values in the first Brillouin zone excludes (encloses) the origin, the Zak phase is given by $\mathcal{Z} = 0$ ($\mathcal{Z} = \pi$) corresponding to the trivial (topological) phase.

Considering all the terms in the Hamiltonian in Eqs. (C.7)-(C.8), the Hamiltonian can be written in a compact form $\hat{H} = \frac{\hbar}{2}\sum_k (\hat{\mathbb{v}}_k)^\dagger \mathbb{h}(k)\hat{\mathbb{v}}_k$ with a vector composed of mode operators $\hat{\mathbb{v}}_k = \left(\hat{a}_k, \hat{b}_k, \hat{a}^\dagger_{-k}, \hat{b}^\dagger_{-k}\right)^T$ and

$$\begin{aligned} \mathbb{h}(k) &= \begin{pmatrix} \omega_0(k) & f(k) & 0 & g(k) \\ f^*(k) & \omega_0(k) & g^*(k) & 0 \\ 0 & g(k) & \omega_0(k) & f(k) \\ g^*(k) & 0 & f^*(k) & \omega_0(k) \end{pmatrix} \\ &= \omega_0(k) \begin{pmatrix} 1 & \frac{c_k - l_k}{2} & 0 & \frac{-c_k - l_k}{2} \\ \frac{c_k^* - l_k^*}{2} & 1 & \frac{-c_k^* - l_k^*}{2} & 0 \\ 0 & \frac{-c_k - l_k}{2} & 1 & \frac{c_k - l_k}{2} \\ \frac{-c_k^* - l_k^*}{2} & 0 & \frac{c_k^* - l_k^*}{2} & 1 \end{pmatrix}, \end{aligned} \tag{C.12}$$

where $f(k) \equiv g_C(k) - g_L(k)$ as before and $g(k) \equiv -g_C(k) - g_L(k)$. Here, $l_k \equiv M_g(k)/L_0$ and $c_k \equiv C_g(k)/C_\Sigma$ are inductive and capacitive coupling normalized to frequency. The dispersion relation can be found by diagonalizing the kernel of the Hamiltonian in Eq. (C.12) with the Bogoliubov transformation

$$\hat{\mathbb{w}}_k = \mathbf{S}_k \hat{\mathbb{v}}_k, \qquad \mathbf{S}_k = \begin{pmatrix} \mathbf{U}_k & \mathbf{V}^*_{-k} \\ \mathbf{V}_k & \mathbf{U}^*_{-k} \end{pmatrix} \tag{C.13}$$

where $\hat{\mathbb{w}}_k \equiv (\hat{a}_{+,k}, \hat{a}_{-,k}, \hat{a}^\dagger_{+,-k}, \hat{a}^\dagger_{-,-k})^T$ is the vector composed of supermode operators and $\mathbf{U}_k$, $\mathbf{V}_k$ are 2×2 matrices forming blocks in the transformation $\mathbf{S}_k$. We want to find $\mathbf{S}_k$ such that $(\hat{\mathbb{v}}_k)^\dagger \mathbb{h}(k)\hat{\mathbb{v}}_k = (\hat{\mathbb{w}}_k)^\dagger \tilde{\mathbb{h}}(k)\hat{\mathbb{w}}_k$, where $\tilde{\mathbb{h}}(k)$ is diagonal. To preserve the commutation relations, the matrix $\mathbf{S}_k$ has to be symplectic, satisfying $\mathbf{J} = \mathbf{S}_k \mathbf{J} (\mathbf{S}_k)^\dagger$, with $\mathbf{J}$ defined as

$$\mathbf{J} = \begin{bmatrix} 1 & 0 & 0 & 0 \\ 0 & 1 & 0 & 0 \\ 0 & 0 & -1 & 0 \\ 0 & 0 & 0 & -1 \end{bmatrix}.$$

Due to this symplecticity, it can be shown that the matrices $\mathbf{J}\mathbb{h}(k)$ and $\mathbf{J}\tilde{\mathbb{h}}(k)$ are similar under transformation $\mathbf{S}_k$. Thus, finding the eigenvalues and eigenvectors of the coefficient matrix

$$\mathbb{m}(k) \equiv \frac{\mathbf{J}\mathbb{h}(k)}{\omega_0(k)} = \begin{pmatrix} 1 & \frac{c_k - l_k}{2} & 0 & \frac{-c_k - l_k}{2} \\ \frac{c_k^* - l_k^*}{2} & 1 & \frac{-c_k^* - l_k^*}{2} & 0 \\ 0 & \frac{c_k + l_k}{2} & -1 & \frac{-c_k + l_k}{2} \\ \frac{c_k^* + l_k^*}{2} & 0 & \frac{-c_k^* + l_k^*}{2} & -1 \end{pmatrix} \tag{C.14}$$

is sufficient to obtain the dispersion relation and supermodes of the system. The eigenvalues of matrix $\mathbb{m}(k)$ are evaluated as

$$\pm\sqrt{1 - \frac{l_k c_k^* + l_k^* c_k}{2} \pm \sqrt{\left(1 - \frac{l_k c_k^* + l_k^* c_k}{2}\right)^2 - (1 - |l_k|^2)(1 - |c_k|^2)}}$$

and hence the dispersion relation of the system taking into account all terms in Hamiltonian (C.12) is

$$\tilde{\omega}_\pm(k) = \tilde{\omega}_0(k)\sqrt{1 \pm \sqrt{1 - \frac{\left[L_0^2 - M_g(-k)M_g(k)\right]\left[C_\Sigma^2 - C_g(-k)C_g(k)\right]}{\left\{L_0 C_\Sigma - \frac{1}{2}\left[M_g(-k)C_g(k) + C_g(-k)M_g(k)\right]\right\}^2}}} \tag{C.15}$$

where

$$\tilde{\omega}_0(k) \equiv \omega_0(k)\sqrt{1 - \frac{M_g(k)C_g(-k) + M_g(-k)C_g(k)}{2L_0 C_\Sigma}}.$$

The two passbands range over frequencies $[\omega_+^{\text{min}}, \omega_+^{\text{max}}]$ and $[\omega_-^{\text{min}}, \omega_-^{\text{max}}]$, where the band-edge frequencies are written as

$$\begin{aligned} \omega_+^{\text{min}} &= \frac{1}{\sqrt{[L_0 + p_2(M_v - M_w)][C_\Sigma - p_2(C_v - C_w)]}} \\ \omega_+^{\text{max}} &= \frac{1}{\sqrt{[L_0 + p_1(M_v + M_w)][C_\Sigma - p_1(C_v + C_w)]}}, \end{aligned} \tag{C.16a}$$

$$\begin{aligned} \omega_-^{\text{min}} &= \frac{1}{\sqrt{[L_0 - p_1(M_v + M_w)][C_\Sigma + p_1(C_v + C_w)]}} \\ \omega_-^{\text{max}} &= \frac{1}{\sqrt{[L_0 - p_2(M_v - M_w)][C_\Sigma + p_2(C_v - C_w)]}}. \end{aligned} \tag{C.16b}$$

Here, $p_1 \equiv \text{sgn}[L_0(C_v + C_w) - C_\Sigma(M_v + M_w)]$ and $p_2 \equiv \text{sgn}[L_0(C_v - C_w) - C_\Sigma(M_v - M_w)]$ are sign factors. In principle, the eigenvectors of the matrix $\mathbb{m}(k)$ in Eq. (C.14) can be analytically calculated to find the transformation $\mathbf{S}_k$ of the original modes to supermodes $\hat{a}_{\pm,k}$. For the sake of brevity, we perform the calculation in the limit of vanishing mutual inductance ($M_v = M_w = 0$), where the matrix $\mathbb{m}(k)$ reduces to

$$\mathbb{m}_C(k) \equiv \begin{pmatrix} 1 & c_k/2 & 0 & -c_k/2 \\ c_k^*/2 & 1 & -c_k^*/2 & 0 \\ 0 & c_k/2 & -1 & -c_k/2 \\ c_k^*/2 & 0 & -c_k^*/2 & -1 \end{pmatrix}. \tag{C.17}$$

In this case, the block matrices $\mathbf{U}_k$, $\mathbf{V}_k$ in the transformation in Eq. (C.13) are written as

$$\mathbf{U}_k = \frac{1}{2\sqrt{2}} \begin{pmatrix} e^{-i\phi(k)} x_{+,k} & x_{+,k} \\ -e^{-i\phi(k)} x_{-,k} & x_{-,k} \end{pmatrix}, \quad \mathbf{V}_k = \frac{1}{2\sqrt{2}} \begin{pmatrix} e^{-i\phi(k)} y_{+,k} & y_{+,k} \\ -e^{-i\phi(k)} y_{-,k} & y_{-,k} \end{pmatrix},$$

where $x_{\pm,k} = \sqrt[4]{1 \pm |c_k|} + \frac{1}{\sqrt[4]{1 \pm |c_k|}}$, $y_{\pm,k} = \sqrt[4]{1 \pm |c_k|} - \frac{1}{\sqrt[4]{1 \pm |c_k|}}$, and $\phi(k) = \arg c_k$. Note that the constants are normalized by relation $x_{\pm,k}^2 - y_{\pm,k}^2 = 4$.

The knowledge of the transformation $\mathbf{S}_k$ allows us to evaluate the Zak phase of photonic bands. In the Bogoliubov transformation, the Zak phase can be evaluated as [310]

$$\begin{aligned} \mathcal{Z} &= i \oint_{\text{B.Z.}} \mathrm{d}k \, \frac{1}{2\sqrt{2}} \begin{pmatrix} \pm e^{-i\phi(k)} x_{\pm,k} & x_{\pm,k} & \pm e^{-i\phi(k)} y_{\pm,k} & y_{\pm,k} \end{pmatrix} \cdot \mathbf{J} \cdot \frac{\partial}{\partial k} \left[\frac{1}{2\sqrt{2}} \begin{pmatrix} \pm e^{i\phi(k)} x_{\pm,k} \\ x_{\pm,k} \\ \pm e^{i\phi(k)} y_{\pm,k} \\ y_{\pm,k} \end{pmatrix} \right] \\ &= i \oint_{\text{B.Z.}} \mathrm{d}k \, \frac{1}{8} \left[i \frac{\partial \phi(k)}{\partial k} (x_{\pm,k}^2 - y_{\pm,k}^2) + \frac{\partial}{\partial k} (x_{\pm,k}^2 - y_{\pm,k}^2) \right] = -\frac{1}{2} \oint_{\text{B.Z.}} \mathrm{d}k \, \frac{\partial \phi(k)}{\partial k}, \end{aligned}$$

identical to the expression within the RWA. Again, the Zak phase of photonic bands is determined by the winding of $f(k)$ around the origin in complex plane, leading to $\mathcal{Z} = 0$ in the trivial phase and $\mathcal{Z} = \pi$ in the topological phase.

Extraction of circuit parameters and the breakdown of the circuit model

As discussed in Fig. 5.2b, the parameters in the circuit model of the topological waveguide is found by fitting the waveguide transmission spectrum of the test structures. We find that two lowest-frequency modes inside the lower passband fail to be captured according to our model with capacitively and inductively coupled LC resonators. We believe that this is due to the broad range of frequencies (about 1.5 GHz) covered in the spectrum compared to the bare resonator frequency $\sim$

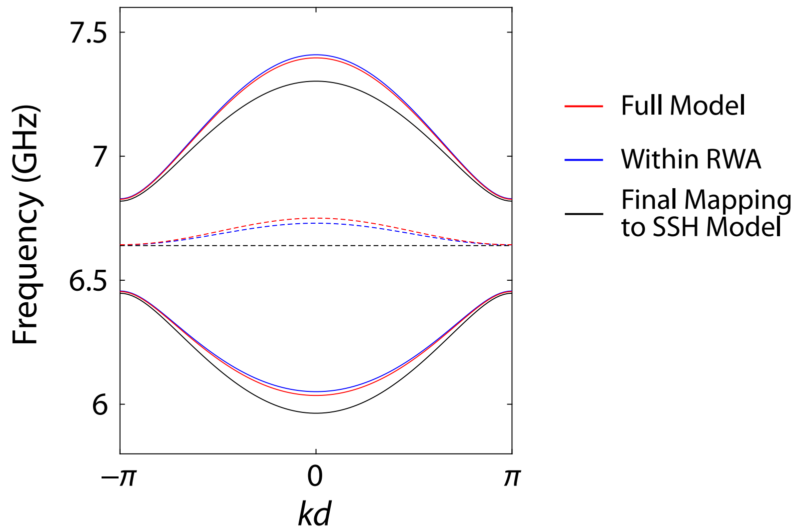

Figure C.2: Band structure of the realized topological waveguide under various assumptions discussed in App. C.2. The solid lines show the dispersion relation in the upper (lower) passband, $\omega_\pm(k)$: full model without any assumptions (red), model within RWA (blue), and the final mapping to SSH model (black) in the weak coupling limit. The dashed lines indicate the uncoupled resonator frequency $\omega_0(k)$ under corresponding assumptions.

6.6 GHz and the distributed nature of the coupling, which can cause our simple model based on frequency-independent lumped elements (inductor, capacitor, and mutual inductance) to break down. Such deviation is also observed in the fitting of waveguide transmission data of Device I (Fig. C.7).

C.2 Mapping of the system to the SSH model and discussion on robustness of edge modes

Mapping of the topological waveguide to the SSH model

We discuss how the physical model of topological waveguide in App. C.1 could be mapped to the photonic SSH model, whose Hamiltonian is given as Eq. (5.1) in the main text. Throughout this section, we consider the realistic circuit parameters extracted from fitting of test structures given in Fig. 5.1: resonator inductance and resonator capacitance, $L_0 = 1.9$nH and $C_0 = 253$fF, and coupling capacitance and parasitic mutual inductance, $(C_v, C_w) = (33, 17)$ fF and $(M_v, M_w) = (-38, -32)$ pH in the trivial phase (the values are interchanged in the topological phase).

To most directly and simply link the Hamiltonian described in Eqs. (C.7)-(C.8) to the SSH model, here we impose a few approximations. First, the counter-rotating terms in the Hamiltonian are discarded such that only photon-number-conserving terms are left. To achieve this, the RWA is applied to reduce the kernel of the Hamiltonian into one involving a 2×2 matrix as in Eq. (C.10). Such an assumption is known to be valid when the coupling terms in the Hamiltonian are much smaller than the frequency scale of the uncoupled Hamiltonian $\hat{H}_0$ [311]. According to the coupling terms derived in Eq. (C.9), this is a valid approximation given that

$$\left|\frac{g_C(k)}{\omega_0(k)}\right| \leq \frac{|C_v + C_w|}{2C_\Sigma} \approx 0.083,$$
$$\left|\frac{g_L(k)}{\omega_0(k)}\right| \leq \frac{|M_v| + |M_w|}{2L_0} \approx 0.018.$$

and the RWA affects the dispersion relation by less than 0.3 % in frequency.

Also different than in the original SSH Hamiltonian, are the k-dependent diagonal elements $\omega_0(k)$ of the single-particle kernel of the Hamiltonian for the circuit model. This k-dependence can be understood as arising from the coupling between resonators beyond nearest-neighbor pairs, which is inherent in the canonical quantization of capacitively coupled LC resonator array (due to circuit topology) as discussed in Ref. [144]. The variation in $\omega_0(k)$ can be effectively suppressed in the limit of $C_v, C_w \ll C_\Sigma$ and $M_v, M_w \ll L_0$ as derived in Eq. (C.6). We note that while our coupling capacitances are small compared to C_Σ ($C_v/C_\Sigma \approx 0.109$, $C_w/C_\Sigma \approx 0.056$ in the trivial phase), we find that they are sufficient to cause the $\omega_0(k)$ to vary by ~1.2 % in the first Brillouin zone. Considering this limit of small coupling capacitance and mutual inductance, the effective capacitance and inductance of (C.6) become quantities independent of k, $C_0^{\text{eff}}(k) \approx C_\Sigma$, $L_0^{\text{eff}}(k) \approx L_0$, and the kernel of the Hamiltonian under RWA reduces to

$$\mathbf{h}(k) = \begin{pmatrix} \omega_0 & f(k) \\ f^*(k) & \omega_0 \end{pmatrix}.$$

Here,

$$\omega_0 = \frac{1}{\sqrt{L_0 C_\Sigma}},$$
$$f(k) = \frac{\omega_0}{2}\left[\left(\frac{C_v}{C_\Sigma} - \frac{M_v}{L_0}\right) + \left(\frac{C_w}{C_\Sigma} - \frac{M_w}{L_0}\right)e^{-ikd}\right].$$

This is equivalent to the photonic SSH Hamiltonian in Eq. (5.1) of the main text under redefinition of gauge which transforms operators as $(\hat{a}_k, \hat{b}_k) \to (\hat{a}_k, -\hat{b}_k)$.

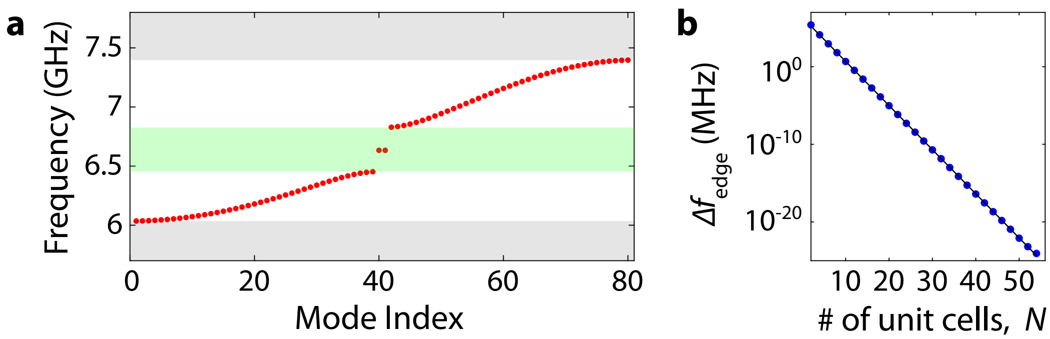

Figure C.3: **a**, Resonant frequencies of a finite system with $N = 40$ unit cells, calculated from eigenmodes of Eq. (C.20). The bandgap regions calculated from dispersion relation are shaded in gray (green) for upper and lower bandgaps (middle bandgap). The two data points inside the middle bandgap (mode indices 40 and 41) correspond to edge modes. **b**, Frequency splitting Δf_{edge} of edge modes with no disorder in the system are plotted against the of number of unit cells N. The black solid curve indicates exponential fit to the edge mode splitting, with decay constant of $\xi = 1.76$.

Here, we can identify the parameters J and δ as

$$J = \frac{\omega_0}{4}\left(\frac{C_v + C_w}{C_\Sigma} - \frac{M_v + M_w}{L_0}\right), \tag{C.18}$$

$$\delta = \frac{L_0(C_v - C_w) - C_\Sigma(M_v - M_w)}{L_0(C_v + C_w) - C_\Sigma(M_v + M_w)}, \tag{C.19}$$

where $J(1 \pm \delta)$ is defined as intra-cell and inter-cell coupling, respectively. The dispersion relations under different stages of approximations mentioned above are plotted in Fig. C.2, where we find a clear deviation of our system from the original SSH model due to the k-dependent reference frequency.

Robustness of edge modes under perturbation in circuit parameters

While we have linked our system to the SSH Hamiltonian in Eq. (5.1) of the main text, we find that our system fails to strictly satisfy chiral symmetry $\mathcal{C}\mathbf{h}(k)\mathcal{C}^{-1} = -\mathbf{h}(k)$ ($\mathcal{C} = \hat{\sigma}_z$ is the chiral symmetry operator in the sublattice space). This is due to the k-dependent diagonal $\omega_0(k)$ terms in $\mathbf{h}(k)$, resulting from the non-local nature of the quantized charge and nodal flux in the circuit model which results in next-nearest-neighbor coupling terms between sublattices of the same type. Despite this, an inversion symmetry, $\mathcal{I}\mathbf{h}(k)\mathcal{I}^{-1} = \mathbf{h}(-k)$ ($\mathcal{I} = \hat{\sigma}_x$ in the sublattice space), still holds for the circuit model. This ensures the quantization of the Zak phase ($\mathcal{Z}$) and the existence of an invariant band winding number ($\nu = \mathcal{Z}/\pi$) for perturbations that maintain the inversion symmetry. However, as shown in Refs. [312, 313], the inversion symmetry does not protect the edge states for highly delocalized coupling along the dimer resonator chain, and the correspondence between winding number and the number of localized edge states at the boundary of a finite section of waveguide is not guaranteed.

For weak breaking of the chiral symmetry (i.e., beyond nearest-neighbor coupling much smaller than nearest neighbor coupling) the correspondence between winding number and the number of pairs of gapped edge states is preserved, with winding number $\nu = 0$ in the trivial phase ($\delta > 0$) and $\nu = 1$ in the topological ($\delta < 0$) phase. Beyond just the existence of the edge states and their locality at the boundaries, chiral symmetry is special in that it pins the edge mode frequencies at the center of the middle bandgap (ω_0). Chiral symmetry is maintained in the presence of disorder in the coupling between the different sublattice types along the chain, providing stability to the frequency of the edge modes. In order to study the robustness of the edge mode frequencies in our circuit model, we perform a simulation over different types of disorder realizations in the circuit illustrated in Fig. C.1. As the original SSH Hamiltonian with chiral symmetry gives rise to topological edge states which are robust against the disorder in coupling, not in on-site energies [206], it is natural to consider disorder in circuit elements that induce coupling between resonators: C_v, C_w, M_v, M_w.

The classical equations of motion of a circuit consisting of N unit cells is written as

$$
\begin{aligned}
V_n^{\mathrm{A}} &= L_0 \frac{\mathrm{d}i_n^{\mathrm{A}}}{\mathrm{d}t} + M_v^{(n)} \frac{\mathrm{d}i_n^{\mathrm{B}}}{\mathrm{d}t} + M_w^{(n)} \frac{\mathrm{d}i_{n-1}^{\mathrm{B}}}{\mathrm{d}t}, \\
i_n^{\mathrm{A}} &= -C_{\Sigma,\mathrm{A}}^{(n)} \frac{\mathrm{d}V_n^{\mathrm{A}}}{\mathrm{d}t} + C_v^{(n)} \frac{\mathrm{d}V_n^{\mathrm{B}}}{\mathrm{d}t} + C_w^{(n-1)} \frac{\mathrm{d}V_{n-1}^{\mathrm{B}}}{\mathrm{d}t} \\
V_n^{\mathrm{B}} &= L_0 \frac{\mathrm{d}i_n^{\mathrm{B}}}{\mathrm{d}t} + M_w^{(n)}, \frac{\mathrm{d}i_{n+1}^{\mathrm{A}}}{\mathrm{d}t} + M_v^{(n)} \frac{\mathrm{d}i_n^{\mathrm{A}}}{\mathrm{d}t}, \\
i_n^{\mathrm{B}} &= -C_{\Sigma,\mathrm{B}}^{(n)} \frac{\mathrm{d}V_n^{\mathrm{B}}}{\mathrm{d}t} + C_v^{(n)} \frac{\mathrm{d}V_n^{\mathrm{A}}}{\mathrm{d}t} + C_w^{(n)} \frac{\mathrm{d}V_{n+1}^{\mathrm{A}}}{\mathrm{d}t},
\end{aligned}
$$

where the superscripts indicate index of cell of each circuit element and

$$
C_{\Sigma,\mathrm{A}}^{(n)} = C_0 + C_v^{(n)} + C_w^{(n-1)}, \quad C_{\Sigma,\mathrm{B}}^{(n)} = C_0 + C_v^{(n)} + C_w^{(n)}.
$$

The $4N$ coupled differential equations are rewritten in a compact form as

$$\frac{\mathrm{d}}{\mathrm{d}t}\begin{pmatrix}\mathbf{u}_1\\ \mathbf{u}_2\\ \vdots\\ \mathbf{u}_N\end{pmatrix} = \mathbf{C}^{-1}\begin{pmatrix}\mathbf{u}_1\\ \mathbf{u}_2\\ \vdots\\ \mathbf{u}_N\end{pmatrix}, \quad \mathbf{u}_n \equiv \begin{pmatrix}V_n^{\mathrm{A}}\\ i_n^{\mathrm{A}}\\ V_n^{\mathrm{B}}\\ i_n^{\mathrm{B}}\end{pmatrix}, \tag{C.20}$$

where the coefficient matrix $\mathbf{C}$ is given by

$$\mathbf{C} \equiv \left(\begin{array}{cccccccccccccc}
0 & L_0 & 0 & M_v^{(1)} & & & & & & & & & & \\
-C_{\Sigma,\mathrm{A}}^{(1)} & 0 & C_v^{(1)} & & & & & & & & & & & \\
 & M_v^{(1)} & 0 & L_0 & 0 & M_w^{(1)} & & & & & & & & \\
C_v^{(1)} & 0 & -C_{\Sigma,\mathrm{B}}^{(1)} & 0 & C_w^{(1)} & & & & & & & & & \\
 & & & M_w^{(1)} & 0 & L_0 & 0 & M_v^{(2)} & & & & & & \\
 & & C_w^{(1)} & 0 & -C_{\Sigma,\mathrm{A}}^{(2)} & 0 & C_v^{(2)} & & & & & & & \\
 & & & & & M_v^{(2)} & 0 & L_0 & 0 & M_w^{(2)} & & & & \\
 & & & & C_v^{(2)} & 0 & -C_{\Sigma,\mathrm{B}}^{(2)} & 0 & C_w^{(2)} & & \ddots & & & \\
 & & & & & & & M_w^{(2)} & & \ddots & & \ddots & & \\
 & & & & & & C_w^{(2)} & & \ddots & & \ddots & & \ddots & \\
 & & & & & & & \ddots & & \ddots & & \ddots & & M_v^{(N)} \\
 & & & & & & & & \ddots & & \ddots & & C_v^{(N)} & \\
 & & & & & & & & & \ddots & & M_v^{(N)} & 0 & L_0 \\
 & & & & & & & & & & C_v^{(N)} & 0 & -C_{\Sigma,\mathrm{B}}^{(N)} & 0
\end{array}\right).$$

Here, the matrix elements not specified are all zero. The resonant frequencies of the system can be determined by finding the positive eigenvalues of $i\mathbf{C}^{-1}$. Considering the model without any disorder, we find the eigenfrequencies of the finite system to be distributed according to the passband and bandgap frequencies from dispersion relation in Eq. (C.15), as illustrated in Fig. C.3. Also, we observe the presence of a pair of coupled edge mode resonances inside the middle bandgap in the topological phase, whose splitting due to finite system size scales as $\Delta f_{\mathrm{edge}} \sim e^{-N/\xi}$ with $\xi = 1.76$.

To discuss the topological protection of the edge modes, we keep track of the set of eigenfrequencies for different disorder realizations of the coupling capacitance and mutual inductance for a system with $N = 50$ unit cells. First, we consider the case when the mutual inductance M_v and M_w between resonators are subject to disorder. The values of $M_v^{(n)}$, $M_w^{(n)}$ are assumed to be sampled uniformly on an interval covering a fraction $\pm r$ of the original values, i.e.,

$$M_v^{(n)} = M_v\left[1 + r\tilde{\delta}_{M_v}^{(n)}\right], \quad M_w^{(n)} = M_w\left[1 + r\tilde{\delta}_{M_w}^{(n)}\right],$$

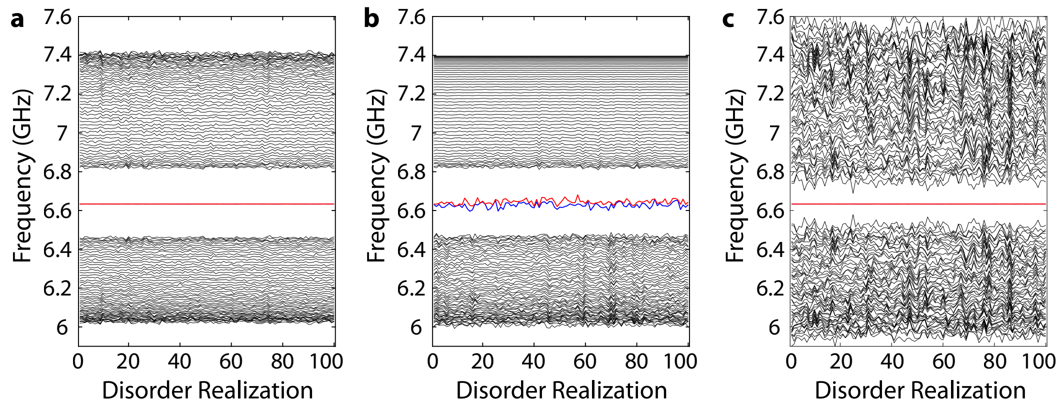

Figure C.4: Eigenfrequencies of the system under 100 disorder realizations in coupling elements. Each disorder realization is achieved by uniformly sampling the parameters within fraction $\pm r$ of the original value. **a**, Disorder in mutual inductance M_v and M_w between neighboring resonators with the strength $r = 0.5$. **b**, Disorder in coupling capacitance C_v and C_w between neighboring resonators with the strength $r = 0.1$. **c**, The same disorder as panel **b** with $r = 0.5$, while keeping the bare self-capacitance C_Σ of each resonator fixed (correlated disorder between coupling capacitances and resonator C_0).

where $\tilde{\delta}_{M_v}^{(n)}, \tilde{\delta}_{M_w}^{(n)}$ are independent random numbers uniformly sampled from an interval $[-1, 1]$. Figure C.4a illustrates an example with a strong disorder with $r = 0.5$ under 100 independent realizations, where we find the frequencies of the edge modes to be stable, while frequencies of modes in the passbands fluctuate to a much larger extent. This suggests that the frequencies of edge modes have some sort of added robustness against disorder in the mutual inductance between neighboring resonators despite the fact that our circuit model does not satisfy chiral symmetry. The reduction in sensitivity results from the fact that the effective self-inductance $L_0^{\text{eff}}(k)$ of the resonators, which influences the on-site resonator frequency, depends on the mutual inductances only to second-order in small parameter $(M_{v,w}/L_0)$. It is this second-order fluctuation in the resonator frequencies, causing shifts in the diagonal elements of the Hamiltonian, which results in fluctuations in the edge mode frequencies. The direct fluctuation in the mutual inductance couplings themselves, corresponding to off-diagonal Hamiltonian elements, do not cause the edge modes to fluctuate due to chiral symmetry protection (the off-diagonal part of the kernel of the Hamiltonian is chiral symmetric).

Disorder in coupling capacitance C_v and C_w are also investigated using a similar model, where the values of $C_v^{(n)}$, $C_w^{(n)}$ are allowed to vary by a fraction $\pm r$ of the original values (uniformly sampled), while the remaining circuit parameters are kept constant. From Fig. C.4b we observe severe fluctuations in the frequencies of the edge modes even under a mild disorder level of $r = 0.1$. This is due to the fact that the coupling capacitance C_v and C_w contribute to the effective self-capacitance of each resonator $C_0^{\text{eff}}(k)$ to first-order in small parameter $(C_{v,w}/C_0)$, thus directly breaking chiral symmetry and causing the edge modes to fluctuate. An interesting observation in Fig. C.4b is the stability of frequencies of modes in the upper passband with respect to disorder in C_v and C_w. This can be explained by noting the expressions for band-edge frequencies in Eqs. (C.16a)-(C.16b), where the dependence on coupling capacitance gets weaker close to the upper band-edge frequency $\omega_+^{\text{max}} = 1/\sqrt{(L_0 + M_v + M_w)C_0}$ of the upper passband.

Finally, we consider a special type of disorder where we keep the bare self-capacitance C_Σ of each resonator fixed. Although unrealistic, we allow C_v and C_w to fluctuate and compensate for the disorder in C_Σ by subtracting the deviation in C_v and C_w from C_0. This suppresses the lowest-order resonator frequency fluctuations, and hence helps stabilize the edge mode frequencies even under strong disorder $r = 0.5$, as illustrated in Fig. C.4c. While being an unrealistic model for disorder in our physical system, this observation sheds light on the fact that the circuit must be carefully designed to take advantage of the topological protection. It should also be noted that in all of the above examples, the standard deviation in the edge mode frequencies scale linearly to lowest order with the standard deviation of the disorder in the inter- and intra-cell coupling circuit elements (only the pre-coefficient changes). Exponential suppression of edge mode fluctuations due to disorder in the coupling elements as afforded by the SSH model with chiral symmetry would require a redesign of the circuit to eliminate the next-nearest-neighbor coupling present in the current circuit layout.

C.3 Device I characterization and Experimental setup

In this section, we provide a detailed description of elements on Device I, where the directional qubit-photon bound state and passband topology experiments are performed. The optical micrograph of Device I is shown in Fig. C.5.

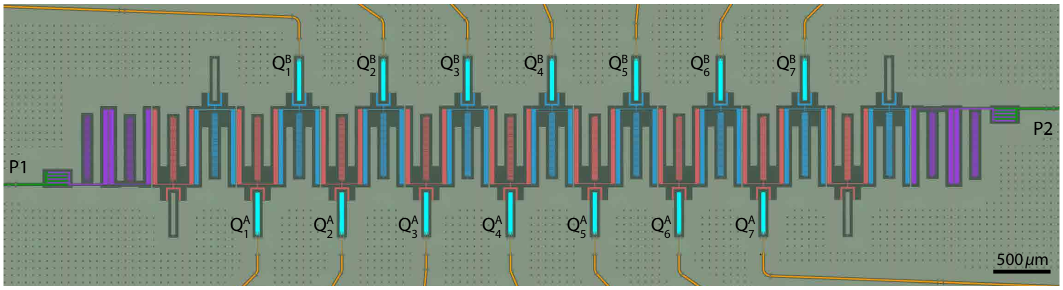

Figure C.5: Optical micrograph of Device I (false-colored). The device consists of a topological waveguide with 9 unit cells (resonators corresponding to A/B sublattice colored red/blue) in the trivial phase, where the intra-cell coupling is larger than the inter-cell coupling. Qubits (cyan, labeled Q_j^α where i=1-7 and α=A,B) are coupled to every site of the seven inner unit cells of the topological waveguide, each connected to on-chip flux-bias lines (orange) for individual frequency control. At the boundary of the topological waveguide are tapering sections (purple), which provide impedance matching to the external waveguides (green) at upper bandgap frequencies. P1 (P2) denotes port 1 (port 2) of the device.

	Q_1^A	Q_1^B	Q_2^A	Q_2^B	Q_3^A	Q_3^B	Q_4^A
$\Gamma'/2\pi$ (kHz)	325.7	150.4	247.4	104.7[a]	268.2	183.2	220.6
	Q_4^B	Q_5^A	Q_5^B	Q_6^A	Q_6^B	Q_7^A	Q_7^B
$\Gamma'/2\pi$ (kHz)	224.4	193.3	263.2	206	332.69	88.1	346.8

[a] Measured in a separate cooldown

Table C.1: Qubit coherence in the middle bandgap. The parasitic decoherence rate Γ' of qubits on Device I at 6.621 GHz inside the MBG. The data for Q_2^B was taken in a separate cooldown due to coupling to a two-level system defect.

Qubits

All 14 qubits on Device I are designed to be nominally identical with asymmetric Josephson junctions (JJs) on superconducting quantum interference device (SQUID) loop to reduce the sensitivity to flux noise away from maximum and minimum frequencies, referred to as “sweet spots”. The sweet spots of all qubits lie deep inside the upper and lower bandgaps, where the coupling of qubits to external ports are small due to strong localization. This makes it challenging to access the qubits with direct spectroscopic methods near the sweet spots. Alternatively, a strong drive tone near resonance with a given qubit frequency was sent into the waveguide to excite the qubit, and a passband mode dispersively coupled to the qubit is simultaneously monitored with a second probe tone. With this method, the lower (upper) sweet spot of $\mathrm{Q}_1^{\mathrm{A}}$ is found to be at 5.22 GHz (8.38 GHz), and the anharmonicity near the upper sweet spot is measured to be 297 MHz (effective qubit capacitance of $C_{\mathrm{q}} = 65$ fF). The Josephson energies of two JJs of $\mathrm{Q}_1^{\mathrm{A}}$ are extracted to be $(E_{J1}, E_{J2})/h = (21.85, 9.26)$ GHz giving the junction asymmetry of $d = \frac{E_{J1}-E_{J2}}{E_{J1}+E_{J2}} = 0.405$.

The coherence of qubits is characterized using spectroscopy inside the middle bandgap (MBG). Here, the parasitic decoherence rate is defined as $\Gamma' \equiv 2\Gamma_2 - \kappa_{e,1} - \kappa_{e,2}$, where $2\Gamma_2$ is the total linewidth of qubit, and $\kappa_{e,1}$ ($\kappa_{e,2}$) is the external coupling rate to port 1 (2) (see Supplementary Note 1 of Ref. [47] for a detailed discussion). Here, Γ' contains contributions from both qubit decay to spurious channels other than the desired external waveguide as well as pure dephasing. Table C.1 shows the parasitic decoherence rate of all 14 qubits at 6.621 GHz extracted from spectroscopic measurement at a power at least 5 dB below the single-photon level (defined as $\hbar\omega\kappa_{e,p}$ with $p = 1, 2$) from both ports.

Utilizing the dispersive coupling between the qubit and a resonator mode in the passband, we have also performed time-domain characterization of qubits. The measurement on $\mathrm{Q}_4^{\mathrm{B}}$ at 6.605 GHz in the MBG gives $T_1 = 1.23\,\mu$s and $T_2^* = 783$ ns corresponding to $\Gamma'/2\pi = 281.3$ kHz, consistent with the result from spectroscopy in Table C.1. At the upper sweet spot, $\mathrm{Q}_4^{\mathrm{B}}$ was hard to access due to the small coupling to external ports arising from short localization length and a large physical distance from the external ports. Instead, $\mathrm{Q}_1^{\mathrm{B}}$ is characterized to be $T_1 = 9.197\,\mu$s and $T_2^* = 11.57\,\mu$s at its upper sweet spot (8.569 GHz).

Metamaterial waveguide and coupling to qubits

As shown in Fig. C.5, the metamaterial waveguide consists of a SSH array in the trivial configuration and tapering sections at the boundary (the design of tapering sections is discussed in App. C.4). The array contains 18 identical LC resonators, whose design is slightly different from the one in test structures shown in Fig. 5.1b of the main text. Namely, the “claw” used to couple qubits to resonators on each site is extended to generate a larger coupling capacitance of $C_g = 5.6$ fF and the resonator capacitance to ground was reduced accordingly to maintain the designed reference frequency. On resonator sites where no qubit is present, an island with shape identical to that of a qubit was patterned and shorted to ground plane in order to mimic the self-capacitance contribution from a qubit to the resonator.

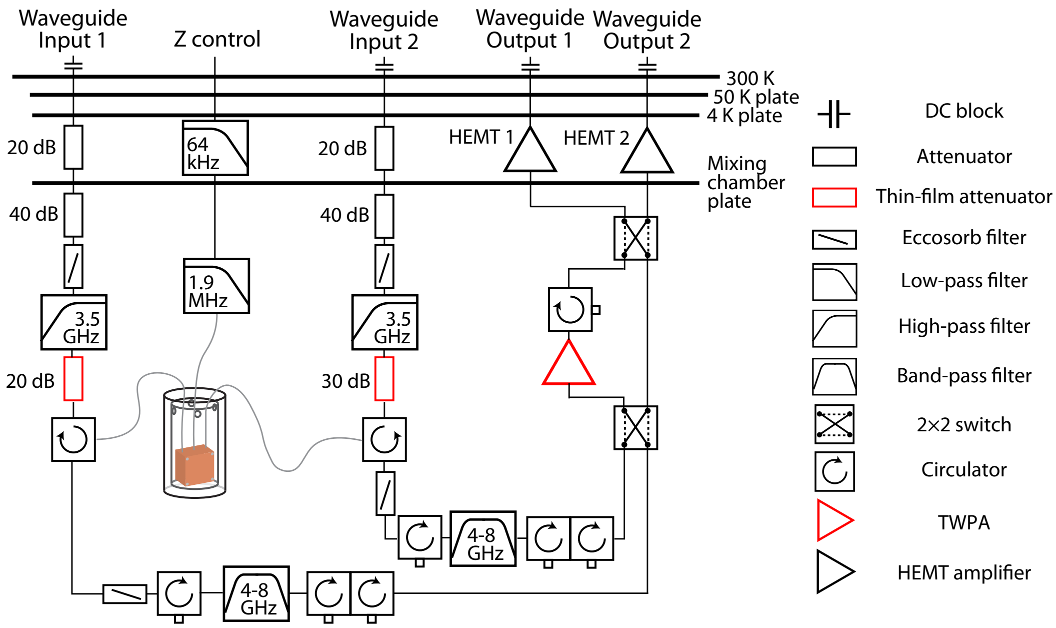

Figure C.6: Schematic of the measurement setup inside the dilution refrigerator for Device I. The meaning of each symbol in the schematic on the left is enumerated on the right. The level of attenuation of each attenuator is indicated with number next to the symbol. The cutoff frequencies of each filter is specified with numbers inside the symbol. Small squares attached to circulator symbols indicate port termination with $Z_0 = 50\ \Omega$, allowing us to use the 3-port circulator as a 2-port isolator. The input pump line for TWPA is not shown in the diagram for simplicity.

The fitting of the whole structure to the waveguide transmission spectrum results in a set of circuit parameters similar yet slightly different from ones of the test structures quoted in Fig. 5.1: $(C_v, C_w) = (35, 19.2)$fF, $(M_v, M_w) = (-38, -32)$pH, $C_0 = 250$ fF, $L_0 = 1.9$ nH. Here, the definition of C_0 includes contributions from coupling capacitance between qubit and resonator, but excludes the contribution to the resonator self-capacitance from the coupling capacitances C_v, C_w between resonators in the array. With these parameters we calculate the corresponding parameters in the SSH model to be $J/2\pi = 356$ MHz and $\delta = 0.256$ following Eq. (C.19), resulting in the localization length $\xi = [\ln(\frac{1+\delta}{1-\delta})]^{-1} = 1.91$ at the reference frequency. From the measured avoided crossing $g_{45}^{\mathrm{AB}}/2\pi = 32.9$ MHz between qubit-photon bound states facing toward each other on nearest-neighboring sites together with J and δ, we infer the qubit coupling to each resonator site to be $g = \sqrt{g_{45}^{\mathrm{AB}} J(1+\delta)} = 2\pi \times 121.3$ MHz [164], close to the value

$$\frac{C_g}{2\sqrt{C_{\mathrm{q}} C_\Sigma}} \omega_0 = 2\pi \times 132\ \mathrm{MHz}$$

expected from designed coupling capacitance [175]. Note that we find an inconsistent set of values $J/2\pi = 368$ MHz and $\delta = 0.282$ (with $\xi = 1.73$ and $g/2\pi = 124.6$ MHz accordingly) from calculation based on the difference in observed band-edge frequencies, where the frequency difference between the highest frequency in the UPB and the lowest frequency in the LPB equals $4J$ and the size of the MBG equals $4J|\delta|$. The inconsistency indicates the deviation of our system from the proposed circuit model (see App. C.1 for discussion), which accounts for the difference between theoretical curves and the experimental data in Fig. 5.2b and left sub-panel of Fig. 5.3c. The values of J, δ and g from the band-edge frequencies are used to generate the theoretical curves in Fig. 5.5 in the main text as well as in Fig. C.11. The intrinsic quality factor of one of the normal modes (resonant frequency 6.158 GHz) of the metamaterial waveguide was measured to be $Q_i = 9.8 \times 10^4$ at power below the single-photon level, similar to typical values reported in Refs. [144, 172].

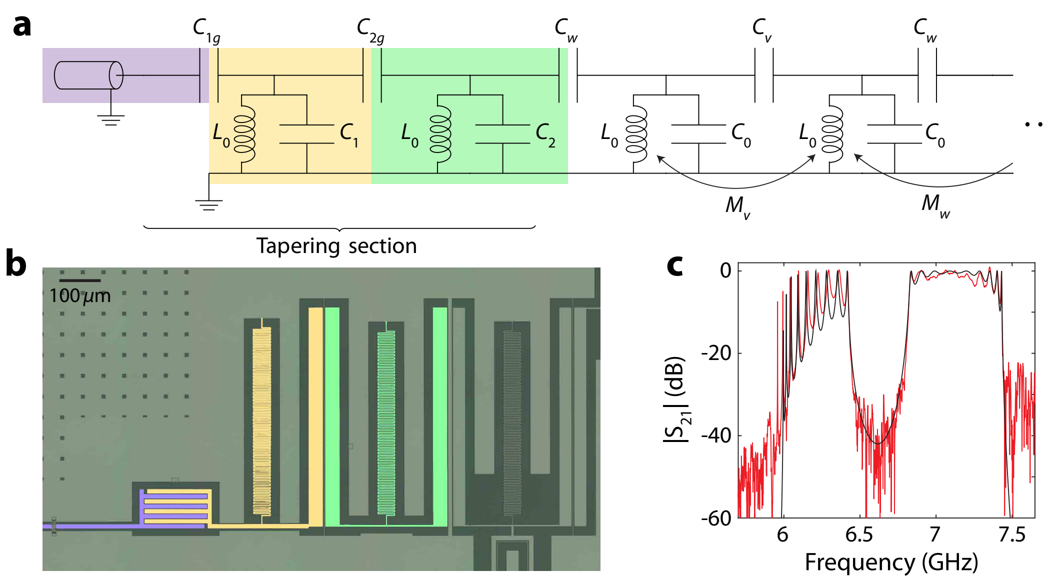

Figure C.7: Tapering section of Device I. **a**, The circuit diagram of the tapering section connecting a coplanar waveguide to the topological waveguide. The coplanar waveguide, first tapering resonator, and second tapering resonator are shaded in purple, yellow, and green, respectively. **b**, Optical micrograph (false colored) of the tapering section on Device I. The tapering section is colored in the same manner as the corresponding components in panel **a**. **c**, Red: measured waveguide transmission spectrum $|S_{21}|$ for Device I. Black: fit to the data with parameters $(C_v, C_w) = (35, 19.2)$ fF, $(M_v, M_w) = (-38, -32)$ pH, $(C_{1g}, C_{2g}) = (141, 35)$ fF, $(C_1, C_2) = (128.2, 230)$ fF, $C_0 = 250$ fF, $L_0 = 1.9$ nH.

Experimental setup

The measurement setup inside the dilution refrigerator is illustrated in Fig. C.6. All the 14 qubits on Device I are DC-biased with individual flux-bias (Z control) lines, filtered by a 64 kHz low-pass filter at the 4K plate and a 1.9 MHz low-pass filter at the mixing chamber plate. The Waveguide Input 1 (2) passes through a series of attenuators and filters including a 20 dB (30 dB) thin-film attenuator developed in B. Palmer's group [177]. It connects via a circulator to port 1 (2) of Device I, which is enclosed in two layers of magnetic shielding. The output signals from Device I are routed by the same circulator to the output lines containing a series of circulators and filters. The pair of 2×2 switches in the amplification chain allows us to choose the branch to be further amplified in the first stage by a traveling-wave parametric amplifier (TWPA) from MIT Lincoln Laboratories. Both of the output lines are amplified by an individual high electron mobility transistor (HEMT) at the 4K plate, followed by room-temperature amplifiers at 300 K. All four S-parameters S_{ij} $(i, j \in \{1, 2\})$ involving port 1 and 2 on Device I can be measured with this setup by choosing one of the waveguide input ports and one of the waveguide output ports, e.g. S_{11} can be measured by sending the input signal into Waveguide Input 1 and collecting the output signal from Waveguide Output 2 with both 2×2 switches in the cross (×) configuration.

C.4 Tapering sections on Device I

The finite system size of metamaterial waveguide gives rise to sharp resonances inside the passband associated with reflection at the boundary (Fig. 5.2b of the main text). Also, the decay rate of qubits to external ports inside the middle bandgap (MBG) is small, making the spectroscopic measurement of qubits inside the MBG hard to achieve. In order to reduce ripples in transmission spectrum inside the upper passband and increase the decay rates of qubits to external ports comparable to their intrinsic contributions inside the middle bandgap, we added two resonators at each end of the metamaterial waveguide in Device I as tapering section.

Similar to the procedure described in Appendix C of Ref. [144], the idea is to increase the coupling capacitance gradually across the two resonators while keeping the resonator frequency the same as other resonators by changing the self capacitance as well. However, unlike the simple case of an array of LC resonators with uniform coupling capacitance, the SSH waveguide consists of alternating coupling capacitance between neighboring resonators and two separate passbands form as a result. In this particular work, the passband experiments are designed to take place at the upper passband frequencies and hence we have slightly modified the resonant frequencies of tapering resonators to perform impedance-matching inside the upper passband. The circuit diagram shown in Fig. C.7a was used to model the tapering section in our system. While designing of tapering sections involves empirical trials, microwave filter design software, e.g. iFilter module in AWR Microwave Office, can be used to aid the choice of circuit parameters and optimization method.

Figure C.7b shows the optical micrograph of a tapering section on Device I. The circuit parameters are extracted by fitting the normalized waveguide transmission spectrum (S_{21}) data from measurement with theoretical circuit models. We find a good agreement in the frequency of normal modes and the level of ripples between the theoretical model and the experiment as illustrated in Fig. C.7c. The level of ripples in the transmission spectrum of the entire upper passband is about 8 dB and decreases to below 2 dB near the center of the band, allowing us to probe the cooperative interaction between qubits at these frequencies.

C.5 Directional shape of qubit-photon bound state

In this section, we provide detailed explanations on the directional shape of qubit-photon bound states discussed in the main text. As an example, we consider a system consisting of a topological waveguide in the trivial phase and a qubit coupled to the A sublattice of the n-th unit cell (Fig. C.8a). Our descriptions are based on partitioning the system into subsystems under two alternative pictures (Fig. C.8b,c), where the array is divided on the left (Description I) or the right (Description II) of the site (n, A) where the qubit is coupled to.

Description I

We divide the array into two parts by breaking the inter-cell coupling $J_w = J(1-\delta)$ that exists on the left of the site (n, A) where the qubit is coupled to, i.e., between sites $(n-1, \mathrm{B})$ and (n, A). The system is described in terms of two subsystems S_1 and S_2 as shown in Fig. C.8b. The subsystem S_1 is a semi-infinite array in the trivial phase extended from the $(n-1)$-th unit cell to the left and the subsystem S_2 comprising a qubit and a semi-infinite array in the trivial phase extended from the n-th unit cell to the right. The coupling between the two subsystems is interpreted to

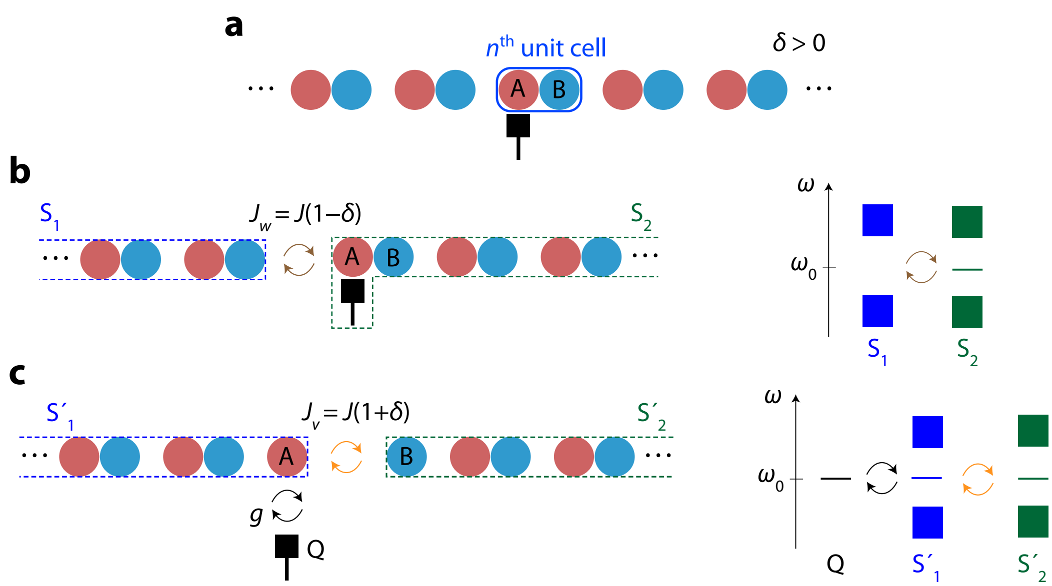

Figure C.8: Understanding the directionality of qubit-photon bound states. **a**, Schematic of the full system consisting of an infinite SSH waveguide with a qubit coupled to the A sublattice of the n-th unit cell and tuned to frequency ω_0 in the center of the MBG. Here we make the unit cell choice in which the waveguide is in the trivial phase ($\delta > 0$). **a**, Division of system in panel **a** into two subsystems S_1 and S_2 in Description I. **a**, Division of system in panel (a) into three subsystems [qubit (Q), S_1', S_2'] in Description II. For panels **b** and **c**, the left side shows the schematic of the division into subsystems and the right side illustrates the mode spectrum of the subsystems and the coupling between them.

take place at a boundary site with coupling strength J_w. When the qubit frequency is resonant to the reference frequency ω_0, the subsystem S_2 can be viewed as a semi-infinite array in the topological phase, where the qubit effectively acts as an edge site. Here, the resulting topological edge mode of subsystem S_2 is the qubit-photon bound state, with photon occupation mostly on the qubit itself and on every B site with a decaying envelope. Coupling of subsystem S_2 to S_1 only has a minor effect on the edge mode of S_2 as the modes in subsystem S_1 are concentrated at passband frequencies, far-detuned from $\omega = \omega_0$. Also, the presence of an edge state of S_2 at $\omega = \omega_0$ cannot induce an additional occupation on S_1 by this coupling in a way that resembles an edge state since the edge mode of S_2 does not occupy sites on the A sublattice. The passband modes S_1 and S_2 near-resonantly couple to each other, whose net effect is redistribution of modes within the passband frequencies. Therefore, the qubit-photon bound state can be viewed as a topological edge mode for subsystem S_2 which is unperturbed by coupling to subsystem S_1. The directionality and photon occupation distribution along the resonator chain of the qubit-photon bound state can be naturally explained according to this picture.

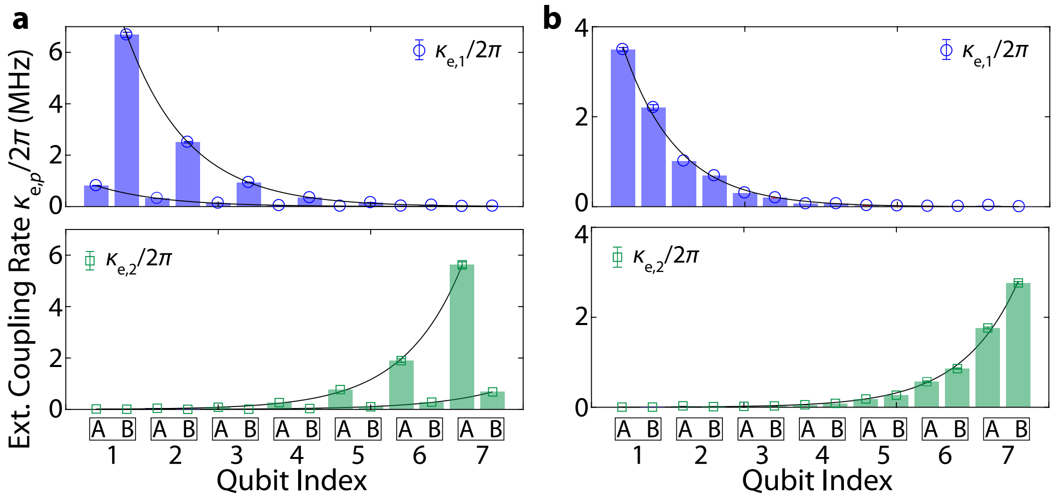

Figure C.9: **a**, Upper (Lower) plots: external coupling rate of the qubit-photon bound states to port 1 (2) at 6.72 GHz in the middle bandgap. Exponential fit (black curve) on the data gives the localization length of $\xi = 2$. **b**, Upper (Lower) plots: external coupling rate of the qubit-photon bound states to port 1 (2) at 7.485 GHz in the upper bandgap. Exponential fit (black curve) on the data gives the localization length of $\xi = 1.8$. The localization lengths are represented in units of lattice constant. For all panels, the error bars show 95% confidence interval and are removed on data points whose error is smaller than the marker size.

Description II

In this alternate description, we divide the array into two parts by breaking the intra-cell coupling $J_v = J(1+\delta)$ that exists on the right of the site (n, A) where the qubit is coupled to, i.e., between sites (n, A) and (n, B). We consider the division of the system into three parts: the qubit, subsystem S'_1, and subsystem S'_2 as illustrated in Fig. C.8c. Here, the subsystem S'_1 (S'_2) is a semi-infinite array in the topological phase extended to the left (right), where the last site hosting the topological edge mode E'_1 (E'_2) at $\omega = \omega_0$ is the A (B) sublattice of the n-th unit cell. The subsystem S'_1 is coupled to both the qubit and the subsystem S'_2 with coupling strength g and $J_v = J(1+\delta)$, respectively. Similar to Description I, the result of coupling between subsystem modes inside the passband is the reorganization of modes without significant change in the spectrum inside the middle bandgap. On the other hand, modes of the subsystems at $\omega = \omega_0$ (qubit, E'_1, and E'_2) can be viewed as emitters coupled in a linear chain configuration, whose eigenfrequencies and corresponding eigenstates in the single-excitation manifold are given by

$$\tilde{\omega}_{\pm} = \omega_0 \pm \sqrt{\tilde{g}^2 + \tilde{J}_v^2},$$
$$|\psi_{\pm}\rangle = \frac{1}{\sqrt{2}} \left(\frac{\tilde{g}}{\sqrt{\tilde{g}^2 + \tilde{J}_v^2}} |100\rangle \pm |010\rangle + \frac{\tilde{J}_v}{\sqrt{\tilde{g}^2 + \tilde{J}_v^2}} |001\rangle \right),$$

and

$$\tilde{\omega}_0 = \omega_0, \quad |\psi_0\rangle = \frac{1}{\sqrt{\tilde{g}^2 + \tilde{J}_v^2}} \left(\tilde{J}_v |100\rangle - \tilde{g} |001\rangle \right),$$

where $|n_1 n_2 n_3\rangle$ denotes a state with (n_1, n_2, n_3) photons in the (qubit, E_1', E_2'), respectively. Here, $\tilde{g}$ ($\tilde{J}_v$) is the coupling between edge mode E_1' and the qubit (edge mode E_2'), diluted from g (J_v) due to the admixture of photonic occupation on sites other than the boundary in the edge modes. Note that in the limit of short localization length, we recover $\tilde{g} \approx g$ and $\tilde{J}_v \approx J_v$. Among the three single-excitation eigenstates, the states $|\psi_{\pm}\rangle$ lie at frequencies of approximately $\omega_0 \pm J$, and are absorbed into the passbands. The only remaining state inside the middle bandgap is the state $|\psi_0\rangle$, existing exactly at $\omega = \omega_0$, which is an anti-symmetric superposition of qubit excited state and the single-photon state of E_2', whose photonic envelope is directed to the right with occupation on every B site. This accounts for the directional qubit-photon bound state emerging in this scenario.

C.6 Coupling of qubit-photon bound states to external ports at different frequencies

As noted in the main text (Fig. 5.3), the perfect directionality of the qubit-photon bound states is achieved only at the reference frequency ω_0 inside the middle bandgap. In this section, we discuss the breakdown of the observed perfect directionality when qubits are tuned to different frequencies inside the middle bandgap by showing the behavior of the external coupling $\kappa_{\mathrm{e},p}$ ($p = 1, 2$) to the ports.

Inside the middle bandgap, detuned from the reference frequency

Figure C.9a shows the external coupling rate of qubits to the ports at 6.72 GHz, a frequency in the middle bandgap close to band-edge. The alternating behavior of external coupling rate is still observed, but with a smaller contrast than in Fig. 5.3 of the main text. The dependence of external linewidth on qubit index still exhibits the

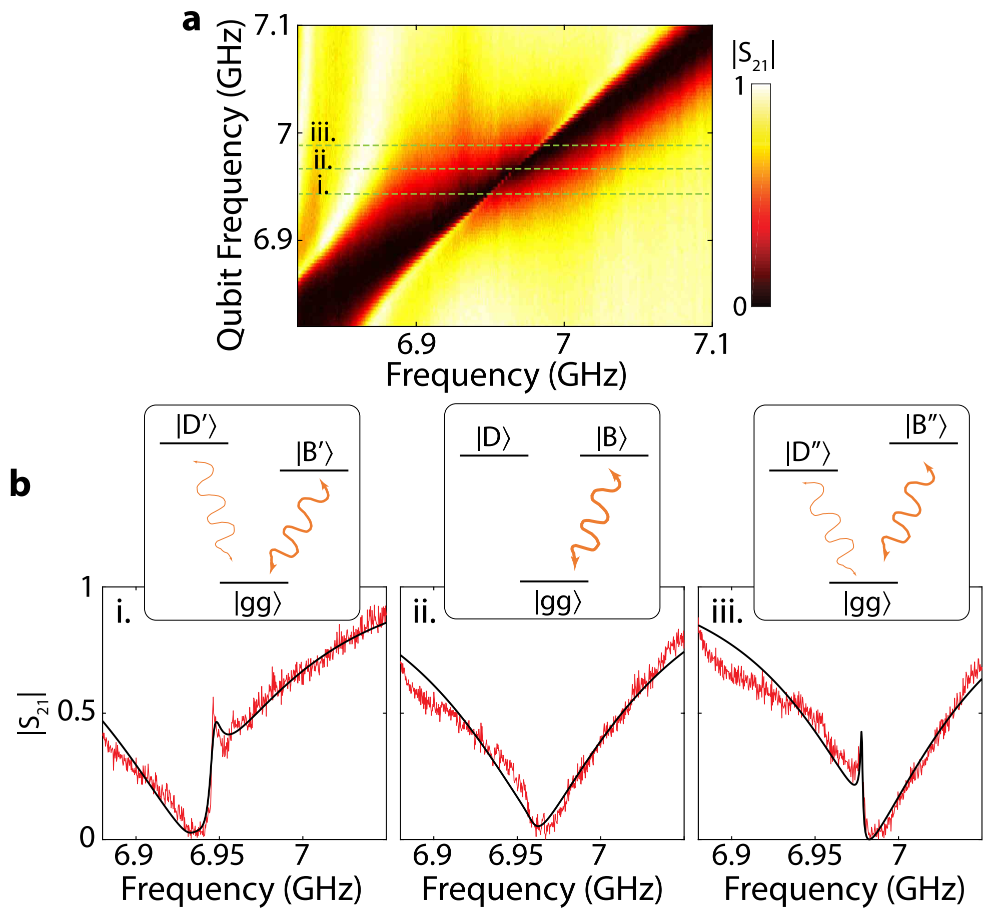

Figure C.10: **a**, Zoomed-in view of the swirl feature near 6.95 GHz of the experimental data illustrated in Fig. 5.5c in the main text. **b**, Transmission spectrum across two-qubit resonance for three different frequency tunings, corresponding to line cuts marked with green dashed lines on panel **a**. The insets to panel **b** show the corresponding level diagram with $|gg\rangle$ denoting both qubits in ground states and $|B\rangle$ ($|D\rangle$) representing the perfect bright (dark) state. The state notation with prime (double prime) in sub-panel i. (iii.) denotes the imperfect super-radiant bright state and sub-radiant dark state, with the width of orange arrows specifying the strength of the coupling of states to the waveguide channel. The sub-panel ii. occurs at the center of the swirl, where perfect super-radiance and sub-radiance takes place (i.e., bright state waveguide coupling is maximum and dark state waveguide coupling is zero). The black and red curves correspond to experimental data and theoretical fit, respectively.

remaining directionality with qubits on A (B) sublattice maintaining large coupling to port 2 (1), while showing small non-zero coupling to the opposite port.

Inside the upper bandgap

Inside the upper bandgap (7.485 GHz), the coupling of qubit-photon bound states to external ports decreases monotonically with the distance of the qubit site to the port, regardless of which sublattice the qubit is coupled to (Fig. C.9b). This behavior is similar to that of qubit-photon bound states formed in a structure with uniform coupling, where bound states exhibit a symmetric photonic envelope surrounding the qubit. Note that we find the external coupling to port 2 ($\kappa_{\mathrm{e},2}$) to be generally smaller than that to port 1 ($\kappa_{\mathrm{e},1}$), which may arise from a slight impedance mismatch on the connection of the device to the external wiring.

C.7 Probing band topology with qubits

Signature of perfect super-radiance

Here we take a closer look at the swirl pattern in the waveguide transmission spectrum – a signature of perfect super-radiance – which is discussed in Fig. 5.5c of the main text. In Fig. C.10 we zoom in to the observed swirl pattern near 6.95 GHz, and three horizontal line cuts. At the center of this pattern (sub-panel ii. of Fig. C.10b), the two qubits form perfect super-/sub-radiant states with maximized correlated decay and zero coherent exchange interaction [145, 149]. At this point, the transmission spectrum shows a single Lorentzian lineshape (perfect super-radiant state and bright state) with linewidth equal to the sum of individual linewidths of the coupled qubits. The perfect sub-radiant state (dark state), which has no external coupling, cannot be accessed from the waveguide channel here and is absent in the spectrum. Slightly away from this frequency, the coherent exchange interaction starts to show up, making hybridized states $|\mathrm{B}'\rangle$, $|\mathrm{D}'\rangle$ formed by the interaction of the two qubits. In this case, both of the hybridized states have non-zero decay rate to the waveguide, forming a V-type level structure [164]. The interference between photons scattering off the two hybridized states gives rise to the peak in the middle of sub-panels (i.) and (iii.) in Fig. C.10b.

The fitting of lineshapes starts with the subtraction of transmission spectrum of the background, which are taken in the same frequency window but with qubits detuned away. Note that the background subtraction in this case cannot be perfect due to the frequency shift of the upper passband modes under the presence of qubits. Such imperfection accounts for most of the discrepancy between the fit and the experimental data. The fit employs the transfer matrix method discussed in Refs. [137, 138, 314]. Here, the transfer matrix of the two qubits takes into account the pure dephasing, which causes the sharp peaks in sub-panels (i.) and (iii.) of Fig. C.10b to stay below perfect transmission level (unity) as opposed to the prediction from the ideal case of electromagnetically induced transparency [222].

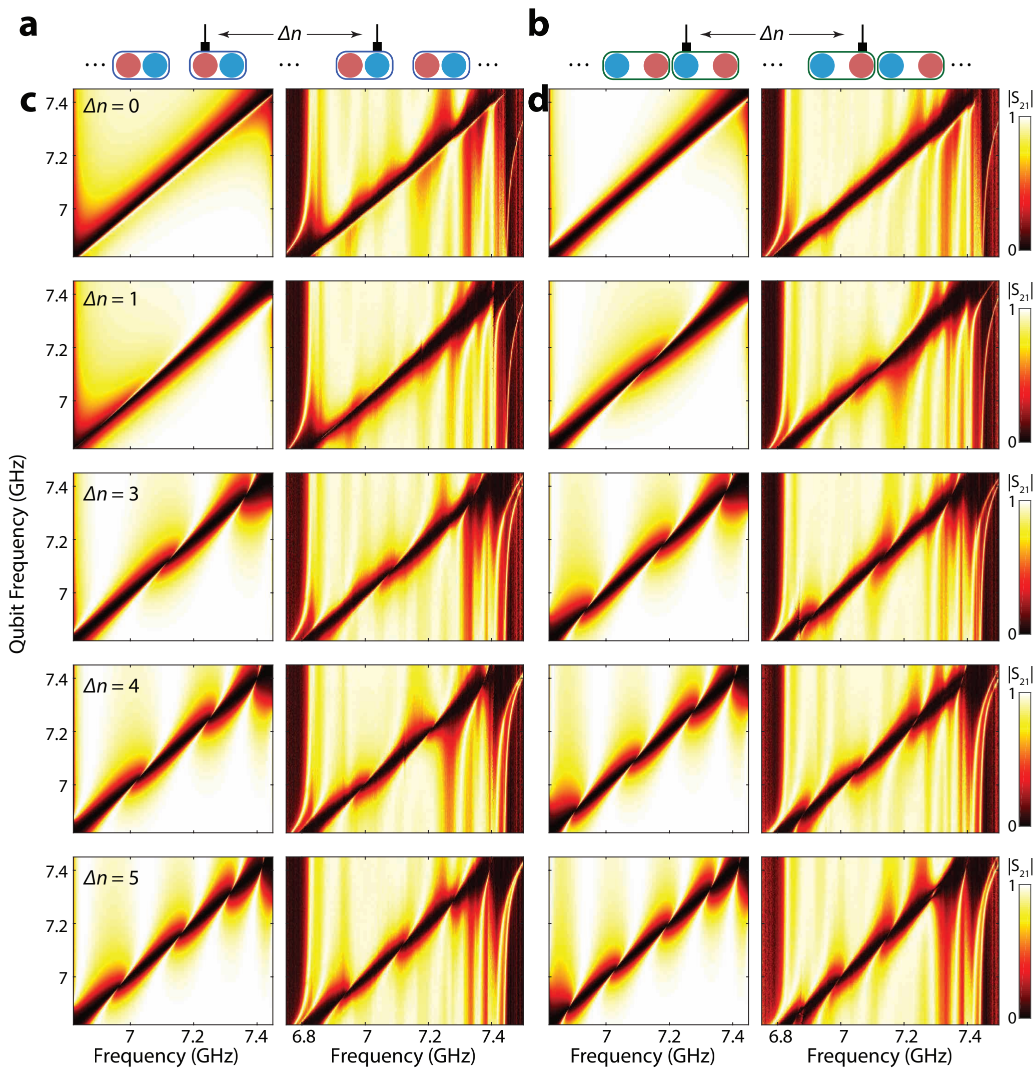

Figure C.11: **a**, Schematic showing two qubits separated by Δn unit cells in the trivial configuration. **b**, Corresponding schematic for topological phase configuration. **c**, Waveguide transmission spectrum $|S_{21}|$ when frequencies of two qubits are resonantly tuned across the upper passband in the trivial configuration. **d**, Waveguide transmission spectrum $|S_{21}|$ for the topological configuration. For both trivial and topological spectra, the left spectrum illustrates theoretical expectations based on Ref. [164] whereas the right shows the experimental data.

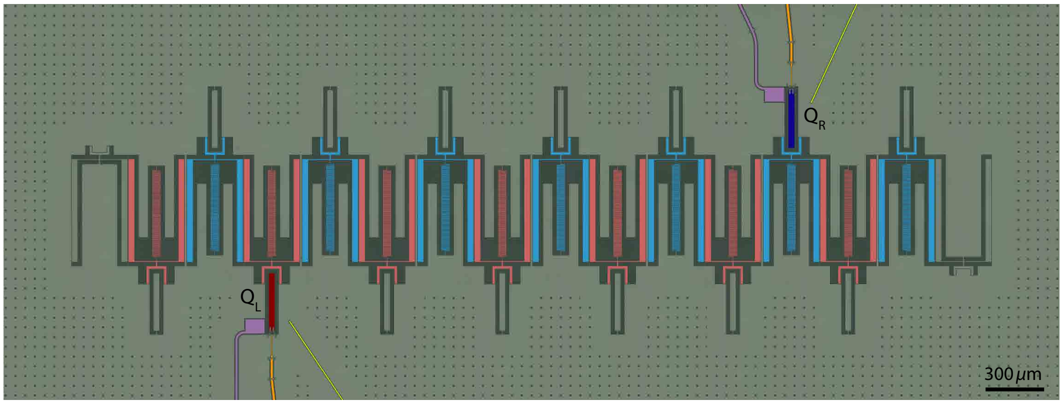

Figure C.12: The device consists of a topological waveguide with 7 unit cells (resonators corresponding to A/B sublattice colored red/blue) in the topological phase, where the inter-cell coupling is larger than the intra-cell coupling. Two qubits Q_L (dark red) and Q_R (dark blue) are coupled to A sublattice of the second unit cell and B sublattice of sixth unit cell, respectively. Each qubit is coupled to a $\lambda/4$ coplanar waveguide resonator (purple) for dispersive read-out, flux-bias line (orange) for frequency control, and charge line (yellow) for local excitation control.

Topology-dependent photon scattering on various qubit pairs

As mentioned in the main text, when two qubits are separated by Δn ($\Delta n > 0$) unit cells, the emergence of perfect super-radiance (vanishing of coherent exchange interaction) is governed by Eq. (5.2). Although Eq. (5.2) is satisfied at the band-edges it does not lead to additional point of super-radiance because the non-Markovianity at these points do not lead to effective correlated decay [157]. Therefore, the perfect super-radiance takes place exactly $\Delta n - 1$ times in the trivial phase and Δn times in the topological phase across the entire passband. The main text shows the case of $\Delta n = 2$. Here we report similar measurements on other qubit pairs with different cell distance Δn between the qubits. Figure C.11 shows good qualitative agreement between the experiment and theoretical result in Ref. [164]. The small avoided-crossing-like features in the experimental data are due to coupling of one of the qubits with a local two-level system defect. An example of this is seen near 6.85 GHz of $\Delta n = 3$ in the topological configuration. For $\Delta n = 0$, there is no perfect super-radiant point throughout the passband for both trivial and topological configurations. For all the other combinations in Fig. C.11, the number of swirl patterns indicating perfect super-radiance agrees with the theoretical model.

Qubit	f_{max} (GHz)	E_C/h (MHz)	$E_{J\Sigma}/h$ (GHz)	$g_E/2\pi$ (MHz)	f_{RO} (GHz)	$g_{\text{RO}}/2\pi$ (MHz)	T_1 (μs)	T_2^* (μs)
Q_L	8.23	294	30.89	58.1	5.30	43.5	4.73	4.04
Q_R	7.99	296	28.98	57.3	5.39	43.4	13.9	8.3

Table C.2: **Qubit parameters on Device II.** f_{max} is the maximum frequency (sweet spot) and E_C ($E_{J\Sigma}$) is the charging (Josephson) energy of the qubit. g_E is the coupling of qubit to the corresponding edge state. The read-out resonator at frequency f_{RO} is coupled to the qubit with coupling strength g_{RO}. T_1 (T_2^*) is the lifetime (Ramsey coherence time) of a qubit measured at the sweet spot.

C.8 Device II characterization and experimental setup

In this section we provide a detailed description of the elements making up Device II, in which the edge mode experiments are performed. The optical micrograph of Device II is illustrated in Fig. C.12.

Qubits

The parameters of qubits on Device II are summarized in Table C.2. The two qubits are designed to have identical SQUID loops with symmetric JJs. The lifetime and Ramsey coherence times in the table are measured when qubits are tuned to their sweet spot. Qubit coherence at the working frequency in the middle bandgap is also characterized, with the lifetime and Ramsey coherence times of Q_L (Q_R) at 6.829 (6.835) GHz measured to be $T_1 = 6.435$ (5.803) μs and $T_2^* = 344$ (539) ns, respectively.

Metamaterial waveguide and coupling to qubits

The resonators in the metamaterial waveguide and their coupling to qubits are designed to be nominally identical to those in Device I. The last resonators of the array are terminated with a wing-shape patterned ground plane region in order to maintain the bare self-capacitance identical to other resonators.

Edge modes

The coherence of the edge modes is characterized by using qubits to control and measure the excitation with single-photon precision. Taking E_L as an example, we

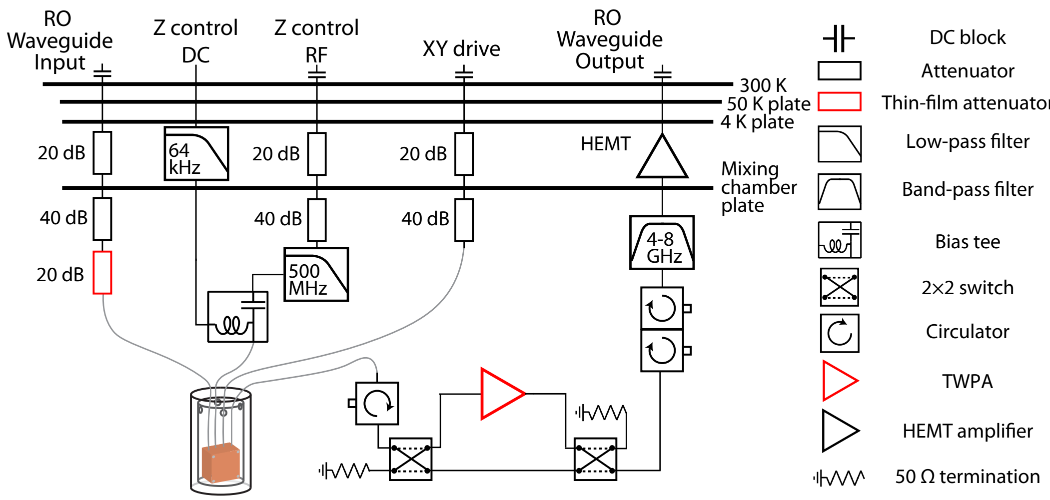

Figure C.13: Schematic of the measurement setup inside the dilution refrigerator for Device II. The meaning of each symbol in the schematic on the left is enumerated on the right. The level of attenuation of each attenuator is indicated with number next to the symbol. The cutoff frequencies of each filter is specified with numbers inside the symbol. Small squares attached to circulator symbols indicate port termination with $Z_0 = 50\ \Omega$, allowing us to use the 3-port circulator as a 2-port isolator. The pump line for the TWPA is not shown in the diagram for simplicity.

define the iSWAP gate as a half-cycle of the vacuum Rabi oscillation in Fig. 5.6d of the main text. For measurement of the lifetime of the edge state $\mathrm{E_L}$, the qubit $\mathrm{Q_L}$ is initially prepared in its excited state with a microwave π-pulse, and an iSWAP gate is applied to transfer the population from $\mathrm{Q_L}$ to $\mathrm{E_L}$. After waiting for a variable delay, we perform the second iSWAP to retrieve the population from $\mathrm{E_L}$ back to $\mathrm{Q_L}$, followed by the read-out of $\mathrm{Q_L}$. In order to measure the Ramsey coherence time, the qubit $\mathrm{Q_L}$ is instead prepared in an equal superposition of ground and excited states with a microwave $\pi/2$-pulse, followed by an iSWAP gate. After a variable delay, we perform the second iSWAP and another $\pi/2$-pulse on $\mathrm{Q_L}$, followed by the read-out of $\mathrm{Q_L}$. An equivalent pulse sequence for $\mathrm{Q_R}$ is used to characterize the coherence of $\mathrm{E_R}$. The lifetime and Ramsey coherence time of $\mathrm{E_L}$ ($\mathrm{E_R}$) are extracted to be $T_1 = 3.68\ (2.96)\ \mu$s and $T_2^* = 4.08\ (2.91)\ \mu$s, respectively, when $\mathrm{Q_L}$ ($\mathrm{Q_R}$) is parked at 6.829 (6.835) GHz. Due to the considerable amount of coupling g_E between the qubit and the edge mode compared to the detuning at park frequency, the edge modes are hybridized with the qubits during the delay time in the above-mentioned pulse sequences. As a result, the measured coherence time of the edge modes is likely limited here by the dephasing of the qubits.

Experimental setup

The measurement setup inside the dilution refrigerator is illustrated in Fig. C.13. The excitation of the two qubits is controlled by capacitively-coupled individual XY microwave drive lines. The frequency of qubits are controlled by individual DC bias (Z control DC) and RF signals (Z control RF), which are combined using a bias tee at the mixing chamber plate. The read-out signals are sent into RO Waveguide Input, passing through a series of attenuators including a 20 dB thin-film attenuator developed in B. Palmer's group [177]. The output signals go through an optional TWPA, a series of circulators and a band-pass filter, which are then amplified by a HEMT amplifier (RO Waveguide Output).

Details on the population transfer process

In step i) of the double-modulation scheme described in the main text, the frequency modulation pulse on Q_R (control modulation) is set to be 2 ns longer than that on Q_L (transfer modulation). The interaction strength induced by the control modulation is 21.1 MHz, smaller than that induced by the transfer modulation in order to decrease the population leakage between the two edge states. For step iii), the interaction strength induced by the control modulation on Q_L is 22.4 MHz, much closer to interaction strength for the transfer than expected (this was due to a poor calibration of the modulation efficiency of qubit sideband). The interaction strengths being too close between $Q_L \leftrightarrow E_L$ and $Q_R \leftrightarrow E_R$ gives rise to unwanted leakage and decreases the required interaction time in step ii). We expect that a careful optimization on the frequency modulation pulses would have better addressed this leakage problem and increase the transfer fidelity (see below).

The fit to the curves in Fig. 5.6e of the main text are based on numerical simulation with QuTiP [21], assuming the values of lifetime (T_1) and coherence time (T_2^*) from the characterization measurements. The free parameters in the simulation are the coupling strengths $\tilde{g}_L$, $\tilde{g}_R$ between qubits and edge states, whose values are extracted from the best fit of the experimental data.

The detailed contributions to the infidelity of the as-implemented population transfer protocol are also analyzed by utilizing QuTiP. The initial left-side qubit population probability is measured to be only 98.4 %, corresponding to an infidelity of 1.6 % in the π-pulse qubit excitation in this transfer experiment (compared to a previously calibrated 'optimized' pulse). In the following steps, we remove the leakage between edge modes and the decoherence process sequentially to see their individual contributions to infidelity. First, we set the coupling strength between the two edge modes to zero during the two iSWAP gates while keeping the above-mentioned initial population probability, coupling strengths, lifetimes, and coherence times. The elimination of unintended leakage during the left and right side iSWAP steps between the edge modes gives the final transferred population probability of 91.9 %, suggesting $91.9\ \% - 87\ \% = 4.9\ \%$ of the infidelity comes from the unintended leakage between edge modes. Also, as expected, setting the population decay and decoherence of the qubits and the edge modes to zero, the final population is found to be identical to the initial value, indicating that $98.4\ \% - 91.9\ \% = 6.5\ \%$ of loss arises from the decoherence processes.

Appendix D

SUPPLEMENTARY INFORMATION FOR CHAPTER 6

D.1 Theoretical modeling of the quantum simulator

In this section, we describe the theoretical modeling of the metamaterial-based quantum simulator used in the main text.

Analytical modeling

In the analytical modeling, we discuss the Hamiltonian description of our quantum simulator by mapping its basic circuit model onto a tight-binding array of coupled cavities with locally coupled qubits under various approximations. We derive the effective Hamiltonian in the qubit subspace, resulting in an analytical form of the metamaterial-mediated coupling between qubits described in the main text.

Approximate canonical quantization of the metamaterial waveguide

The metamaterial waveguide consists of an array of inductor-capacitor (LC) resonators with inductance L_0 and capacitance C_0 coupled with capacitance C_t illustrated in Fig. D.1. We denote the flux variable of each node of the metamaterial as $\Phi_n(t) \equiv \int_{-\infty}^{t} \mathrm{d}t'\, V_n(t')$. The Lagrangian in the position space reads

$$\mathcal{L} = \sum_{n=0}^{N} \left[\frac{C_t}{2} \left(\dot{\Phi}_{n+1} - \dot{\Phi}_n \right)^2 + \frac{C_0}{2} \left(\dot{\Phi}_n \right)^2 - \frac{\Phi_n^2}{2L_0} \right] \tag{D.1}$$

where $\Phi_{n=0} = \Phi_{n=N+1} \equiv 0$. Starting from this Lagrangian, the canonical quantization of the metamaterial waveguide can be performed approximately in the position space. The node charge variable Q_n conjugate to the node flux variable Φ_n is evaluated as

$$Q_n = \frac{\partial \mathcal{L}}{\partial \dot{\Phi}_n} = C_{w0} \dot{\Phi}_n - C_t \left(\dot{\Phi}_{n+1} + \dot{\Phi}_{n-1} \right), \tag{D.2}$$

where $C_{w0} = C_0 + 2C_t$ is the effective self-capacitance of LC resonators forming the metamaterial waveguide. Using a vector notation $\boldsymbol{\Phi} \equiv (\Phi_1, \Phi_2, \cdots, \Phi_N)^\top$, $\boldsymbol{Q} \equiv (Q_1, Q_2, \cdots, Q_N)^\top$, the linear relation between node charges and voltages can be written in a compact form $\boldsymbol{Q} = \boldsymbol{C}\dot{\boldsymbol{\Phi}}$, with the capacitance matrix $\boldsymbol{C}$ given by

$$\boldsymbol{C} = C_{w0}\boldsymbol{I} - C_t\boldsymbol{J}_1. \tag{D.3}$$

Here, $\boldsymbol{I}$ is an $N \times N$ identity matrix and $\boldsymbol{J}_k$ is a matrix with components $[\boldsymbol{J}_k]_{n,n'} = \delta_{n,k+n'} + \delta_{n+k,n'}$, i.e., unity on the kth off-diagonal. Also, the Lagrangian in Eq. D.1 can be rewritten as $\mathcal{L} = \frac{1}{2}\dot{\boldsymbol{\Phi}}^\top\boldsymbol{C}\dot{\boldsymbol{\Phi}} - \frac{1}{2L_0}\boldsymbol{\Phi}^\top\boldsymbol{\Phi}$ using this vector notation. The Legendre transformation $H = \sum_n Q_n\dot{\Phi}_n - \mathcal{L}$ [315] gives the Hamiltonian of the metamaterial waveguide

$$H = \frac{1}{2}\boldsymbol{Q}^\top\boldsymbol{C}^{-1}\boldsymbol{Q} + \frac{1}{2L_0}\boldsymbol{\Phi}^\top\boldsymbol{\Phi}. \tag{D.4}$$

The first-order approximation to the inverse of capacitance matrix is given by

$$\begin{aligned}\boldsymbol{C}^{-1} &= [C_{w0}(\boldsymbol{I} - r\boldsymbol{J}_1)]^{-1} = C_{w0}^{-1}(\boldsymbol{I} + r\boldsymbol{J}_1 + r^2\boldsymbol{J}_1^2 + \cdots) \\ &\approx \frac{1}{C_{w0}}\boldsymbol{I} + \frac{C_t}{C_{w0}^2}\boldsymbol{J}_1 + \mathcal{O}(r^2),\end{aligned} \tag{D.5}$$

where $r = C_t/C_{w0} < 1$ is the ratio of the coupling capacitance to the self capacitance, which is assumed to be small. Using this, the Hamiltonian of the metamaterial waveguide is evaluated as

$$H \approx \sum_{n=1}^{N}\left(\frac{Q_n^2}{2C_{w0}} + \frac{\Phi_n^2}{2L_0} + \frac{C_t}{C_{w0}^2}Q_nQ_{n+1}\right) \tag{D.6}$$

up to first order in r, where $Q_{N+1} \equiv 0$. Note that higher-order approximations to the inverse of capacitance matrix can be calculated using the matrix relations

$$\boldsymbol{J}_1^2 \approx 2\boldsymbol{I} + \boldsymbol{J}_2,\ \boldsymbol{J}_1^3 \approx 3\boldsymbol{J}_1 + \boldsymbol{J}_3,\ \boldsymbol{J}_1^4 \approx 6\boldsymbol{I} + 4\boldsymbol{J}_2 + \boldsymbol{J}_4,\ \cdots,$$

under which the Hamiltonian exhibits long-range coupling beyond nearest neighbors. Here, the magnitude of charge-charge coupling between a pair of resonators at sites (i,j) scales as $\sim r^{|i-j|}$, exponentially decaying with the distance $|i-j|$ between resonators.

We promote the flux and charge variables to quantum operators by imposing the canonical commutation relation $[\hat{\Phi}_n, \hat{Q}_{n'}] = i\hbar\delta_{n,n'}$. The annihilation (creation) operator $\hat{a}_n$ ($\hat{a}_n^\dagger$), defined with

$$\hat{\Phi}_n = \sqrt{\frac{\hbar Z_w}{2}}\left(\hat{a}_n + \hat{a}_n^\dagger\right),\ \hat{Q}_n = \frac{1}{i}\sqrt{\frac{\hbar}{2Z_w}}\left(\hat{a}_n - \hat{a}_n^\dagger\right) \tag{D.7}$$

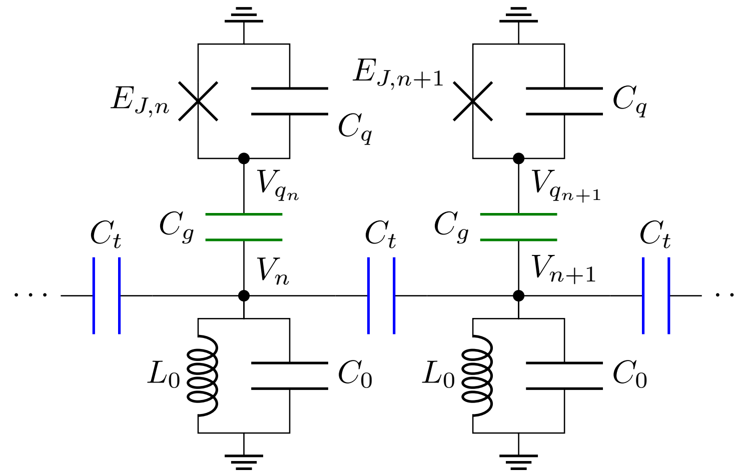

Figure D.1: **Basic circuit model of the metamaterial-based quantum simulator.** The metamaterial waveguide is described by an array of LC resonators with inductance L_0 and capacitance C_0 capacitively coupled to nearest neighbors with a capacitance C_t (colored blue). Superconducting transmon qubits, each represented as a parallel circuit of a Josephson junction and a capacitor, are coupled to each metamaterial resonator site with a capacitance C_g (colored green). The Josephson energy and the capacitance of the qubit at the nth site is given by $E_{J,n}$ and C_q, respectively.

where $Z_{w0} = \sqrt{L_0/C_{w0}}$, satisfies the commutation relation $[\hat{a}_n, \hat{a}^\dagger_{n'}] = \delta_{n,n'}$. Substituting Eq. D.7 into Eq. D.6, we obtain an approximate second-quantized Hamiltonian of the metamaterial under the rotating-wave approximation (RWA), corresponding to the Hamiltonian of an array of nearest-neighbor-coupled cavities [157, 255, 316] illustrated in Fig. 6.1a of the main text. The Hamiltonian is written as

$$\hat{H} = \hbar \sum_{n=1}^{N} \left[\omega_c \hat{a}^\dagger_n \hat{a}_n + t \left(\hat{a}^\dagger_n \hat{a}_{n+1} + \hat{a}^\dagger_{n+1} \hat{a}_n \right) \right], \tag{D.8}$$

where the cavity frequency ω_c and the coupling t between neighboring cavities are given by

$$\omega_c = \frac{1}{\sqrt{L_0(C_0 + 2C_t)}}, \quad t = \frac{C_t}{2(C_0 + 2C_t)} \omega_c. \tag{D.9}$$

Coupling of superconducting qubits to the metamaterial waveguide

We assume coupling a transmon qubit (in the schematic form of a Josephson junction with energy E_J and parallel capacitance C_q) to each metamaterial resonator site via a capacitance C_g as illustrated in Fig. D.1. Following the procedures similar to the above, the full Hamiltonian of the qubit-metamaterial system can be obtained up to first order in the coupling capacitances C_g and C_t, written as

$$\hat{H} \approx \sum_n \left(\frac{\hat{Q}_n^2}{2C_{w\Sigma}} + \frac{\hat{\Phi}_n^2}{2L_0} + \frac{C_t}{C_{w\Sigma}^2}\hat{Q}_n\hat{Q}_{n+1} \right.$$
$$\left. + \frac{\hat{Q}_{q_n}^2}{2C_{q\Sigma}} - E_{J,n}\cos\frac{2\pi\hat{\Phi}_{q_n}}{\Phi_0} + \frac{C_g}{C_{w\Sigma}C_{q\Sigma}}\hat{Q}_n\hat{Q}_{q_n} \right). \tag{D.10}$$

Here, $\hat{\Phi}_n$ ($\hat{Q}_n$) and $\hat{\Phi}_{q_n}$ ($\hat{Q}_{q_n}$) are the node flux (charge) operators of the metamaterial resonator and the qubit at the nth unit cell, respectively, and $\Phi_0 = h/2e$ is a magnetic flux quantum. The self-capacitance of metamaterial resonators and qubits are renormalized to $C_{w\Sigma} = C_{w0} + C_g$ and $C_{q\Sigma} = C_q + C_g$, respectively, redefining the parameters of the cavity array in Eq. D.9 into

$$\omega_c = \frac{1}{\sqrt{L_0(C_0 + C_g + 2C_t)}}, \quad t = \frac{C_t}{2(C_0 + C_g + 2C_t)}\omega_c. \tag{D.9$'$}$$

Introducing the annihilation and the creation operators following a procedure similar to that of Eq. D.7 and restricting the subspace of qubits to their lowest two energy levels, we obtain the Hamiltonian of the metamaterial-qubit system in a second-quantized form

$$\hat{H} = \hbar\sum_n \left[\omega_c \hat{a}_n^\dagger \hat{a}_n + t\left(\hat{a}_n^\dagger \hat{a}_{n+1} + \hat{a}_{n+1}^\dagger \hat{a}_n\right) \right.$$
$$\left. + \frac{\omega_{q_n}}{2}\hat{\sigma}_n^z + g_n\left(\hat{a}_n^\dagger\hat{\sigma}_n^- + \hat{a}_n\hat{\sigma}_n^+\right) \right], \tag{D.11}$$

where

$$g_n = \frac{C_g}{2\sqrt{C_{w\Sigma}C_{q\Sigma}}}\sqrt{\omega_c\omega_{q_n}} \tag{D.12}$$

is the coupling between a qubit and a metamaterial resonator at the nth unit cell. Here, $\hat{\sigma}_n^\alpha$ ($\alpha \in \{\pm, x, y, z\}$) denotes the Pauli operator of qubit at the nth unit cell. We can use the annihilation operators $\hat{a}_k = \frac{1}{\sqrt{N}}\sum_n e^{-iknd}\hat{a}_n$ in the momentum space (satisfying the commutation relation $[\hat{a}_k, \hat{a}_{k'}^\dagger] = \delta_{k,k'}$) to rewrite the Hamiltonian of the metamaterial waveguide in terms of its normal modes, where d is the lattice constant. In this case, the Hamiltonian is given by

$$\hat{H}/\hbar = \sum_k \omega_k \hat{a}_k^\dagger \hat{a}_k + \sum_n \frac{\omega_{q_n}}{2}\hat{\sigma}_n^z$$
$$+ \sum_{n,k}\left(g_{k,n}\hat{a}_k^\dagger\hat{\sigma}_n^- + g_{k,n}^*\hat{a}_k\hat{\sigma}_n^+\right). \tag{D.13}$$

Here, $\omega_k = \omega_c + 2t\cos(kd)$ is the dispersion relation of the metamaterial waveguide (plotted in Fig. 6.1b of the main text) up to first order in $C_t/C_{w\Sigma}$ and $g_{k,n} \equiv g_n e^{-iknd}/\sqrt{N}$ is the coupling of a qubit at site n to a metamaterial mode with wavevector k.

Effective Hamiltonian in the dispersive limit

The effective Hamiltonian $\hat{H}_{\text{eff}}$ of the system can be calculated by performing the Schrieffer-Wolff transformation

$$\hat{U} = \exp\left(\sum_{k,n} \frac{g^*_{k,n}\hat{a}_k\hat{\sigma}^+_n - g_{k,n}\hat{a}^\dagger_k\hat{\sigma}^-_n}{\Delta_{n,k}}\right)$$

on the original Hamiltonian in Eq. D.13, where $\Delta_{n,k} = \omega_{q_n} - \omega_k$ is the detuning of the nth qubit from the metamaterial mode at wavevector k. The result of this transformation is given by

$$\begin{aligned}\hat{H}_{\text{eff}}/\hbar = &\sum_k \omega_k \hat{a}^\dagger_k\hat{a}_k + \sum_n \frac{\omega_{q_n}}{2}\hat{\sigma}^z_n \\ &+ \sum_{n,n'} J_{n,n'}\hat{\sigma}^+_n\hat{\sigma}^-_{n'} + \sum_{k,k',n} K_{k,k',n}\hat{\sigma}^z_n\hat{a}^\dagger_k\hat{a}_{k'},\end{aligned} \tag{D.14}$$

where $K_{k,k',n}$ denotes coupling between a pair of metamaterial modes (k,k') dependent on the state of the nth qubit, giving rise to qubit-state-dependent shift of the metamaterial given by

$$K_{k,k',n} = \frac{g_{k,n}g^*_{k',n}}{2}\left(\frac{1}{\Delta_{n,k}} + \frac{1}{\Delta_{n,k'}}\right), \tag{D.15}$$

and the exchange interaction $J_{n,n'}$ between a qubit pair (n,n') is written as

$$J_{n,n'} = \sum_k \frac{g_{k,n'}g^*_{k,n}}{2}\left(\frac{1}{\Delta_{n,k}} + \frac{1}{\Delta_{n',k}}\right). \tag{D.16}$$

We focus on this exchange interaction, the interaction between qubits mediated by the virtual photons of the metamaterial, by evaluating the sum

$$\begin{aligned}J_{n,n'} = &\sum_k \frac{g_n g_{n'}}{N}\frac{e^{ik(n-n')d}}{2} \\ &\times\left[\frac{1}{\Delta_n - 2t\cos(kd)} + \frac{1}{\Delta_{n'} - 2t\cos(kd)}\right]\end{aligned} \tag{D.17}$$

where $\Delta_n \equiv \omega_{q_n} - \omega_c$ is the detuning of the nth qubit from the bare cavity frequency ω_c. In the discrete model consisting of a finite number of unit cells N, the wavevectors of the metamaterial mode are equally spaced by $\Delta k = 2\pi/Nd$. In the continuum limit, the summation on the right-hand side of Eq. D.17 is cast into

$$\begin{aligned}
&\frac{g_n g_{n'}}{2}\frac{d}{2\pi}\int_{-\pi/d}^{\pi/d}\mathrm{d}k\left[\frac{e^{ik(n-n')d}}{\Delta_n - 2t\cos(kd)} + \frac{e^{ik(n-n')d}}{\Delta_{n'} - 2t\cos(kd)}\right] \\
&= -\frac{g_n g_{n'}}{4\pi}\frac{1}{2t}\left[I(n-n', a_n) + I(n-n', a_{n'})\right],
\end{aligned}$$

where $a_n = -\Delta_n/2J$ and I is the integral function defined and evaluated as

$$\begin{aligned}
I(n,a) &\equiv \int_{-\pi}^{\pi}\mathrm{d}k\frac{e^{ikn}}{a+\cos k} \\
&= \begin{cases} \frac{2\pi}{\sqrt{a^2-1}}(-1)^{|n|}e^{-|n|/\lambda}, & \text{if } a > 1 \\ -\frac{2\pi}{\sqrt{a^2-1}}e^{-|n|/\lambda}, & \text{if } a < -1 \end{cases}.
\end{aligned} \tag{D.18}$$

Here, $\lambda = 1/\mathrm{arccosh}(|a|) = 1/\ln\left(|a| + \sqrt{a^2-1}\right)$. In the following, we describe the behavior of metamaterial-mediated coupling $J_{n,n'}$ between qubits in the bandgap regime.

(a) Lower bandgap. When qubits are tuned to the lower bandgap, i.e., $\Delta_n = \omega_{q_n} - \omega_c < -2t$ and $a_n > 1$, the exchange interaction $J_{n,n'}$ between the qubits mediated by virtual photons of the metamaterial waveguide is calculated as

$$\begin{aligned}
J_{n,n'} = &-(-1)^{|n-n'|}\frac{g_n g_{n'}}{2} \\
&\times\left(\frac{e^{-|n-n'|/\lambda_n}}{\sqrt{\Delta_n^2 - 4t^2}} + \frac{e^{-|n-n'|/\lambda_{n'}}}{\sqrt{\Delta_{n'}^2 - 4t^2}}\right),
\end{aligned} \tag{D.19}$$

where λ_n is the localization length given by

$$\frac{1}{\lambda_n} = \mathrm{arccosh}\left(\frac{|\Delta_n|}{2t}\right). \tag{D.20}$$

Note that the diagonal components $J_{n,n} = -g_n^2/\sqrt{\Delta_n^2 - 4t^2}$ corresponds to the Lamb shift and takes negative values inside the lower bandgap as the metamaterial modes are located at frequencies higher than that of the qubit. Considering the off-diagonal components, if the qubits at sites n and n' are resonant with one another ($\Delta_n = \Delta_{n'}$), the coupling $J_{n,n'}$ falls off exponentially with the distance $|n - n'|$ at a length scale λ_n determined by the detuning Δ_n of qubits and the tunneling rate t. In addition, the coupling $J_{n,n'}$ alternates sign with a factor

$(-1)^{|n-n'|}$ due to the fact that localized modes inside the lower bandgap have quasi-wavevectors k with the real part of π/d. This is because the lowest frequency of the band takes place at $k = \pi/d$ according to the dispersion relation, and any localized modes inside the lower bandgap must have a real part of the wavevector that is an analytic continuation of the lowest-frequency point.

(b) *Upper bandgap.* When qubits are tuned to the upper bandgap, $\Delta_n = \omega_{q_n} - \omega_c > 2t$ and $a_n < -1$, the exchange interaction $J_{n,n'}$ is evaluated as

$$J_{n,n'} = \frac{g_n g_{n'}}{2} \left(\frac{e^{-|n-n'|/\lambda_n}}{\sqrt{\Delta_n^2 - 4t^2}} + \frac{e^{-|n-n'|/\lambda_{n'}}}{\sqrt{\Delta_{n'}^2 - 4t^2}} \right), \tag{D.21}$$

with the localization length λ_n having a form identical to Eq. D.20. The diagonal components $J_{n,n} = g_n^2/\sqrt{\Delta_n^2 - 4t^2}$ (i.e., the Lamb shift) takes positive values inside the upper bandgap since the metamaterial modes are located at frequencies lower than that of the qubits. Similar to the case of lower bandgap, the coupling $J_{n,n'}$ between qubits at sites n and n' inside the upper bandgap falls off exponentially with the distance $|n - n'|$ at a length scale λ_n. However, the alternating sign factor is not present in the upper bandgap case due to the fact that the quasi-wavevector inside the upper bandgap has real part of zero. Therefore, the coupling $J_{n,n'}$ mediated by the metamaterial waveguide is always positive inside the upper bandgap.

Numerical modeling

While the analytical modeling discussed in Sec. D.1 is useful for understanding the basic processes in our quantum simulator, the presence of long-range coupling between metamaterial resonators (due to large coupling capacitance values) and parasitic coupling mechanisms in the realized device complicate the picture, causing our experimental data to deviate significantly from the simplest analytical theory. To resolve this, we come up with a theory for numerical modeling that allows us to find realistic parameters of the device.

Derivation of Hamiltonian

We assume a general circuit model illustrated in Fig. D.2, extended from the one used in the analytical modeling in Fig. D.1 which consists of an array of LC resonators with

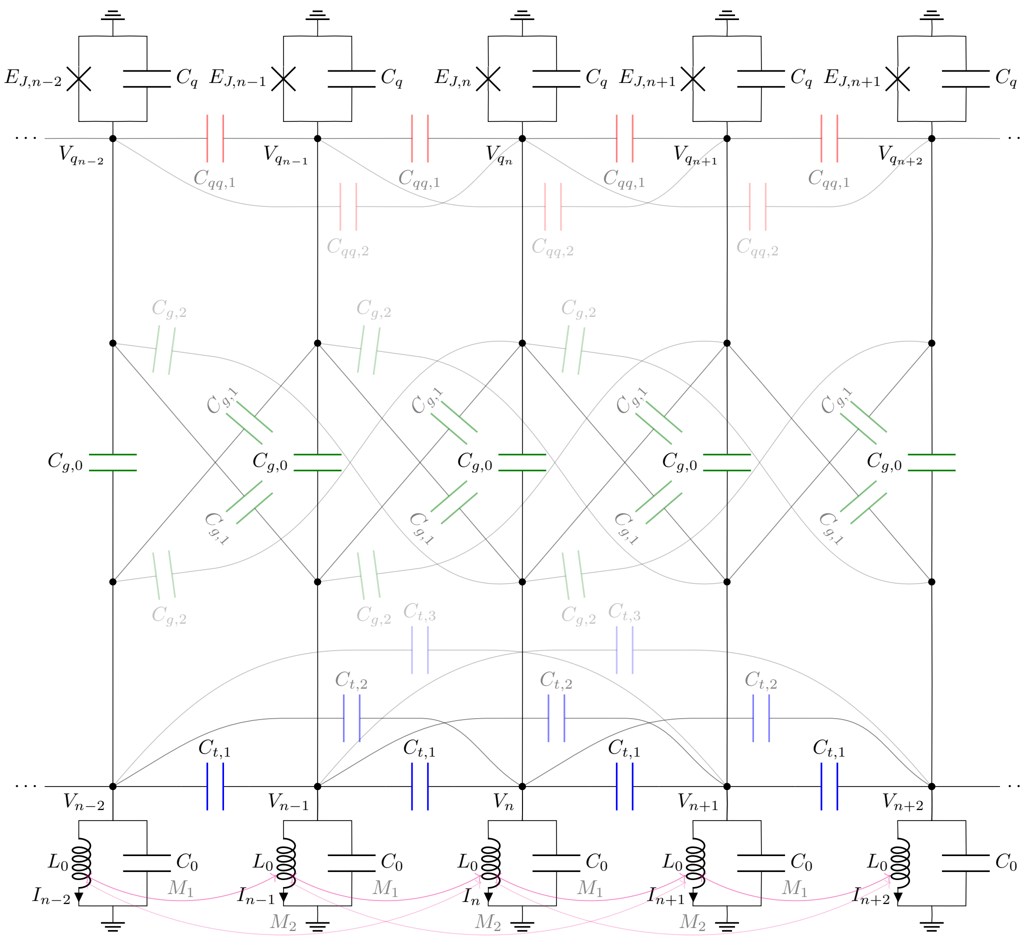

Figure D.2: **General circuit model of the metamaterial-based quantum simulator for numerical modeling.** L_0 (C_0) is the self-inductance (self-capacitance) of metamaterial resonators and $E_{J,n}$ (C_q) is the Josephson energy (capacitance) of qubit coupled to the nth unit cell. The capacitance between metamaterial resonators (qubits) separated by a distance $x = 1, 2, \cdots$ is denoted as $C_{t,x}$ ($C_{qq,x}$), colored blue (red). The mutual inductance between inductors of metamaterial resonators at a distance $x = 1, 2, \cdots$, colored magenta, is denoted as M_x. The distributed coupling of a qubit to the metamaterial is specified by capacitance $C_{g,x}$ between a qubit to a metamaterial resonator at a distance $x = 0, 1, 2, \cdots$, colored green. Opaque elements in the figure represent parasitic capacitive and mutual inductive contributions, processes of which are shown only up to second order.

inductance L_0 and capacitance C_0 forming the metamaterial waveguide and qubits with Josephson energy $E_{J,n}$ and capacitance C_q. Here, the capacitance $C_{t,1} \equiv C_t$ between nearest-neighboring metamaterial resonators and capacitance $C_{g,0} \equiv C_g$

between a qubit and a metamaterial resonator at each unit cell give rise to the desired couplings in the system. In addition, this model includes parasitic capacitance $C_{t,x}$ ($x = 2, 3, \cdots$) and mutual inductance M_x ($x = 1, 2, \cdots$) between metamaterial resonators not limited to nearest neighbors, parasitic long-range capacitance between qubits $C_{qq,x}$ ($x = 1, 2, \cdots$), and distributed capacitive coupling between qubits and metamaterial resonators represented by capacitance $C_{g,x}$ ($x = 1, 2, \cdots$).

The capacitive part $\mathcal{L}_C$ of the Lagrangian contains terms that are quadratic in time-derivatives of the node flux variables $\Phi_n(t) \equiv \int_{-\infty}^{t} \mathrm{d}t'\, V_n(t')$ and $\Phi_{q_n}(t) \equiv \int_{-\infty}^{t} \mathrm{d}t'\, V_{q_n}(t')$, written as

$$\begin{aligned}\mathcal{L}_C = \sum_n \Bigg[& \frac{C_0}{2}\dot{\Phi}_n^2 + \sum_{x>0} \frac{C_{t,x}}{2}(\dot{\Phi}_{n+x} - \dot{\Phi}_n)^2 \\ & + \frac{C_q}{2}\dot{\Phi}_{q_n}^2 + \sum_{x>0} \frac{C_{qq,x}}{2}(\dot{\Phi}_{q_{n+x}} - \dot{\Phi}_{q_n})^2 \\ & + \sum_x \frac{C_{g,|x|}}{2}(\dot{\Phi}_{q_n} - \dot{\Phi}_{n+x})^2 \Bigg].\end{aligned} \tag{D.22}$$

The node charge variables $Q_n = \partial\mathcal{L}_C/\partial\dot{\Phi}_n$ and $Q_{q_n} = \partial\mathcal{L}_C/\partial\dot{\Phi}_{q_n}$ canonically conjugate to the flux variables are evaluated as

$$\begin{aligned}Q_n = & \left(C_0 + \sum_{x\neq 0} C_{t,|x|} + \sum_x C_{g,|x|} \right) \dot{\Phi}_n \\ & - \sum_{x\neq 0} C_{t,|x|}\dot{\Phi}_{n+x} - \sum_x C_{g,|x|}\dot{\Phi}_{q_{n+x}},\end{aligned} \tag{D.23a}$$

$$\begin{aligned}Q_{q_n} = & \left(C_q + \sum_{x\neq 0} C_{qq,|x|} + \sum_x C_{g,|x|} \right) \dot{\Phi}_{q_n} \\ & - \sum_{x\neq 0} C_{qq,|x|}\dot{\Phi}_{q_{n+x}} - \sum_x C_{g,|x|}\dot{\Phi}_{n+x}.\end{aligned} \tag{D.23b}$$

Equations D.23a-D.23b can be rewritten in a compact form by introducing a vector of node charge variables $\boldsymbol{Q} = (Q_1, Q_2, \cdots, Q_{q_1}, Q_{q_2}, \cdots)^\top$ and a vector of node flux variables $\mathbf{\Phi} = (\Phi_1, \Phi_2, \cdots, \Phi_{q_1}, \Phi_{q_2}, \cdots)^\top$, giving $\boldsymbol{Q} = \boldsymbol{C}\dot{\mathbf{\Phi}}$ where

$$\boldsymbol{C} = \begin{pmatrix} C_{w\Sigma} & -C_{t,1} & -C_{t,2} & \cdots & -C_{g,0} & -C_{g,1} & \cdots \\ -C_{t,1} & C_{w\Sigma} & -C_{t,1} & \cdots & -C_{g,1} & -C_{g,0} & \cdots \\ -C_{t,2} & -C_{t,1} & C_{w\Sigma} & \cdots & -C_{g,2} & -C_{g,1} & \cdots \\ \vdots & \vdots & \vdots & \ddots & \vdots & \vdots & \ddots \\ -C_{g,0} & -C_{g,1} & -C_{g,2} & \cdots & C_{q\Sigma} & -C_{qq,1} & \cdots \\ -C_{g,1} & -C_{g,0} & -C_{g,1} & \cdots & -C_{qq,1} & C_{q\Sigma} & \cdots \\ \vdots & \vdots & \vdots & \ddots & \vdots & \vdots & \ddots \end{pmatrix}. \tag{D.24}$$

Here, the effective self-capacitance $C_{w\Sigma}$ ($C_{q\Sigma}$) of a metamaterial resonator (qubit) is given by

$$C_{w\Sigma} = C_0 + \sum_{x\neq 0} C_{t,|x|} + \sum_{x} C_{g,|x|}, \tag{D.25a}$$

$$C_{q\Sigma} = C_q + \sum_{x\neq 0} C_{qq,|x|} + \sum_{x} C_{g,|x|}. \tag{D.25b}$$

Note that the capacitance matrix $\boldsymbol{C}$ is symmetric, satisfying $\boldsymbol{C}^\top = \boldsymbol{C}$.

The inductive part $\mathcal{L}_L$ of the Lagrangian reads

$$\begin{aligned} \mathcal{L}_L &= \sum_n \left(-\frac{1}{2} L_0 I_n^2 - \sum_{x>0} M_x I_n I_{n+x} \right) \\ &= -\frac{1}{2} \sum_n I_n \left(L_0 I_n + \sum_{x\neq 0} M_{|x|} I_{n+|x|} \right), \end{aligned} \tag{D.26}$$

where I_n is the current flowing through the inductor of the nth metamaterial resonator. The node flux Φ_n and current I_n satisfies the relation

$$\Phi_n = L_0 I_n + \sum_{x\neq 0} M_{|x|} I_{n+x}, \tag{D.27}$$

which can be compactly written in terms of a vector of node flux variables of metamaterial resonators $\mathbf{\Phi}_w \equiv (\Phi_1, \Phi_2, \cdots)^\top$ and that of current variables $\boldsymbol{I}_w \equiv (I_1, I_2, \cdots)^\top$ as $\mathbf{\Phi}_w = \boldsymbol{L}_w \boldsymbol{I}_w$, where

$$\boldsymbol{L}_w = \begin{pmatrix} L_0 & M_1 & M_2 & M_3 & \cdots \\ M_1 & L_0 & M_1 & M_2 & \cdots \\ M_2 & M_1 & L_0 & M_1 & \cdots \\ M_3 & M_2 & M_1 & L_0 & \cdots \\ \vdots & \vdots & \vdots & \vdots & \ddots \end{pmatrix} \tag{D.28}$$

is a symmetric matrix, i.e., $\boldsymbol{L}_w^\top = \boldsymbol{L}_w$. This allows us to rewrite Eq. D.26 as

$$\mathcal{L}_L = -\frac{1}{2}\boldsymbol{I}_w^\top \boldsymbol{\Phi}_w = -\frac{1}{2}\boldsymbol{\Phi}_w^\top \boldsymbol{L}_w^{-1}\boldsymbol{\Phi}_w. \tag{D.29}$$

The last part of the Lagrangian $\mathcal{L}_J$ comes from the Josephson junctions forming qubits

$$\mathcal{L}_J = \sum_n E_{J,n}\cos\frac{2\pi\Phi_{q_n}}{\Phi_0}. \tag{D.30}$$

The Lagrangian of the system is given by sum of the three contributions mentioned above, i.e., $\mathcal{L} = \mathcal{L}_C + \mathcal{L}_L + \mathcal{L}_J$. The Hamiltonian can be obtained by the Legendre transformation

$$\begin{aligned} H &= \sum_n \left(Q_n\dot{\Phi}_n + Q_{q_n}\dot{\Phi}_{q_n}\right) \\ &= \frac{1}{2}\boldsymbol{Q}^\top \boldsymbol{C}^{-1}\boldsymbol{Q} + \frac{1}{2}\boldsymbol{\Phi}_w^\top \boldsymbol{L}_w^{-1}\boldsymbol{\Phi}_w - \sum_n E_{J,n}\cos\frac{2\pi\Phi_{q_n}}{\Phi_0}. \end{aligned} \tag{D.31}$$

Finally, we expand the cosine potential of the Josephson junctions according to

$$\cos\frac{2\pi\Phi_{q_n}}{\Phi_0} \approx 1 - \frac{1}{2}\left(\frac{2\pi\Phi_{q_n}}{\Phi_0}\right)^2 + \frac{1}{24}\left(\frac{2\pi\Phi_{q_n}}{\Phi_0}\right)^4, \tag{D.32}$$

which gives the final form of the Hamiltonian

$$\begin{aligned} H = &\frac{1}{2}\boldsymbol{Q}^\top \boldsymbol{C}^{-1}\boldsymbol{Q} + \frac{1}{2}\boldsymbol{\Phi}_w^\top \boldsymbol{L}_w^{-1}\boldsymbol{\Phi}_w \\ &+ \sum_n \frac{E_{J,n}}{2}\left(\frac{2\pi\Phi_{q_n}}{\Phi_0}\right)^2 - \sum_n \frac{E_{J,n}}{24}\left(\frac{2\pi\Phi_{q_n}}{\Phi_0}\right)^4. \end{aligned} \tag{D.33}$$

Second quantization

We promote the node flux and charge variables to quantum operators by imposing the canonical commutation relation $[\hat{\Phi}_n, \hat{Q}_{n'}] = [\hat{\Phi}_{q_n}, \hat{Q}_{q'_n}] = i\hbar\delta_{n,n'}$. We also decompose the inverse capacitance and inductance matrices into their diagonal (D) and off-diagonal (O) parts, i.e., $\boldsymbol{C}^{-1} = (\boldsymbol{C}^{-1})_D + (\boldsymbol{C}^{-1})_O$ and $\boldsymbol{L}_w^{-1} = (\boldsymbol{L}_w^{-1})_D + (\boldsymbol{L}_w^{-1})_O$. Then the Hamiltonian in Eq. D.33 can be rearranged into $\hat{H} = \hat{H}_0 + \hat{V}$, where

$$\hat{H}_0 = \sum_n \left[\frac{(\boldsymbol{C}^{-1})_{n,n}}{2} \hat{Q}_n^2 + \frac{(\boldsymbol{L}_w^{-1})_{n,n}}{2} \hat{\Phi}_n^2 + \frac{(\boldsymbol{C}^{-1})_{q_n,q_n}}{2} \hat{Q}_{q_n}^2 + \frac{E_{J,n}}{2} \left(\frac{2\pi \hat{\Phi}_{q_n}}{\Phi_0} \right)^2 - \frac{E_{J,n}}{24} \left(\frac{2\pi \hat{\Phi}_{q_n}}{\Phi_0} \right)^4 \right] \tag{D.34a}$$

contains components associated with the diagonal part of the inverse matrices and the cross coupling terms are described by

$$\hat{V} = \frac{1}{2} \hat{\boldsymbol{Q}}^\top (\boldsymbol{C}^{-1})_O \hat{\boldsymbol{Q}} + \frac{1}{2} \hat{\boldsymbol{\Phi}}_w^\top (\boldsymbol{L}_w^{-1})_O \hat{\boldsymbol{\Phi}}_w. \tag{D.34b}$$

The second quantization can be performed by writing the canonical flux and charge operators in terms of annihilation and creation operators by noting the form of $\hat{H}_0$ in Eq. D.34a:

$$\hat{\Phi}_n = \sqrt{\frac{\hbar Z_n}{2}} \left(\hat{a}_n + \hat{a}_n^\dagger \right), \tag{D.35a}$$

$$\hat{Q}_n = \frac{1}{i} \sqrt{\frac{\hbar}{2 Z_n}} \left(\hat{a}_n - \hat{a}_n^\dagger \right), \tag{D.35b}$$

$$\hat{\Phi}_{q_n} = \sqrt{\frac{\hbar Z_{q_n}}{2}} \left(\hat{a}_{q_n} + \hat{a}_{q_n}^\dagger \right), \tag{D.35c}$$

$$\hat{Q}_{q_n} = \frac{1}{i} \sqrt{\frac{\hbar}{2 Z_{q_n}}} \left(\hat{a}_{q_n} - \hat{a}_{q_n}^\dagger \right), \tag{D.35d}$$

where the effective impedance of the metamaterial resonator (qubit) at the nth unit cell is given by

$$Z_n = \sqrt{\frac{(\boldsymbol{C}^{-1})_{n,n}}{(\boldsymbol{L}_w^{-1})_{n,n}}}, \quad Z_{q_n} = \sqrt{\frac{(\boldsymbol{C}^{-1})_{q_n,q_n}}{(2\pi/\Phi_0)^2 E_{J,n}}}. \tag{D.36}$$

Using the above expressions, Eq. D.34a can be rewritten under the RWA as

$$\hat{H}_0/\hbar = \sum_n \left[\omega_n \hat{a}_n^\dagger \hat{a}_n + \omega_{q_n} \hat{a}_{q_n}^\dagger \hat{a}_{q_n} + \frac{U_{q_n}}{2} (\hat{a}_{q_n}^\dagger)^2 (\hat{a}_{q_n})^2 \right], \tag{D.37}$$

where the bare resonator frequency ω_n, the transition frequency ω_{q_n} and the anharmonicity U_{q_n} of the bare qubit at the nth unit cell are given by

$$\omega_n = \sqrt{(\boldsymbol{C}^{-1})_{n,n}(\boldsymbol{L}_w^{-1})_{n,n}} \tag{D.38a}$$

$$\omega_{q_n} = \frac{\sqrt{8E_{J,n}E_{C,n}} - E_{C,n}}{\hbar} \tag{D.38b}$$

$$U_{q_n} = -E_{C,n}. \tag{D.38c}$$

Here, $E_{C,n} = e^2(\boldsymbol{C}^{-1})_{q_n,q_n}/2$ is the charging energy of the qubit at the nth unit cell where e is the electron charge. The coupling terms in Eq. D.34b can also be written in the form of

$$\begin{aligned} \hat{V}/\hbar = \sum_{n,n'} \Big[& t_{n,n'}\left(\hat{a}_n^\dagger \hat{a}_{n'} + \hat{a}_{n'}^\dagger \hat{a}_n\right) \\ & + g_{n,q_{n'}}\left(\hat{a}_n^\dagger \hat{a}_{q_{n'}} + \hat{a}_{q_{n'}}^\dagger \hat{a}_n\right) \\ & + J'_{q_n,q_{n'}}\left(\hat{a}_{q_n}^\dagger \hat{a}_{q_{n'}} + \hat{a}_{q_{n'}}^\dagger \hat{a}_{q_n}\right)\Big]. \end{aligned} \tag{D.39}$$

where $t_{n,n'}$ is the coupling between metamaterial resonators, $g_{n,q_{n'}}$ is the coupling between a qubit and a metamaterial resonator, and $J'_{q_n,q_{n'}}$ is the parasitic direct coupling between qubits, given by

$$t_{n,n'} = \frac{1}{2}\left[\frac{(\boldsymbol{C}^{-1})_{n,n'}}{\sqrt{Z_n Z_{n'}}} + (\boldsymbol{L}_w^{-1})_{n,n'}\sqrt{Z_n Z_{n'}}\right], \tag{D.40a}$$

$$g_{n,q_{n'}} = \frac{(\boldsymbol{C}^{-1})_{n,q_{n'}}}{2\sqrt{Z_n Z_{q_{n'}}}}, \tag{D.40b}$$

$$J'_{q_n,q_{n'}} = \frac{(\boldsymbol{C}^{-1})_{q_n,q_{n'}}}{2\sqrt{Z_{q_n} Z_{q_{n'}}}}. \tag{D.40c}$$

Fitting based on the numerical model

With a set of electrical circuit parameters, we can perform numerical diagonalization of the exact Hamiltonian in Eqs. D.37 and D.39, enabling us to calculate various properties of our simulator and fit the experimental data. Assuming a qubit couples to the middle unit cell of a 50-resonator metamaterial waveguide with an open boundary condition, we numerically diagonalize the Hamiltonian in the single- and two-excitation manifold to obtain the eigenfrequency ω_{01} (ω_{02}) of the first (second) excited state $|1\rangle$ ($|2\rangle$) relative to the ground state $|0\rangle$ as a function of E_J. The on-site

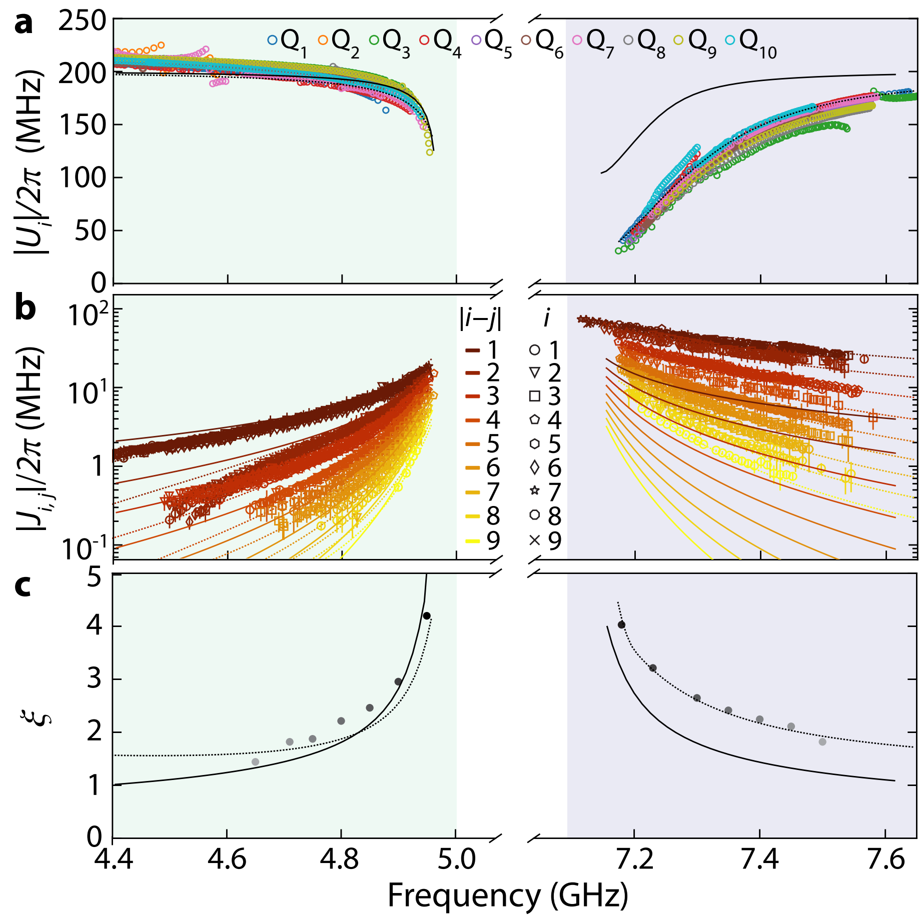

Figure D.3: **Comparison of the tight binding numerical modeling with the experimental data.** Magnitude of on-site interaction U_i (panel **a**), amplitude of hopping $J_{i,j}$ (panel **b**), and localization length ξ (panel **c**) as a function of frequency with the solid curves in each panel showing the fitting based on numerical modeling. The fitting curves are obtained from numerical optimization assuming the approximate tight-binding Hamiltonian in Eq. D.10. The dotted curves are obtained from fitting assuming the capacitive and inductive coupling beyond nearest neighbor elements, the full model of which shown in Fig. D.2. The experimental data (colored or grayscale markers) and the fit curves of the full model are identical to the ones in Fig. 6.3 of the main text.

interaction can be calculated by $U = \omega_{02} - 2\omega_{01}$, which is shown in Fig. 6.3a of the main text. The effective coupling $J_{i,j}$ between two transmon sites Q_i and Q_j is obtained by diagonalizing the Hamiltonian of two qubits coupled to two unit cells separated by a distance $|i-j|$ near the center of the 50-resonator metamaterial. The two single-excitation eigenstates in the bandgaps correspond to the even and

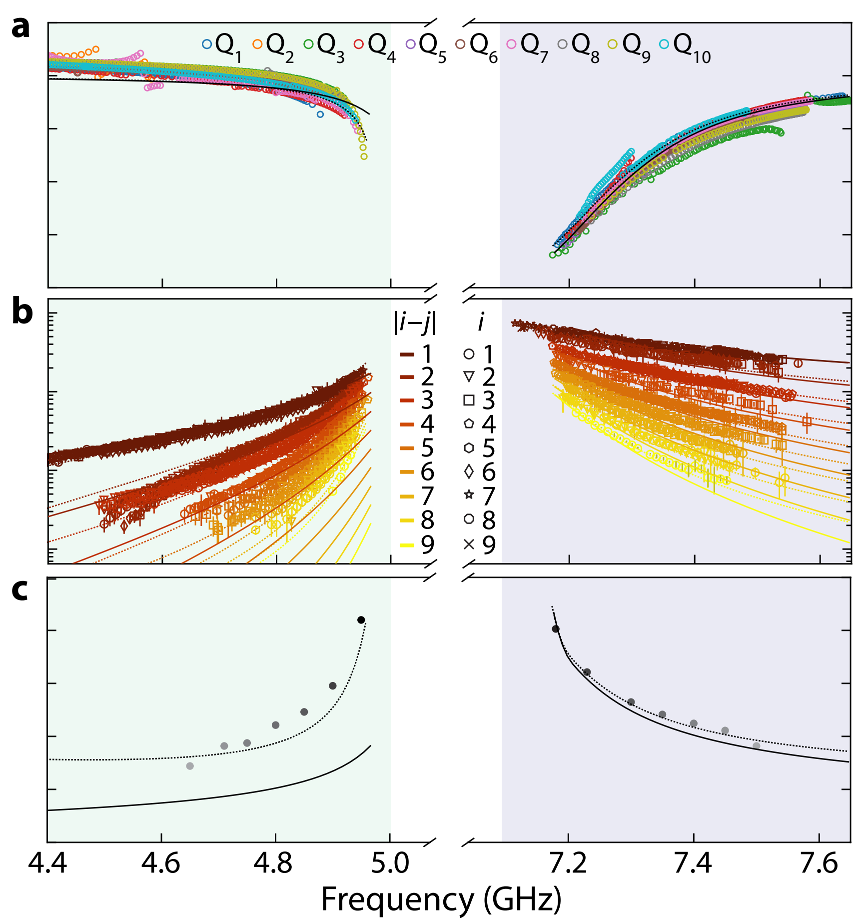

Figure D.4: **Comparison of the NN-coupled circuit modeling with the experimental data.** Magnitude of on-site interaction U_i (panel **a**), amplitude of hopping $J_{i,j}$ (panel **b**), and localization length ξ (panel **c**) as a function of frequency with the solid curves in each panel showing the fitting based on numerical modeling. The fitting curves assume the nearest-neighbor-coupled circuit model with the form of Hamiltonian in Eqs. D.37 and D.39. The dotted curves are obtained from fitting assuming the capacitive and inductive coupling beyond nearest neighbor elements, the full model of which shown in Fig. D.2. The experimental data (colored or grayscale markers) and the fit curves of the full model are identical to the ones in Fig. 6.3 of the main text.

odd superposition of the two bound states with the eigenenergy difference (sum) of $2J_{i,j}$ ($2\omega_{01}$). This allows us to numerically calculate $J_{i,j}$ as a function of ω_{01} shown in Fig. 6.3b of the main text. Fitting the exponential decay of $J_{i,j}$ as a function of distance $|i-j|$ at a fixed frequency ω_{01} gives the localization length ξ plotted in Fig. 6.3c of the main text. The solid curves in Fig. 6.3 are calculated from an identical set of circuit parameters, with $L_0 = 2.04\,\mathrm{nH}$ extracted from electromagnetic simulation (Sonnet®), $C_{q\Sigma} = 92.7\,\mathrm{fF}$ calculated from the average charging energy of $\overline{E_C}/h = e^2/(2hC_{q\Sigma}) = 220\,\mathrm{MHz}$ measured at the lower sweet spot (see Table. D.1), and the free parameters obtained from numerical fitting of the experimental data (Nelder-Mead optimization) given by $C_0 = 242.19\,\mathrm{fF}$, $C_{t,1} = 60.17\,\mathrm{fF}$, $C_{t,2} = 0.542\,\mathrm{fF}$, $M_1 = -18.1\,\mathrm{pH}$, $M_2 = 13.5\,\mathrm{pH}$, $M_3 = -1.09\,\mathrm{pH}$, $M_4 = 0.438\,\mathrm{pH}$, $C_{g,0} = 9.19\,\mathrm{fF}$, $C_{g,1} = 0.368\,\mathrm{fF}$, and $C_{qq,1} = 10.1\,\mathrm{aF}$. The long-range coupling capacitance assumes the form $C \propto 1/r^3$ where r is the distance between two planar electrodes [317], giving

$$C_{t,|x|} = C_{t,2}(2/|x|)^3 \quad (|x| \geq 2)$$

and the form of $C_{qq,|x|}$, $C_{g,|x|}$ ($|x| > 1$) following the physical distance on the device. In addition, the long-range mutual inductance between metamaterial resonators assumes $M_{|x|} \propto (-1)^x \ln(1 + 1/|x|)$ for $|x| \geq 4$, adapted from the form of mutual inductance between two parallel wires [318].

The exact Hamiltonian in Eqs. D.37 and D.39 taking into account both the long-range capacitance and mutual inductance was necessary to sufficiently explain the data in Fig. 6.3 in both the LBG and the UBG. For example, assuming an approximate form of Hamiltonian in Eq. D.10 with only nearest-neighbor coupling, we were not able to reproduce the wide tuning range of U_i and large $|J_{i,j}|$ in the UBG (Fig. D.3). This indicates that the asymmetry between LBG and UBG partly originates from beyond-nearest-neighbor coupling in the Hamiltonian. Additionally, the capacitance ratio from the fitted parameters above is $C_{t,1}/(C_0+2C_{t,1}+C_{g,0}) = 0.162$, which suggests the invalidity of the small-coupling approximation in Eq. D.5 in the derivation of this analytically solvable model. Another numerical fitting using an exact Hamiltonian in Eqs. D.37 and D.39 with zero capacitive and inductive coupling beyond nearest-neighbor, corresponding to the circuit diagram in Fig. D.1 with inductive coupling between adjacent resonators, also fails to fit the experimental data with a good agreement. Although this model captures the behavior of $|U_i|$, $J_{i,j}$, and ξ inside the UBG, as shown in Fig. D.4, the long-range part in $J_{i,j}$ inside the LBG is underestimated, resulting in a smaller ξ than the experimental results. Only when the full circuit model in Fig. D.2 is assumed can we recover the trend in the LBG, implying the importance of long-range capacitive and inductive coupling especially when the hopping strength $|J_{i,j}|$ is small.

D.2 Device characterization and experimental setup

In this section, we summarize the details of the device and the experimental setup used in our work.

Parameters		Q_1	Q_2	Q_3	Q_4	Q_5	Q_6	Q_7	Q_8	Q_9	Q_{10}	Avg.	Stdev.
Lower sweet spot $\omega_{01,\mathrm{min}}/2\pi$ (GHz)		3.738	3.520	3.601	3.513	3.743	3.467	3.671	3.532	3.557	3.396	3.574	0.108
Upper sweet spot $\omega_{01,\mathrm{max}}/2\pi$ (GHz)		7.636	7.506	7.650	7.577	7.575	7.494	7.584	7.573	7.578	7.483	7.566	0.053
Lifetime T_1 (μs)	at $\omega_{01,\mathrm{min}}$	7.56	75.4	–	73.0	5.13	74.2	22.4	54.3	24.9	39.1	41.8	26.9
Ramsey T_2^* (μs)		4.69	10.4	–	0.81	1.48	13.6	6.97	16.7	4.80	16.2	8.4	5.7
Hahn echo T_{2E} (μs)		10.8	70.1	–	51.7	7.34	82.5	24.8	52.4	20.4	32.2	39.1	24.9
Anharmonicity $U/2\pi$ (MHz)		-211	-222	–	-223	-239	-220	-207	-221	-215	-224	-220	9
Lifetime T_1 (μs)	at $\omega_{01}/2\pi \approx 4.72\,\mathrm{GHz}$	4.89	31.0	22.6	25.0	14.5	33.8	11.3	32.7	12.1	28.0	21.6	9.7
Ramsey T_2^* (μs)		1.08	1.05	1.07	1.03	1.18	1.37	1.25	1.20	1.26	1.14	1.16	0.10
Hahn echo T_{2E} (μs)		4.67	5.87	6.84	6.20	5.64	6.83	4.83	5.35	5.48	4.73	5.64	0.76
Anharmonicity $U/2\pi$ (MHz)		-195	-203	-205	-194	-202	-199	-195	-203	-205	-198	-200	4
Lifetime T_1 (μs)	at $\omega_{01}/2\pi \approx 7.35\,\mathrm{GHz}$	3.37	2.47	2.22	3.18	3.39	5.95	6.45	4.83	4.74	3.74	4.03	1.34
Ramsey T_2^* (μs)		1.49	1.30	1.19	1.31	1.80	2.87	2.63	2.67	2.93	2.06	2.02	0.66
Hahn echo T_{2E} (μs)		3.18	1.89	1.31	1.73	3.28	4.53	6.26	4.83	5.56	3.28	3.59	1.59
Anharmonicity $U/2\pi$ (MHz)		-134	-126	-112	-131	-132	-125	-129	-118	-123	-134	-126	7
Lifetime T_1 (μs)	at $\omega_{01,\mathrm{max}}$	4.58	8.52	2.60	14.2	7.65	10.1	9.64	10.4	4.37	8.49	8.1	3.3
Ramsey T_2^* (μs)		5.53	5.78	3.02	12.0	7.34	5.67	9.54	10.6	6.09	10.5	7.6	2.7
Hahn echo T_{2E} (μs)		7.12	5.67	3.18	16.7	9.29	11.5	13.6	10.9	7.28	12.5	9.8	3.9
Anharmonicity $U/2\pi$ (MHz)		-181	-162	-177	-177	-170	-161	-176	-165	-168	-166	-170	7
Resonator frequency $\omega_r/2\pi$ (GHz)		5.833	6.084	6.328	5.574	6.008	5.907	5.622	6.236	6.169	5.741	5.950	0.245
Resonator decay $\kappa_r/2\pi$ (MHz)		11.47	8.38	16.95	14.08	9.85	8.09	10.46	10.57	21.95	6.16	11.80	4.46

Table D.1: **Basic characterization of qubits and read-out resonators.** Various parameters of the qubits and the read-out resonators used in this work are summarized. The last two columns of the table show the average and the standard deviation of each parameter over all qubits or read-out resonators.

Device details

Qubit

The ten transmon qubits in the device are designed to be nominally identical, with asymmetric Josephson junctions on superconducting quantum interference device (SQUID) loop to reduce sensitivity to flux noise while maintaining a tuning range wide enough to cover both the lower bandgap (LBG) and the upper bandgap (UBG). Each qubit is individually addressed by a charge drive line (XY control) with a designed capacitance of $C_d = 80\,\mathrm{aF}$ and a flux bias line (Z control) with a mutual inductance of $M_\Phi \approx 1\,\Phi_0/\mathrm{mA} \approx 2\,\mathrm{pH}$ to the qubit's SQUID loop. The staggered qubit placement with respect to the metamaterial, i.e., Q$_i$ and Q$_{i+1}$ located on the opposite sides of the metamaterial waveguide, is employed in order to minimize the parasitic near-field coupling between qubits. We perform basic characterization of each qubit in its entire tuning range inside the bandgaps by sweeping over DC current sent along its flux bias line while parking the remaining qubits inside the opposite bandgap. We measure the lifetime T_1, Ramsey coherence time T_2^*, Hahn echo coherence time T_{2E}, and anharmonicity U as a function of qubit frequency, which are summarized in Table D.1 at a few different frequencies.

Read-out resonator

The compact read-out resonators in our device consists of a meander inductor of $1\,\mu$m pitch and a planar capacitor. They are designed to have frequencies near the center of the passband, enabling dispersive read-out when the qubits are tuned inside the bandgaps. The resonant frequencies of read-out resonators, controlled by the length of the meander inductor, are designed to have larger separation for physically adjacent read-out resonators in order to avoid deleterious effects from parasitic near-field coupling. The read-out resonator frequency ω_r measured from waveguide transmission spectroscopy and the decay rate κ_r extracted from ring-down measurement are shown in Table D.1. The variations in the decay rates originate from the dispersion of the metamaterial waveguide. To achieve a high-fidelity read-out, we design the coupling between a qubit and its read-out resonator to be $g_{qr}/2\pi = 250\,\mathrm{MHz}$, giving the dispersive shift of $\chi/2\pi \approx 6\,\mathrm{MHz}$ when the qubit is parked at 4.5 GHz or 7.5 GHz.

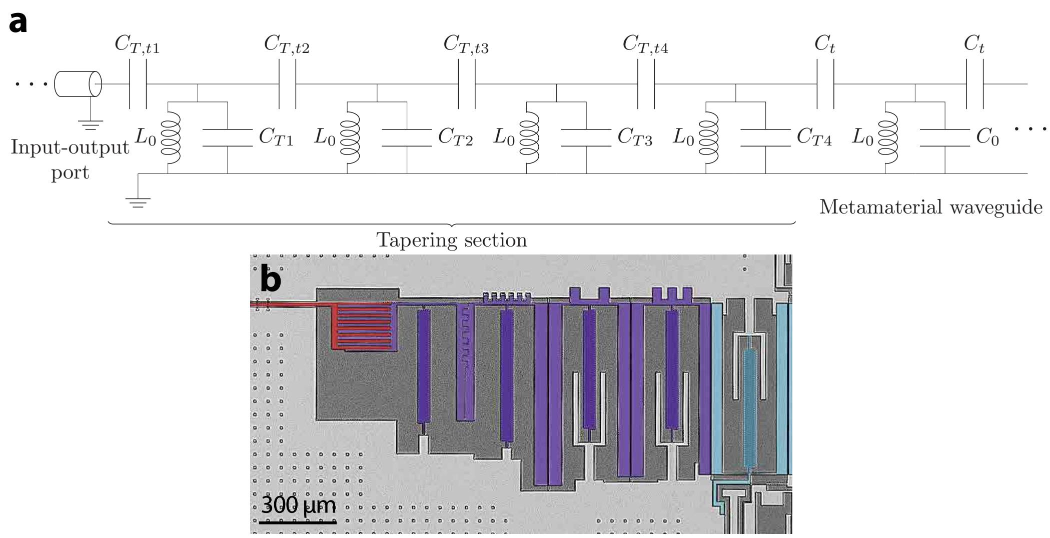

Figure D.5: **Tapering section.** **a**, Schematic diagram of the tapering section consisting of four LC resonators coupled to an external input-output port on the left indicated with a transmission line symbol and the regular metamaterial waveguide section on the right. **b**, Optical micrograph (false colored) of the tapering section of the fabricated device. Here, the metamaterial waveguide, the tapering section, and the input-output port are colored blue, purple, and red, respectively.

Metamaterial waveguide

As mentioned in the main text, the metamaterial waveguide consists of an array of nominally identical 42 compact resonators each formed by a meander inductor of $2\,\mu$m pitch and a planar capacitor. Each resonator of the ten inner unit cells of the metamaterial waveguide (labeled by $i = 1$–10) is capacitively coupled to a qubit Q_i and simultaneously to its read-out resonator R_i. On each metamaterial resonator without a qubit, we keep the capacitors of a qubit and a read-out resonator to maintain the total capacitance of the metamaterial resonator and minimize the discrepancy in resonator frequencies. The two metamaterial resonators close to the auxiliary qubits (colored yellow in Fig. 6.2a of the main text) have capacitors which are redesigned to compensate for the absence of qubit and read-out resonator capacitors. The metamaterial waveguide is connected to external input-output ports via tapering sections.

Tapering section

The tapering section in our device is a network of inductors and capacitors designed to reduce impedance mismatch between the metamaterial waveguide and the external 50-Ω input-output ports at the passband frequencies [131, 144]. This significantly decreases the level of ripples in the transmission spectrum near the center of the passband (shown in Fig. 6.1d of the main text), enabling the use of metamaterial waveguide as a resource-efficient feedline for qubit read-out. We utilize a design illustrated in Fig. D.5a where four LC resonators with an identical inductance L_0 are capacitively coupled to each other with gradually changing capacitance values given by $C_{T,t1} = 222.8$ fF, $C_{T1} = 51.0$ fF, $C_{T,t2} = 77.3$ fF, $C_{T2} = 210.7$ fF, $C_{T,t3} = 53.8$ fF, $C_{T3} = 298.1$ fF, $C_{T,t4} = 65.3$ fF, and $C_{T4} = 293.1$ fF. An optical micrograph of the tapering section realized in our device is shown in Fig. D.5b. Note that our tapering design becomes less efficient at frequencies close to the band-edges, creating a dense spectrum of high-Q modes.

Experimental setup

Room-temperature electronics

The electronic setup at the room temperature for synthesis of qubit control signals and processing of qubit read-out signals is illustrated in Fig. D.6. Static component of qubit frequency control (slow Z) signal is generated by a stable DC voltage source (QDevil, QDAC) passed through a 10 kΩ resistor. Dynamic qubit frequency control (fast Z) is achieved by employing arbitrary waveforms generated from a digital-to-analog converter (DAC) channel with an analog bandwidth of 400 MHz at 1 ns temporal resolution, sent through a 10 dB attenuator before entering the dilution refrigerator. For microwave synthesis of drive signals on each qubit (XY), we prepare a pair of intermediate frequency (IF) signals from DAC channels passed through a low-pass filter with 400 MHz cutoff. The pair of IF signals are attenuated and multiplied to a local oscillator (LO) signal generated by a microwave signal generator (Rohde & Schwarz, SMB100A) by using a IQ mixer (Marki Microwave, MMIQ-0218L) for upconversion, enabling synthesis of signals in approximately 800 MHz-wide frequency band about the LO frequency. This is followed by attenuation and filtering with a low-pass filter with 10 GHz cutoff (Mini-Circuits, ZXLF-K14+) and a high-pass filter with 2.9 GHz cutoff (Mini-Circuits, VXHF-292M+) and a subsequent low-noise amplification (Mini-Circuits, ZX60-83-LN-S+). Note that

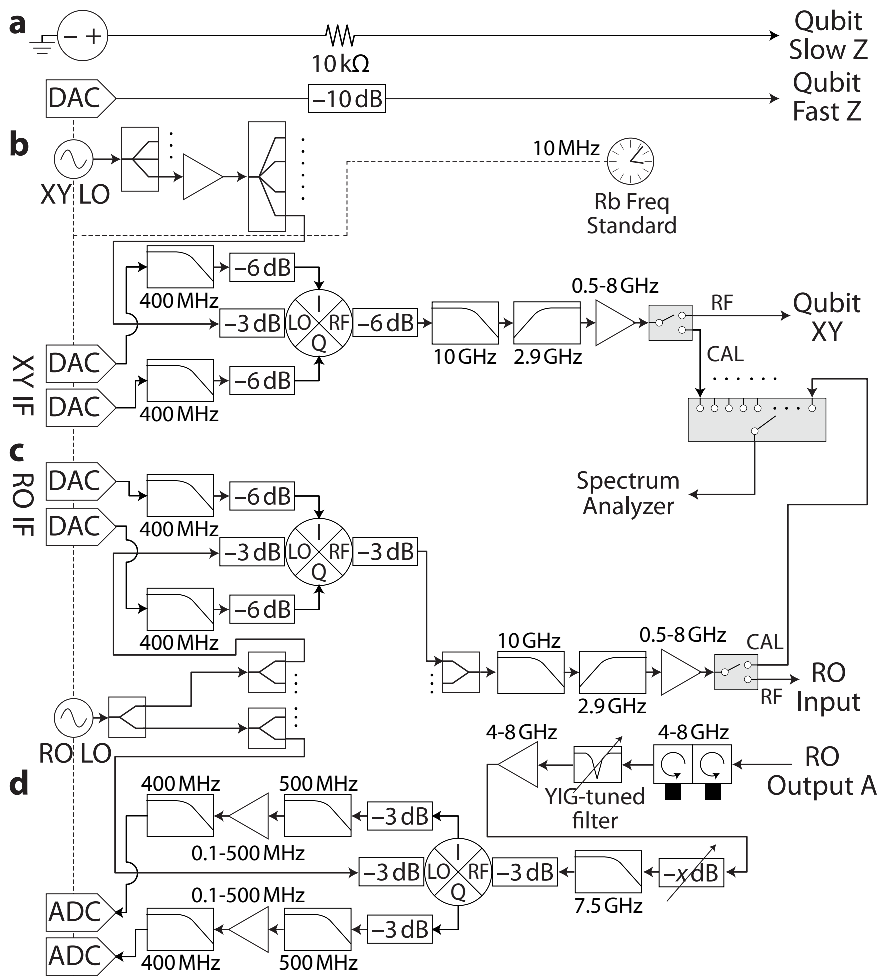

Figure D.6: **Schematic of the room-temperature electronic setup outside the dilution refrigerator.** The diagram for synthesizing the signals for qubit frequency control (slow and fast Z control, panel **a**, qubit drive (XY control, panel **b**, and read-out input (panel **c**) are shown, together with the analog downconversion and the filtering procedures for the output read-out signals (panel **d**). The manufacturers and the model numbers of the parts and the instruments used in the diagram are enumerated in Sec. D.2.

we distribute the LO signal generated from a single, common microwave signal generator to multiple IQ mixers used for synthesis of qubit drive signals by using a suitable combination of power splitters and amplifiers. Together with synchronized DAC channels used on all qubits, this ensures that the phase relation between qubit XY drive signals sent to different qubits is deterministic and constant over the repetition of experiments. The read-out input signals are synthesized in a way similar to the XY signals by IQ mixing with a separate LO dedicated for read-out. Each qubit XY and read-out input signals are optionally directed to a spectrum analyzer by digitally controlled microwave switches, enabling calibration of each IQ mixers to suppress their spurious LO and image leakage tones. The read-out output signals from the refrigerator are passed through a room-temperature dual-junction circulator (Fairview Microwave, FMCR1019) and a yttrium iron garnet (YIG)-tuned band-reject filter (Micro Lambda Wireless, MLBFR-0212) to suppress leakage tones at the JTWPA pump frequency. This signal is then amplified with a high-gain low-noise amplifier (L3Harris Narda-MITEQ, LNA-40-04000800-07-10P), a tunable attenuator (Vaunix, Lab Brick LDA-133), and a low-pass filter with 7.5 GHz cutoff (Marki Microwave, FLP-0750). Then, the signals are downconverted to IF band by using IQ mixers pumped by the same read-out LO used for upconversion of read-out input signals and suitably filtered (Mini-Circuits, VLFX-400+ and VLFX-500+) and amplified (Mini-Circuits, ZFL-500LN+) before digitization at analog-to-digital converter (ADC) channels. The DAC and ADC channels used in this work are analog output and analog input channels, respectively, of Quantum Machines OPX+. All the microwave instruments used in our work are referenced to an external 10 MHz reference from a Rubidium frequency standard (Stanford Research Systems, FS725).

Cryogenic setup

The experimental setup inside the cryogen-free dilution refrigerator (Bluefors, BF-LD250) used in our work is illustrated in Fig. D.7. The refrigerator consists of multiple temperature stages named 50 K flange, 4 K flange, still flange, cold plate (CP), and mixing chamber (MXC) flange with typical temperatures of 50 K, 3.6 K, 0.7 K, 60 mK, and under 7 mK, respectively, during normal operations. The frequency of each qubit is controlled statically by a DC bias (slow Z) passing through a resistor-capacitor-resistor (RCR) low-pass filter (Aivon Ltd., Therma-uD25-G) with 64 kHz cutoff thermalized to the 4 K plate and dynamically by RF pulses (fast Z) passing through a series of XMA cryogenic attenuators (2082-6418-□□-CRYO) with stainless steel enclosure whose attenuation values are given by 1 dB, 30 dB, 0 dB and 0 dB at 50 K, 4 K, Still and CP stages, respectively. This is followed by reflective low-pass filtering with a 400 MHz filter (Mini-Circuits, VLFX-400+) and a 12 GHz "clean-up" filter (K&L Microwave, 6L250-12000/T26000-OP/O) at the mixing chamber plate. The DC bias and the RF pulses for Z control are then combined with a DC-coupled bias tee obtained by shorting the capacitor of a Mini-Circuits ZFBT-4R2GW+ bias

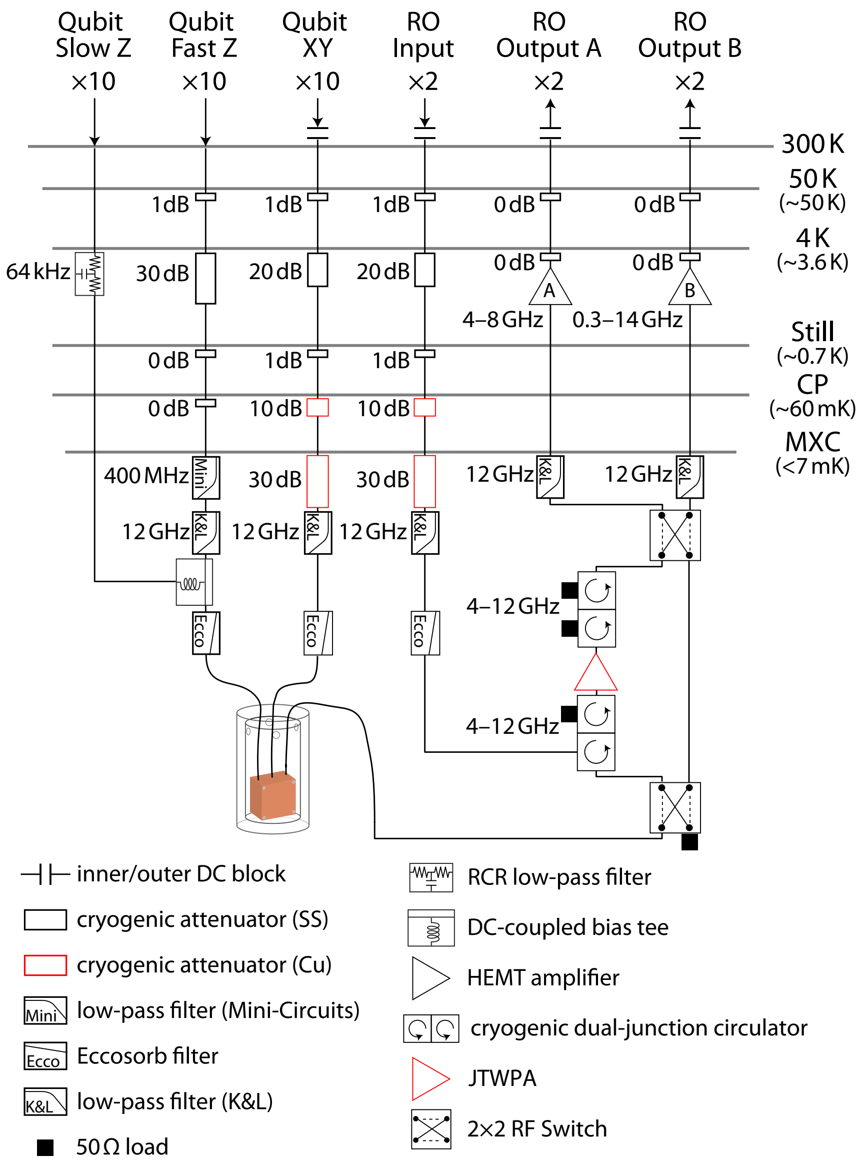

Figure D.7: **Schematic of the experimental setup inside the dilution refrigerator.** The cryogenic setup consists of slow and fast Z lines for qubit frequency control, XY lines for qubit drive, and RO input/output lines for qubit read-out. The meaning of the symbols used in the diagram is enumerated at the bottom. The attenuation values of cryogenic attenuators, cutoff frequencies of low-pass filters, and bandwidths of circulators and amplifiers are shown next to the components. The input pump line for JTWPA's are not shown in the diagram for brevity. The manufacturers and the model numbers of the parts used in the diagram are enumerated in Sec. D.2.

tee, followed by infrared filtering with an Eccosorb filter at the mixing chamber before connecting to the flux bias line on the device. The microwave signals for XY drive of each qubit is attenuated by 1 dB, 20 dB, and 1 dB at the 50 K, 4 K, and Still stages, respectively, using the XMA cryogenic attenuators. Also, 10 dB and 30 dB cryogenic attenuators made with oxygen-free high-conductivity (OFHC) copper enclosure (Quantum Microwave, QMC-CRYOATT-□□) are placed at the CP and MXC stages, respectively, in order to achieve good thermalization at temperatures below 100 mK (similar to the attenuators in Ref. [177]). This is followed by infrared filtering by a 12 GHz K&L low-pass filter and an Eccosorb filter before entering the device. A pair of read-out input lines go through the same attenuation and filtering as the XY drive lines and connect to wideband dual-junction circulators (Low-Noise Factory, LNF-CICIC4_12A). Each circulator connects to an input-output port of the metamaterial waveguide via a 2×2 RF switch (Radiall, R577432000), playing the role of both sending waveguide input signal into the device and directing waveguide output signal to amplification chains of read-out output lines. The output signal is amplified by a Josephson traveling-wave parametric amplifier (JTWPA) from MIT Lincoln Laboratory sandwiched by two sets of dual-junction circulators at the mixing chamber and then a high-electron-mobility transistor (HEMT) amplifier (Low-Noise Factory, LNF-LNC4_8C and LNF-LNC0.3_14A for amplification in the 4–8 GHz and 0.3–14 GHz bands, respectively) at the 4K flange before further amplification at room temperature. The two external ports (1 and 2) of the metamaterial waveguide connect to two individual sets of input-output line and amplification chain. With four 2×2 RF switches in total, we can configure the setup to measure both transmission (S_{21} and S_{12}) and reflection (S_{11} and S_{22}) from both waveguide ports with an option to bypass JTWPA in transmission measurements. Also, with individual amplification chains, the transmitted and the reflected signals can be measured simultaneously (e.g., S_{21} and S_{11}). We place inner/outer DC blocks (Inmet, 8039 or Centric RF, CD9519) along all the cryogenic coaxial lines before connection to room-temperature electronics to break ground loops, except for the qubit Z control lines where a full bandwidth from DC to 400 MHz is necessary in order to minimize pulse distortion.

D.3 Details of the metamaterial Purcell filter

Besides providing a frequency band for read-out, the metamaterial waveguide also acts as a hardware-efficient Purcell filter. The dispersion of the metamaterial and the large number of unit cells in this realization effectively prevent qubits at bandgap frequencies from accessing the external ports, as evidenced by the large extinction

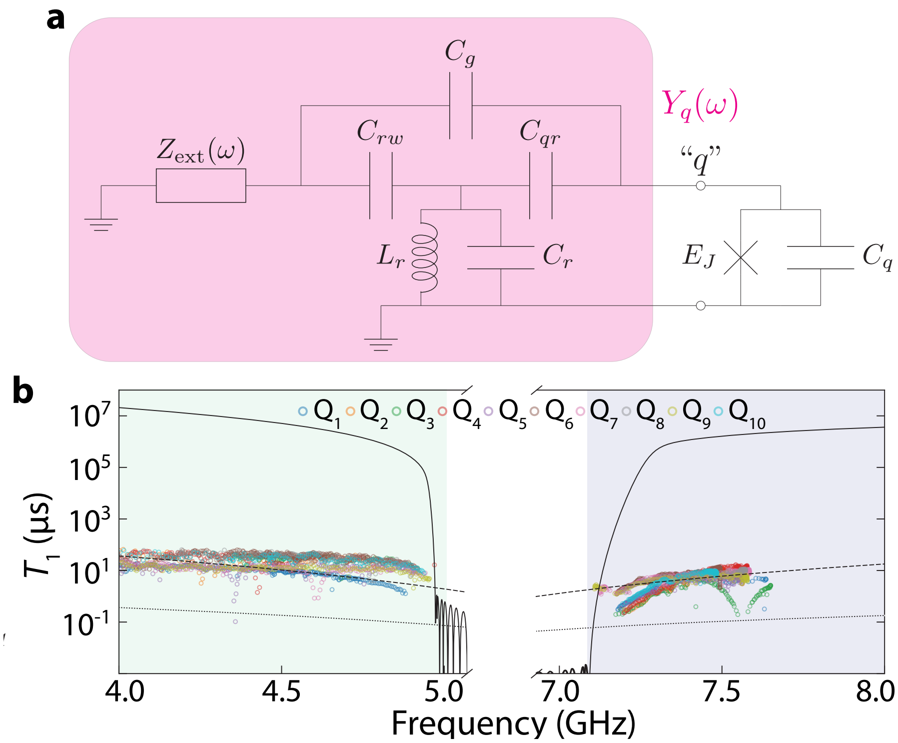

Figure D.8: **Metamaterial Purcell filter.** **a**, General circuit model for dispersive qubit read-out. A qubit, represented as a parallel circuit of a Josephson junction (Josephson energy E_J) and a capacitor (capacitance C_q), couples to an external port with impedance $Z_{\text{ext}}(\omega)$ via a read-out resonator (inductance L_r and capacitance C_r). The circuit elements in the shaded region is taken into account when calculating the admittance $Y_q(\omega)$ seen from the qubit node "q". **b**, Qubit lifetime T_1 plotted against frequency. Calculated Purcell-limited lifetime is shown (with read-out resonator frequency $\omega_{\mathrm{R}_5}/2\pi = 6.01\,$GHz, decay rate $\kappa_{\mathrm{R}_5}/2\pi = 9.85\,$MHz, and qubit-resonator coupling of 250 MHz) when the read-out resonator couples to an external port directly (dotted curve), via a single-pole Purcell filter with $Q = 15$ (dashed curve), and via the metamaterial Purcell filter in this device (solid curve). The measured T_1 of ten qubits are shown in colored circles. The lower and the upper bandgaps of the metamaterial waveguide are shaded green and purple, respectively.

ratio and sharp transition at the band-edges illustrated in Fig. 6.1d of the main text. Here, both the direct decay of qubits into the metamaterial and the Purcell decay via read-out resonators are strongly suppressed. To show this, we compare in this section the performance of our metamaterial Purcell filter with traditional circuit QED settings [167, 168] where read-out resonators are coupled to external ports directly or via a single-pole Purcell filter.

Purcell decay

A general scheme for qubit read-out in circuit QED involves a qubit coupled to a read-out resonator which could be accessed from an external port, an example electrical circuit of which is illustrated in Fig. D.8a. In the dispersive regime where the qubit-resonator coupling g_{qr} is small compared to the magnitude of their detuning $\Delta_{qr} \equiv \omega_{01} - \omega_r$, the frequency of the read-out resonator depends on the state of the qubit, enabling quantum non-demolition read-out [319, 320]. However, this coupling simultaneously introduces an unwanted qubit decay channel into the external port via the read-out resonator, known as the Purcell decay, which could be mitigated by engineering a Purcell filter [237, 321, 322] that suppresses the density of states at the qubit frequency. The rate of Purcell decay when the read-out resonator is coupled to an external port with impedance $Z_{\mathrm{ext}}(\omega)$ is given by [323]

$$\Gamma_1^{\mathrm{Purcell}} = \frac{g_{qr}^2}{\Delta_{qr}^2} \frac{\mathrm{Re}[Z_{\mathrm{ext}}(\omega_{01})]}{\mathrm{Re}[Z_{\mathrm{ext}}(\omega_r)]} \kappa_r, \tag{D.41}$$

where κ_r is the decay rate of the read-out resonator.

Modeling of the metamaterial Purcell filter

In the case of a metamaterial waveguide, the external impedance $Z_{\mathrm{ext}}(\omega)$ is highly frequency-dependent with an impedance close to $Z_0 = 50\,\Omega$ inside the passband after tapering and in principle a purely imaginary Bloch impedance inside the bandgaps [171]. As a result, the Purcell decay rate $\Gamma_1^{\mathrm{Purcell}}$ in Eq. D.41 is strongly suppressed by the ratio of the real part of the external impedance at the qubit transition frequency ω_{01} to that at the read-out resonator frequency ω_r.

In our circuit construction, the real part $\mathrm{Re}[Z_{\mathrm{ext}}(\omega_{01})]$ of external impedance at the qubit transition frequency is not zero due to finite number of unit cells. Taking into account the direct coupling capacitance C_g between the qubit and the metamaterial waveguide (see Fig. D.8a), we calculate the qubit decay rate into the external port by using the relation [321, 322]

$$\Gamma_1^{\mathrm{Purcell}} = \frac{\mathrm{Re}[Y_q(\omega_{01})]}{C_{q\Sigma}}, \tag{D.42}$$

where $Y_q(\omega)$ is the admittance seen from the qubit node "q" illustrated in Fig. D.8a. To numerically evaluate the expression, we use the read-out resonator R_5 as an example with parameters $C_r = 130.5\,\mathrm{fF}$ and $L_r = 4.518\,\mathrm{nH}$, together with metamaterial parameters from the numerical fit results discussed in Sec. D.1 and the designed coupling capacitance values $C_{qr} = 10.3\,\mathrm{fF}$, $C_{rw} = 6.8\,\mathrm{fF}$. Note that the admittance $Y_q(\omega)$ also depends on the details of the tapering section, design parameters of which are enumerated in Sec. D.2. With the set of circuit parameters listed above, we utilize AWR Microwave Office® to calculate the Purcell-limited lifetime $T_1^{\mathrm{Purcell}} = 1/\Gamma_1^{\mathrm{Purcell}}$ based on Eq. D.42, indicated by the black solid curve in Fig. D.8b.

Comparison to traditional qubit read-out settings

For comparison, we also consider two conventional qubit read-out scenarios in circuit QED where the read-out resonator is coupled to an external port directly or via a single-pole Purcell filter ($C_g = 0$ is assumed in these cases).

Direct coupling

In the case of direct coupling of a read-out resonator to an external port, the external impedance is simply given by $Z_{\mathrm{ext}}(\omega) = Z_0 = 50\,\Omega$ with no frequency dependence and hence Eq. D.41 recovers the basic form of the Purcell decay [319] at a rate of

$$\Gamma_{1,\mathrm{direct}}^{\mathrm{Purcell}} = \left(\frac{g_{qr}}{\Delta_{qr}}\right)^2 \kappa_r, \tag{D.43}$$

which is utilized to obtain the dotted curve in Fig. D.8b assuming the capacitance values listed above.

Single-pole Purcell filter

In the case of a single-pole Purcell filter [237, 324] consisting of a resonator with decay rate κ_r at frequency ω_r, it can be shown that the external impedance is given by the form [171]

$$Z_{\mathrm{ext}}(\omega) = \frac{Z_0}{1 + 2j(\omega - \omega_f)/\kappa_f}. \tag{D.44}$$

Substituting Eq. D.44 into Eq. D.41 gives the Purcell decay rate of

$$\Gamma_{1,\text{single-pole}}^{\mathrm{Purcell}} = \frac{g_{qr}^2}{\Delta_{qr}^2} \frac{1}{1 + (2\Delta_{qf}/\kappa_f)^2} \tilde{\kappa}_r, \tag{D.45}$$

where $\Delta_{qf} = \omega_{01} - \omega_f$ is the detuning of the qubit from the filter resonator and $\tilde{\kappa}_r = \kappa_r\{1 + [2(\omega_r - \omega_f)/\kappa_f]^2\}$ is the decay rate of the read-out resonator modified by the presence of the filter resonator. Here, we need to choose a bandwidth of the filter wide enough to accommodate ten read-out resonators, playing a role similar to our metamaterial waveguide. As an example, we assume a filter quality factor of $Q_f = \omega_f/\kappa_f = 15$ (half the value used in Ref. [237]), corresponding to a full-width half-maximum linewidth of $\kappa_f/2\pi \approx 400\,$MHz, with the Purcell filter resonant to the read-out resonator at $\omega_{\mathrm{R}_5}/2\pi = 6.01\,$GHz. The expected Purcell-limited lifetime using this set of parameters for the single-pole Purcell filter is indicated by the dashed curve in Fig. D.8b.

Discussion

In Fig. D.8b, the Purcell-limited qubit lifetime is shown to be below 1 μs in the case of direct coupling and approximately 10 μs in the case of a single-pole Purcell filter [237] with $Q = 15$, suggesting that such strategies for mitigating qubit decay are incompatible with the desired rapid qubit read-out. However, with the metamaterial waveguide acting as a Purcell filter, the expected decay rate of a qubit into the external ports is suppressed by more than five orders of magnitude, lifting the Purcell limitation on qubit lifetime. The measured lifetime T_1 of qubits in our device lies in the range of 10.3–47.2 μs (3.6–9.8 μs) at 4.5 GHz (7.45 GHz) in the LBG (UBG), which surpasses the Purcell limit of the aforementioned traditional settings but remains far below the ideal prediction due to other material-related decay channels.

D.4 Qubit read-out methods and characterization

In this section, we provide details of the qubit read-out procedures used in this work and additional read-out characterization results.

Qubit state discrimination

As discussed in the main text, we utilize both the reflected and the transmitted fields from read-out resonators to perform qubit state discrimination in order to achieve the best quantum efficiency available in our setup. In the simplest case of a read-out resonator symmetrically coupled to a read-out feedline [169], qubit state information from the read-out resonator is equally divided into the forward (transmitted) and the backward (reflected) directions. Therefore, collection of both the reflected and the transmitted fields is expected to give read-out signal-to-noise ratio (SNR) about

3 dB larger than what could be obtained by using only one of the two fields. In our device, however, we observe frequency-dependent asymmetric coupling of read-out resonators to the two external input-output ports associated with the dispersion of the metamaterial waveguide. Here, the transfer functions from a qubit to the external ports becomes asymmetric away from the eigenfrequencies of the metamaterial. While the tapering sections help mitigate this effect by reducing the sharpness of the transmission response, the ratio of forward and backward decay rates of read-out resonators is expected to be as large as ten at certain frequencies under numerical modeling. For these reasons, it is essential to collect the read-out signals from both input-output ports of the device for qubit state discrimination, which gives a smooth experimental workflow with the highest read-out SNR without concerns about this undesired asymmetry.

In order to achieve the highest read-out SNR from the addition of the two read-out fields, we pass the two fields through independent analog signal processing branches consisting of near-quantum-limited amplification, filtering, and downconversion, which gives a pair of complex-valued IF signals $\boldsymbol{s}_p(t) = \boldsymbol{a}_p(t)e^{i\omega_{\mathrm{IF}}t}$ from the ports $p = 1, 2$. Here, $\boldsymbol{a}_p(t)$ denotes the complex-valued baseband waveform and ω_{IF} is the IF frequency of the read-out. The pair of IF signals are independently digitized into discrete-time waveforms $\boldsymbol{s}_p(t_m)$ ($m = 0, 1, \cdots, M-1$), which undergo digital demodulation

$$\boldsymbol{x}_p = \sum_{m=0}^{M-1} \boldsymbol{w}_p^*(t_m)\boldsymbol{s}_p(t_m)e^{-i\omega_{\mathrm{IF}}t_m} = \sum_{m=0}^{M-1} \boldsymbol{w}_p^*(t_m)\boldsymbol{a}_p(t_m) \qquad \text{(D.46)}$$

weighted by complex-valued integration weights $\boldsymbol{w}_p(t_m)$. Here, the integration weights $\boldsymbol{w}_p(t_m)$ can be chosen to be either a constant, e.g., $\boldsymbol{w}_p(t_m) = 1$, or samples optimized for maximum separability of qubit-state-dependent read-out signals [325, 326]. The demodulated complex scalar variables $\boldsymbol{x}_p$ are then summed with weights $\boldsymbol{v}_p$ according to $\boldsymbol{x} = \sum_p \boldsymbol{v}_p^* \boldsymbol{x}_p$, followed by thresholding to discriminate the state of a qubit, which is based on a pre-calibrated distribution of $\boldsymbol{x}$ obtained with initialization of the qubit in its standard basis states. The optimal values of the weights $\boldsymbol{v}_p$ maximizing the separability in $\boldsymbol{x}$ can be obtained from the distribution of demodulated scalars $\boldsymbol{x}_p$ of each port by performing linear discriminant analysis (LDA) [327, 328]. Our method is superior to the approach used in Ref. [329] where the placement of a power combiner before the first amplification stage led to reduction in SNR by at least 3 dB, counteracting the 3 dB gain expected from the addition. Also, our method of applying digital signal processing to combine the two signals takes into account the phase and gain imbalance of the independent branches, allowing for noise-matched and phase-coherent addition of the read-out signals, with the effective SNR being the sum of SNR available from each branch.

Utilizing a FPGA-based control architecture (Quantum Machines OPX+) to synthesize and analyze read-out signals, we carry out the digital signal processing procedures mentioned above in real time, including weighted demodulation of digitized IF waveforms, weighted sum of demodulated quadrature variables, and thresholding. This allows us to perform low-latency ($< 1\,\mu$s) feedback control over qubits conditioned on measurement outcomes, a demonstration of which in the form of active qubit reset is described in Sec. D.5.

Read-out control parameter tune-up

An important prerequisite to high-fidelity single-shot read-out of a qubit is to find a set of parameters that determine pulses sent to a read-out resonator. In a regular setting [168], a frequency between the read-out resonator frequencies $\omega_r^{|0\rangle} = \omega_r + \chi$ and $\omega_r^{|1\rangle} = \omega_r - \chi$ under qubit preparation in states $|0\rangle$ and $|1\rangle$, respectively, is chosen to maximize the $|0\rangle$-$|1\rangle$ signal separation at a fixed read-out power. This is followed by a read-out power sweep at this frequency to find an optimal power that maximizes the read-out fidelity while being unaffected by parasitic state transitions associated with the measurement [330, 331]. In our experiment, however, the dispersion of the metamaterial waveguide affects the validity of this method in two ways. First, the colorful transmission response of the metamaterial waveguide on the order of a few dB prohibits us from making a frequency sweep with a fixed power arriving at the resonator, making it challenging to find the optimal read-out frequency. Also, as noted in Sec. D.4, the dispersion of the metamaterial waveguide causes the decay rate of read-out resonator to be highly frequency-dependent in cases with a large dispersive shift χ. In this case, the intra-resonator photon occupation $\overline{n}_r \propto 1/[\Delta_r^2 + (\kappa_r/2)^2]$ during the read-out [332] becomes highly asymmetric between the qubit states $|0\rangle$ and $|1\rangle$, making the behavior associated with read-out-induced state transition hard to predict.

Due to the challenges mentioned above, we devise a more general read-out tune-up procedure based on a fast real-time sweep over both frequency and power of the read-out. Given a read-out pulse envelope, we sweep over frequency and power of read-out to find a combination that maximizes the read-out fidelity without parasitic qubit state transitions. This is achieved by repeating the qubit read-out under initialization of qubit in each standard basis state $\{|0\rangle, |1\rangle\}$ for n_{rep} times. From the resulting distribution of demodulated quadrature variables $\boldsymbol{x}_p$ in Eq. D.46, we perform LDA [328] to extract the assignment fidelity and outlier counting for estimating the probability of parasitic state transitions, similar to the method discussed in Ref. [333], at each combination of read-out frequency and power. Specifically, we choose the first $n_{\mathrm{rep}}/2$ samples in the dataset to train the LDA discriminator and the remainder are used to determine the read-out fidelity with out-of-sample validation at a low statistical error [334]. For outlier counting, we draw a 3σ-radius circle with respect to the center of distribution calculated from the LDA and compute the portion of datapoints lying outside the regions enclosed by the circles. We choose a frequency and power combination that realizes the maximum read-out fidelity, simultaneously having an outlier probability below a certain user-defined threshold.

Parameters	Q_1	Q_2	Q_3	Q_4	Q_5	Q_6	Q_7	Q_8	Q_9	Q_{10}	Avg.	Stdev.
Qubit frequency $\omega_{01}/2\pi$ (GHz)	4.02	4.78	4.44	4.20	4.42	4.48	3.80	–	4.78	4.50		
Read-out frequency $\omega_{\mathrm{RO}}/2\pi$ (GHz)	5.845	6.122	6.339	5.615	6.047	5.935	5.687	–	6.196	5.788		
Read-out fidelity $\mathcal{F}_{1\mathrm{Q}}$	0.983	0.980	0.974	0.991	0.983	0.985	0.984	–	0.968	0.989	0.982	0.007

Table D.2: **Characterization of rapid single-qubit read-out.** The highest read-out fidelity achieved for each qubit, utilizing a rapid read-out method described in Sec. D.4, is summarized with corresponding qubit and read-out frequencies used for the characterization. The calibration of Q_8 was interrupted by an unforeseen issue of the dilution refrigerator, and hence was excluded from comparison with other qubits under the same condition.

This sweep is first coarsely performed with a small number of repetitions $n_{\mathrm{rep}} \sim 10^2$, where reset is performed by waiting about 400 μs for the qubit to relax between pulse sequences. The next round of the sweep is performed with a larger number of repetition $n_{\mathrm{rep}} \sim 10^4$ at a much higher repetition rate to reduce statistical fluctuations, efficiently implemented by employing active reset (see Sec. D.5) based on the single-shot read-out calibrated from the first round of the sweep. Optionally, an additional round of a finer version of the sweep is performed to find a condition that achieves the highest read-out fidelity. The total time spent on this tune-up procedure is about 2–4 minutes, limited by communication latency associated with data retrieval from the stream processor of OPX+.

For multiplexed read-out, we follow a similar tune-up procedure involving simultaneous real-time sweep over the frequency and power sent into all ten read-out resonators, whose sweep ranges are centered at the optimal condition determined from the single-qubit read-out calibration described above. Such multiplexed read-out calibration helps avoid spurious processes associated with parasitic near-field coupling between read-out resonators and qubits as well as mitigate the decrease in read-out fidelity due to the non-linearity of the measurement chain.

Read-out characterization

Here, we summarize the characterization results of single-shot read-out achieved in our system.

Rapid single-qubit read-out

We quantify the performance of single-shot read-out of each qubit with its assignment fidelity $\mathcal{F}_{1\mathrm{Q}}$, which is obtained by preparing the qubit in its standard basis states $\{|0\rangle, |1\rangle\}$ followed by measurement, repeated over $n_{\mathrm{rep}} \sim 10^5$ experimental counts. A rapid read-out is achieved by employing a 148 ns-long square pulse with an initial 20 ns kick with two times large amplitude for fast ring-up [335], convolved with a Gaussian envelope of 10 ns standard deviation. The resulting output read-out signals are demodulated and integrated with optimal weights [325, 326]. Here, we use a 100 ns-longer integration window to collect transient read-out signals associated with ring-up and ring-down of the read-out resonator, timescales of which are about $1/\overline{\kappa_{\mathrm{R}_i}} \approx 13.5$ ns (see Table D.1).

The characterization results of the highest read-out fidelity achieved on each qubit, on par with the state-of-the-art performance achieved in superconducting quantum circuits [336, 337], are summarized in Table D.2.

Multiplexed read-out

We characterize multiplexed read-out when the qubits are parked at their idle frequencies shown in Fig. D.11. Here, we use 400 ns-long square pulses, convolved with a Gaussian envelope of 10 ns standard deviation, sent to all read-out resonators by frequency multiplexing (calibrated using the tune-up procedures discussed in

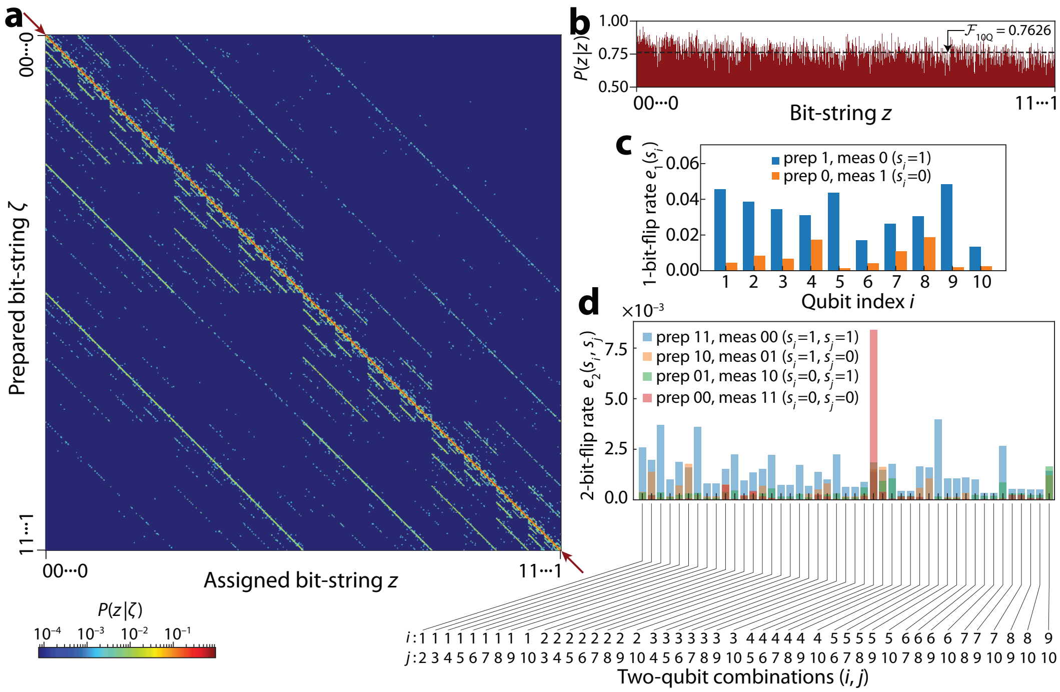

Figure D.9: **Characterization of multiplexed read-out of qubits.** **a**, Assignment probability matrix $P(z|\zeta)$ of prepared bit-strings ζ and assigned bit-strings z arranged in the ascending order. **b**, The diagonal elements $P(z|z)$ of the assignment probability matrix, indicated by the dark red arrows in panel **a**, is plotted as a function of 10-bit strings z in the ascending order. The dashed line indicates the average of diagonal elements over all bit-strings, corresponding to the 10-qubit read-out fidelity $\mathcal{F}_{10\mathrm{Q}} = 0.7626$. **c**, Single-qubit bit-flip error rate $e_1(s_i)$ during the read-out, given by the average of assignment probability matrix elements corresponding to preparation of a state s_i and assignment of the flipped state $\neg s_i$ on qubit Q_i while the states of the remaining qubits are fixed. **d**, Two-qubit bit-flip error rate $e_2(s_i, s_j)$ during the read-out, corresponding to the average of assignment probability matrix elements corresponding to preparation of states (s_i, s_j) and assignment of the flipped states $(\neg s_i, \neg s_j)$ on qubits (Q_i,Q_j) while the states of the remaining qubits are fixed.

Sec. D.4). The output signals from read-out resonators are demodulated and integrated with constant weights in 100 ns-longer integration window. The characterization is performed by initializing the system in a state of random 10-bit-string by a choice of local gates (I or X) on all qubits sent in parallel followed by the multiplexed read-out, repeated over $n_{\mathrm{rep}} > 10^6$ experimental realizations.

The performance of the multiplexed read-out is quantified by the probability $P(z|\zeta)$ of assigning a bit-string z when the system is prepared in a bit-string ζ, known as the assignment probability matrix, which is illustrated in Fig. D.9a. The average probability of correct assignment, i.e., mean of diagonal elements $P(z|z)$ of the assignment probability matrix, gives the fidelity of multiplexed read-out for discriminating 2^{10} standard basis states of 10 qubits, which is calculated to be $\mathcal{F}_{10\mathrm{Q}} = 0.7626$ (see Fig. D.9b). In the absence of correlated multi-qubit read-out errors, this corresponds to an average single-qubit read-out fidelity of $(\mathcal{F}_{10\mathrm{Q}})^{1/10} \approx 0.9733$, which is slightly lower than the average of best single-qubit rapid read-out fidelity shown in Table D.2.

The sources of infidelity can be qualitatively understood by noting the non-zero off-diagonal elements of the assignment probability matrix. For example, the dominant infidelity components of the assignment matrix in Fig. D.9a, on the order of 10^{-2}, form a fractal pattern situated in the lower triangular part of the matrix. This corresponds to a single-qubit decay error, where a bit of a bit-string prepared in state 1 is assigned to be in state 0 while the remaining bits of the assigned bit-string are identical to the originally prepared ones. In order to perform a quantitative analysis of the errors during the multiplexed read-out, we define bit-flip error rates calculated from the infidelity components of the assignment probability matrix (see Fig. D.9c and d). The single-qubit bit-flip error rate is written as

$$e_1(s_i) \equiv \overline{P(\cdots \neg s_i \cdots | \cdots s_i \cdots)}, \tag{D.47}$$

which is the average of assignment probability matrix elements corresponding to preparation of a state s_i and assignment of the flipped state $\neg s_i$ on qubit Q_i while the assigned bits of the remaining qubits are identical to the prepared ones. It is observed in Fig. D.9c that the single-qubit decay $|1\rangle \to |0\rangle$ (few percent on average) is the dominant contributor to the infidelity of the read-out, which is believed to be associated with the limited lifetimes T_1 of qubits resulting in non-negligible decay during the on-time of read-out pulses. Similarly, the two-qubit bit-flip error rate is defined as

$$e_2(s_i, s_j) \equiv \overline{P(\cdots \neg s_i \cdots \neg s_j \cdots | \cdots s_i \cdots s_j \cdots)}, \tag{D.48}$$

which is the average of assignment probability matrix elements corresponding to preparation of states (s_i, s_j) and assignment of the flipped states $(\neg s_i, \neg s_j)$ on qubits (Q_i,Q_j) while the other bits remain identical between the preparation and the assignment. We find that the two-qubit error rates shown in Fig. D.9d are dominated by two-qubit decay process $|11\rangle \to |00\rangle$ in most cases with error rates an order of magnitude smaller than the single-qubit error rates in Fig. D.9c. Such behavior is expected in a system with independent single-qubit error sources. We also note the prevalence of non-trivial two-qubit error processes in few combinations of qubit pairs, e.g., two-qubit excitation $|00\rangle \rightarrow |11\rangle$ on (Q_4,Q_6) and population swap $|01\rangle \rightarrow |10\rangle$ on (Q_9,Q_{10}). We attribute these processes to state preparation errors associated with always-on qubit-qubit couplings and frequency collision in our system as well as parasitic read-out-induced state transitions, which are under active investigation. We observe that the higher-order error processes make negligible contributions to the 10-qubit read-out fidelity $\mathcal{F}_{10\mathrm{Q}}$.

Discussion

We note that although the implementation of hardware-efficient qubit read-out through the metamaterial bus waveguide is feasible for 10 qubits, the current scheme of coupling all the read-out resonators to the same bus waveguide is not scalable. Instead, for constructing large-scale quantum processors based on metamaterials—extensions of this work—we envision creating a single bus waveguide dedicated to mediating long-range qubit-qubit interactions while utilizing separate read-out metamaterial feedlines [127] allocated for every ten qubits.

D.5 Qubit control methods

In this section, we provide details about single- and multi-qubit control methods, including qubit XY and Z control methods, qubit reset procedures, and experimental pulse sequences described in the main text.

Qubit XY control

The XY control of a qubit is realized by sending a microwave pulse on the qubit's charge drive line at the transition frequency. Throughout the experiments described in this work, we use 40-ns-long Gaussian pulses with a standard deviation of 10 ns, corrected with the derivative removal by adiabatic gate (DRAG) method [226]. The pulses are calibrated following the procedures outlined in Ref. [166].

Qubit Z control

The transition frequency of a qubit is controlled by current sent into its flux-bias line, which generates magnetic field threading the qubit's SQUID loop. The DC flux bias (slow Z) sets the static frequency while the flux bias pulses (fast Z) dynamically

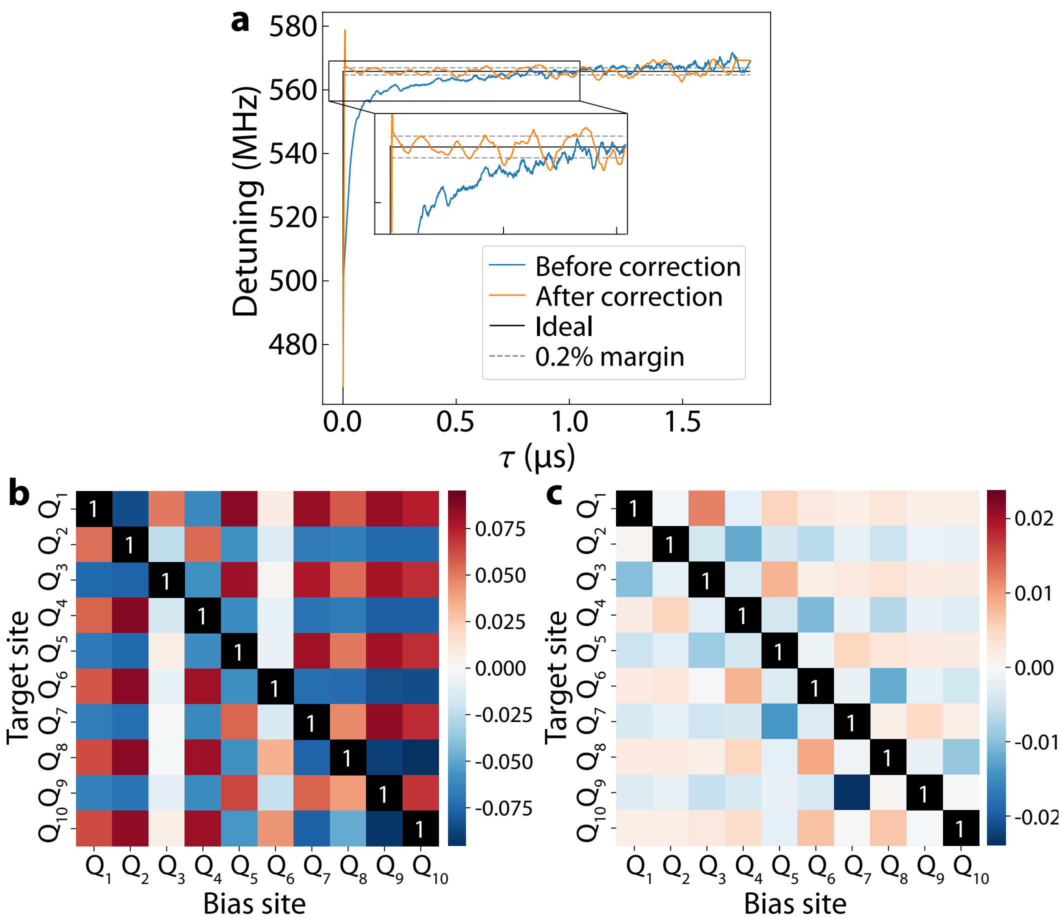

Figure D.10: **Flux bias corrections.** **a**, Qubit detuning by a flux pulse as a function of pulse duration τ. The detuning is plotted for the flux pulse before distortion correction (blue), after distortion correction (orange), and for the ideal pulse at the qubit (black). The margin of $\pm 0.2\%$ around the ideal pulse is shown in dashed gray lines. The inset gives a magnified view of the initial part of the pulses. **b/c**, The crosstalk matrix for the slow/fast flux bias with the diagonal elements equal to unity and values of off-diagonal elements indicated by colors.

tune the qubit to, e.g., the interaction frequency during an experimental sequence. Here, we provide details on the corrections applied on the flux bias of the qubits.

Pulse distortion

A flux pulse is distorted after passing through microwave components along a flux bias line, which introduces a significant error in the frequency control of qubits.

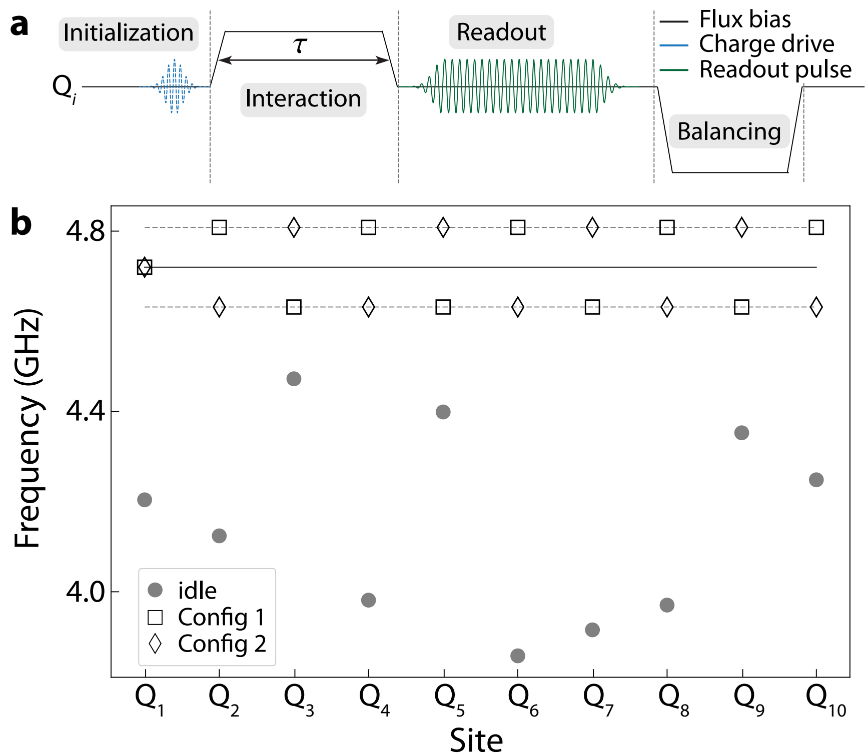

Figure D.11: **Experimental pulse sequence.** **a**, Detailed illustration of pulses on site Q_i for the sequence shown in Fig. 6.4b of the main text. The flux bias pulse, the charge drive pulse, and the read-out pulse are shown in black, blue, and green, respectively. The dashed lineshape during the initialization represents either a π-pulse or a wait applied to the qubit. **b**, Frequencies of sites during the pulse sequence and the frequency alignment calibration. The idle frequencies of qubits and the interaction frequency $\omega_{\mathrm{int}}/2\pi = 4.72\,\mathrm{GHz}$ for the 10-qubit experiments in the main text are indicated by circles and a solid line, respectively. The frequencies used during the frequency alignment calibration are shown in dashed gray lines together with two frequency configurations to align Q_1 to interaction frequency, indicated by square and diamond markers.

Here, we characterize the pulse distortion utilizing an in situ method involving a Ramsey-like sequence [338] and perform correction by using pre-distorted waveforms. To show the effectiveness of the correction, we measure the frequency detuning of a qubit during the on-time of a square flux pulse with and without correction, which are illustrated in Fig. D.10a. We observe a low-pass response in the uncorrected pulse and a response close to the ideal step function after the correction. The rise time of the remaining low-pass response of the corrected pulse is 6 ns with approximately 2 ns-long overshoot originating from the finite bandwidth of the waveform generator to faithfully implement the pre-distortion. The deviation of the corrected pulse remains mostly within the $\pm 0.2\%$ margin of the ideal response for short pulses, while a larger fluctuation is observed at pulse durations greater than 1 μs limited by the coherence of the qubit during the characterization.

Flux crosstalk

For a multi-qubit device, the flux crosstalk, i.e., the flux bias on one qubit affecting the frequency of another qubit, poses challenges on precise simultaneous control over the frequency of multiple qubits. To compensate for the flux crosstalk, we characterize a crosstalk matrix $\boldsymbol{C}_V$ defined by $\boldsymbol{V}_{\text{eff}} = \boldsymbol{C}_V \boldsymbol{V}_{\text{app}}$, where $\boldsymbol{V}_{\text{eff}}$ $(\boldsymbol{V}_{\text{app}})$ is a vector of effective (applied) flux bias voltages on all the qubits. Assuming that the diagonal components of the crosstalk matrix are close to the unity, i.e., $[\boldsymbol{C}_V]_{i,i} = \Delta V_{\text{eff},i}/\Delta V_{\text{app},i} \approx 1$, we characterize each off-diagonal crosstalk element $[\boldsymbol{C}_V]_{i,j}$ $(i \neq j)$ by measuring the ratio of flux tuning rates of a target site Q_i from biasing the sites Q_j and Q_i, giving

$$[\boldsymbol{C}_V]_{i,j} \equiv \frac{\Delta V_{\text{eff},i}}{\Delta V_{\text{app},j}} \approx \frac{\Delta V_{\text{app},i}}{\Delta V_{\text{app},j}} = \frac{\Delta\omega_{01,i}/\Delta V_{\text{app},j}}{\Delta\omega_{01,i}/\Delta V_{\text{app},i}}. \tag{D.49}$$

The measurement of flux tuning rate $\Delta\omega_{01,i}/\Delta V_{\text{app},j}$ is performed at biases where the frequency of a qubit is nearly linear in the flux bias. During the characterization of $[\boldsymbol{C}_V]_{i,j}$, sites other than the target site Q_i is detuned by at least 3 GHz to minimize the influence of coupling between sites. In the DC flux crosstalk characterization, the target qubit frequency tuning $\Delta\omega_{01,i}$ is calibrated from Ramsey fringes experiments, yielding an average magnitude of crosstalk elements of 0.059 (see Fig. D.10b). For the fast flux pulse crosstalk, $\Delta\omega_{01,i}$ is measured from a Ramsey sequence with a flux pulse of increasing duration (up to 1 μs) between two $\pi/2$ pulses. The resulting flux pulse crosstalk matrix is shown in Fig. D.10c with the average magnitude of crosstalk elements calculated as 0.004, more than an order of magnitude smaller than its DC flux counterpart. The crosstalk matrices can then be used for calculating the bias voltage to apply in order to achieve the effective ideal bias by $\boldsymbol{V}_{\text{app}} = \boldsymbol{C}_V^{-1} \boldsymbol{V}_{\text{eff}}$. We iterate the crosstalk calibrations based on existing corrections until the remainder of the crosstalk element exhibits no further decrease in magnitude, giving the crosstalk level below 1×10^{-4} for the majority of elements.

Qubit reset

Before the start of an experimental sequence, the qubits are required to be in the ground state, which is achieved by qubit reset. The traditional way to reset a qubit is to wait for a time much longer than its lifetime to ensure the population decay. For the qubits on this device, wait time around 1 ms is necessary, limiting the repetition rate of the experiment below 10^3 counts per second. In most experiments, we utilize the ability of real-time feedback operations with an FPGA-based controller (Quantum Machines OPX+) to perform active reset of the qubits. The single-qubit reset is achieved by measuring the state of the qubit and applying a subsequent π pulse if it is detected to be in state $|1\rangle$ [339]. Similarly, the active reset of multiple qubits is implemented by performing multiplexed read-out and applying subsequent π pulses on the qubits measured to be in state $|1\rangle$. The procedure is deemed successful once we measure the single qubit or all qubits to be in the ground state for N_r consecutive rounds of repeated read-out and reset. Typically, we use $N_r = 2$ or 6 for single-qubit or 10-qubit experiments, respectively. The duration of a round of active reset includes the read-out time (about 500 ns) and the feedback latency (below 1 μs). The active reset significantly reduces the reset time and enables the fast repetition rate of our experiments, which is essential for efficiently analyzing the bit-string statistics with low statistical fluctuations.

Experimental pulse sequence

The experimental pulse sequence shown in Fig. 6.4b of the main text is detailed in Fig. D.11a for a single qubit. We park the qubit at its idle frequency during the initialization stage where a local XY gate is utilized to prepare the qubit in its standard basis states $|0\rangle$ or $|1\rangle$, realized by waiting or by applying a microwave π-pulse, respectively. A square flux pulse is then used to dynamically tune the qubit to the interaction frequency for time τ followed by the read-out after the qubit returns to its idle frequency. At the end of the sequence, we apply a flux balancing pulse to achieve zero-average flux on the bias line during the whole sequence.

The idle frequencies are chosen to achieve high-fidelity multiplexed read-out (see Sec. D.4) and decrease frequency collision of both ω_{01} and ω_{12} between sites with strong coupling. The set of idle frequencies used in Figs. 6.5, 6.6, and 6.7 of the main text is shown in Fig. D.11b. During the interaction stage, all ten sites are aligned to the same frequency by flux pulses whose amplitudes are calibrated using the following procedures. First, we perform a coarse tuning using the crosstalk matrices and the pre-calibrated tuning curve (site frequency vs. bias voltage) for individual sites. To obtain the precise flux pulse amplitude for tuning a qubit to the interaction frequency ω_{int} and account for remaining crosstalk, we perform a fine tuning by pulsing a target site Q_i to ω_{int} and other sites to $\omega_{\text{int}} \pm 2\pi \times 88\,\text{MHz}$ (calibration frequency), measuring the frequency of Q_i by Ramsey sequence, and adjusting the pulse amplitude on Q_i to compensate for deviations. We repeat the above procedures until the measured frequency $\omega_{01,i}$ of the target qubit is sufficiently close to the desired interaction frequency ω_{int}. To minimize the frequency shift induced by the coupling between Q_i and other sites, we have the calibration frequencies staggered in two configurations illustrated in Fig. D.11b. Then we use the average of the pulse amplitudes on Q_i achieving $\omega_{01,i} = \omega_{\text{int}}$ in the two configurations for the multi-qubit interaction stage, which effectively cancels the influence from possible residual flux crosstalk.

D.6 Hamiltonian learning using a many-body fidelity estimator

The goal of Hamiltonian learning is to find the set of parameters of an estimated Hamiltonian $\hat{H}'$ that is closest to the many-body Hamiltonian $\hat{H}$ realized in an experiment [340]. Here, we learn the Hamiltonian by comparing the measurement outcomes from evolving the experimental system under its Hamiltonian and the numerical results from simulating the evolution of an estimated Hamiltonian. We experimentally prepare an initial state $|\Psi_0\rangle$ and evolve it for time τ under a Hamiltonian $\hat{H}$ realized in the experiments, which results in a state represented by a density matrix $\hat{\rho}(\tau)$. Assume we can classically simulate the same process for a guessed Hamiltonian $\hat{H}'$ and obtain the time-evolved state $e^{-i\hat{H}'\tau/\hbar}|\Psi_0\rangle$. The many-body fidelity is the overlap between the experimental and guessed states:

$$F(\tau, \hat{H}') \equiv \langle\Psi_0|e^{i\hat{H}'\tau/\hbar}\hat{\rho}(\tau)e^{-i\hat{H}'\tau/\hbar}|\Psi_0\rangle. \tag{D.50}$$

If the fidelity can be efficiently estimated, the Hamiltonian can then be learned by maximizing $F(\tau, \hat{H}')$ over a family of trial Hamiltonians $\{\hat{H}'\}$. It is numerically found [257] that this approach remains robust even in the presence of small errors from state preparation and measurement (SPAM) and decoherence processes. In such scenarios, the optimized many-body fidelity F is smaller than one, but is maximized at approximately the correct Hamiltonian parameter values.

Many-body fidelity estimator F_d

In practice, it is cumbersome to obtain the many-body fidelity F by either directly measuring non-local observables in the expression of F [341–343] or characterizing the experimental density matrix $\hat{\rho}(\tau)$ via quantum state tomography [344]. Recently, Ref. [257] introduced the estimator F_d to approximate the many-body fidelity between simulated and experimental time evolution in Eq. D.50. Crucially, this estimator only requires measurements in a fixed basis—here the computational z-basis—and requires a relatively small number of measurement samples. Based on universal statistical fluctuations and operator spreading, this estimator works in a variety of quantum devices, including bosonic and fermionic itinerant particles on optical lattices, trapped ions, and arrays of Rydberg atoms. Through F_d, the fidelity F can be estimated with a small number of samples for different parameter sets in $\{\hat{H}'\}$, yielding parameter values that are most likely to generate the observed data. To illustrate the effectiveness of this estimator in our system, we show in Fig. D.12 that the F_d closely tracks the many-body fidelity F in a numerical simulation of our system Hamiltonian shown in Eq. 6.1 of the main text in the presence of random phase-flip errors.

F_d calculation with experimental data

We describe the procedure used to calculate F_d and obtain the optimized Hamiltonian parameters shown in Fig. 6.4 of the main text. This procedure is adapted from the protocol detailed in Ref. [257].

On the experimental side, following the pulse sequence illustrated in Fig. D.11a, we prepare a randomly chosen five-excitation initial state, e.g., $z_{\text{init}} = 1001101010$, evolve the system for time τ, and read out the states of ten sites to get a bit-string z. Repeating the sequence $M = 4000$ times for the same z_{init} gives the probability of measuring each bit-string. We use the assignment probability matrix obtained from Sec. D.4 to mitigate the effect of read-out error, and only keep the bit-strings with five excitations considering the excitation-number-conserving Hamiltonian. This gives an estimate of the bitstring probability $p_z(\tau)$.

In the numerical simulation, we compute the theoretical probability $p_z^{(\mathrm{T})}(\tau, \hat{H}')$ of measuring the bit-string z after evolution under $\hat{H}'$ for a time τ

$$p_z^{(\mathrm{T})}(\tau, \hat{H}') \equiv |\langle z|\exp(-i\hat{H}'\tau/\hbar)|\Psi_0\rangle|^2 \, , \tag{D.51}$$

and its time-average $\overline{p}_z^{(\mathrm{T})}(\hat{H}')$

$$\overline{p}_z^{(\mathrm{T})}(\hat{H}') \equiv \lim_{\mathcal{T}\to\infty} \frac{1}{\mathcal{T}} \int_0^{\mathcal{T}} p_z^{(\mathrm{T})}(\tau, \hat{H}')\mathrm{d}\tau \tag{D.52}$$

where $|\Psi_0\rangle = |z_{\mathrm{init}}\rangle$.

Combining the results from experiments, the many-body fidelity estimator is given by

$$F_d(\tau, \hat{H}') = 2\frac{\sum_z p_z(\tau)p_z^{(\mathrm{T})}(\tau, \hat{H}')/\overline{p}_z^{(\mathrm{T})}(\hat{H}')}{\sum_z p_z^{(\mathrm{T})}(\tau, \hat{H}')^2/\overline{p}_z^{(\mathrm{T})}(\hat{H}')} - 1. \tag{D.53}$$

To reduce possible systematic errors, we repeat the above procedure for $M_{\mathrm{init}} = 40$ different initial states. In Fig. 6.4c of the main text, we plot the average and standard deviation over different initial states for $F_d(\tau, \hat{H}')$ with different parameter values of $\{\hat{H}'\}$.

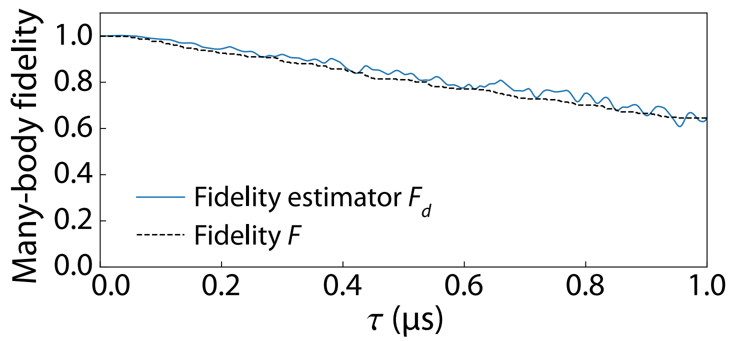

Figure D.12: **Numerical simulation of many-body fidelity F and its estimator F_d under dephasing errors.** The many-body fidelity F is calculated using Eq. D.50 for an evolution under the system Hamiltonian described in Eq. 6.1 of the main text, with injected phase-flip errors. The initial state is chosen to be $z_{\mathrm{init}} = 1100100101$ at random. The corresponding fidelity estimator F_d is shown for comparison, which is obtained from Eq. D.53 with the bit-string probabilities p_z and $p_z^{(\mathrm{T})}$ obtained from the numerical simulations of evolution with and without errors, respectively.

Parameter optimization

To address the complexity of optimizing over a large parameter space, a greedy algorithm was introduced in Ref. [257] for multi-parameter estimation. We follow the same procedure to obtain the optimized values for hopping terms $\{J_{i,j}\}$, including the nearest-neighbor hopping $J_{i,i+1}$ with $i = 1, \cdots, 9$ and the longer-range hopping $\overline{J_{i,i+k}}$ with $k = 2, \cdots, 9$, averaged over qubits i. We compute $F_d(\tau, \hat{H}')$ at a fixed evolution time τ, for the family of Hamiltonians $\hat{H}'(\{J_{i,j}\})$ in Eq. 6.1 of the main text. Here, we use the measured on-site interactions U_i (Fig. 6.3a of the main text) and assume a constant site energy $\epsilon_i/2\pi = 4.72\,\mathrm{GHz}$. To avoid systematic errors, we use the averaged estimated fidelity $\overline{F_d}(\hat{H}')$ over several times $\tau \in \{76, 148, 260, 420, 600, 780\}$ ns. For each guess of $\{J_l\}$, we randomly choose one element $l \in \{1, \cdots, 17\}$, then maximize $\overline{F_d}(\hat{H}')$ over a single J_l while keeping other parameters fixed. After optimizing for all 17 parameters, we repeat this process multiple times over distinct random permutations of $\{1, \cdots, 17\}$. After 11 rounds, both $\overline{F_d}$ and the optimized $\{J_{i,j}\}$ converge and are displayed in Fig. 6.4c and d in the main text.

Confidence intervals of fitted distributions

The confidence intervals for our estimated parameters were calculated with an analytic expression. The analytic expression is obtained under the following assumptions: (1) F_d is a good estimator for the many-body fidelity F, (2) our estimated fidelity exhibits independent Gaussian additive statistical errors, and (3) our estimated parameters are sufficiently close to their true values. In such cases, one can evaluate the covariance of the errors in estimated parameters, from which one can compute the confidence interval (the full derivation will appear in upcoming work).

In general, given a set of data of M randomly drawn samples, the fitted parameters $\boldsymbol{\theta}$ will have random fluctuations, expressed as $\boldsymbol{\theta} = \boldsymbol{\theta}^* + \boldsymbol{\delta\theta}$. Here, $\boldsymbol{\theta}^*$ is the true parameter value and $\boldsymbol{\delta\theta}$ is a random vector with a mean of zero and covariance given by

$$\mathrm{cov}(\boldsymbol{\theta}) = \frac{2}{M} \boldsymbol{H}\left[\tilde{F}_d(\boldsymbol{\theta}^*)\right]^{-1}, \tag{D.54}$$

with the Hessian $\boldsymbol{H}[\tilde{F}_d(\theta)]_{\mu\nu} \equiv \frac{\partial^2 \tilde{F}_d(\theta)}{\partial\theta_\mu \partial\theta_\nu}$. Knowledge of $\mathrm{cov}(\boldsymbol{\theta})$ gives the confidence intervals of our extracted parameters.

In our setting, we wish to learn the parameters $\boldsymbol{\theta}$ of an unknown Hamiltonian. We express our family of Hamiltonians as $H(\boldsymbol{\theta}) \approx H_0 + \sum_\mu (\theta_\mu - \theta_\mu^*) V^{(\mu)}$, where $H_0 \equiv H(\boldsymbol{\theta}^*)$ is the true Hamiltonian and $V^{(\mu)} \equiv \partial_\mu H(\boldsymbol{\theta})|_{\boldsymbol{\theta}=\boldsymbol{\theta}^*}$. While the Hessian $\boldsymbol{H}[F_d]$ is difficult to evaluate, we approximate it with the Hessian of the fidelity

$\boldsymbol{H}[F]$, whose analytical expression can be calculated using

$$\begin{aligned}
&\partial_\mu \partial_\nu F(\boldsymbol{\theta}) \\
&= \langle \Psi_0 | e^{iH_0 t} \partial_\mu \partial_\nu \left[e^{-iH(\boldsymbol{\theta})t} | \Psi_0 \rangle \langle \Psi_0 | e^{iH(\boldsymbol{\theta})t} \right] e^{-iH_0 t} | \Psi_0 \rangle \\
&\approx -2t^2 \Bigg[\sum_j \left| \langle E_j | \Psi_0 \rangle \right|^2 V_{jj}^{(\mu)} V_{jj}^{(\nu)} \\
&\qquad - \sum_j \left| \langle E_j | \Psi_0 \rangle \right|^2 V_{jj}^{(\mu)} \sum_k \left| \langle E_k | \Psi_0 \rangle \right|^2 V_{kk}^{(\nu)} \Bigg].
\end{aligned} \tag{D.55}$$

Here, $\{|E_j\rangle\}$ are the eigenstates of H_0 and $V_{jj}^{(\mu)} \equiv \langle E_j | V^{(\mu)} | E_j \rangle$.

We have verified that our expression is in agreement with Monte Carlo simulations of finite sets of samples. Note that the Monte Carlo sampling becomes computationally infeasible with a large number of parameters, while our analytic expression can be readily evaluated.

Influence of decoherence

A unitary time evolution of a quantum state under a Hamiltonian cannot capture the effect of decoherence present in experimental systems. In the context of Hamiltonian learning, the dominant decoherence channels in our system—population decay and dephasing—can affect the processes discussed in the previous sections by lowering the estimated many-body fidelity value from its decoherence-free counterpart. Here, we explain possible mitigation strategies in the processing of experimental data and discuss how these effects can be taken into account in numerical simulations.

The population decay lowers the excitation number in the system, leading to a finite lifetime T_1. Given the experimental Hamiltonian that conserves excitation numbers, we post-select the measured bit-strings z with the excitation numbers the same as the initial bit-string z_{init}. The purpose of this post-selection is to analyze the outcomes without quantum jump events [345, 346], thus mitigating the influence of population decay processes. However, if the lifetimes of different qubits exhibit a large variance, the post-selection will favor states with excitations on long-lived qubits at evolution times longer than the qubit lifetimes, failing to mitigate the population decay.

On the other hand, the dephasing errors can destroy the phase coherence within the same excitation number sector and cannot be corrected by post-selection, which results in a lower many-body fidelity F. This can be numerically simulated by injecting random phase-flip errors during the state evolution under the system Hamiltonian, which is shown in Fig. D.12. Here, the rate of phase-flip errors is chosen such that the resulting single-qubit coherence time is $T_2^* = 1.14\,\mu$s, close to the measured coherence time at $\omega_{01}/2\pi = 4.72\,$GHz shown in Table D.1. We note that the optimized F_d in Fig. 6.4c of the main text exhibits similar decay rate as the numerical simulation result illustrated in Fig. D.12, suggesting that dephasing is the dominant mechanism for the fidelity decay during the evolution. The offset between the two curves is a signature of SPAM errors independent of the evolution time. Possible sources of SPAM errors in our system include qubit XY crosstalk and pulse distortion, error in the read-out assignment probability matrix due to the infidelity of state preparation, and imperfect correction of the flux pulse distortion.

D.7 Numerical simulation of quantum walk at different interaction frequencies

To corroborate the observations in Fig. 6.5 of the main text, we numerically simulate the same set of evolutions using QuTiP [21]. We obtain the on-site interaction U_i from Fig. 6.3a of the main text, assume the evolution at the interaction frequency of $\omega_{01}/2\pi = 4.50\,$GHz, $4.55\,$GHz, $4.72\,$GHz, and $4.80\,$GHz, and use the hopping terms $J_{i,j}$ from the parameter optimization procedure described in Sec. D.6 to simulate the quantum walk dynamics (Fig. D.13a). The probability of measuring the bit-string z with excitations on sites Q$_i$ and Q$_j$ ($i \neq j$) is $p_z = \langle \hat{n}_i \hat{n}_j \rangle$, which is used to calculate the second moment $\mu_2 = \sum_z p_z^2$ shown in Fig. D.13b. The decoherence-free simulation results exhibit good agreement with the experimental results in Fig. 6.5 of the main text, confirming that (i) Hamiltonians with longer hopping ranges will converge to the ergodic limit $\mu_2^{\mathrm{e}} = 2/(D+1)$ at earlier times and (ii) decoherence does not visibly affect the quantum walk patterns.

D.8 Probing ergodic dynamics from global bit-string statistics

Integrability of 1D Bose-Hubbard models

In this section, we discuss the integrability of 1D Bose-Hubbard models in different parameter regimes. The standard 1D Bose-Hubbard model with only nearest-neighbor (NN) hopping corresponds to the spin-1/2 XY model in the limit of diverging on-site interaction $|U| \to \infty$, where the Hilbert space of a site is truncated to only $|0\rangle$ and $|1\rangle$, i.e., the hard-core limit. This model is known to be integrable and can be solved exactly with the Bethe ansatz [347]. The integrability of the

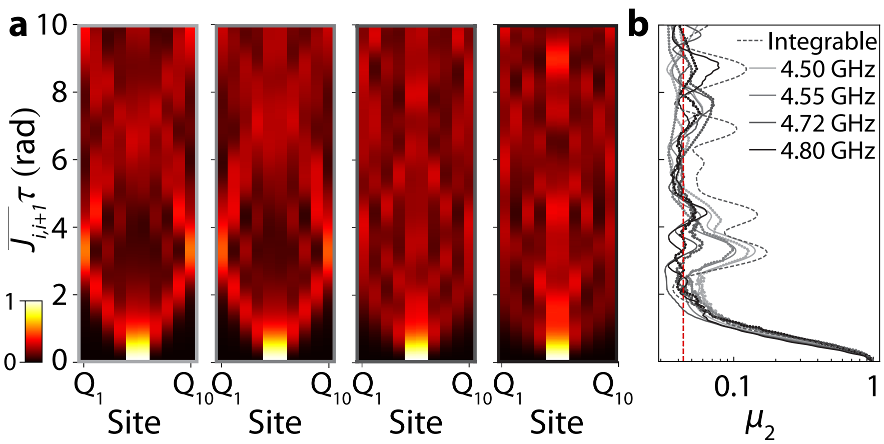

Figure D.13: **Numerical simulation of two-particle quantum walk with increasing hopping range.** **a**, Evolution of the population $\langle \hat{n}_i \rangle$ on sites Q_1–Q_{10} as a function of normalized evolution time $\overline{J_{i,i+1}}\tau$. The system is initialized in $z_{\text{init}} = 0000110000$ and the evolution occurs at $\omega_{01}/2\pi = 4.50$ GHz, 4.55 GHz, 4.72 GHz, and 4.80 GHz from left to right. **b**, The second moment μ_2 as a function of normalized evolution time $\overline{J_{i,i+1}}\tau$. Results calculated from the numerical simulation in panel **a** and the corresponding measurement in Fig. 6.5a of the main text are shown in gray-scale solid and dotted curves, respectively. The result from numerical simulation of the integrable Hamiltonian is shown as the gray dashed curve. The expected final value of the second moment μ_2^{e} for a generic ergodic system is indicated by the red dashed line.

hard-core Bose-Hubbard model can be broken by either adding long-range hopping terms or taking a finite on-site interaction strength.

Here, we emphasize that, in our system, finite on-site interaction $|U|$ is not the major factor that induces ergodicity. This is because the experiments illustrated in Figs. 6.5, 6.6, and 6.7 of the main text are performed at $\omega_{01}/2\pi \leq 4.80$ GHz, featuring a finite $|U/J| > 36$, much greater than unity. To further illustrate the effect of finite $|U/J|$, we simulate the standard Bose-Hubbard model with finite $|U/J|$ and without long-range hopping, where the Hamiltonian is obtained by removing the long-range hopping terms in Eq. 6.1 of the main text while using the on-site interaction U_i from Fig. 6.3a of the main text. In this case, while the simulated model is ergodic in a strict sense, the resulting second moment μ_2 is the same as the numerical simulation of the integrable model at evolution times $\tau < 2\,\mu$s, gradually approaching the ergodic limit at long evolution times $\tau > 5\,\mu$s (see the purple curve of Fig. D.14). Therefore, we conclude that the experimentally observed ergodic behavior, which emerges at an intermediate evolution time of $\tau \approx 360\,\mathrm{ns}$, originates from the long-range hopping terms.

Porter-Thomas distribution

In this section, we first introduce the Porter-Thomas (PT) distribution [254, 261] and then explain why we expect the PT distribution in our system. The PT distribution can be obtained from the distribution of overlap probabilities $p_z = |\langle z|\Phi\rangle|^2$ between a particular measurement outcome $|z\rangle$ and a state $|\Phi\rangle$ drawn from the Haar ensemble, the distribution of states on a Hilbert space that is invariant under any unitary operations. Specifically, in a Hilbert space of dimension D, the distribution of p_z takes the form [256, 261]

$$P(p_z)\,\mathrm{d}p_z = (D-1)(1-p_z)^{D-2}\,\mathrm{d}p_z, \tag{D.56}$$

which converges to the PT distribution in the limit of large D

$$P(p_z) \xrightarrow{D\to\infty} D\exp\left(-Dp_z\right). \tag{D.57}$$

Note that the second moment of $\{p_z\}$ from this distribution is given by

$$\mu_2 \equiv \sum_z p_z^2 = D\int_0^1 \mathrm{d}p_z\, p_z^2 P(p_z) = \frac{2}{D+1},$$

which is identical to the ergodic value μ_2^{e} described in the main text.

The PT distribution reflects the randomness of the measured wavefunction and has been shown to occur in Bose-Hubbard model with time-dependent random parameters [348] and deep random unitary circuits [49, 254]. Additionally, a large class of time-independent Hamiltonian is also shown to exhibit the normalized probability distribution $\tilde{p}_z \equiv p_z/\overline{p}_z$ following the PT distribution [257], where $\overline{p}_z$ is the time-averaged probability defined in Eq. D.52. This includes the ergodic Bose-Hubbard model with long-range hopping realized in our system. Although our Hamiltonian in Eq. 6.1 of the main text conserves excitation number, the dynamics exhibits this universal randomness within the two-excitation, hard-core sector[1] with a Hilbert space dimension of $D = 45$.

[1]We verify that the doublon states have a population of $\lesssim 1\%$ using numerical simulations, confirming that we are in the hard-core limit.

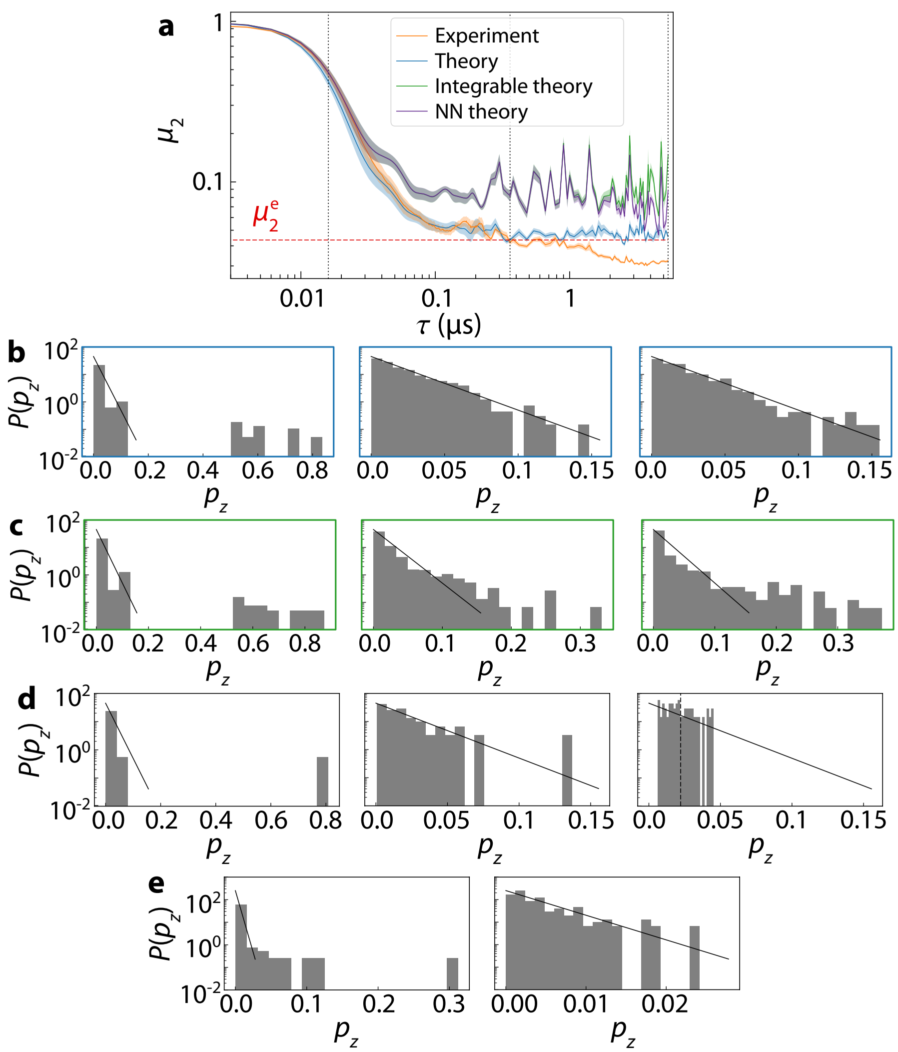

Figure D.14: **Additional results of bit-string statistics at 4.72 GHz.** **a**, Second moment μ_2 as a function of evolution time τ in our system from the experiment (orange) and the theory with the optimized parameter set in Fig. 6.4d of the main text (blue), compared to theoretical predictions of the integrable model (green) and the Bose-Hubbard model with NN hopping (purple). The shading on each curve corresponds to a standard deviation of the mean second moment for 20 randomly chosen initial bit-strings z_{init} in the two-excitation sector, and the red dashed line represents the ergodic value μ_2^{e}. **b** (**c**), Density histogram $P(p_z)$ of the distribution of theory (integrable theory) bit-string probabilities $\{p_z\}$ with the 20 initializations z_{init}'s at evolution times $\tau = 16$ ns, 360 ns, and 5.4 μs from left to right (indicated by the dotted lines in panel **a**). The solid lines show the PT distribution. **d**, Density histogram $P(p_z)$ of the distribution of experimental bit-string probabilities $\{p_z\}$ with a two-excitation initial state $z_{\text{init}} = 0000110000$ at evolution times $\tau = 16$ ns, 360 ns, and 5.4 μs from left to right. **e**, Density histogram $P(p_z)$ of the distribution of experimental bit-string probabilities $\{p_z\}$ with a five-excitation initial state $z_{\text{init}} = 0100111010$ at evolution times $\tau = 16$ ns and 360 ns in the left and right panels, respectively.

Furthermore, we claim that the time-averaged probability $\overline{p}_z$ is approximately constant due to the effective infinite temperature[2] of the initial and measurement states, and thus the unnormalized $\{p_z\}$ follows the PT distribution at intermediate evolution times, following the arguments below.

The notion of the effective temperature of a state is conventionally used to understand its *local* properties [349]: it is believed that an initial state, when quench-evolved under an ergodic Hamiltonian, will quickly thermalize such that its expectation value of a local observable $\hat{A}$ is very close to the value $\langle \hat{A}(t) \rangle \approx \mathrm{Tr}(\hat{A}\hat{\rho}_\beta)$ of a corresponding thermal state $\hat{\rho}_\beta$. In particular, the thermal state with infinite effective temperature $\hat{\rho}_{\beta=0}$ gives the expectation value $\langle \hat{A}(t) \rangle \approx \mathrm{Tr}(\hat{A})/D$. Here, we extend the above expectation beyond local quantities to the time-average of a global quantity $\overline{p}_z$ and expect this normalization factor $\overline{p}_z$ to be approximately constant since our initial state and measurement states are at infinite temperature. Consequently, we expect the raw, unnormalized $\{p_z\}$ to follow the PT distribution at intermediate evolution times, as shown in the middle panel of Fig. 6.6b in the main text.

Additional results of bit-string distribution

In this section, we provide additional results of numerical simulations and experimental data as a supplement to the bit-string distributions shown in Fig. 6.6b of the main text.

Numerical simulations of bit-string distributions

In addition to the experimental bit-string distribution shown in Fig. 6.6b, we present the results from numerical simulations of the system Hamiltonian in Eq. 6.1 of the main text and the integrable (nearest-neighbor and hard-core) Bose-Hubbard Hamiltonian in Fig. D.14b and c, respectively. After a short evolution time of $\tau = 16\,\mathrm{ns}$, the distribution is similar in the three cases of experiment (Fig. 6.6b of the main text, left), theory (Fig. D.14b, left), and integrable theory (Fig. D.14c, left), exhibiting a large probability p_z of bit-strings close to z_{init}. At intermediate evolution times (e.g. $\tau = 360\,\mathrm{ns}$), both the experimental (Fig. 6.6b in the main

[2] In detail, the effective temperature is infinite because in the rotating frame of $\omega = \omega_{01}$, the computational z-basis states have zero averaged energy $\langle \hat{H} \rangle_z = 0$ [see Eq. 6.1 of the main text]. It is the same as the averaged energy of a thermal state $\hat{\rho}_\beta$ at infinite temperature $\mathrm{Tr}(\hat{H}\hat{\rho}_{\beta=0}) = \mathrm{Tr}(\hat{H}\mathbb{I})/D = 0$, where $\beta = 1/T^*$ is the inverse effective temperature and $\hat{\rho}_{\beta=0} = \mathbb{I}/D$.

text, middle) and the theoretical (Fig. D.14b, middle) bit-string distributions follow the PT distribution while the integrable theory predicts more bitstrings with large p_z, resulting in a larger second moment μ_2. Due to the absence of decoherence processes, the distributions stay the same for the numerical simulations at long evolution times, e.g. $\tau = 5.4\,\mu$s (right panels of Fig. D.14b and c).

Experimental bit-string distribution from a single, two-excitation initial state

The probability distributions shown in Fig. D.14b and c and in Fig. 6.6b of the main text are obtained by combining the results from 20 randomly chosen initial states z_{init} to reduce statistical errors. Here, we show that the experimental results from a single initial state ($z_{\text{init}} = 0000110000$), displayed in Fig. D.14d, obey the same trend as predicted by the ergodic evolution. Due to the limited counts $N(p_z) = D = 45$ of p_z's, the tail of PT distribution is not very clear in the middle panel of Fig. D.14d. Nonetheless, the distinction among the three panels in Fig. D.14d is obvious, with p_z aggregating towards $1/D$ in the right panel due to decoherence. Note that the effect of limited Hilbert space dimension is negligible for the combined statistics in Fig. 6.6b of the main text.

Experimental bit-string distribution from a five-excitation initial state

To illustrate that the bit-string distribution during ergodic evolution is universal for various excitation numbers, we show the experimental bit-string distribution obtained from preparing a randomly chosen five-excitation initial state $z_{\text{init}} = 0100111010$ in Fig. D.14e. The left panel displays the initial evolution stage at $\tau = 16$ ns and the right panel shows a histogram at $\tau = 360$ ns that is closer to the PT distribution than the middle panel of Fig. D.14d owing to the larger Hilbert space dimension $D = 252$.

Effect of decoherence

In the measurement and data processing of bit-string statistics, we use the same pulse sequence and post-select the sector that conserves the excitation number discussed in Sec. D.6, which mitigates the effects of population decay. To illustrate the effect of dephasing on bit-string statistics, we calculate the second moment μ_2 and the histogram of bit-string probability distribution $\{p_z\}$ using data from the numerical

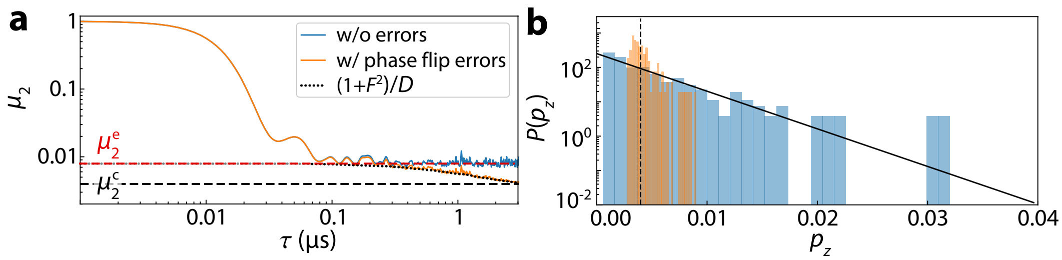

Figure D.15: **Numerical simulation of bit-string statistics under dephasing errors.** **a**, The evolution of second moment μ_2 of a five-excitation initial state $z_{\text{init}} = 1100100101$ assuming the error-free model (blue) and the model with added phase-flip errors (orange). The red (black) dashed line shows the ergodic (classical) limit μ_2^{e} (μ_2^{c}) of the second moment and the dotted curve shows the decay of the second moment predicted by the many-body fidelity as $\mu_2 \approx (1 + F^2)/D$. **b**, The histogram of bit-string probability distribution $\{p_z\}$ obtained at evolution time $\tau = 3\,\mu$s in panel **a**. The error-free result and the result with dephasing are shown in blue and orange, respectively. The solid line represents the PT distribution and the dashed line shows the uniform classical distribution $p_z = 1/D$.

simulation of the system Hamiltonian without errors and with added phase-flip errors that generates Fig. D.12. Here, we find that the second moment of the error-free simulation converges to the ergodic limit μ_2^{e} after the quench while μ_2 obtained from the simulation with phase-flip errors keeps decreasing (see Fig. D.15a). The second moment eventually converges to the classical limit

$$\mu_2^{\text{c}} = \sum_z p_z^2 = \sum_z \frac{1}{D^2} = \frac{1}{D}. \tag{D.58}$$

The corresponding histogram at a long evolution time $\tau = 3\,\mu$s, displayed in Fig. D.15b, follows the PT distribution for the error-free simulation and approaches the classical distribution for the simulation with dephasing. The above numerical simulations qualitatively reproduce the experimental results shown in Fig. 6.6a and b of the main text and in Fig. D.14a.

We also provide a heuristic argument to show that the decay of the second moment μ_2 can be predicted by a quantity $(1 + F^2)/D$ involving the many-body fidelity F under certain error models. This can be understood by utilizing an ansatz

$$p_z = F q_z + (1 - F) q_z^{\perp} \tag{D.59}$$

introduced in Refs. [257, 350], which relates the empirical distribution of p_z in the presence of noise with the ideal PT distribution of q_z and a classical distribution of $q_z^\perp \approx 1/D$, uncorrelated with q_z, with a second moment close to $1/D$, i.e., $\sum_z (q_z^\perp)^2 \approx \mu_2^{\mathrm{c}} = 1/D$. Using this ansatz, the second moment is predicted to be $\mu_2 = \sum_z p_z^2 \approx (1 + F^2)/D$, which is supported by our numerical simulations with dephasing errors[3] in Fig. D.15a.

[3]However, we note that this result depends on the specific error model. For example, if the dominant error source is qubit decay from the $|1\rangle$ to $|0\rangle$ state, the term $q_z^\perp$ will favor bit-strings with 0's, converging over time to a single bit-string $00\cdots0$. This limiting distribution has a large second moment $\sum_z \delta^2_{z=0\cdots0} = 1$, hence the overall second moment μ_2 grows over time.